접착 및 계면 제6권 제1호, 2005년
<연구논문>

Journal of Adhesion and Interface
Vol. 6, No. 1, 2005

A Strategy for the Simulation of Adhesive Layers

A. Öchsner†, G. Mishuris[1], and J. Gràcio

Department of Mechanical Engineering Centre for Mechanical Technology and Automation, University of Aveiro, Campus Universitrio de Santiago, 3810-193 Aveiro, Portugal

[1]*Department of Mathematics, Rzeszow University of Technology, W. Pola 2, 35-959 Rzeszow, Poland*

(Received December 28, 2004; Accepted January 14, 2005)

Abstract: The high accurate simulation of very thin glue layers based on the finite element method is still connected to many problems which result from the necessity to construct a complicated mesh of essentially different sizes of elements. This can lead to a loss of accuracy, unstable calculations and even loss of convergence. However, the implementation of special transmission elements along the glue line and special edge-elements in the near-edge region would lead to a dramatic decrease of the number of finite elements in the mesh and thus, prevent unsatisfactory phenomena in numerical analysis and extensive computation time. The theoretical basis for such special elements is the knowledge about appropriate transmission conditions and the edge effects near the free boundary of the adhesive layer. Therefore, recently proposed so-called non-classical transmission conditions and the behavior near the free edge are investigated in the context of the single-lap tensile-shear test of adhesive technology.

Keywords: *adhesive layers, interface, transmission conditions, finite element method, free-edge effects*

1. Introduction

Different approximation procedures for the solution of partial differential equations are known (cf. Figure 1) and each of the method possess its own advantages or disadvantages. The finite element method (FEM) is derived from variation principles or the principle of virtual work and results in a symmetric system of equations with a diagonally dominant matrix. Many commercial codes are available and such codes are widely used for industrial simulations. Even with commercial codes, arbitrary geometries and non-linearities, e.g. plastic or visco-elastic material behavior, can nowadays be considered. The finite difference method (FDM) is derived from differential equations of the corresponding field problem and can result in a non-symmetric and diagonally dominant matrix. This method is easily to transform into computational codes but reveals its disadvantages for complex geometries, singular crack behavior or non-continuous solutions. The boundary element method (BEM) is derived from integral equations and results in a non-symmetric and full matrix. The advantage of this method is that only the boundary needs to be discretisized. The main disadvantage is that arbitrary inhomogeneous structures and non-linearities are difficult to transform completely into integral equations. Therefore, this method is reserved for special applications, e.g. fracture mechanics.

Nevertheless, the application of the finite element method requires a lot of experience and many problems are still unsolved or unsatisfactory with respect to economic requirements. The high-accurate simulation of thin adhesive layers requires in the framework of the finite element simulation the introduction of a huge amount of finite elements. The generation of such computational models is on the one hand difficult to automatize and extremely time-consuming and on the other hand later on, the solving of the resulting system of equations may also take considerable time. Furthermore, complicated meshes with elements of essentially different sizes and deformed transition elements can lead to numerical problems, such as loss of accuracy or even loss of convergence[2,3]. A further problem is connected with the fact that the aspect ratio, i.e. length-width ratio, is limited for classical finite elements to a maximum number of 1:2 in order to avoid numerical instability. The improvement of such calculations is therefore not only an economic requirement but also the necessity for a better dimensioning of structural applications which will lead to maximum utilization of the materials and higher reliability and service life of entire structures and applications.

A simplified adhesively bonded joint under shear load is

† Corresponding author: e-mail: aoechsner@mec.ua.pt

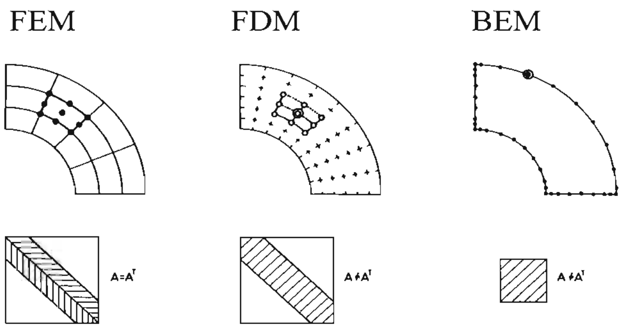

Figure 1. Numerical approximation procedures for partial differential equations.

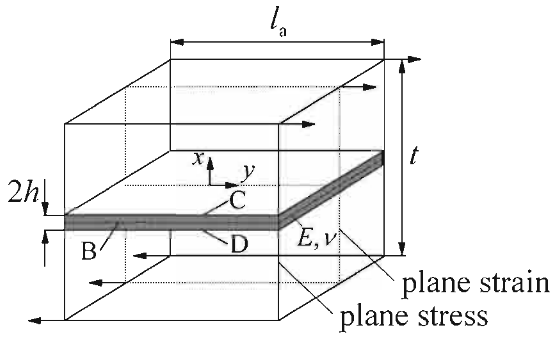

Figure 2. Schematic representation of an adhesively bonded joint.

shown in Figure 2 with its geometrical dimensions. The real three-dimensional behavior can be approximated by two-dimensional limiting cases in order to reduce the dimensionality (this leads to significant less finite elements in the computational model): the plane strain case which holds inside the joint and the plane stress case which holds at the free surface. In the following, we are going to present and to investigate so called non-classical transmission conditions which are the theoretical basis for the introduction of novel finite elements for adhesive layers. It should be mentioned here that the overall deformation behavior is determined by the plane strain case. However, the total description based on two-dimensional models requires also the consideration of the plane stress case.

2. Transmission Conditions

The idea of transmission conditions can easily be introduced based on simple one-dimensional structural elements, such as springs or rods (cf. Figure 3). The relative displacements of both ends for symmetric loading, $[u_x] = u_1\text{-}(-u_1)$, can be related to the acting force F in the spring or the stress σ in the rod according to Eq. (1) (k: spring stiffness; E: Young's modulus; A: cross-sectional area; l: length).

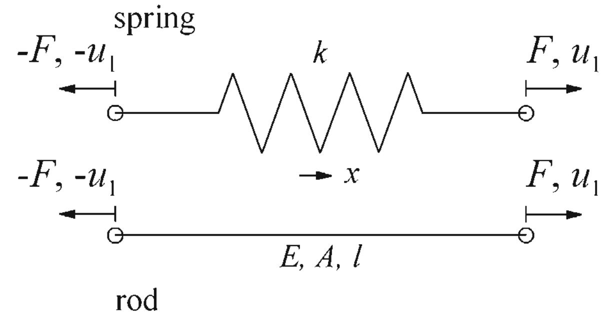

Figure 3. Simple one-dimensional structural elements.

Table 1. Possible sets of transmission conditions along the line $x = 0$ depending on the relative properties of the thin intermediate layer. 2D case

Interface	Transmission conditions			
soft	$[u_y]\text{-}a_2\sigma_{xy}=0$	$[u_x]\text{-}a_1\sigma_x = 0$	$[\sigma_{xy}] = 0$	$[\sigma_x] = 0$
comparable	$[u_y] = 0$	$[u_x] = 0$	$[\sigma_{xy}] = 0$	$[\sigma_x] = 0$
stiff	$[u_y] = 0$	$[u_x] = 0$	$[\sigma_{xy}]+\partial/\partial x(a_3\,\partial u_y/\partial y)$	$[\sigma_x] = 0$

Table 2. Parameters $a_i(y)$ for the plane strain and plane stress case

Case	a_1	a_2	a_3
plane strain	$\frac{2h(1+v)(1-2v)}{E(1-v)}$	$\frac{4h(1+v)}{E}$	$\frac{2hE}{1-v^2}$
plane stress	$\frac{2h(1-v^2)}{E}$	$\frac{4h(1+v)}{E}$	$2hE$

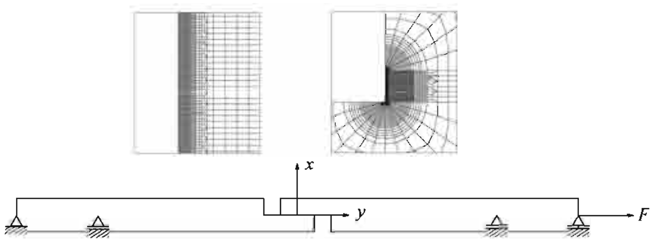

Figure 4. Two-dimensional mesh (details) and boundary conditions.

$$\text{(spring); } [u_x]=2u_1=\frac{F}{k} \quad [u_x]=2u_1\frac{l}{E}\cdot\sigma \text{ (rod)} \qquad (1)$$

Recently, so-called non-classical transmission conditions for two-dimensional problems were proposed which relate the difference of displacements $[u]$ and stresses $[\sigma]$ at the adhesive/adherend interface (cf. line C, D in Figure 2) to the behavior in the middle of the adhesive layer (cf. line B in Figure 2, $x = 0$). Table 1 and 2 summarize these non-classical transmission conditions for isotropic elastic material behavior[4,5]. The elastic constants E and v are related to the adhesive layer of thickness $2h$.

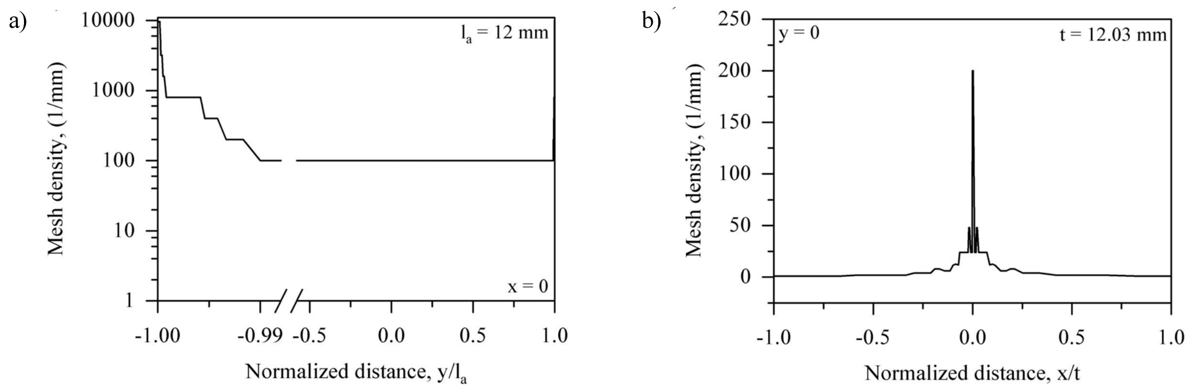

Figure 5. Mesh density: a) along the glue line (x = 0); b) transverse to the glue line (y = 0).

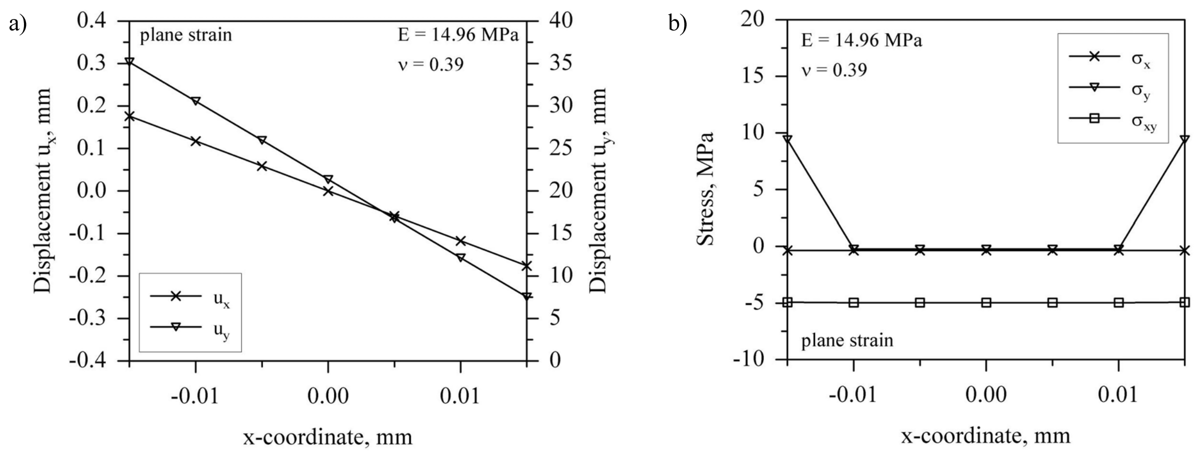

Figure 6. Stress orthogonal the bond line for an adhesive with ν = 0.39 and E = 14.96 MPa.

The classification soft, comparable and stiff relates to the relationship between the stiffness of the adhesive and the adherend (E/E_s). The formulae in Table 2 have been found under the assumption that the material parameters of the adhesive layer do not change perpendicular to the glue line. General expressions which incorporate any functional dependency can be found in[6].

The knowledge about the validity of these conditions will enable the derivation of novel elements.

3. Finite Element Modeling

The validity of the indicated non-classical transmission conditions will be numerically investigated in the framework of the single-lap tensile-shear test of adhesive technology (cf. Figure 4)[7]. Later on, this procedure will be used for the experimental verification of the novel computation method. Figure 5 shows the high mesh density which is required for accurate solutions especially near the free boundary of the adhesive layer. Special elements with reduced integration using an assumed strain formulation written in natural coordinates which insures good representation of the shear strains in the element were used. A commercial finite element software (MSC.Marc) was used for simulating the mechanical behavior of the thin adhesive layer with a thickness of $2h = 30$ mm. In the following, the results are presented for stepped brass adherends ($E_s = 119704$ MPa, $\nu_s =$ 0.3395, length 106 mm, width 25 mm, total depth 12 mm) and an adhesive ($E = 14.96$ MPa; $\nu = 0.39$) which can be classified as soft according to Table 1. We assumed for these calculations that the adhesive layer is isotropic and homogeneous. Both cases, i.e. the plane strain and plane stress case were investigated. However, to reduce the amount of presented results, only the plane strain case is presented here. It should be mentioned here that the plane stress case reveals similar results.

4. Results

First of all, Figure 6 shows the displacement and stress distribution perpendicular to the glue line, this means along the line where $y = 0$ holds, in order to verify some basic

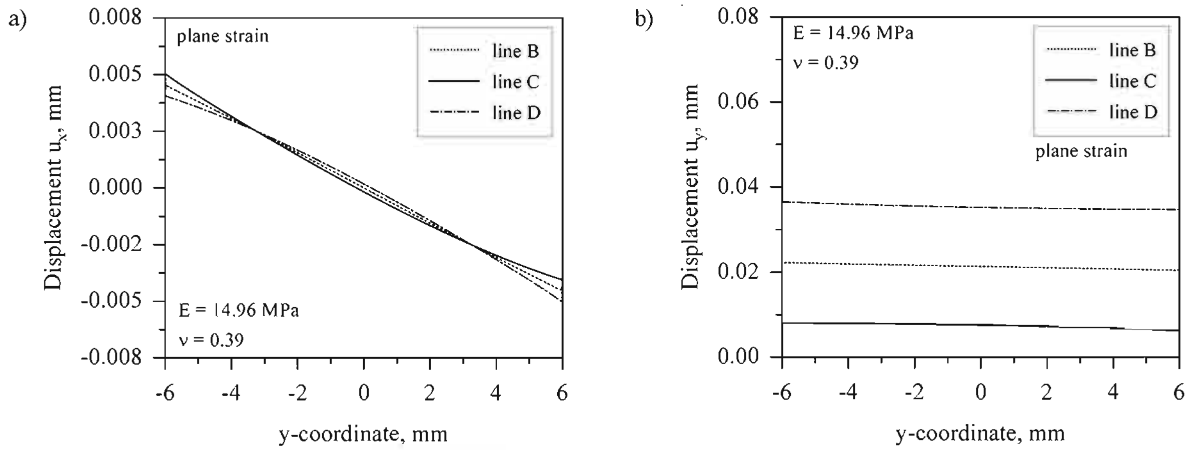

Figure 7. Displacement distribution for lines B, C and D.

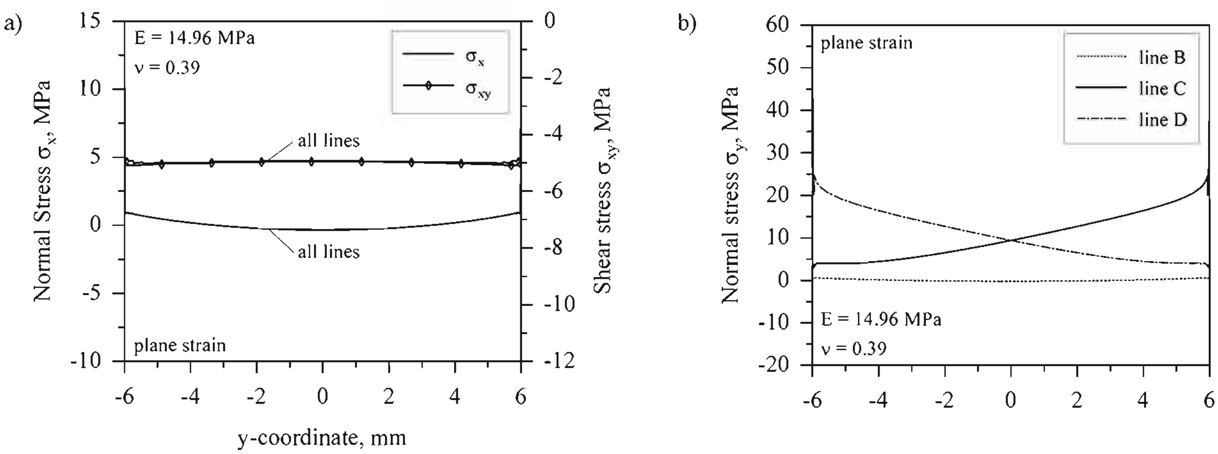

Figure 8. Normal and shear stress distribution for lines B, C and D.

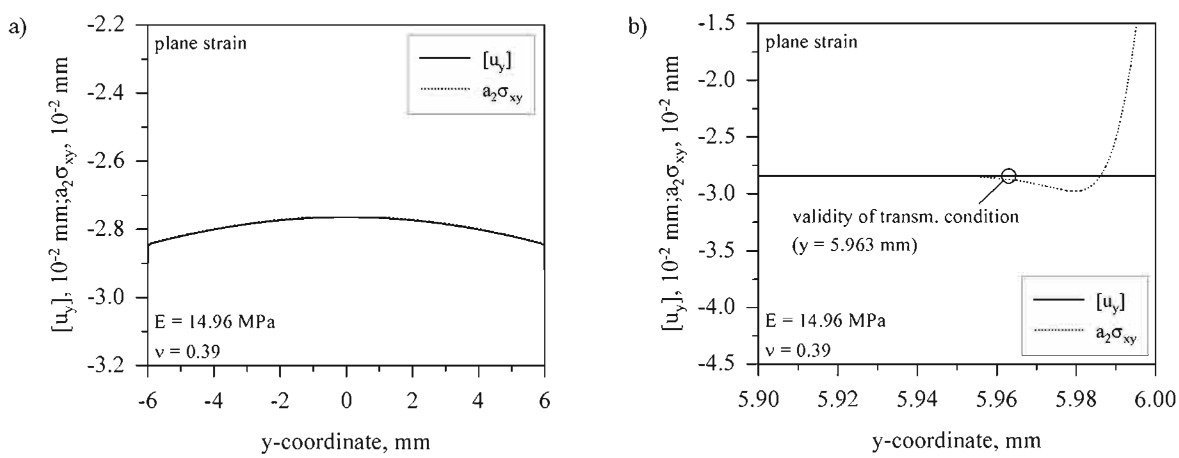

Figure 9. Verification of the first transmission condition along the imperfect interface (plane strain).

assumptions used for the derivation of the transmission conditions. It can be seen that the justified linear behavior for the displacements and the constant behavior for the stresses inside the adhesive layer are fulfilled. Furthermore, this result holds for any line $y = const$ (except the region near the free boundary). The behavior of the σ_y component results from the averaging of the adhesive and adherend values at the interface node. However, the correct extra-

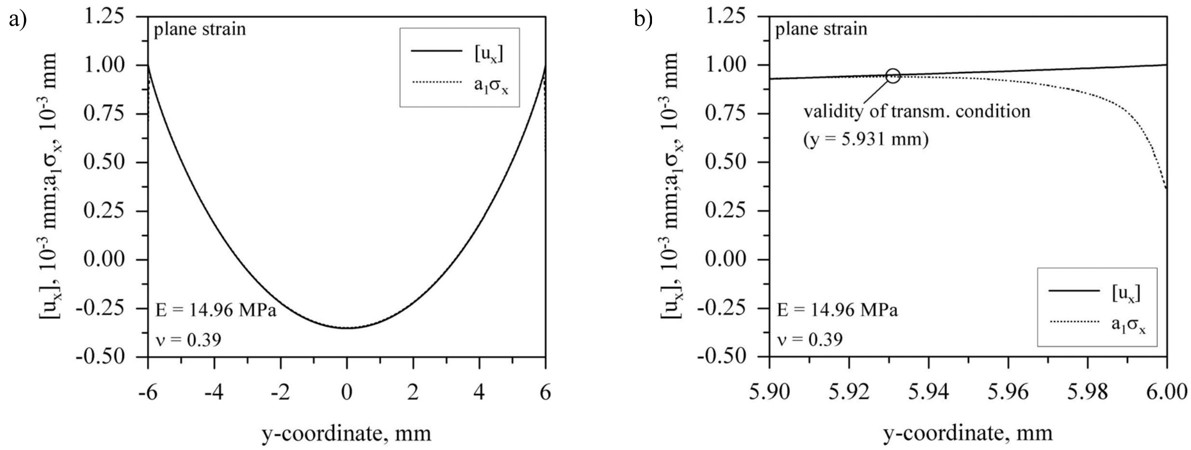

Figure 10. Verification of the second transmission condition along the imperfect interface (plane strain).

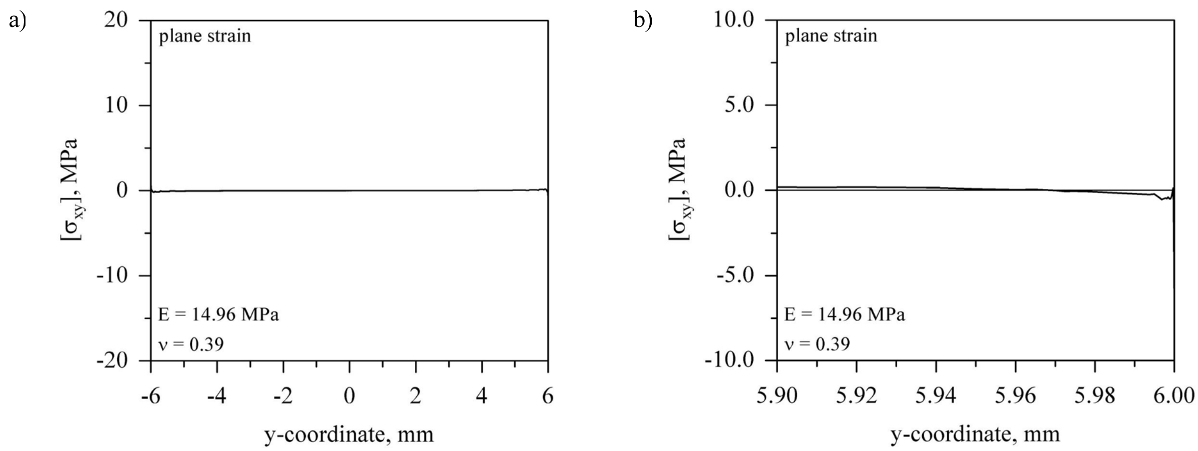

Figure 11. Verification of the third transmission condition along the imperfect interface (plane strain).

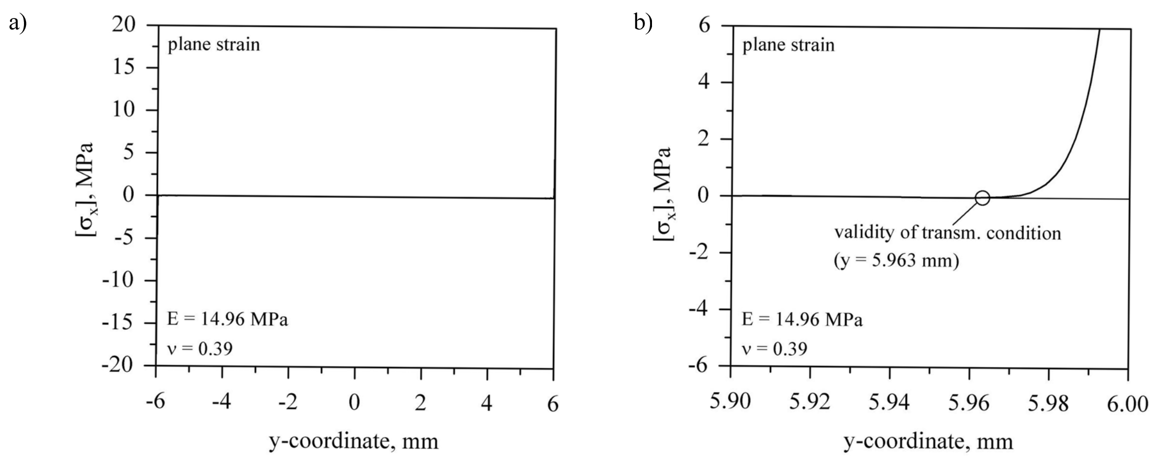

Figure 12. Verification of the fourth transmission condition along the imperfect interface (plane strain).

polation of this value (i.e. constant value in the whole adhesive layer) can be done without any loss of generality of the presented results. To avoid this behavior it would be necessary to refine significantly the finite element mesh also in this region. However, it would increase the total amount of unknowns in such a way that it would be difficult to compute the 2D problem on a standard PC with 1.5 GB of RAM.

Figures 7 and 8 illustrate the displacement and stress distribution along the glue line ($x = 0$) and the interface lines C and D (cf. Figure 1). These values which were derived from FEM analysis will be evaluated according to the relationships given in Table 1 and 2 in order to investigate the validity of the given conditions.

Figures 9 ~ 12 show the evaluation of all four transmission conditions given in Table 1 along the whole glue line and additionally, for magnifications near the free surface. It can be seen in Figures 9 and 10 that the transmission conditions are fulfilled along a very long range of the glue line and that only very near the free surface the conditions fail. In this region, also the influence of the stress singularity becomes visible. Thus, special singularity elements need to be derived in order to offer a complete set of special adhesive elements for the whole range of the glue line. The validity of the transmission conditions is based in our evaluation on a 1% criterion for the deviation between the left and right hand side of the equations presented in Table 1.

However, the application of the 1% criterion is difficult to realize for the jump $[\sigma_{xy}]$ and $[\sigma_x]$ shown in Figures 11 and 12 because the values should be equal to zero. Nevertheless, it can be seen that the conditions are fulfilled in the same range as indicated in Figures 9 and 10.

5. Conclusions and Outlook

In the present work, non-classical transmission conditions were presented and their validity investigated in the framework of the single-lap tensile-shear test of adhesive technology. It could be shown that the proposed transmission conditions are valid over a very long range of the glue line. Only near the free surface, the conditions fail and the size of this zone is obtained more or less independently of the evaluated transmission condition.

The knowledge about the validity region makes it possible to drastically decrease the number of finite elements in the constructed mesh by introducing special transmission elements instead of the thin intermediate zone between the different materials and also to prevent unsatisfactory phenomena in the numerical analysis. The development of such special elements and the implementation into a finite element code is the topic of our future research work. Furthermore, non-linear material, i.e. plastic and visco-elastic, will be investigated and corresponding transmission conditions will be derived and their validity examined.

Acknowledgments

A. Öchsner is grateful to Portuguese Foundation of Science and Technology for financial support.

G. Mishuris participated in this research during his Visiting Fellowship at LSBU granted by the Leverhulme Trust.

References

1. K. Knothe and H. Wessel, Finite Elemente, Springer, Berlin (1992).
2. A. E. Hatheway, in Proceedings MSC/NASTRAN User's Conference, Universal City, USA (1986).
3. S. C. Pradhan, K. Y. Lam, and T. E. Tay, *Int. J. Adhes.*, **50**, 395 (2000).
4. G. Mishuris and A. Öchsner, *Comp. Struc.*, to appear (2005).
5. G. Mishuris, A. Öchsner, and G. Kuhn, *Finite Elem. Anal. Des.*, Submitted for publication.
6. G. Mishuris, A. Öchsner, and G. Kuhn, *Finite Elem. Anal. Des.*, Submitted for publication.
7. ISO 11003-2. Adhesives - Determination of shear behaviour of structural bonds - Part 2: Thick-adherend tensile-test method (1993).

 CMC, vol.2, no.4, pp.227-238, 2005

FEM-Analysis of Nonclassical Transmission Conditions between Elastic Structures Part 1: Soft Imperfect Interface.

G. Mishuris[1], A. Öchsner[2] and G. Kuhn[3]

Abstract: FEM-evaluation of imperfect transmission conditions has been performed for a modelling problem of an elastic structure with a thin intermediate interface. Very good correlations with theoretical results have been obtained. Additionally, the possible error connected with introducing the transmission conditions instead of the intermediate zone has been estimated depending on mechanical properties of the zone.

keyword: Elasticity, imperfect interface, nonclassical transmission conditions, finite element method

1 Introduction

Composite materials are usually considered as nonhomogeneous solids with perfect bonding between different phases of the composites [Allen(1969) and Ashby, Fleck, Gibson, Hutchinson, and Wadley (2000)]. On the other hand, such structures, in fact, contain thin intermediate layers matching materials of the phases together. Moreover, features of the layers may play an important role and influence the composite properties. However, when a structure consists of components of essentially different sizes and properties, FEM analysis of the structure becomes very difficult. This fact follows from the necessity to construct a complicated mesh structure which, in turn, may lead to unstable numerical calculations [Hatheway (1989)].

The aim of this paper is to investigate by FEM analysis one of the possible approaches to avoid such problems. Namely, we are going to consider in detail the so-called imperfect interface approach. It consists of replacing the real thin interphase which is connecting the different materials by special transmission conditions. These conditions are accurately extracted by asymptotic analysis taking into account possible small parameters involved in the problem. Such a small parameter is definitely here the thickness of the interphase between the materials. However, other parameter can also appear which are connected with the relative difference in the mechanical properties of the interphase and the bonded materials. Three cases can be separated: i.e. the soft interphase, the stiff interphase and a comparable interphase with respect to mechanical properties. The main efforts are made in the paper to verify the accuracy of the transmission conditions not in terms of the asymptotic analysis estimate (like $O(\varepsilon)$), but in exact values.

In the next section, we accurately discuss the asymptotic procedure to evaluate the transmission conditions for the soft inhomogeneous interface. In the case of the interphase with properties comparable to those of the matched materials, we refer the prospective reader to the monograph [Movchan and Movhan (1995)]. We verify the applicability of the obtained conditions and discuss edge effects appearing in the problem. Various combinations of the material parameters are under consideration. In this paper, we restrict ourselves to simple load cases and symmetrical samples for homogeneous and nonhomogeneous interphases. Stiff interphases and other effects (nonsymmetric samples, complicated loadings, norm estimates) will be investigated in the second part of the paper.

2 Asymptotic evaluation of transmission conditions between elastic bodies for soft interphase (2D-problem)

Let us consider a model plane strain problem for a bimaterial elastic solid in the rectangle $\Omega_h = \Omega_+ \cup \Omega_- \cup \Omega$, where $\Omega_\pm = \{(x,y), \pm y \geq h\}$, $\Omega = \{(x,y), |y| \leq h\}$ (see Fig. 1). We assume that the intermediate layer Ω is inhomogeneous and isotropic, while the bonded materials are isotropic and homogeneous.

Let $\mathbf{u}_\pm(x,y)$ and $\mathbf{u}(x,y)$ be vectors of displacements: $\mathbf{u}_\pm = [u_x^\pm, u_y^\pm]^\top$, $\mathbf{u} = [u_x, u_y]^\top$. They satisfy Lamé equa-

[1] RzUT, Rzeszow, POLAND.
[2] UA, Aveiro, PORTUGAL.
[3] FAU, Erlangen, GERMANY.

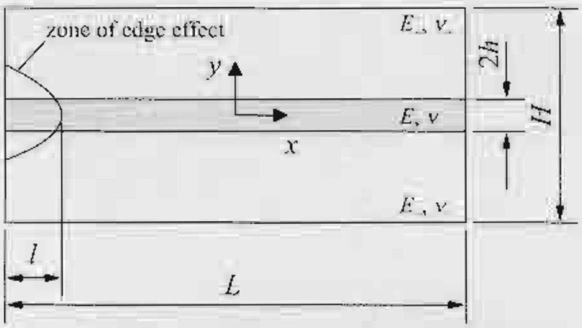

Figure 1 : Schematic representation of the problem

tions in the corresponding domains:

$$\mathcal{L}_\pm \mathbf{u}_\pm = \mathbf{0}, \quad (x,y) \in \Omega_\pm, \qquad \mathcal{L}\mathbf{u} = \mathbf{0}, \quad (x,y) \in \Omega, \tag{1}$$

where the differential operators $\mathcal{L}_\pm$ and $\mathcal{L}$ are defined in the following manner:

$$\mathcal{L}_\pm = \begin{pmatrix} (\lambda_\pm + 2\mu_\pm)D_x^2 + \mu_\pm D_y^2 & (\lambda_\pm + \mu_\pm)D_x D_y \\ (\lambda_\pm + \mu_\pm)D_x D_y & (\lambda_\pm + 2\mu_\pm)D_y^2 + \mu_\pm D_x^2 \end{pmatrix}, \tag{2}$$

$$\mathcal{L} = \begin{pmatrix} D_x(\lambda + 2\mu)D_x + D_y \mu D_y & D_x \lambda D_y + D_y \mu D_x \\ D_y \lambda D_x + D_x \mu D_y & D_y(\lambda + 2\mu)D_y + D_x \mu D_x \end{pmatrix}. \tag{3}$$

Here D_x and D_y are the respective partial derivatives, while the material parameters can change their values within the interphase:

$$\mu = \mu(x,y), \quad \lambda = \lambda(x,y). \tag{4}$$

Some boundary conditions are assumed to be satisfied on the exterior boundaries:

$$\begin{aligned} \mathcal{B}_\pm \mathbf{u}_\pm &= \mathbf{0}, \quad (x,y) \in \partial\Omega_h \cap \partial\Omega_\pm, \\ \mathcal{B}\mathbf{u} &= \mathbf{0}, \quad (x,y) \in \partial\Omega_h \cap \partial\Omega. \end{aligned} \tag{5}$$

We do not use precise forms of the boundary operators $\mathcal{B}_\pm$ and $\mathcal{B}$ because they will not play any role in a formal asymptotic procedure. However, they are extremely important, of course, for justification of the final asymptotic estimate for the obtained solution.

Along the interior boundaries $y = \pm h$, the perfect transmission conditions (6) should be satisfied (the vectors of displacements and stresses are continuous across the interface):

$$\mathbf{u}_\pm(x, \pm h) = \mathbf{u}(x, \pm h), \quad \sigma_\pm^{(y)}(x, \pm h) = \sigma^{(y)}(x, \pm h). \tag{6}$$

where $\sigma_\pm^{(y)}(x, \pm h)$ and $\sigma^{(y)}(x, \pm h)$ are tractions along the boundaries of the thin interphase between the adherends which are calculated from Hooke's law:

$$\sigma_\pm^{(y)}(x,y) = \mathcal{M}_\pm \mathbf{u}_\pm(x,y), \quad \sigma^{(y)}(x,y) = \mathcal{M}\mathbf{u}(x,y). \tag{7}$$

$$\mathcal{M} = \begin{pmatrix} \mu D_y & \mu D_x \\ \lambda D_x & (\lambda + 2\mu)D_y \end{pmatrix}, \tag{8}$$

and $\mathcal{M}_\pm$ are defined in the same manner by replacing μ and λ with $\mu_\pm$ and $\lambda_\pm$.

We assume that the intermediate layer is essentially thinner in comparison to the characteristic size of the body: $h << \min\{L, H\}$. This allows us to introduce in the problem a small dimensionless parameter $\varepsilon << 1$ in the following manner: $(x,y) \in \Omega$

$$y = \varepsilon\xi, \qquad \xi \in [-h_0, h_0], \quad h_0 \sim \min\{L, H\}. \tag{9}$$

This makes it possible to use asymptotic methods to perform an analysis of the problem. It is a well known fact that the perfect transmission conditions are still applicable if the elastic constants of the intermediate layer are comparable in values with those of the matched materials (see, for example, [Movchan and Movhan (1995)]).

We assume in this paper that there is a significant difference in the elastic properties. Namely, there exists an additional small parameter connected with the mechanical properties of the bimaterial structure (the interphase is essentially softer than the both matched materials):

$$\mu(x,y) = \varepsilon\mu_0(x,\xi), \quad \lambda(x,y) = \varepsilon\lambda_0(x,\xi), \tag{10}$$

$$\mu_0 \sim \lambda_0, \quad \mu_0 \sim \mu_\pm. \tag{11}$$

Let us denote by $\mathbf{w}(x,\xi) = \mathbf{u}(x,\varepsilon\xi)$ the solution within the domain $\Omega_0 = \{(x,\xi), |\xi| \le h_0\}$. In the new notations, all operators can be rewritten as follows:

$$\mathcal{L} = \varepsilon^{-1}\mathcal{L}_0 + \mathcal{L}_1 + \varepsilon\mathcal{L}_2, \quad \mathcal{M} = \mathcal{M}_0 + \varepsilon\mathcal{M}_1, \tag{12}$$

where $\mathcal{L}_0 = D_\xi \mathbf{A}_0 D_\xi$, $\mathcal{L}_2 = D_x \mathbf{A}_2 D_x$, $\mathcal{M}_0 = \mathbf{A}_0 D_\xi$, $\mathcal{M}_1 = \mathbf{A}_1 D_x$, $\mathbf{A}_0\mathbf{A}_2 = \mu_0(2\mu_0 + \lambda)\mathbf{I}$ and

$$\mathcal{L}_1 = \begin{pmatrix} 0 & D_x\lambda_0 D_\xi + D_\xi \mu_0 D_x \\ D_\xi \lambda_0 D_x + D_x \mu_0 D_\xi & 0 \end{pmatrix}, \tag{13}$$

$$\mathbf{A}_0 = \begin{pmatrix} \mu_0 & 0 \\ 0 & \lambda_0 + 2\mu_0 \end{pmatrix}, \quad \mathbf{A}_1 = \begin{pmatrix} 0 & \mu_0 \\ \lambda_0 & 0 \end{pmatrix}. \tag{14}$$

Then, a part of the problem under consideration within the domain Ω_0 can be reformulated in the following manner: we should look for the solution $\mathbf{w}$ in the domain Ω_0 satisfying the equation:

$$\left(\mathcal{L}_0+\varepsilon\mathcal{L}_1+\varepsilon^2\mathcal{L}_2\right)\mathbf{w}=\mathbf{0}, \quad (x,\xi)\in\Omega_0, \tag{15}$$

and the interior transmission conditions:

$$\begin{aligned}\mathbf{u}_\pm(x,\pm\varepsilon h_0)&=\mathbf{w}(x,\pm h_0),\\ \sigma_\pm^{(y)}(x,\pm\varepsilon h_0)&=\left(\mathcal{M}_0+\varepsilon\mathcal{M}_1\right)\mathbf{w}|_{\xi=\pm h_0}.\end{aligned} \tag{16}$$

According to a standard procedure [Movchan and Movhan (1995)], the solution within corresponding domains will be sought in form of asymptotic series:

$$\mathbf{w}(x,\xi)=\sum_{j=0}^{\infty}\varepsilon^j\mathbf{w}_j(x,\xi), \quad \mathbf{u}_\pm(x,y)=\sum_{j=0}^{\infty}\varepsilon^j\mathbf{u}_j^\pm(x,y). \tag{17}$$

As a result, sequence of the BVPs determining respective terms in asymptotic expansions (17) will be found. Thus, for the first term $\mathbf{w}_0$, one can obtain:

$$D_\xi\mathbf{A}_0D_\xi\mathbf{w}_0=\mathbf{0}, \quad (x,\xi)\in\Omega_0, \tag{18}$$

$$\mathbf{u}_0^\pm(x,\pm 0)=\mathbf{w}_0(x,\pm h_0), \tag{19}$$

$$\sigma_{0\pm}^{(y)}(x,\pm 0)=\mathbf{A}_0D_\xi\mathbf{w}_0|_{\xi=\pm h_0}. \tag{20}$$

From (18) and (20) one can immediately conclude that

$$\sigma_{0+}^{(y)}(x,+0)=\sigma_{0-}^{(y)}(x,-0), \tag{21}$$

while equation (18) is easily integrated to obtain:

$$\mathbf{w}_0(x,\xi)=\mathbf{u}_0^-(x,-0)+\int_{-h_0}^{\xi}\mathbf{A}_0^{-1}(x,t)dt\cdot\sigma_0^{(y)}(x,0). \tag{22}$$

Finally, taking condition (19) into account, one can observe that an additional condition has to be satisfied for solvability of the problem (18) - (20):

$$\mathbf{u}_0^+(x,+0)-\mathbf{u}_0^-(x,-0)=\int_{-h_0}^{h_0}\mathbf{A}_0^{-1}(x,t)dt\cdot\sigma_0^{(y)}(x,0). \tag{23}$$

Let us note that equations (21) and (23) constitute the sought for imperfect transmission conditions for the solutions $u_0^\pm$ within the bonded materials. These transmission conditions together with the boundary conditions $(5)_1$ allow us to find the solution of equations $(1)_1$ valid in the matched materials. Then, the main term of the solution within the interphase is simply calculated due to (22).

Continuing the procedure, one can obtain the solution within the whole domain with an arbitrary accuracy with respect to the small parameter ε. However, such solutions will still contain an error connected with the fact that the constructed solution does not satisfy boundary condition $(5)_2$.

In the case of the plane stress problem, all the results are still valid if λ is changed to $\lambda_*=2\lambda\mu/(\lambda+2\mu)$. This means that we have for plane strain problems :

$$\mu=\frac{E}{2(1+\nu)}, \quad \lambda=\frac{\nu E}{(1+\nu)(1-2\nu)}, \tag{24}$$

in case of plane stress problems, these parameters are defined as follows:

$$\mu_*=\frac{E}{2(1+\nu)}, \quad \lambda_*=\frac{\nu E}{1-\nu^2}, \quad 2\mu_*+\lambda_*=\frac{E}{1-\nu^2}. \tag{25}$$

Summarizing the obtained results, imperfect transmission conditions for the soft inhomogeneous interface can be written in the following manner:

$$[\sigma^{(y)}]|_{y=0}=\mathbf{0}, \quad [\mathbf{u}]|_{y=0}=\begin{pmatrix}\tau_1(x) & 0\\ 0 & \tau_2(x)\end{pmatrix}\cdot\sigma_0^{(y)}(x,0), \tag{26}$$

where the symbol $[f]|_S$ denotes the jump of a function f across an arbitrary boundary S, while new parameters are defined:

$$\tau_1(x)=\int_{-h_0}^{h_0}\frac{d\xi}{\mu_0(x,\xi)}=\int_{-h}^{h}\frac{dy}{\mu(x,y)}, \tag{27}$$

$$\tau_2(x)=\int_{-h}^{h}\frac{dy}{2\mu(x,y)+\lambda(x,y)}. \tag{28}$$

As it follows from Eq. (20), the main terms of the stress components σ_y, σ_{xy} are constants inside the interphase. Let us consider the last component σ_x:

$$\sigma_x=(2\mu+\lambda)\varepsilon_x+\lambda\varepsilon_y=\left[\varepsilon(2\mu_0+\lambda_0)\frac{\partial}{\partial x},\lambda_0\frac{\partial}{\partial\xi}\right]\cdot\mathbf{w}(x,\xi).$$

The main term with respect to the small parameter ε is

$$\sigma_x(x,\xi)=\lambda_0\frac{\partial}{\partial\xi}[0,1]\cdot\mathbf{w}_0(x,\xi)+O(\varepsilon),$$

then taking into account Eq. (22), one can conclude:

$$\sigma_x(x,\xi) = \frac{\lambda_0}{2\mu_0+\lambda_0}[0,1]\cdot\sigma_0^{(s)}(x,0)+O(\varepsilon),$$

or finally inside the interphase the last stress component varies in direction perpendicular to the interphase only if Poisson's ratio depends on the variable ξ:

$$\sigma_x(x,\xi) = \frac{\nu(x,\xi)}{1-\nu(x,\xi)}\sigma_y(x,0)+O(\varepsilon), \quad \varepsilon\to 0. \tag{29}$$

Thus, whereas the value of Young's modulus of the interphase depends on the variable ξ, the stress component σ_x does not depend on this variable because Poisson's ratio is constant.

Let us consider two particular cases of the transmission conditions. The first one appears when all the elastic parameters of the interphase are constant. Then, the interfacial parameters are also constants:

$$\tau_1 = \frac{4h(1+\nu)}{E}, \qquad \tau_2 = \frac{2(1+\nu)(1-2\nu)h}{(1-\nu)E} \tag{30}$$

for the plane strain and

$$\tilde{\tau}_1 = \tau_1, \qquad \tilde{\tau}_2 = \frac{2(1-\nu^2)h}{E} \tag{31}$$

for the plane stress case.

In the case when Poisson's ratio is a constant while Young's modulus of the interphase is a function of both variables, one can easily extract from (27) and (28) the same formulae as in (30) and (31), where the modulus E has to be only replaced by the auxiliary function:

$$\hat{E}(x) = \left(\int_{-h}^{h}\frac{dy}{E(x,y)}\right)^{-1}. \tag{32}$$

However, we have to mention in this place an essential difference between plane strain and plane stress problems. Namely, if the elastic intermediate phase is weakly compressible ($\nu = 0.5-\varepsilon\nu_0,\ \nu_0>0$), then the condition $\mu\sim\lambda$ is not true (cf. (11)) in general. As a result, transmission conditions (26) are not justified for the weakly compressible interface in the case of plane strain problems [Mishuris (2004)].

One of the main questions, as it usually appears in asymptotic approaches, is: which magnitude of error will be introduced in the problem if one replaces the real thin interphase by the evaluated imperfect transmission conditions. An additional problem which everywhere appears after formal asymptotic analysis is the estimation of regions where the asymptotic formulae give an acceptable result and where other methods (other conditions in this case) should be applied to correct the solution.

If one models the soft intermediate layer by the imperfect transmission conditions (26) then the relative error connected with such an approach can be estimated a priori from the asymptotic analysis in terms of $O(\varepsilon)$ except the regions near the intersections of the layer and the external boundary (Fig. 1). Nevertheless, it is impossible to estimate in value the ranges of the mentioned regions and the real error introduced in the solution.

One of the aims of this work is to provide numerical estimates for the aforementioned error as well as to clarify the sizes of the edge zone effects by FEM modelling of the thin intermediate layer in composite structures. We are not going to discuss here any questions concerning implementation of the imperfect transmission conditions in the numerical codes wich is also an important problem to be solved.

3 FEM simulation

The commercial finite element code MSC.Marc is used for the simulation of the mechanical behavior of the thin intermediate layer with a dimension of $2h = H/100 = 0.01$ and $L = 10$. The two-dimensional FE-mesh is built up of four-node, isoparametric elements with bilinear interpolation functions. In order to investigate the edge effect (cf. Fig. 1, left and right hand side of the interphase), a strong mesh refinement is performed in this region. Furthermore, the mesh is generated in such a way that it is possible to evaluate the displacements and stresses along the axes of symmetry (cf. Fig. 2, lines A and B) and along the transition zone of the materials (cf. Fig. 2, lines C and D). In Fig. 2, the lines C^e and D^e belong to the bonded material and the lines C^i and D^i to the interphase. The MSC.Marc user subroutine feature is used to automatically derive the data along the above mentioned lines.

The final mesh and some details of the interphase with its strong mesh refinement are shown in Fig. 3. The whole mesh consists of 108544 Elements whereof 39512 Elements account for the interphase. The resulting

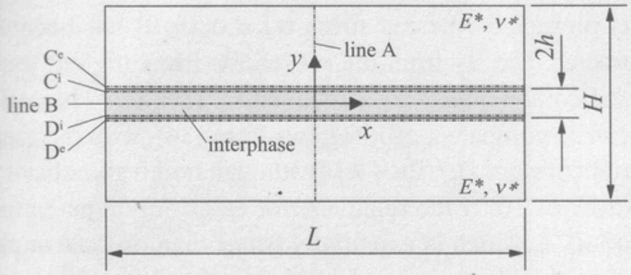

Figure 2 : Evaluation paths of the investigated structure

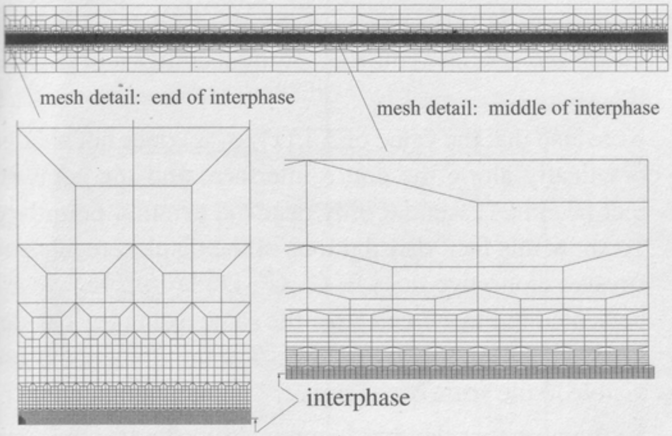

Figure 3 : Two-dimensional FE-mesh: strong mesh refinement in the investigated area

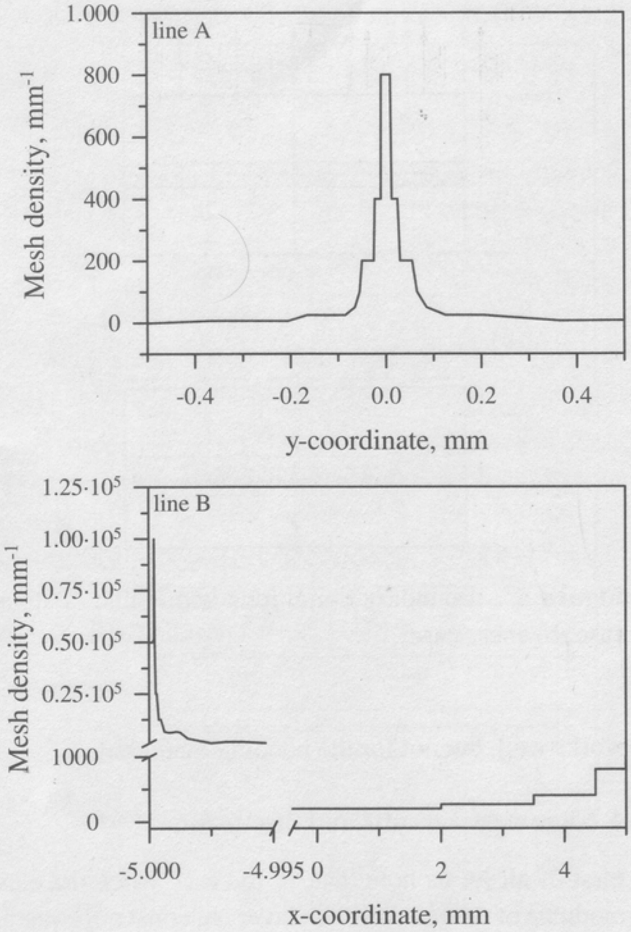

Figure 4 : Mesh density with reference to Fig. 2

linear system of equations is still possible to solve in a short time on a standard personal computer with 1.5 GB RAM. Fig. 4 describes the mesh in more detail with the so-called mesh density (elements per length).

In the framework of the presented work, we investigate two load cases. In the so-called simple tensile case (cf. Fig. 5 a)), all nodes with $y = +H/2$ have a constant y-displacement and the x-displacement is constrained to zero. At the lower boundary ($y = -H/2$), all degrees of freedom are constrained to zero. In the so-called simple shear case (cf. Fig. 5 b)), the same fixed boundary is used at $y = -H/2$ and to all nodes with $y = +H/2$ a constant x-displacement is applied, whereas the y-displacement of these nodes is constrained to zero. Let us underline here that the simple shear case in our paper is not a pure shear state because bending is superimposed to the shear state due to the boundary conditions.

For these model calculations, the elastic constants, Young's modulus $E_{\pm} = E^* = 72700$ MPa and Poisson's ratio $\nu_{\pm} = \nu^* = 0.34$, of the aluminum alloy AlCuMg1 (2017) are assigned to the bonded material (cf. Fig. 2). Differing elastic constants are chosen for the intermediate layer and the calculations are carried out for the plane stress and plane strain case.

We have restricted ourselves to the cases of the mentioned simple tensile and simple shear loading because the constructed FEM mesh is definitely appropriated for them. We have checked this fact by comparing the test results where $x = 0$ holds for the completely homogeneous elastic domain without intermediate zone ($E^* = E$, $\nu^* = \nu$) with two solutions. Theoretical solutions for simple tensile, shear and bending problems in rectangles can be found for example in [Flügge (1962)]. We also have compared those FEM solutions for our mesh with the FEM solutions for standard regular (without transition elements) mesh for the homogeneous elastic rectangle. As a result, we have made sure that for the tensile and shear loadings the constructed mesh with transition elements

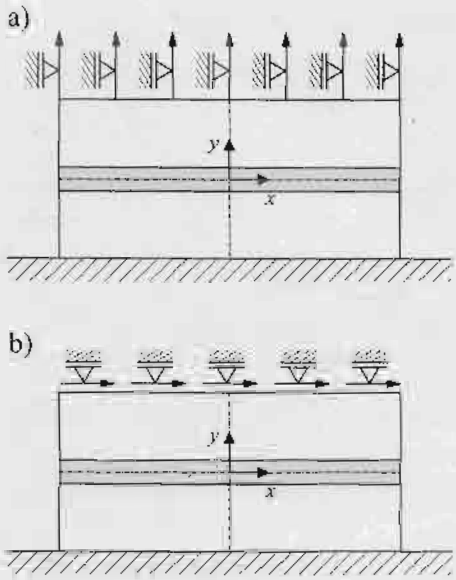

Figure 5 : Boundary conditions and loads: a) tensile case; b) shear case

works well, but not for the bending loading.

4 Numerical results and discussion

First of all let us note that, in the case when the elastic modulae of the intermediate layer are constant, equations (22) and (23) can be rewritten in the following form:

$$\mathbf{w}(x,\xi) = \mathbf{u}^{-}(x,-0) + (\xi + h_0)\mathbf{A}_0^{-1}\sigma^{(y)}(x,0)\,, \tag{33}$$

$$[\mathbf{u}]_{y=0} = \begin{pmatrix} 2h/\mu & 0 \\ 0 & 2h/(2\mu+\lambda) \end{pmatrix} \sigma^{(y)}(x,0)\,. \tag{34}$$

In the following, we will discuss the obtained numerical results in detail only for one case as an example: i.e. plane stress tensile loading with interface constants: $E = 813$ MPa, $\nu = 0.4999$. In Fig. 6, distributions of displacements and stresses along the line A (cf. Fig. 2) are presented. Note that the stress component $\sigma_x(0,y)$ is discontinuous at the interface boundaries, as it should be expected, while all other components are continuous. Although the ratio E/E^* can only be estimated as 0.1 while $2h/H = 0.01$, one can see that the distribution of the displacements within the interface exhibits linear character, which coincides with (33). Moreover, we can now check condition (34) at least at the point $x = 0$. For this reason, we calculate the difference between displacements $\Delta u_y = u_y^+ - u_y^-$ from different sides of the interface. In the first line of the table 2, the calculated value of $\Delta u_y/\sigma_y$ is presented whereas stress $\sigma_y = \sigma_y(0,0)$ has been extracted directly from the subroutine (the different material combinations are explained in Tab. 1). This value can be compared, as it follows from (34), with the material constant $2h/(2\mu+\lambda)$. Although both values have an order of 10^{-7}, the relative error takes only a magnitude of 10^{-7}, which is essentially better than one can expect from the theoretical result where an estimate $O(\varepsilon^2)$ can be only justified ($\varepsilon^2 \sim 10^{-4}$). This fact can be probably explained in that way that next terms in the asymptotic expansions (17) disappear in this case, as an exception, due to the special symmetry of the loadings and geometry.

Note also that the value of $\Delta u_y(x)/\sigma_y(x)$ does not change practically along the entire interface, and the edge effect becomes essential only near the external boundary. To show this fact, distributions of the displacements and stresses along five lines B, C^i, C^e, D^i, D^e (cf. Fig. 2) are presented in Figs. 7 and 8 for the same example. The deviation between the lines of Fig. 7 at the free edge is not visible in the scale of the figure.

Let us note that the first component in the transmission condition (34) is satisfied identically for the entire interface as it follows from Figs. 7 and 8 due to tensile loading. In the case of the shear loading, the same results have been obtained for the second component of (34). These facts are simple consequences of the symmetry in geometrical and mechanical properties of the example under consideration. It is important to note that although the displacement is continuous along the interphase boundary, it is not smooth in y-direction and therefore, a visible difference of displacement for lines C^e, C^i and D^e, D^i can be observed in Fig. 7b. Furthermore, the decrease of σ_z at the free ends is not possible to observe in the given scale of Fig. 8 but indicated by the markers.

One can think that the displacements should behave in opposite way at the free edge in comparison with that presented in Figs. 7b and 8. At the first glance, the interphase stiffness seems to increase near the free edge, because the displacement decreases. In Fig. 9a, the final shape of the free edge boundary after the deformation is presented for the same sample with simple tensile loading. It is clear that such a behavior of the displacements near the free edge is reasonable because of the contraction. In order to compare two limiting cases of Poisson's ratio, the shape is drawn for the same tensile sample in Fig. 9b with another Poisson's ratio of $\nu = 0.0001$. Now,

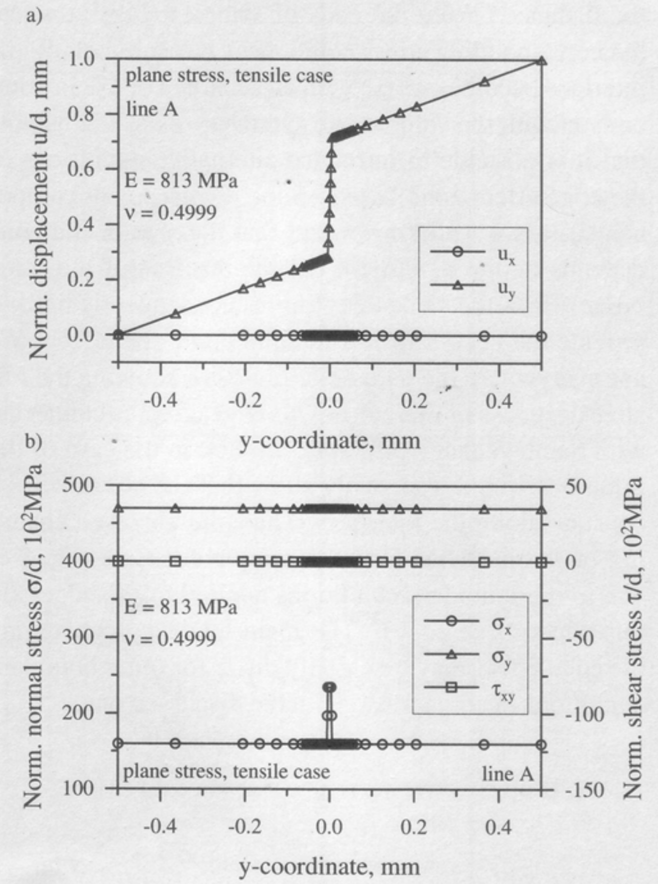

Figure 6 : Normalized displacement and stress distribution along line A (cf. Fig. 2)

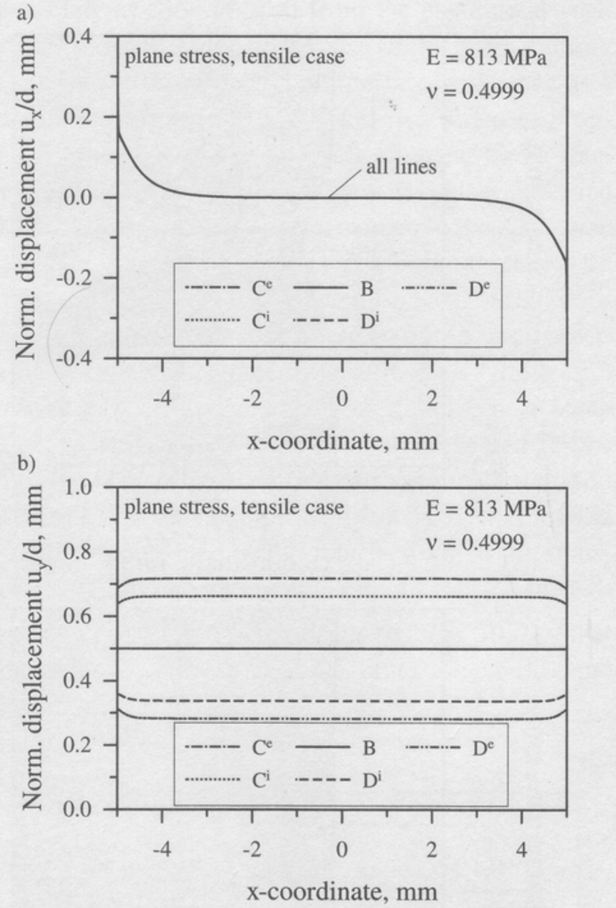

Figure 7 : Normalized displacement distribution along lines B, C and D (cf. Fig. 2)

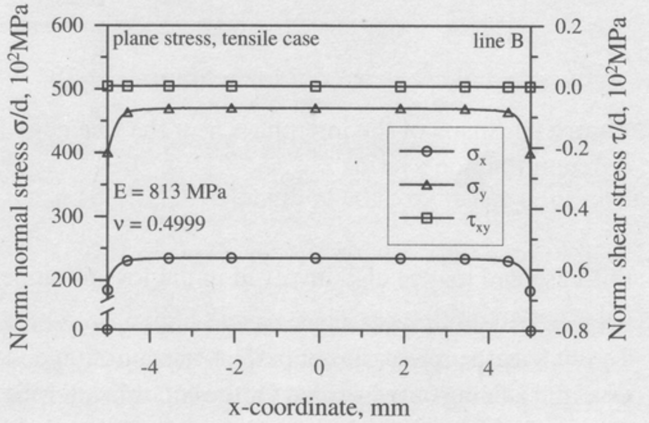

Figure 8 : Normalized normal and shear stress distribution along line B (cf. Fig. 2)

there is practically no contraction of the interphase material. However, the distance from the free edge, measured where the stress component σ_y is no longer a straight line, is practically the same for both cases with an accuracy of 1% in the reference coordinate system.

In Tables 2-5 similar numerical results are presented for numerous combinations of the elastic constants, loadings and plane states. For the shear loading in plane strain, all results are practically the same as in the case of the simple shear loading in plane stress, which is evident from the problem formulation. To show this fact, we have presented only the first case for the weakly compressible interface in Table 5. Let us note that, in the case of the weakly compressible interface under plane strain conditions, the accuracy becomes to be essentially worse in comparison with all other cases under consideration. The explanation is quite simple. As we have mentioned earlier, the transmission conditions evaluated in the first section are no longer valid in such a case [Mishuris (2004)]. However, so-called locking phenomena also can occur in

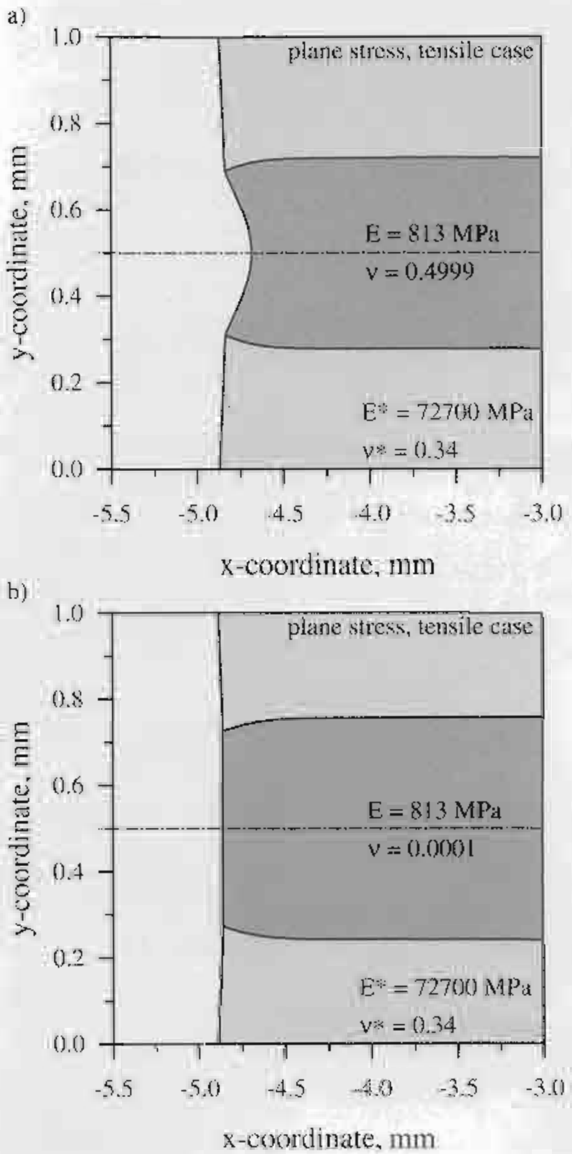

Figure 9 : Shape of the interphase near the free edge for different Poisson's ratios

this case and maybe also involved in the loss of numerical accuracy.

To our great surprise, the imperfect transmission conditions (34), being only justified for the soft thin interphase, are true for practically all examples on a sufficiently long distance along the interface from the center of the samples, as it follows from the tables. However, with increase of the ratio E/E^*, the region where this fact is observable becomes smaller.

The edge effect manifests its influence deeper within the sample. To estimate this influence we have introduced the distance l from the ends of samples (Fig. 1) where the corresponding stress component measured along the interface becomes worse with an accuracy of 1% in comparison with the value at the symmetry axis. Let us note that it is possible to introduce alternative definitions of the edge effect zone based on the displacement components. It is a well known fact that the size of the zone depends on the definition, but the result is of the same order. Thus, the same definition is consequently used to provide the necessary information about the effect. We use everywhere the parameter $\delta = 2l/L$ showing the relative deepness of this zone. This edge effect is connected with Saint-Venant's principle. In fact, in the case of the infinite strip one can easily show that the stress will be constant along the interface. Thus, the observed changing of the behavior near the sample edges in Fig. 8 is due to the boundary conditions applied to the edges (in this paper: free edge). The main tendency concerning the edge effect may essentially differ for other boundary conditions in comparison with the discussed one.

Table 1 : Investigated material cases (MC)

MC	E	ν
1	8138	0.4999
2	813	0.4999
3	81	0.4999
4	5427	0.0001
5	542	0.0001
6	54	0.0001
7	8138	0.3000
8	813	0.3000
9	81	0.3000
10	271270	0.3000

In Figs. 10-12, corresponding values of δ are presented for different cases under consideration. Except the case of the weakly compressible interface ($\nu = 0.4999$) under plane strain conditions for tensile loading, all curves in Figs. 10-12 $\delta = \delta(E/E^*)$ exhibit a similar behavior. Namely, for small values of the ratio $E/E^* \sim 10^{-3}$, δ takes a value near 0.05 and for smaller values (see Fig. 12) it becomes comparable with the accuracy of δ due to the definition. Moreover, the magnitude of Poisson's ratio slightly influences the value of δ, except the mentioned case of the weakly compressible interface under plane strain conditions and tensile loading.

Table 2 : Plane stress, tensile case, line A

MC	$\frac{\Delta u_y(0,0)}{\sigma_y(0,0)}$	$\frac{2h(1-\nu^2)}{E}$	rel. error
1	$9.2173\cdot10^{-7}$	$9.2173\cdot10^{-7}$	$1.085\cdot10^{-7}$
2	$9.2264\cdot10^{-6}$	$9.2263\cdot10^{-6}$	$3.577\cdot10^{-6}$
3	$9.2605\cdot10^{-5}$	$9.2605\cdot10^{-5}$	$9.719\cdot10^{-7}$
4	$1.8426\cdot10^{-6}$	$1.8426\cdot10^{-6}$	$-1.085\cdot10^{-6}$
5	$1.8450\cdot10^{-5}$	$1.8450\cdot10^{-5}$	$1.626\cdot10^{-6}$
6	$1.8519\cdot10^{-4}$	$1.8519\cdot10^{-4}$	$1.080\cdot10^{-6}$
7	$1.1182\cdot10^{-6}$	$1.1182\cdot10^{-6}$	$8.943\cdot10^{-6}$
8	$1.1193\cdot10^{-5}$	$1.1193\cdot10^{-5}$	$2.680\cdot10^{-6}$
9	$1.1235\cdot10^{-4}$	$1.1235\cdot10^{-4}$	$8.901\cdot10^{-7}$
10	$3.3550\cdot10^{-8}$	$3.3546\cdot10^{-8}$	$1.264\cdot10^{-4}$

Table 3 : Plane strain, tensile case, line A

MC	$\frac{\Delta u_y(0,0)}{\sigma_y(0,0)}$	$\frac{2h(1+\nu)(1-2\nu)}{E(1-\nu)}$	rel. error
1	$7.7872\cdot10^{-10}$	$7.3709\cdot10^{-10}$	0.0565
2	$7.4210\cdot10^{-9}$	$7.3781\cdot10^{-9}$	0.0058
3	$7.3850\cdot10^{-8}$	$7.4054\cdot10^{-8}$	−0.0028
4	$1.8426\cdot10^{-6}$	$1.8426\cdot10^{-6}$	$4.342\cdot10^{-6}$
7	$9.1285\cdot10^{-7}$	$9.1283\cdot10^{-7}$	$3.177\cdot10^{-5}$

Table 4 : Plane stress, shear case, line A

MC	$\frac{\Delta u_x(0,0)}{\sigma_{xy}(0,0)}$	$\frac{4h(1+\nu)}{E}$	rel. error
1	$3.6862\cdot10^{-6}$	$3.6862\cdot10^{-6}$	$-1.899\cdot10^{-6}$
2	$3.6898\cdot10^{-5}$	$3.6898\cdot10^{-5}$	$1.084\cdot10^{-6}$
3	$3.7035\cdot10^{-4}$	$3.7035\cdot10^{-4}$	$7.020\cdot10^{-6}$
4	$3.6856\cdot10^{-6}$	$3.6856\cdot10^{-6}$	$-5.155\cdot10^{-6}$
5	$3.6904\cdot10^{-5}$	$3.6904\cdot10^{-5}$	$1.074\cdot10^{-7}$
6	$3.7041\cdot10^{-4}$	$3.7041\cdot10^{-4}$	$-4.050\cdot10^{-6}$
10	$9.5851\cdot10^{-8}$	$9.5845\cdot10^{-8}$	$5.842\cdot10^{-5}$

Table 5 : Plane strain, shear case, line A

MC	$\frac{\Delta u_x(0,0)}{\sigma_{xy}(0,0)}$	$\frac{4h(1+\nu)}{E}$	rel. error
1	$3.6860\cdot10^{-6}$	$3.6862\cdot10^{-6}$	$5.154\cdot10^{-5}$

This phenomenon shows that the edge effect zone is not only connected with the edge boundary conditions but also with properties of the bimaterial strip. Such a behavior can be easily explained. In fact, when the ratio of Young's modulus E/E^* tends to zero, one can expect that the top part of the strip will move as a rigid body (without any traction applied from the absolutely weak interface). Alternatively, in the case of the other limiting case - strong stiff interface, the interface will move as a rigid straight line parallel itself and two different problems for the strips of the thickness h appear under total deformation $U/2$ of each strip. Then, it is clear that such a case should be equivalent, with respect to the edge zone analysis, with the homogeneous strip of the thickness $2h$ and total deformation U. However, because of the problem linearity, the edge zone should be of the same order. This means that with increasing ratio E/E^* the length of the edge zone has a tendency to stabilize near some plateau as it is easy to observe from all presented graphs in Figs 10 - 12. Moreover, one can easy realize that in the case of the weakly compressible interface two bonded half-strip are connected by this interface which still transmits forces from one part to another.

On the other hand, $\delta = 0.05$ means that $l = 50h$, so that the depth of the edge zone is 25 times longer than the thickness of the interphase.

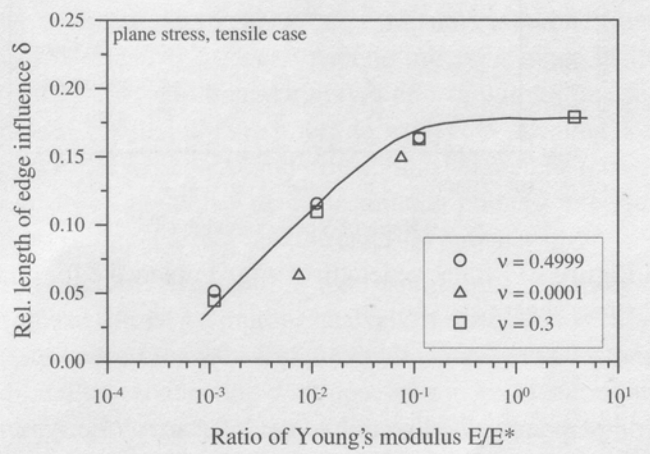

Figure 10 : Relative length of edge influence δ for plane stress tensile case

Finally, we would like to check the validity of the transmission condition in the case of the soft nonhomogeneous interface. For this reason we choose as an example a parabolic behavior of the interphase Young's modulus in the form $E(y) = 696.86(1+22680.0y^2)$, while Poisson's ratio remains constant $\nu = 0.4999$. As a result, the auxiliary parameter $\hat{E}$ defined in (32) takes the same value $\hat{E} = 813.0$ as discussed in one of the homogeneous cases under consideration.

In Fig. 13, distributions of the displacements and stresses

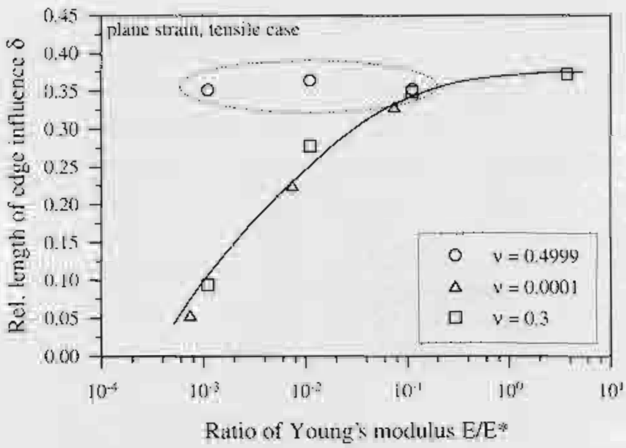

Figure 11 : Relative length of edge influence δ for plane strain tensile case

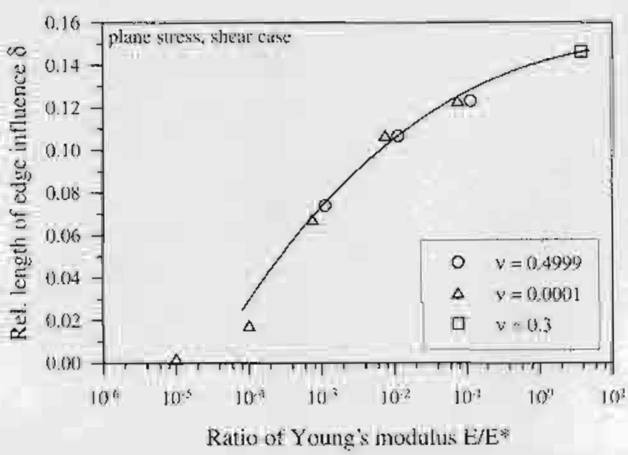

Figure 12 : Relative length of edge influence δ for plane stress shear case

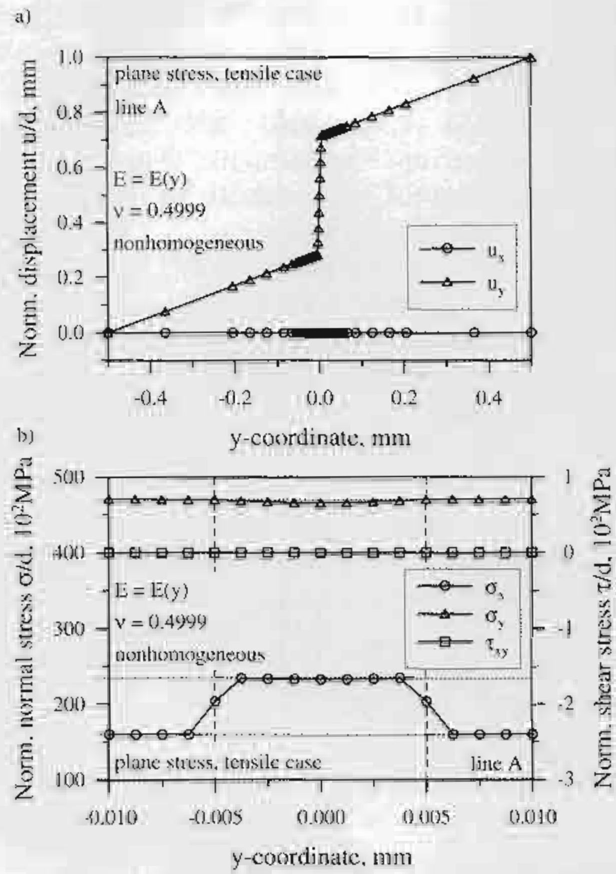

Figure 13 : Normalized displacement and stress distribution along line A (cf. Fig. 2)

in perpendicular direction to the interface at the symmetry line $x = 0$ are presented. The only difference between the graphs in Fig. 6b and Fig. 13b is the scaling. We do not present such magnification earlier in of Fig. 6 where the stresses took practically constant values within the interface (with accuracy more than 0.01%, which, in fact, is better than it has been predicted by the asymptotic analysis). This is no more valid with the same accuracy for the nonhomogeneous interphase. It is clear from Fig. 13b that in the case under consideration the stresses within the interface differ now about 2.4% in the worst point from the constant behavior.

However, it is important to note that the increase of the gradient in the definition of Young's modulus leads to a loss of accuracy in the calculation. This behavior is connected with the small amount of nodes in direction perpendicular to the interphase used in the constructed mesh (only 9 nodes within the interface in perpendicular direction). Let us also note that the stress component σ_x is a constant within and outside the interphase ($|y| < h$) and has a jump at the interface lines ($y = \pm h$). However, this jump is not well approximated due to the few finite elements in that region. Of course, one can easily draw the right behavior.

On the other hand, when we decrease the gradient in the material properties of the interphase, the stress inside the interphase becomes again to be constant. However, even with the chosen sufficiently large change in material properties within the interphase, the accuracy of the transmission conditions is still very high.

To clarify this, two terms which are involved in one of the imperfect transmission conditions, i.e. Δu_y and $\tau_I \sigma_y(x, 0)$, are presented in Fig. 14. The other condition

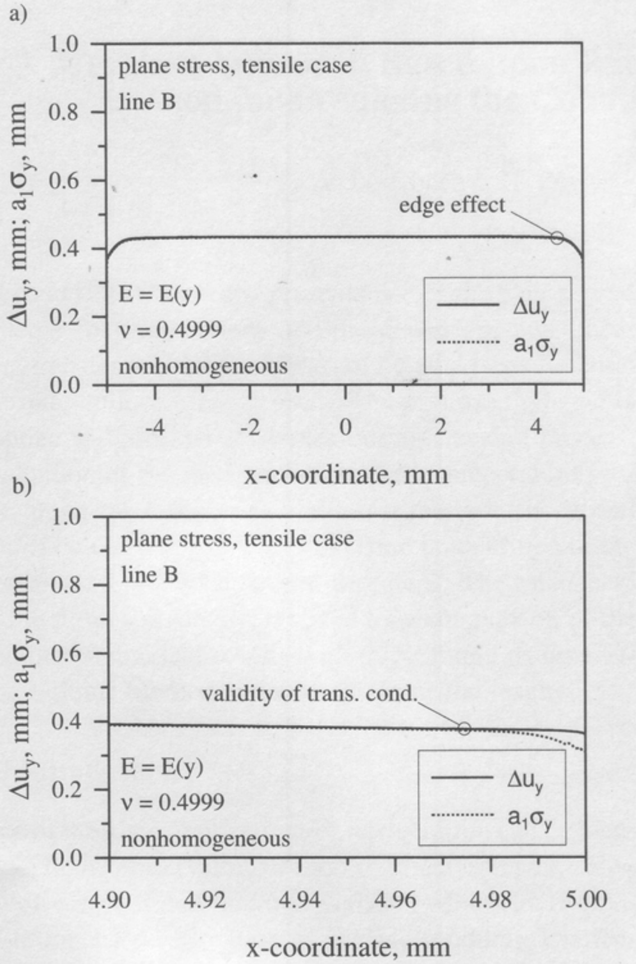

Figure 14 : Determination of the edge effect and the validity of the transmission conditions for a nonhomogeneous interphase (with the normalization $d = 1$)

is a priory satisfied due to the problem symmetry. As one can see no difference between the functions can be observed. The edge effect zone can be determined for the simple tensile loading by defining 1% accuracy of the values of both functions from that at the symmetry point $x = 0$. On the other hand, one can also observe that the transmission conditions are still valid within the edge effect zone! To show this fact, a magnification of the graph is presented near the right hand side of the free edge. It is known from the asymptotic analysis that the evaluated transmission conditions cannot be valid along the whole interface up to the very end. However, as it follows from the figure, the region where they fail is extremely smaller than the edge effect zone itself.

5 Conclusion and further work

As it follows from the presented numerical results, imperfect transmission conditions for the soft interphase (34) obtained analytically by asymptotic analysis are satisfactory with a very good accuracy even in the case $\varepsilon = 0.01$.

The edge effect appears only on a distance comparable with twenty five times the thickness of the interface in the case of the soft interface and it even decreases when E/E^* becomes smaller. However, the zone increases essentially with increasing ratio E/E^* approaching some limiting value. However, the transmission conditions are still valid within the edge effect zone and they fail only near the singularity dominated domain which is extremely small.

In the second part of this paper, we are going to consider asymmetric cases, i.e. different bonded materials, to verify whether a so high accuracy of the imperfect transmission conditions in comparison with the theoretical prediction is connected with the problem symmetry. Also we are planning to check other transmission conditions valid for stiff interfaces. Among others, a range of its applicability and boundary layer effects will be investigated. Finally, we are going to analyze a phenomenon connected with the singularity dominated regions (possible stress singularity near the singular points - intersections of the interface and the external boundary).

Although FEM analysis is very useful for verification in value of formal asymptotic analysis, it has its own restrictions concerning values of the small parameter and strong difficulties connecting with necessity to build a complicated mesh which can be additionally depending on the type of loading, as it occurred in our investigations for bending. It is also difficult to define an unknown form of corresponding transmission conditions from the FEM analysis. However, in the case when one can suppose any specific conditions, they can be numerically verified. In such a way there is a possibility to evaluate imperfect transmission conditions in the case when respective asymptotic analysis is difficult to be carried out. Taking this fact into account, we are going to evaluate and verify transmission conditions for thin plastic interphases.

Acknowledgement: A. Öchsner is grateful to Portuguese Foundation of Science and Technology for financial support. G. Mishuris is grateful to EU Marie Curie grant MTKD-CT-2004-509809.

References

Allen, H.G. (1969): *Analysis and Design of Structural Sandwich Panels*, Pergamon Press, Oxford.

Antipov, Y.A.; Avila-Pozos, O.; Kolaczkowski, S.T.; Movchan, A.B. (2001): Mathematical model of delamination cracks on imperfect interfaces. *Int J Solids Struct*, vol. 38, pp. 6665-6697.

Ashby, M.F.; Evans, A.; Fleck, N.A.; Gibson, L.J.; Hutchinson, J.W.; Wadley, H.N.G. (2000): *Metal Foams: A Design Guide*, Butterworth-Heinemann, Boston.

Flügge, W. (1962): *Handbook of Engineering Mechanics*, McGraw-Hill Book Company, New York.

Hatheway, A.E. (1989): Evaluating Stresses in Adhesive Bond Lines. In: *Proc. MSC/NASTRAN Users' Conference*, Universal City.

Mishuris, G. (2004): Imerfect transmission conditions for a thin weakly compressible interface. 2D problems. *Arch Mech*, vol. 56, pp. 143-154.

Mishuris, G.; Kuhn, G. (2001): Asymptotic Behaviour of the Elastic Solution near the Tip of a Crack Situated at a Nonideal Interface. *ZAMM*, vol. 81, pp. 811-826.

Movchan A.B.; Movhan, N.V. (1995): *Mathematical Modelling of Solids with Nonregular Boundaries*, CRC Press, Boca Raton.

Pradhan, S.C.; Lam, K.Y.; Tay, T.E. (2000): Determination of Fracture Parameters of Laminated Thermoplastic Composite Materials: A Finite Element Approach. *Int J Adhes*, vol. 50, pp. 395-401.

CMC, vol.4, no.3, pp.137-151, 2006

FEM-analysis of nonclassical transmission conditions between elastic structures. Part 2: Stiff imperfect interface

G. Mishuris[1], A. Öchsner[2] and G. Kuhn[3]

Abstract: Nonclassical transmission conditions for dissimilar elastic structures with imperfect interfaces are investigated. The thin interface zone is assumed to be soft or stiff in comparison with the bonded materials and the transmission conditions for stiff interfaces are evaluated based on asymptotic analysis. The accuracy of the transmission conditions is clarified not only in terms of asymptotic estimate, but, which is especially important for users, also in values by accurate FEM calculations. The ranges of applicability of the conditions are discussed.

keyword: Elasticity, Imperfect interface, Nonclassical transmission conditions, Finite element method

1 Introduction

In the first part of the paper Mishuris (2005b), symmetrical elastic structures consisting of two thick layers matched by a thin interphase layer exhibiting different material properties under conditions of simple shear and tensile loading have been considered. Transmission conditions for the soft interface have been analytically evaluated there by asymptotic analysis to compare with the results obtained by FEM analysis of the structure. It has been shown that the numerical error in these special cases is essentially smaller than it could be expected from the theory. Even in the case of the stiff interface, where other transmission conditions should rather be applied, satisfying agreement has been obtained. In this paper, dissimilar elastic structures have been analysed under different loading (simple or complex one) by the same FEM techniques. Additionally, transmission conditions for the stiff interface will be evaluated by asymptotic methods and later numerically verified in order to estimate the possible error connected with its application. Finally, such important values, for practical numerical calculations dealing with bimaterial structures with thin interfaces, as ranges of edge effect zone, validity of the discussed transmission conditions and singularity dominated zone will be evaluated. These effects are the main reason for cracking and delamination in composite materials [Akisania (1997); Boichuk (2001); Kokhanenko (2003); Li (2004); Qian (1998); Yu (2001)].

[1] RzUT, Rzeszow, POLAND.
[2] UA, Aveiro, PORTUGAL.
[3] FAU, Erlangen, GERMANY.

2 Asymptotic evaluation of transmission conditions between two elastic materials with a stiff elastic interphase (2D-problem)

Let us consider a model plane problem for a bimaterial elastic solid in the rectangle $\Omega_h = \Omega_+ \cup \Omega_- \cup \Omega$, where $\Omega_\pm = \{(x,y), \pm y \geq h\}$, $\Omega = \{(x,y), |y| \leq h\}$ (see Fig. 1). We assume that the intermediate layer Ω is inhomogeneous and isotropic, while the bonded materials are isotropic and homogeneous. Let $\mathbf{u}_\pm(x,y)$ and $\mathbf{u}(x,y)$ be vectors of displacements: $\mathbf{u}_\pm = [u_x^\pm, u_y^\pm]^\top$, $\mathbf{u} = [u_x, u_y]^\top$.

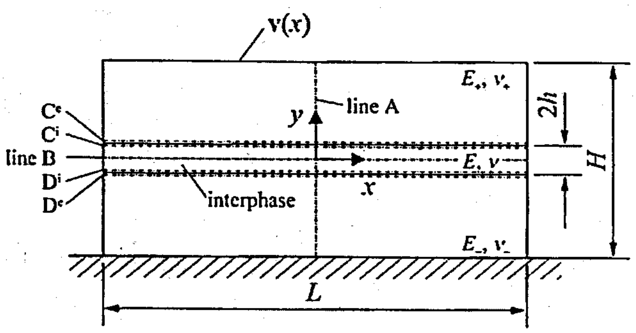

Figure 1 : Schematic representation of evaluation paths and boundary conditions of the investigated structure

They satisfy Lamé equations in the corresponding domains :

$$\mathcal{L}_\pm \mathbf{u}_\pm = 0, \quad (x,y) \in \Omega_\pm, \quad \mathcal{L}\mathbf{u} = 0, \quad (x,y) \in \Omega, \quad (1)$$

where the differential operators $\mathcal{L}_\pm$ and $\mathcal{L}$ are defined in the following manner:

$$\mathcal{L}_\pm = \begin{pmatrix} (\lambda_\pm+2\mu_\pm)D_x^2+\mu_\pm D_y^2 & (\lambda_\pm+\mu_\pm)D_xD_y \\ (\lambda_\pm+\mu_\pm)D_xD_y & (\lambda_\pm+2\mu_\pm)D_y^2+\mu_\pm D_x^2 \end{pmatrix}, \tag{2}$$

$$\mathcal{L} = \begin{pmatrix} D_x(\lambda+2\mu)D_x+D_y\mu D_y & D_x\lambda D_y+D_y\mu D_x \\ D_y\lambda D_x+D_x\mu D_y & D_y(\lambda+2\mu)D_y+D_x\mu D_x \end{pmatrix}, \tag{3}$$

where D_x and D_y denote respective partial derivatives.

On the exterior boundary some boundary conditions are assumed to be satisfied:

$$\mathcal{B}_\pm \mathbf{u}_\pm = 0, \quad (x,y)\in\partial\Omega_h\cap\partial\Omega_\pm,$$

$$\mathcal{B}\mathbf{u} = 0, \quad (x,y)\in\partial\Omega_h\cap\partial\Omega. \tag{4}$$

We do not precise here the forms of the boundary operators $\mathcal{B}_\pm$ and $\mathcal{B}$, because they will not play any role in the formal asymptotic procedure. However, they are very important, of course, in order to prove the final asymptotic estimate for the asymptotic solution obtained in some functional spaces.

Along the interior boundaries, i.e. $y=\pm h$, the perfect transmission conditions should be satisfied:

$$\mathbf{u}_\pm(x,\pm h) = \mathbf{u}(x,\pm h), \quad \sigma_\pm^{(y)}(x,\pm h) = \sigma^{(y)}(x,\pm h), \tag{5}$$

where

$$\sigma_\pm^{(y)}(x,y) = \mathcal{M}_\pm \mathbf{u}_\pm(x,y), \quad \sigma^{(y)}(x,y) = \mathcal{M}\mathbf{u}(x,y), \tag{6}$$

$$\mathcal{M}_\pm = \begin{pmatrix} \mu_\pm D_y & \mu_\pm D_x \\ \lambda_\pm D_x & (\lambda_\pm+2\mu_\pm)D_y \end{pmatrix},$$

$$\mathcal{M} = \begin{pmatrix} \mu D_y & \mu D_x \\ \lambda D_x & (\lambda+2\mu)D_y \end{pmatrix}. \tag{7}$$

Let us assume that the intermediate layer is essentially thinner in comparison with the characteristic size of the body: $h << \min\{L,H\}$. This allows us to introduce in the problem a small dimensionless parameter $\varepsilon << 1$ in the following manner:

$$\varepsilon h_0 = h \tag{8}$$

and rescale the variable within the intermediate layer:

$$(x,y)\in\Omega \quad y=\varepsilon\xi, \qquad \xi\in[-h_0,h_0], \quad h_0\sim\min\{L,H\}. \tag{9}$$

We assume through out this section that the interphase material is essentially stiffer in comparison with both bonded materials:

$$\mu(x,y)=\varepsilon^{-1}\mu_0(x,\xi), \ \ \lambda(x,y)=\varepsilon^{-1}\lambda_0(x,\xi), \quad \mu_0\sim\mu_\pm, \tag{10}$$

and denote by $\mathbf{w}(x,\xi)=\mathbf{u}(x,\varepsilon\xi)$ the solution within the domain $\Omega_0=\{(x,\xi),\ |\xi|\le h_0\}$. In this new notation, all operators can be rewritten as follows:

$$\mathcal{L}=\varepsilon^{-3}\mathcal{L}_0+\varepsilon^{-2}\mathcal{L}_1+\varepsilon^{-1}\mathcal{L}_2, \quad \mathcal{M}=\varepsilon^{-2}\mathcal{M}_0+\varepsilon^{-1}\mathcal{M}_1, \tag{11}$$

where

$$\mathcal{L}_0 = D_\xi \mathbf{A}_0 D_\xi, \tag{12}$$

$$\mathcal{L}_1 = \begin{pmatrix} 0 & D_x\lambda_0 D_\xi + D_\xi\mu_0 D_x \\ D_\xi\lambda_0 D_x + D_x\mu_0 D_\xi & 0 \end{pmatrix}, \tag{13}$$

$$\mathcal{L}_2 = D_x\mathbf{A}_2 D_x, \quad \mathcal{M}_0 = \mathbf{A}_0 D_\xi, \quad \mathcal{M}_1 = \mathbf{A}_1 D_x, \tag{14}$$

$$\mathbf{A}_0 = \begin{pmatrix} \mu_0 & 0 \\ 0 & \lambda_0+2\mu_0 \end{pmatrix}, \quad \mathbf{A}_1 = \begin{pmatrix} 0 & \mu_0 \\ \lambda_0 & 0 \end{pmatrix},$$

$$\mathbf{A}_2 = \begin{pmatrix} \lambda_0+2\mu_0 & 0 \\ 0 & \mu_0 \end{pmatrix}. \tag{15}$$

Then, a part of the problem under consideration within the domain Ω_0 can be reformulated in the following manner: we should seek for the solution $\mathbf{w}$ in the domain Ω_0 satisfying the equation:

$$\left(\mathcal{L}_0+\varepsilon\mathcal{L}_1+\varepsilon^2\mathcal{L}_2\right)\mathbf{w}=0, \quad (x,\xi)\in\Omega_0, \tag{16}$$

and the interior transmission conditions:

$$\mathbf{u}_\pm(x,\pm\varepsilon h_0) = \mathbf{w}(x,\pm h_0),$$

$$\varepsilon^2\sigma_\pm^{(y)}(x,\pm\varepsilon h_0) = \left(\mathcal{M}_0+\varepsilon\mathcal{M}_1\right)\mathbf{w}|_{\xi=\pm h_0}. \tag{17}$$

The solution within the corresponding domains will be sought in form of asymptotic series:

$$\mathbf{w}(x,\xi)=\sum_{j=0}^{\infty}\varepsilon^j\mathbf{w}_j(x,\xi),\quad \mathbf{u}_\pm(x,y)=\sum_{j=0}^{\infty}\varepsilon^j\mathbf{u}_j^\pm(x,y). \tag{18}$$

As a result, sequence of the BVPs determining respective terms in the asymptotic expansions (18) will be found. Thus, for the first term $\mathbf{w}_0$ one can obtain:

$$D_\xi\mathbf{A}_0D_\xi\mathbf{w}_0=\mathbf{0},\quad (x,\xi)\in\Omega_0, \tag{19}$$

$$\mathbf{u}_0^\pm(x,\pm0)=\mathbf{w}_0(x,\pm h_0), \tag{20}$$

$$\mathbf{A}_0D_\xi\mathbf{w}_0|_{\xi=\pm h_0}=\mathbf{0}. \tag{21}$$

From (19) and (21) one can obtain that

$$\mathbf{w}_0(x,\xi)=\mathbf{a}_1(x), \tag{22}$$

while the unknown function $\mathbf{a}_1(x)$ has to be found from (20):

$$\mathbf{a}_1(x)=\mathbf{u}_0^-(x,-0), \tag{23}$$

and an additional condition has to be satisfied:

$$[\mathbf{u}_0]_{y=0}\equiv\mathbf{u}_0^+(x,+0)-\mathbf{u}_0^-(x,-0)=\mathbf{0}. \tag{24}$$

Note that equation (24) constitutes the first unknown imperfect transmission condition for the external solutions $\mathbf{u}_0^\pm$ within the bonded materials.

To find the next sought for the transmission condition for the first term of the external asymptotic expansion, $\mathbf{u}_0^\pm$, one can continue the procedure to analyse the second internal BVP:

$$D_\xi\mathbf{A}_0D_\xi\mathbf{w}_1+\mathcal{L}_1\mathbf{w}_0=\mathbf{0},\quad (x,\xi)\in\Omega_0, \tag{25}$$

$$\pm h_0D_y\mathbf{u}_0^\pm(x,\pm0)+\mathbf{u}_1^\pm(x,\pm0)=\mathbf{w}_1(x,\pm h_0), \tag{26}$$

$$\mathbf{A}_0D_\xi\mathbf{w}_1|_{\xi=\pm h_0}+\mathcal{M}_1\mathbf{w}_0|_{\xi=\pm h_0}=\mathbf{0}. \tag{27}$$

Taking into account the properties (22) of the internal solution $\mathbf{w}_0$, one can rewrite equations (25) and (27) in equivalent forms:

$$D_\xi\mathbf{A}_0D_\xi\mathbf{w}_1+D_\xi\mathbf{A}_1D_x\mathbf{w}_0=\mathbf{0},\quad (x,\xi)\in\Omega_0, \tag{28}$$

$$\mathbf{A}_0D_\xi\mathbf{w}_1|_{\xi=\pm h_0}+\mathbf{A}_1D_x\mathbf{w}_0|_{\xi=\pm h_0}=\mathbf{0}. \tag{29}$$

The solution to this problem is easily calculated as:

$$\mathbf{w}_1(x,\xi)=\mathbf{a}_2(x)-\int_0^\xi\mathbf{A}_0^{-1}(x,t)\mathbf{A}_1(x,t)dt\cdot D_x\mathbf{w}_0(x), \tag{30}$$

where

$$\mathbf{a}_2(x)=\int_0^{-h_0}\mathbf{A}_0^{-1}(x,t)\mathbf{A}_1(x,t)dt\cdot D_x\mathbf{w}_0(x) -h_0D_y\mathbf{u}_0^-(x,-0)+\mathbf{u}_1^-(x,-0), \tag{31}$$

and an additional transmission condition has to be satisfied for the solution $\mathbf{u}_1$ of the second external BVP:

$$[\mathbf{u}_1]_{y=0}=-\int_{-h_0}^{h_0}\mathbf{A}_0^{-1}(x,t)\mathbf{A}_1(x,t)dt\cdot D_x\mathbf{w}_0(x) -2h_0\langle D_y\mathbf{u}_0\rangle_{y=0}. \tag{32}$$

There, we have introduced the standard notation

$$\langle f\rangle=\frac{1}{2}(f_++f_-). \tag{33}$$

As it follows from this step, it is not enough to consider even the second term of the internal asymptotic expansion, $\mathbf{w}_1$, to find the still missing transmission solution for the first term of the external expansion, $\mathbf{u}_0^\pm$. Thus, one needs to continue the asymptotic procedure. Let us consider the internal BVP for the third term of the internal asymptotic expansion (18):

$$D_\xi\mathbf{A}_0D_\xi\mathbf{w}_2+\mathcal{L}_1\mathbf{w}_1+\mathcal{L}_2\mathbf{w}_0=\mathbf{0},\quad (x,\xi)\in\Omega_0, \tag{34}$$

$$\frac{1}{2}h_0^2D_y^2\mathbf{u}_0^\pm(x,\pm0)\pm h_0D_y\mathbf{u}_1^\pm(x,\pm0)+\mathbf{u}_2^\pm(x,\pm0) =\mathbf{w}_2(x,\pm h_0), \tag{35}$$

$$\sigma_0^{(y\pm)}(x,0)=\mathbf{A}_0D_\xi\mathbf{w}_2|_{\xi=\pm h_0}+\mathcal{M}_1\mathbf{w}_1|_{\xi=\pm h_0}. \tag{36}$$

Equations (34) and (36) can be simplified using the results from the previous steps:

$$D_\xi\mathbf{A}_0D_\xi\mathbf{w}_2+D_\xi\mathbf{A}_1D_x\mathbf{w}_1+D_x\mathbf{A}_3D_x\mathbf{w}_0=\mathbf{0},\quad (x,\xi)\in\Omega_0, \tag{37}$$

$$\sigma_0^{(y\pm)}(x,0)=\mathbf{A}_0D_\xi\mathbf{w}_2|_{\xi=\pm h_0}+\mathbf{A}_1D_x\mathbf{w}_1|_{\xi=\pm h_0}, \tag{38}$$

where we have introduced a new notation:

$$\mathbf{A}_3=\tau\begin{pmatrix}1&0\\0&0\end{pmatrix},\quad \tau=\frac{4\mu_0(\lambda_0+\mu_0)}{\lambda_0+2\mu_0}=\frac{2\mu_0}{1-\nu_0}. \tag{39}$$

Equation (38) can be integrated to give:

$$A_0 D_\xi w_2 + A_1 D_x w_1$$
$$= a_3(x) - D_x \int_0^\xi A_3(x,t)dt \cdot D_x w_0, \quad (x,\xi) \in \Omega_0. \quad (40)$$

From this equation and (38) one can immediately conclude that

$$[\sigma_0^{(y)}]_{y=0} + D_x \int_{-h_0}^{h_0} A_3(x,t)dt \cdot D_x w_0 = 0. \quad (41)$$

However, taking into account relations (22)-(24), last equation can be rewritten in the form:

$$[\sigma_0^{(y)}]_{y=0} + D_x \int_{-h_0}^{h_0} A_3(x,t)dt \cdot D_x u_0|_{y=0} = 0, \quad (42)$$

which constitutes together with (24) the sought for necessary transmission conditions for the first external BVP in the case of the stiff interface.

Summarizing the obtained result with those concerning imperfect transmission conditions from [Antipov (2001); Movchan (1995); Mishuris (2005b)] one can collect them together within Table 1. It is assumed that the imperfect interface is always situated along the coordinate line $y = 0$.

Table 1 : Possible sets of transmission conditions depending on the relative properties of the thin intermediate layer: 2-D problems

interface		
soft	comparable	stiff
$[u_x] - a_2\sigma_{xy} = 0$	$[u_x] = 0$	$[u_x] = 0$
$[u_y] - a_1\sigma_y = 0$	$[u_y] = 0$	$[u_y] = 0$
$[\sigma_{xy}] = 0$	$[\sigma_{xy}] = 0$	$[\sigma_{xy}] + \frac{\partial}{\partial x}(a_3 \frac{\partial u_x}{\partial x}) = 0$
$[\sigma_y] = 0$	$[\sigma_y] = 0$	$[\sigma_y] = 0$

Here, the parameters a_j in formulae from Table 1 are, generally speaking, functions with respect to the variable x and have to be calculated according to the equations in Table 2. Under the additional assumption that the material properties of the interface do not vary in direction perpendicular to the interface (do not depend on variable y in this case) these equations can be simplified and rewritten in forms presented in Table 3, where all mechanical and geometrical parameters can be only functions of variable x (change its values only along the imperfect interface).

Table 2 : General representation of the parameters $a_j(x)$ in Table 1 for plane strain and plane stress case

case	plane strain	plane stress
$a_1(x)$	$\int_{-h}^{h} \frac{(1+\nu)(1-2\nu)}{E(1-\nu)} dy$	$\int_{-h}^{h} \frac{(1-\nu^2)}{E} dy$
$a_2(x)$	$\int_{-h}^{h} \frac{2(1+\nu)}{E} dy$	$\int_{-h}^{h} \frac{2(1+\nu)}{E} dy$
$a_3(x)$	$\int_{-h}^{h} \frac{E}{1-\nu^2} dy$	$\int_{-h}^{h} E\, dy$

Table 3 : Particular representation of the parameters $a_j(x)$ in Table 1 for plane strain and plane stress case

case	plane strain	plane stress
$a_1(x)$	$\frac{2h(1+\nu)(1-2\nu)}{E(1-\nu)}$	$\frac{2h(1-\nu^2)}{E}$
$a_2(x)$	$\frac{4h(1+\nu)}{E}$	$\frac{4h(1+\nu)}{E}$
$a_3(x)$	$\frac{2hE}{1-\nu^2}$	$2hE$

3 Numerical results

3.1 *Dissimilar layer with soft imperfect interface under simple shear and tensile loading*

Let us consider a dissimilar elastic structure with a thin elastic interphase which exhibits other properties than the bonded materials (Fig. 1). The thickness of the interface zone is assumed to be small $\varepsilon = 2h/H = 0.01$ and this value will be considered through out the paper as a small parameter. In this subsection, results similar to those presented in paper [Mishuris (2005b)] will be evaluated. The only difference is now that the matched materials are not the same. The top part of the structure is represented by steel with elastic constants $E_+ = 210000$ MPa, $\nu_+ =$ 0.3, while the bottom part is of aluminum ($E_- = 72700$

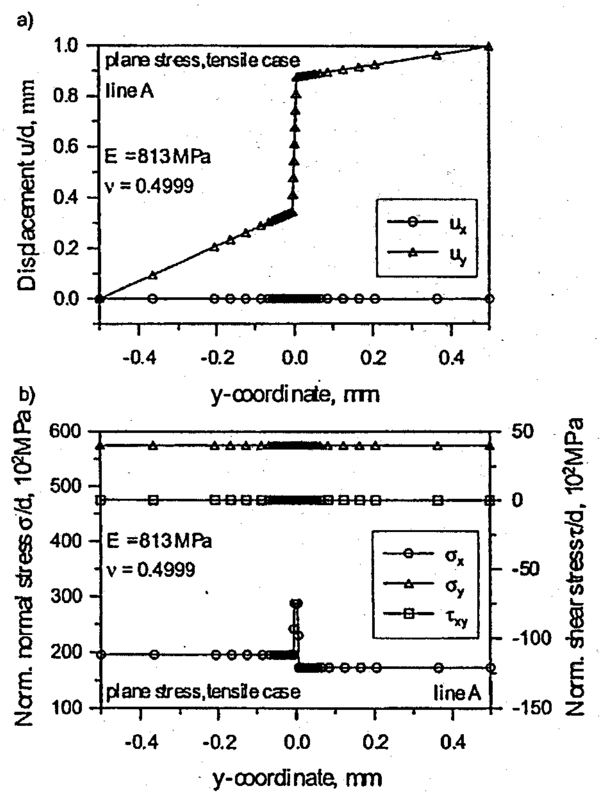

Figure 2 : Displacement and stress distribution along line A for the asymmetric sample and the simple tensile loading

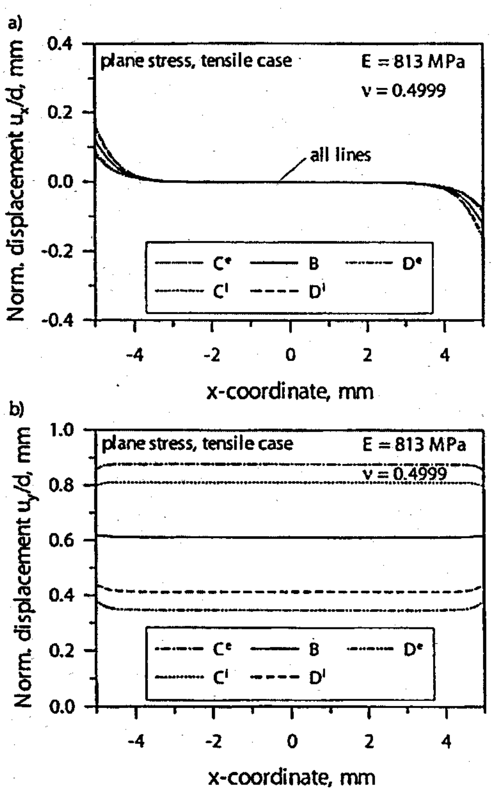

Figure 3 : Displacement distribution along lines B, C and D for the asymmetric sample and the simple tensile loading

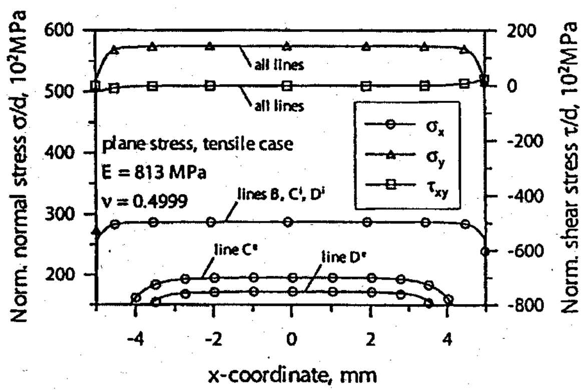

Figure 4 : Normal and shear stress distribution along horizontal lines B, C and D for the asymmetric sample and the simple tensile loading

MPa, $\nu_- = 0.34$). Various elastic constants for the interphase material are considered in the same way as it has been done in Mishuris (2005b) for easy comparison of the obtained results. First, simple tensile and simple shear loadings are considered: $v_x(x) = 0$, $v_y(x) = 1 \cdot d$ (where d is an arbitrary dimensionless parameter for normalization) and $v_x(x) = 1 \cdot d$, $v_y(x) = 0$, respectively. All calculations have been done by the FE code MSC.Marc. For details concerning the constructed FEM-mesh for the considered structure we refer the reader to the first part of the paper [Mishuris (2005b)].

In Figs. 2, 3 and 4, the normalized distributions of the displacements and the stresses in direction perpendicular to the interface (along the line A) and along the interface (lines B, C^e, C^i, D^e, D^i) are presented (see Fig. 1 for the used notations). The material parameters of the soft weakly compressible intermediate layer in this case are: $E = 813$ MPa, $\nu = 0.4999$ (the same as in paper [Mishuris (2005b)] for the reason of comparison).

It is easy to see that the solution has lost its symme-

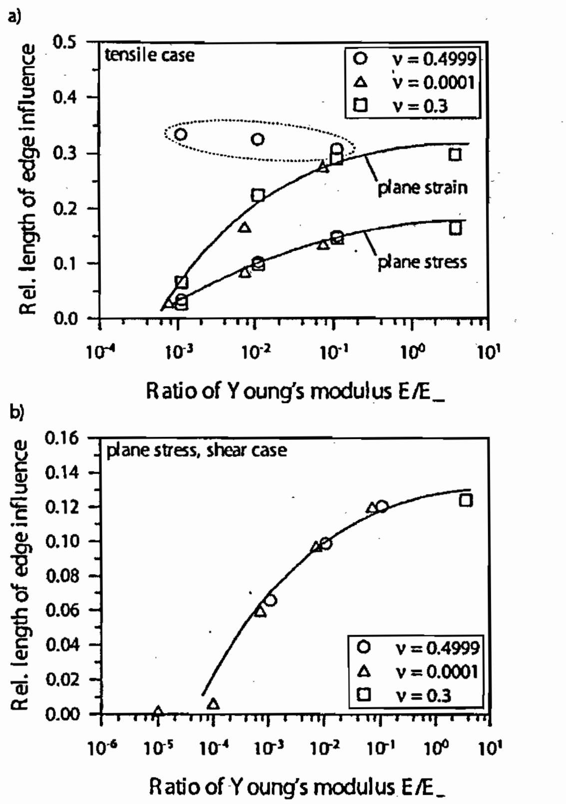

Figure 5 : Relative length of the edge effect zone for the asymmetric sample

try which is natural to the problem definition. However, because of simple tensile loading, displacements and stresses on lines B, C^e, C^i, D^e, D^i are still practically constants along the major part of the imperfect interface. This enables us to easily define the size of the edge zone with the same 1% accuracy criterion from changing the constant behavior of the traction along the interface. Corresponding results are included in Fig. 5. Similarly as in the symmetrical case, only the weakly compressible interface for the plane strain case under tensile loading exhibits irregular behavior in comparison with all other cases.

Let us note that there is no practical difference in the case of the shear loading for plane strain and plane stress states. This phenomenon has been explained in [Mishuris (2005b)], and is a simple consequence of the fact that the components of both solutions responsible for the shear deformation satisfy the same equations, boundary and transmission conditions (cf. Table 1). Because of this fact, we present here in Fig. 5b only the plane stress case. On the other hand, the straight line behavior of the solution within the sample give us an occasion to restrict our interest to the accuracy of the transmission conditions in one point and we have chosen the symmetry point $x = 0$ in the middle of the rectangle, i.e. the same point as in [Mishuris (2005b)]. Corresponding results have been collected in Tables 4-7. In Table 7 for the plane strain case we have presented one case for comparison with Table 6.

Within the edge zone, the behavior of the solutions for the dissimilar body may essentially differ in comparison with the symmetrical case due to the distinct limited asymptotic behavior of the solution near the corner points of the intermediate layer and the external boundary (intersection points). This fact is manifested by Fig. 3. However, even within the edge effect zone, the corresponding transmission transmission conditions from Table 1 are still valid. We discuss this phenomenon in details later in the fourth subsection.

3.2 *Dissimilar layer with soft imperfect interface under complex loading.*

In the first part of this paper [Mishuris (2005b)], only symmetrical structures with simple external loading, i.e. simple tensile or simple shear, were considered for a soft interphase and the accuracy of the transmission conditions turned out to be much better than one could expect from the theoretical point of view. In order to investigate if this fact was based on the simple cases under consideration, we are going to investigate in this subsection the influence of complex loading on the accuracy of the transmission conditions for asymmetric samples. First of all, it is necessary to underline once again that the conditions checked up till now numerically, have been satisfied with an error smaller than that predicted from the asymptotic theory. We are going to show now that this is because of the applied simple loading and, in case of a complex one, the theoretical predictions simply coincide with the numerical calculations.

Let us consider a more complicated tensile loading in the same dissimilar structure with the same soft interface as in the previous subsection. Namely, instead of the uniform external loading, a complex tensile loading defined as follows: $u_y(x,h/2) = v_y(x) = dx^2/25$, $v_x(x) = 0$ is applied in the plane stress case.

Numerical results in graphical form for such loading,

Table 4 : Relative errors for the second and fourth transmission conditions from Table 1 for the asymmetric plane stress simple tensile case along line A

E	ν	$\frac{\Delta u_y(0,0)}{\sigma_y(0,0)}$	$\frac{2h(1-\nu^2)}{E}$	rel. error	$\frac{\Delta\sigma_y(0,0)}{\sigma_y(0,0)}$
8138	0.4999	$9.217259\cdot10^{-7}$	$9.217252\cdot10^{-7}$	$6.916\cdot10^{-7}$	$-9.088\cdot10^{-9}$
813	0.4999	$9.226338\cdot10^{-6}$	$9.226322\cdot10^{-6}$	$1.735\cdot10^{-6}$	$-3.479\cdot10^{-8}$
81	0.4999	$9.260510\cdot10^{-5}$	$9.260494\cdot10^{-5}$	$1.724\cdot10^{-7}$	$-1.008\cdot10^{-8}$
5427	0.0001	$1.842648\cdot10^{-6}$	$1.842639\cdot10^{-6}$	$5.084\cdot10^{-6}$	$-1.001\cdot10^{-8}$
542	0.0001	$1.845021\cdot10^{-5}$	$1.845018\cdot10^{-5}$	$1.538\cdot10^{-6}$	$-2.662\cdot10^{-8}$
54	0.0001	$1.851854\cdot10^{-4}$	$1.851852\cdot10^{-4}$	$1.286\cdot10^{-6}$	$-1.934\cdot10^{-8}$
8138	0.3000	$1.118216\cdot10^{-6}$	$1.118211\cdot10^{-6}$	$4.183\cdot10^{-6}$	$-9.285\cdot10^{-9}$
813	0.3000	$1.119313\cdot10^{-5}$	$1.119311\cdot10^{-5}$	$1.404\cdot10^{-6}$	$-1.936\cdot10^{-8}$
81	0.3000	$1.123458\cdot10^{-4}$	$1.123457\cdot10^{-4}$	$1.450\cdot10^{-7}$	$-1.205\cdot10^{-8}$
271270	0.3000	$3.354742\cdot10^{-8}$	$3.354591\cdot10^{-8}$	$4.490\cdot10^{-4}$	$-2.460\cdot10^{-8}$

Table 5 : Relative errors for the second and fourth transmission conditions from Table 1 for the asymmetric plane strain simple tensile case along line A

E	ν	$\frac{\Delta u_y(0,0)}{\sigma_y(0,0)}$	$\frac{2h(1+\nu)(1-2\nu)}{E(1-\nu)}$	rel. error	$\frac{\Delta\sigma_y(0,0)}{\sigma_y(0,0)}$
8138	0.4999	$7.472625\cdot10^{-10}$	$7.370853\cdot10^{-10}$	$1.362\cdot10^{-2}$	$2.465\cdot10^{-5}$
813	0.4999	$7.387995\cdot10^{-9}$	$7.378106\cdot10^{-9}$	$1.195\cdot10^{-3}$	$3.102\cdot10^{-5}$
81	0.4999	$7.407831\cdot10^{-8}$	$7.405432\cdot10^{-8}$	$3.238\cdot10^{-4}$	$1.119\cdot10^{-5}$
5427	0.0001	$1.842650\cdot10^{-6}$	$1.842639\cdot10^{-6}$	$5.980\cdot10^{-6}$	$-1.122\cdot10^{-7}$
8138	0.3000	$9.128290\cdot10^{-7}$	$9.128252\cdot10^{-7}$	$4.142\cdot10^{-6}$	$-1.205\cdot10^{-7}$

Table 6 : Relative errors for the second and fourth transmission conditions from Table 1 for the asymmetric plane stress simple shear case along line A

E	ν	$\frac{\Delta u_x(0,0)}{\sigma_{xy}(0,0)}$	$\frac{4h(1+\nu)}{E}$	rel. error	$\frac{\Delta\sigma_{xy}(0,0)}{\sigma_{xy}(0,0)}$
8138	0.4999	$3.686151\cdot10^{-6}$	$3.686164\cdot10^{-6}$	$-3.381\cdot10^{-6}$	$5.612\cdot10^{-8}$
813	0.4999	$3.689783\cdot10^{-5}$	$3.689791\cdot10^{-5}$	$-2.034\cdot10^{-6}$	$6.127\cdot10^{-8}$
81	0.4999	$3.703429\cdot10^{-4}$	$3.703431\cdot10^{-4}$	$-7.541\cdot10^{-6}$	$3.947\cdot10^{-8}$
5427	0.0001	$3.685663\cdot10^{-6}$	$3.685646\cdot10^{-6}$	$4.565\cdot10^{-6}$	$2.806\cdot10^{-8}$
542	0.0001	$3.690406\cdot10^{-5}$	$3.690406\cdot10^{-5}$	$-8.265\cdot10^{-8}$	$6.128\cdot10^{-8}$
54	0.0001	$3.704048\cdot10^{-4}$	$3.704074\cdot10^{-4}$	$-7.147\cdot10^{-6}$	$3.948\cdot10^{-8}$
271270	0.3000	$9.585672\cdot10^{-8}$	$9.584547\cdot10^{-8}$	$1.174\cdot10^{-4}$	$7.586\cdot10^{-7}$

Table 7 : Relative errors for the second and fourth transmission conditions from Table 1 for the asymmetric plane strain simple shear case along line A

E	ν	$\frac{\Delta u_x(0,0)}{\sigma_{xy}(0,0)}$	$\frac{4h(1+\nu)}{E}$	rel. error	$\frac{\Delta\sigma_{xy}(0,0)}{\sigma_{xy}(0,0)}$
8138	0.4999	$3.686143\cdot10^{-6}$	$3.686164\cdot10^{-6}$	$-5.665\cdot10^{-6}$	$2.806\cdot10^{-8}$

analogous to those in Figs. 2-4, are presented in Figs. 6-8. As earlier, it is easy to see that the displacements are still linearly distributed within the considered soft weakly compressible interface, while the stresses are constant in the direction perpendicular to the interface. Moreover, the stress components σ_{xy} and σ_y are continuous across the interface as it follows from Fig. 8 a) and the remaining component σ_x exhibits a discontinuous behavior, as

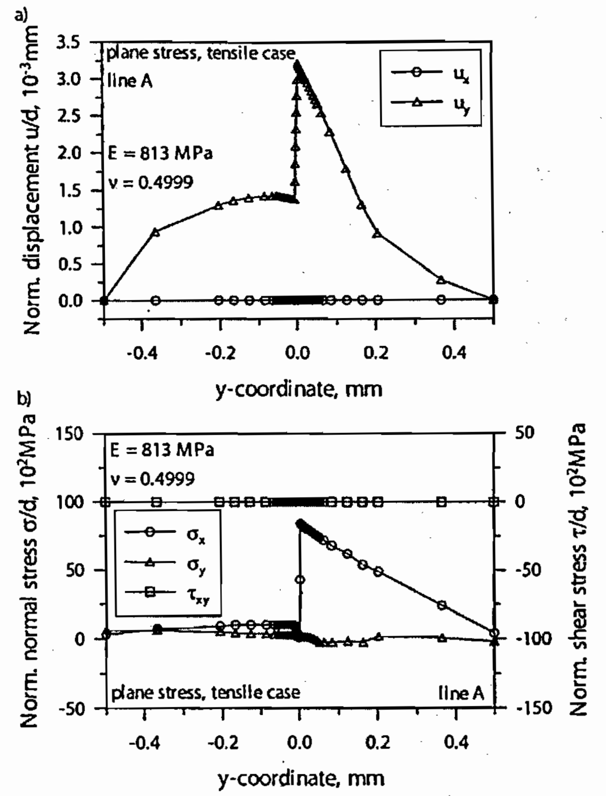

Figure 6 : Displacement and stress distribution for the asymmetric sample and the asymmetric tensile loading

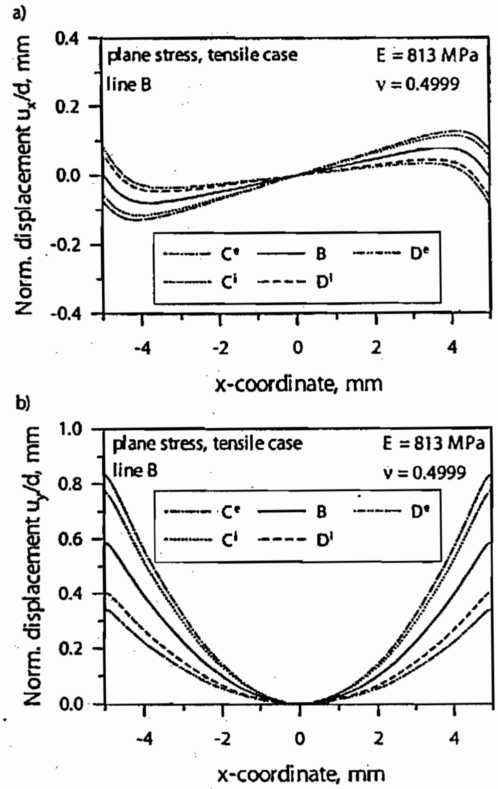

Figure 7 : Displacement distribution for the asymmetric sample and the asymmetric tensile loading along lines B, C and D

it should be expected.

However, distributions of displacement and stress components along the interface (cf. Figs. 7-8) are no longer practically constants and essentially change its behavior along the interface. Nevertheless, the vector of stresses is continuous through the interface as it follows from Fig. 8b and as it has to be according to the transmission conditions (Table 1). As a result, it is more difficult in this case to determine the edge effect zone. In the previous subsection a simple exact analytical solution has existed far away from the external edge boundary (constant stresses within each material). Now, to find the size of the edge effect zone we propose to apply another technique. Namely, we additionally load the right (and left) hand sides of the rectangle (Fig. 1) by some additional loading having zero main vectors and observe the changes in the respective solution. As we have expected, the obtained results are similar to those reported in Fig. 5 and corresponding results are presented in the first row of Table 9. One can see that the edge effect zone (calculated by the perturbation method) differs depending on which displacement or stress components it has been extracted from. However, this is not an unexpected phenomenon. For example, for the symmetrical sample and symmetrical loading, one pair of the stress and displacement components gives the edge effect zone of zero length at all due to the symmetry (cf. [Mishuris (2005b)]). In [Boichuk (2001); Kokhanenko (2003)] even the edge effect zones are determined for each component of stresses. Moreover, the sizes of the zones essentially depend on the chosen criterium. It is evident that only a crude estimation of the edge zone can be obtained in the early proposed way. Because of this, we restrict ourself in these numerical simulations to the accuracy of 0.1 in the absolute value. In the author's opinion, such information is absolutely enough to clarify the range of the phenomenon. A more important value

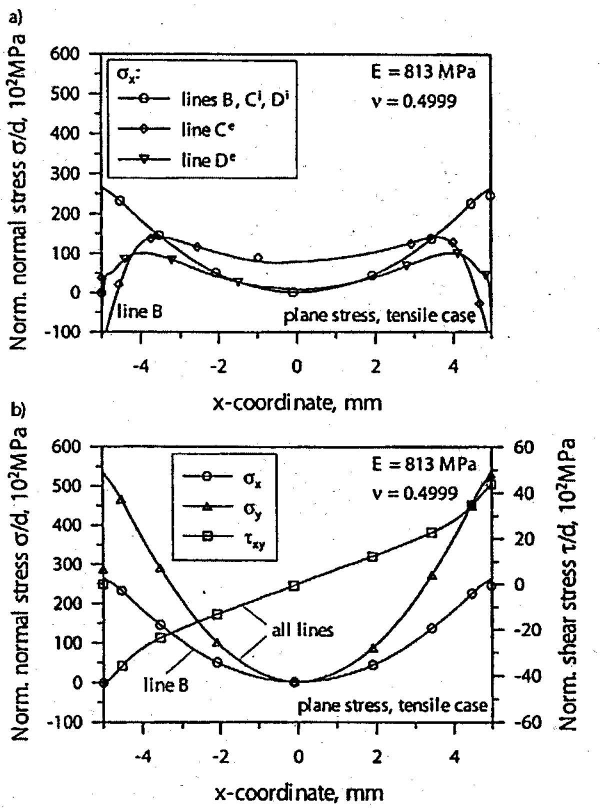

Figure 8 : Normal and shear stress distribution for the asymmetric sample and the asymmetric tensile loading along horizontal lines B, C and D

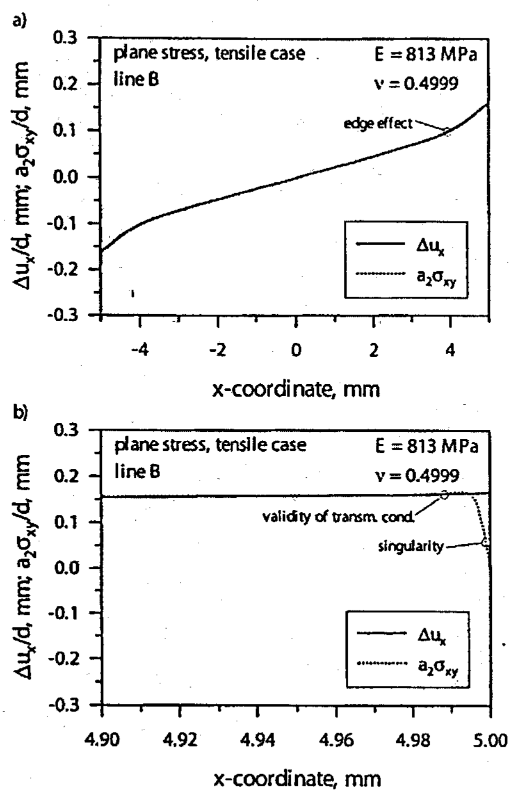

Figure 9 : Verification of the first transmission condition for the soft interface from Table 1 ($d = 1$)

for users is the size of the region where the transmission conditions hold true.

In order to find this region with a good accuracy we have additionally calculated the jumps of the corresponding displacement components from different sides of the thin interface, $[u_x]$ and $[u_y]$, and the stress components σ_{xy} and σ_y, along the middle line of the interface which have been normalized by the respective constants a_1 and a_2 according to Table 1. Corresponding results are presented in Figs. 9, 10.

One can observe a good correlation between the functions and, from the first glance, the same excellent agreement with respect to the transmission condition accuracy. However, if one wants to calculate the relative error between the values, the error has a different range in different points. This is because of the variation of the function values along the interface that makes it impossible to provide any conclusions uniquely based on the relative error estimation at any a priori chosen point, as it has been done earlier. Moreover, in the center of the sample all values even disappear with machine zero accuracy. As a result, it is impossible to directly extract the error at point $x = 0$ at all. To clarify this fact, we present in Table 8 relative errors connected with the second and the fourth transmission conditions from Table 1. The errors have been calculated in two different points at $x = 0$ (by extrapolation from the nearest points) and far away from the center (at point $x = 3.0$). From the first glance, it follows from Table 8 that the accuracy of the transmission conditions drastically changes in comparison with the previous simple loading. However, this is not an accurate conclusion.

Let us remind ourselves that the analytical estimation which has been proved for the case under consideration (the soft interface) in [Mishuris (2005b)] gives us the theoretical prediction of the order $O(\varepsilon)$. From the asymptotic analysis point of view, this only means that any

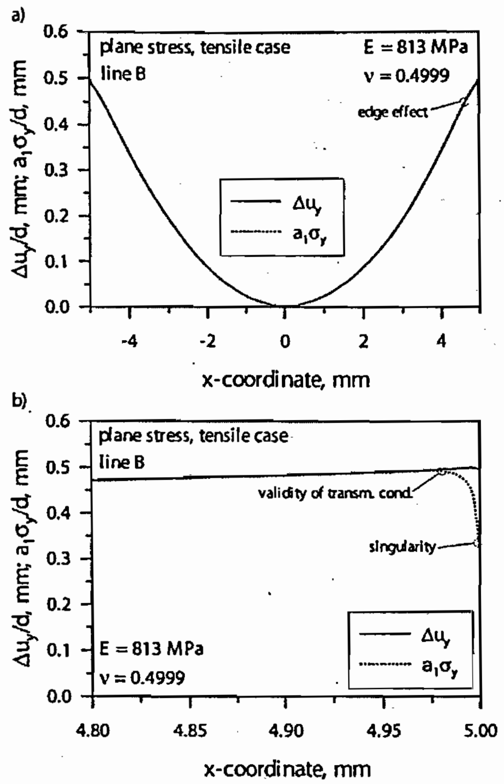

Figure 10 : Verification of the second transmission condition for the soft interface from Table 1 ($d = 1$)

value along the interface (e.g. components of the displacement or stress) is represented in the form: $z(x) = z_0(x) + \varepsilon z_1(x)$, where εz_1, in fact, is the mentioned error. However, this fact is not influenced by the relative error which is $\varepsilon z_1(x)/z(x) = O(\varepsilon)$ at an arbitrary point of the interface. This is not true, for example, near the point where $z_0(x) = 0$ holds. An appropriate approach consists in comparison of any norms of the functions that gives correct result: $||\varepsilon z_1||/||z|| = O(\varepsilon)$. Of course, in the case of a constant value ($z(x) = \text{const}$) point by point and norm definitions of the relative error coincides themselves.

Let us return to the evaluation of such value which is of extremely interest for users and researchers as the range of the validity of the nonclassical transmission conditions. Fortunately, it is still possible to determine the zone of validity of the transmission conditions with the 1% accuracy criterion based on a point by point relative error estimate starting from a point far away from the center. It is important to note that the transmission conditions are still valid within the edge effect zone. For the case under consideration the limits of the edge effect zone are marked by points in Figs. 9a and 10a. However, it is impossible to see in these figures where the transmission conditions are not valid. For this reason, we have prepared corresponding magnifications near the right-hand side of the dissimilar sample. One can easily see from the figures that the transmission conditions are still valid within the edge effect zone. The corresponding regions have been calculated with the 1% criterion and are presented in the second row of Table 10.

Let us note that there are two singular points (intersection of the interface boundaries with the external boundaries of the sample). Moreover, in the case of the dissimilar body, corresponding stress singularities are different. From the results presented in Figs. 9b and 10b one can conclude that the singularity dominated region is extremely small. Its length consists of 10^{-4} or $0.01 \cdot 2h$ that coincides with results of Akisanya reported in [Akisania (1997)]. In Figs. 9b and 10b it is easy to see that the singularity dominated region is even essentially smaller than the region where the transmission conditions are not valid. In fact, the region between the depicted points in Figs. 9b and 10b is a transmission zone between two absolutely different solution behaviors. Moreover, the singularity only appears in the respective stress term (displacement discontinuities are bonded functions). The accurate range of this zone can be calculated within the same 1% accuracy in determination of stress singularity exponent (cf. Table 9). It must be remembered that the constructed FEM mesh is very dense near the singular points.

Finally, in Table 10 norm estimate for the first two transmission conditions from Table 1 have been presented not only along the whole interface (interval (-5,5)) but also within the interval of the transmission condition validity. One can see from these results that in such a way defined relative norm error is always within range of $\varepsilon = 10^{-2}$ for the complex loading, which coincides with the theoretically predicted from the asymptotic analysis, and essentially better for the simple loading, as it has been mentioned above. Moreover, within the zone of the condition validity, the calculated integral error is an order smaller than the predicted one. Also the mentioned great influence of the applied loading on the final estimate is clearly observed.

Table 8 : Point by point verification of the transmission conditions. Plane stress, asymmetric sample and the asymmetric tensile loading, $E = 813$ MPa, $\nu = 0.4999$

x	$\frac{\Delta u_y}{\sigma_y}$	$\frac{2h(1-\nu^2)}{E}$	rel. error	$\frac{\Delta\sigma_x}{\sigma_y}$
0.0	$8.621439 \cdot 10^{-6}$	$9.226322 \cdot 10^{-6}$	$-7.016 \cdot 10^{-2}$	$-3.088 \cdot 10^{-2}$
3.0	$9.221909 \cdot 10^{-6}$	$9.226322 \cdot 10^{-6}$	$-4.785 \cdot 10^{-4}$	$-2.728 \cdot 10^{-4}$

Table 9 : Ranges of the different edge phenomena. Plane stress, $E = 813$ MPa, $\nu = 0.4999$

	asymmetric tensile loading		simple tensile loading	
	$(\Delta u_y, \sigma_y)$	$(\Delta u_x, \sigma_{xy})$	$(\Delta u_y, \sigma_y)$	$(\Delta u_x, \sigma_{xy})$
range of the edge effect	4.6	3.9	4.5	3.4
range of validity of the transmission condition	4.9803	4.9883	4.9803	4.9894
range of the singularity dominated domain	4.999...	4.999...	4.999...	4.999...

Table 10 : Norm verification of the transmission conditions. Plane stress, asymmetrical tensile loading, $E = 813$ MPa, $\nu = 0.4999$

error	interval	$\frac{\|\Delta u_x - a_2\sigma_{xy}\|_2}{\|\Delta u_x\|_2}$	$\frac{\|\Delta u_y - a_1\sigma_y\|_2}{\|\Delta u_y\|_2}$
simple loading	$(-5.00, 5.00)$	$6.563 \cdot 10^{-2}$	$6.876 \cdot 10^{-3}$
	$(-4.98, 4.98)$	$2.390 \cdot 10^{-3}$	$5.460 \cdot 10^{-4}$
complex loading	$(-5.00, 5.00)$	$3.575 \cdot 10^{-2}$	$1.614 \cdot 10^{-2}$
	$(-4.98, 4.98)$	$1.778 \cdot 10^{-2}$	$1.153 \cdot 10^{-3}$

3.3 *Stiff nonideal interface in dissimilar structure*

In this subsection the stiff imperfect interface discussed in the introduction is numerically investigated. For this aim, the same steel-aluminum dissimilar rectangle, but with a thin stiff intermediate layer (elastic constants: $E = 21 \cdot 10^6$ MPa, $\nu = 0.3$), is under consideration. The same simple tensile loading $u_y(x, H/2) = v_y(x) = 1 \cdot d$, $u_x(x, H/2) = v_x(x) = 0$ as in subsection 3.1 has been applied in this case. Corresponding distributions of all components of the displacement and stress along the line A (in the middle line of the sample within the interphase) and along the lines B-D (parallel to the interface) are presented in Fig. 11a and Figs. 12-13, respectively. As it follows from the asymptotic solution (cf. (19)-(21)), the displacements within the interphase should be constant in the direction perpendicular to the interface. This fact is confirmed by FEM-calculations in Figs. 11a-12. On the other hand, according to the obtained numerical results in Fig. 11b, the stress components are also constants, while one can conclude from (36), (38) and (40) that the shear stress should rather change its behavior in direction perpendicular to the interface. There is, nevertheless, a simple explanation of the fact observed in the calculations. Namely, one can notify that $\frac{\partial^2}{\partial x^2}u_x = 0$ at point $x = 0$ due to the symmetry conditions (and it is easy to observe in the numerical calculations presented in Fig. 12). Moreover, from Fig. 13 where stress distributions are shown along different lines parallel to the interface and are lying in and out of the interface, one can conclude that all stress components behave exactly in the way as predicted by asymptotic analysis. In this case, only the validity of the fourth transmission condition from Table 1 is not evident in advance. For this reason, we additionally calculated the jump of the shear stress from different parts of the interface, $[\sigma_{xy}]$, and the second derivative of the displacement u_x normalized by the parameter a_3 due to Table 1. Figure 14 confirms a good agreement between the functions.

The edge effect zone can be easily estimated from Fig. 12b and 13a where one of the displacement components u_y and two stress components σ_x and σ_y practically

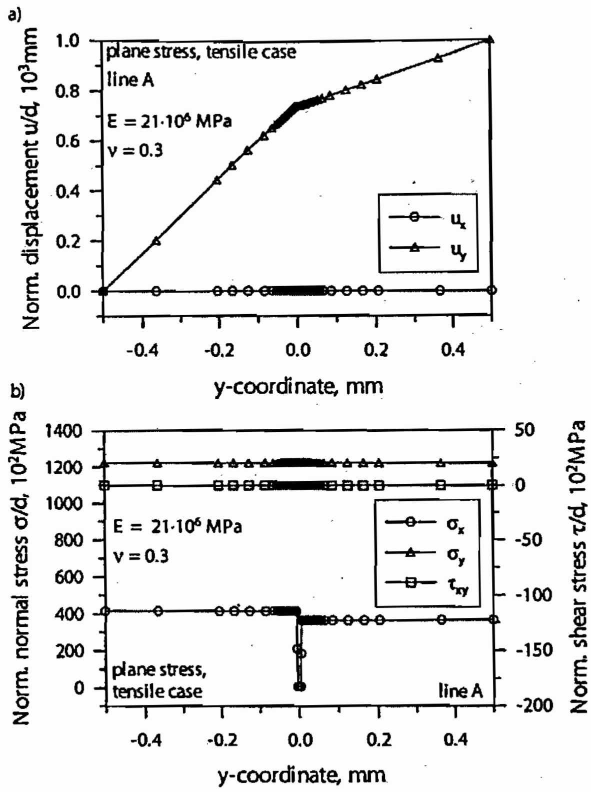

Figure 11 : Displacement and stress distribution along the symmetry axis perpendicular to the interface in the asymmetric sample and the simple tensile loading for the stiff interface

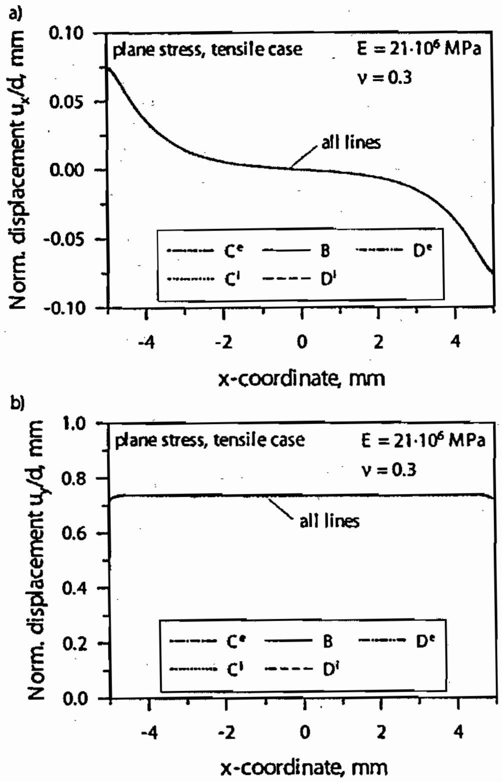

Figure 12 : Displacement distribution along lines B, C and D parallel to the interface in the asymmetric sample and the simple tensile loading for the stiff interface ($d = 1$)

exhibit a constant behavior along the interface. The corresponding distance from the external boundary is even smaller than in the case of the soft interface. To calculate the region where the considered transmission condition is valid, we prepared as earlier a magnification (cf. Fig. 14b) near the right-hand side boundary. Corresponding points on the figure illustrate the respective values. The singularity dominated region is of the same length, while the zone where the transmission condition does not hold true is now two times longer. Moreover, the second derivative of the displacement at the middle line of the interphase ($y = 0$) is bounded near the free boundary. This is an additional proof that the singularity dominated domain is essentially smaller than the thickness of the interface. Otherwise, one should observe a higher growth of the derivative near the free boundary.

Finally, we have also tried to verify the stiff transmission condition in the case of the complex loading which has been introduced in the previous section for the soft interface. However, our FEM-mesh leaded to the same unsatisfactory behavior of the solution, as it has been discussed in the introduction of the first part [Mishuris (2005b)]. This is because bending plays an important role for such loading together with the stiff interface and makes it impossible to use the constructed mesh for the verification of the transmission conditions in this case.

4 Discussions and Conclusions

As it follows from the numerical results by FEM analysis presented here and in paper [Mishuris (2005b)], imperfect transmission conditions for the thin soft and stiff interphases analytically obtained by asymptotic analysis are satisfactory with a very good accuracy even in the case of $\varepsilon = 0.01$. Moreover, in the case of simple symme-

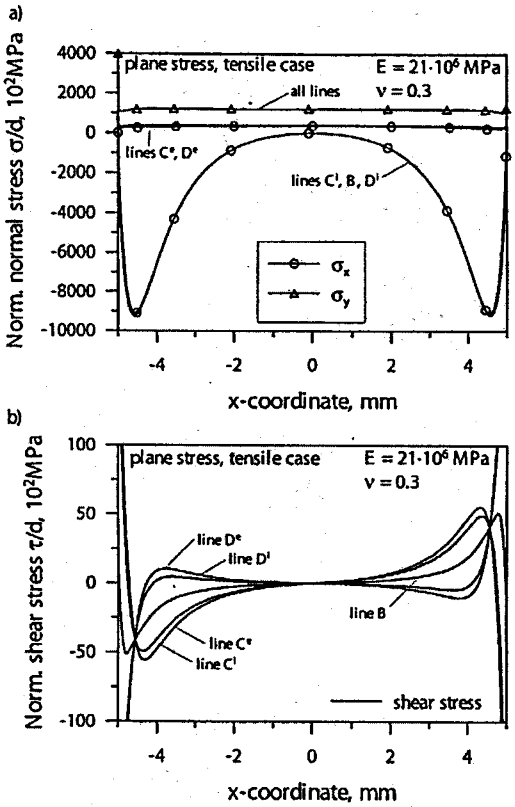

Figure 13 : Normal and shear stress distribution along lines B, C and D parallel to the interface in the asymmetric sample and the simple tensile loading for the stiff interface

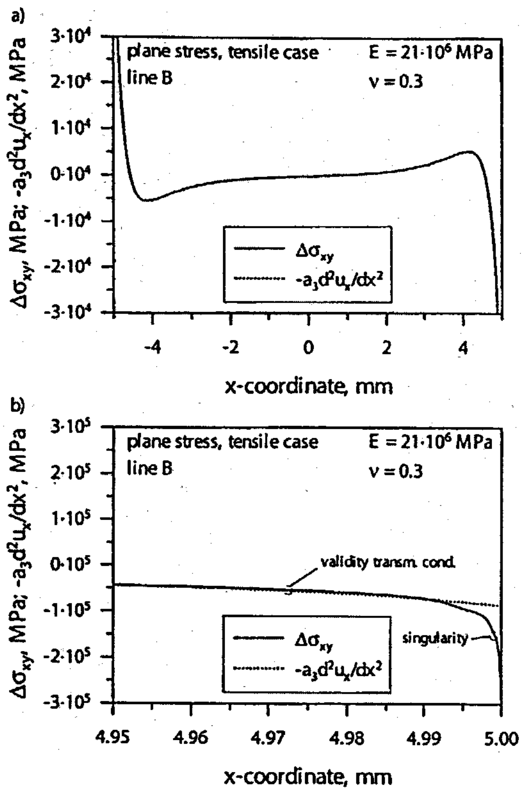

Figure 14 : Verification of the fourth transmission condition for the stiff interface from Table 1 ($d = 1$)

try, the accuracy is essentially better than that predicted by theory. Only in the case of the plane strain problem for the soft weakly compressible interface, the error manifests an essentially different behavior. Let us note that in this case Lamé parameters of the interphase material are not comparable in value and one of the main necessary assumptions to prove the transmission conditions obtained are not valid.

As a result, in the case of the thin intermediate layer between two elastic materials different transmission conditions can be applied depending on relations between the material parameters of the bonded materials and the interphase zone. The question when one can use particular transmission conditions has been answered taking into account relations between the problem parameters. However, it is enough to use, in fact, only two of them - for the stiff and the soft interface. Namely, if the interphase is stiffer than the bonded materials then it makes sense to use the stiff interface transmission conditions, while in the case when the material parameters of the thin layer are smaller than the matched ones then it is necessary to use the transmission conditions for the soft interface. Then in the intermediate case of the comparable in value interface parameters a_j have the same degree $O(\varepsilon)$ with respect to the only small parameter $\varepsilon = h/H$ as the theoretically predicted error.

However, there are still some questions which still remain to be clarified. First, it is necessary to evaluate transmission conditions in the case of the weakly compressible interphase and estimate by the same FEM-analysis the range of their applicability. This phenomenon has been observed in [Ryabenkov (1999)] but no solution has been suggested. On the other hand, it is highly important to estimate an error introduced into final calculations by utilization of any of the proposed imperfect transmission conditions from the initial stage.

Hence, the analysis will be not complete if one does not calculate numerical solutions based on the imperfect transmission conditions and does not compare it with the accurate numerical solutions for the finite thin interface. Moreover, such comparison has been done in the whole domain not only near the imperfect interface. Let us note that the estimates for the zones presented in Table 7 give us the possibility to properly locate special singular and transmission elements of respective sizes in a constructed FEM mesh. These problems will be pointed out in future investigations.

The edge effect appears on a distance comparable with twenty five times the thickness of the interface. In fact, this zone can be considered as a region where Saint-Venant's principle fails. The interesting and important fact is that this zone essentially depends on the type of interface that is not so evident from the first glance. Namely, the size of the edge effect zone monotonically depends on the ratio E/E_{-}. However, the verified transmission conditions fail only on a distance of two interface thickness, while the singularity dominated zone extends on a distance of only $h/100$. Of course, the lengths of the zones are strongly influenced by the chosen criterion. We have applied a 1% accuracy criterion throughout the paper which corresponds to the predicted accuracy of the transmission conditions $O(\varepsilon)$. However, regardless of the criterion choice the region where the transmission conditions are not valid is essentially smaller than the size of the edge zone.

Although FEM analysis is very useful for verification in value in comparison with the formal asymptotic analysis, it has its own restrictions concerning values of the small parameter and strong difficulties connecting with necessity to build a complicated mesh which can be additionally depending on the type of loading, as it occurred in our investigations for bending. Also it is difficult to define an unknown form of corresponding transmission conditions from FEM analysis. However, in the case when one can suppose any specific conditions, they might be numerically verified. In such a way there is a possibility to evaluate imperfect transmission conditions in the case when respective asymptotic analysis is difficult to carry out. Taking this fact into account, we are going to evaluate and verify transmission conditions for thin plastic interphases. First attempt have been done in [Mishuris (2005a)].

Acknowledgement: G. Mishuris is grateful for support provided by the NATO collaborative linkage grant PST.CLG.980398. A. Öchsner is grateful to Portuguese Foundation of Science and Technology for financial support.

References

Akisania, A.R.; Fleck, N. (1997): Interfacial cracking from the free-edge of a long bi-material strip. *Int J Solids Structures*, vol. 34, pp. 1645–1665.

Antipov, Y.A.; Avila-Pozos, O.; Kolaczkowski, S.T.; Movchan, A.B. (2001): Mathematical model of delamination cracks on imperfect interfaces. *Int. J. Solids and Structures*, vol. 38, pp. 6665–6697.

Boichuk, V. (2001): Edge effects in a composite weakly reinforced with fibers of rectangular cross section. *Int Appl Mech*, vol. 37, pp. 682–688.

Kokhanenko, Y.V.; Fesenko, S. (2003): Influence of young's moduli of a laminated composite with a periodic system of cracks on edge effects. *Int Appl Mech*, vol. 39, pp. 99–104.

Li, W.; Siegmund, T. (2004): Numerical study of indentation delamination of strongly bonded films by use of a cohesive zone model. *CMES: Computer Modeling in Engineering & Sciences*, vol. 5, no. 1, pp. 81–90.

Mishuris, G.; Öchsner, A. (2005): Transmission conditions for a soft elasto-plastic interphase between two elastic materials. plane strain state. *Arch Mech*, vol. 57, pp. 157–169.

Mishuris, G.; Öchsner, A.; Kuhn, G. (2005): Fem-analysis of nonclassical transmission conditions between elastic structures. part 1: Soft imperfect interface. *CMC: Computers, Materials & Continua*, vol. 2, pp. 227–238.

Movchan, A.B.; Movhan, N. (1995): *Mathematical Modelling of Solids of with Nonregular Boundaries*. CRC Press, Boca Raton.

Qian, Z.; Akisanya, A. (1998): An experimental investigation of failure initiatian in bonded joints. *Acta Mater*, vol. 46, pp. 4895–4904.

Ryabenkov, N. (1999): On the accuracy of determination of mechanical properties of an adhesive. *Ind Lab*, vol. 65, pp. 124–125.

Available online at www.sciencedirect.com
SCIENCE DIRECT®
Composite Structures 68 (2005) 409–417
COMPOSITE STRUCTURES
www.elsevier.com/locate/compstruct

Edge effects connected with thin interphases in composite materials

Gennady Mishuris [a,*], Andreas Öchsner [b,c]

[a] Department of Mathematics, Rzeszow University of Technology, 35-959 Rzeszow, Poland
[b] Institute of Applied Mechanics, University of Erlangen-Nuremberg, D-91058 Erlangen, Germany
[c] Centre for Mechanical Technology and Automation, University of Aveiro, 3810-193 Aveiro, Portugal

Available online 25 May 2004

Abstract

Different imperfect transmission conditions modelling a thin intermediate layer between two bonded materials in a dissimilar elastic strip are analysed from the point of view of possible free-edge effects. The type of imperfect model depends essentially on the mechanical properties of the interphase and can be classified as soft, comparable and stiff interfaces. Corresponding transmission conditions have been derived by asymptotic analysis. However, they are not valid, generally speaking, at a region near the free edge, where an additional boundary layer should be constructed. By using FEM the size of this region is estimated and all possible edge-effects phenomena are classified.

Keywords: Elasticity; Imperfect interface; Non-classical transmission conditions; Finite element method; Free-edge effects; Stress singularity; Interphase

1. Introduction

Most modern engineering structures make use of elements which are produced from the technology of joining materials (i.e. composites, adhesive joints, etc.). Analytical and numerical investigations of the edge effects which can be observed at the free boundaries of the bonded dissimilar materials, have, in the past, be mainly based on three approaches. The first of these, and the most popular, assumes that the bi-material interface is of zero-thickness, which allows the so-called "perfect contact condition" to be satisfied along the whole length of the interface [2,7–9,27]. The perfect contact conditions occur when the displacements and tractions remain continuous across the whole of the interface. From the point of view of the edge effect analysis, such an approach provides a stress singularity at the intersection between the interface and the external boundary. Corresponding stress singularities can be calculated from respective transcendental equations taking into account all boundary and transmission conditions. In the two-dimensional (2D) case, the equation has been written for the first time in [5] and later it is discussed for different wedge geometries in [2,27]. It has been shown that the classical square root stress singularity is no longer valid and it has been shown to depend upon the angle between the interface and the boundary as well as on two-dimensionless material parameters (Dundurs parameters), which describe the relative properties of the two bonded materials (cf. [9]). Nevertheless, the singularity can be easily calculated and implemented in FEM code with the corresponding special elements.

A region within the neighbourhood of the singular point is susceptible to microcracking originating from the point of the stress singularity. This may lead to a decrease in the mechanical strength/stability of the whole structure which may ultimately lead to its destruction [1,2,4,13,25,26,28]. To estimate the risk of crack appearance, Cherepanov [8] suggested and Akisanya later, with the help of his co-authors [2,27], developed the idea of using the value of a so-called generalised "stress intensity factor" in fracture mechanics analysis. However, such an approach makes it impossible to take into account any internal peculiarities of the real interphase between the matched materials. On the other hand, properties of adhesive materials may differ fundamentally from those of the bonded materials. For this reason, another (second) approach has been implemented in the

*Corresponding author. Tel.: +48-17-8651660; fax: +48-17-8543116.
E-mail address: miszuris@prz.rzeszow.pl (G. Mishuris).

0263-8223/$ - see front matter
doi:10.1016/j.compstruct.2004.04.007

modelling of bonded dissimilar materials. It consists of the assumption that there is an additional thin layer of finite thickness with its own mechanical properties (see review in [10]). However, with modern technology very thin glue layers (thin films) are used [14,30]. This fact makes it difficult to perform any numerical calculations using FEM taking into account the need to build a complicated mesh of fundamentally different sized elements that can lead to a loss in accuracy, unstable calculations and even loss of convergence [22]. In such a case, the third approach may be very successful: the so-called imperfect interface approach. This consists of using some special non-classical transmission conditions which take into account the internal properties of the thin interphase, but the conditions are still applicable along the imaginary zero-thickness interface (glue line). Such transmission conditions can be obtained from some phenomenological assumptions (cf. [8,10,30]) or from the accurate asymptotic analysis [3,12,15,16,22,23] taking into account various features of the intermediate layer. However, to the best knowledge of the authors, only the very first attempts (in the papers [11,12,23]) have been made to estimate the influence of such imperfect modelling on the edge effects seen within composite structure.

In this paper we will be investigating all the possible imperfect interfaces (i.e. soft, comparable and stiff). The three classifications come from the asymptotic analysis [22,23] and do not contradict or overlap with that found in [12], where, in fact, only the soft and comparable interfaces in our classification are under consideration. The edge effects seen related to the problem under consideration are divided up into three groups: edge effect, validity of transmission condition and singularity dominated zone.

2. Transmission conditions and FEM modelling

Let us consider a plane problem (that being: a two-dimensional problem) for modelling a dissimilar body (Fig. 1). The bonded materials from the top and the bottom part of the dissimilar strip posses the elastic

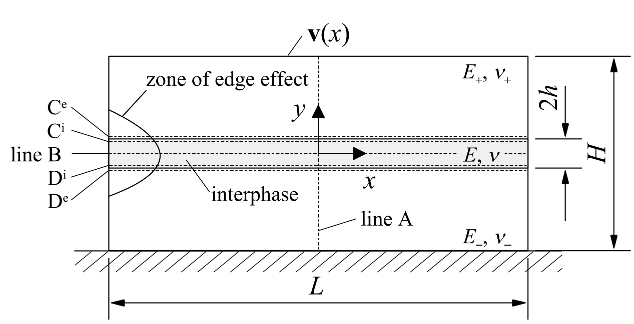

Fig. 1. Schematic representation of the problem, evaluation paths and boundary conditions of the investigated structure.

parameters μ_+, ν_- and μ_-, ν_-, (the shear modulae and Poisson's ratios, respectively). The interphase is assumed to be isotropic, with the elastic constants μ, ν. In this section, possible transmission conditions which can be evaluated by asymptotic methods are presented without any details. The corresponding analysis has been done in [22,23]. The interphase is assumed to be very thin so that $h = \epsilon h_0$ and $h_0 \sim L$, where L is a characteristic dimension of the bonded components, while ϵ is a small dimensionless parameter ($\epsilon \ll 1$).

Three different interphases can be distinguished: soft interface $\mu \sim \epsilon\mu_\pm$, comparable interface: $\mu \sim \mu_\pm$, and, finally, stiff interface: $\mu \sim \epsilon^{-1}\mu_\pm$. Additionally, it is assumed that the interface may be slightly curved and the elastic constants of the bonded materials do not differ significantly when compared to the value of the small parameter ϵ. These assumptions mean that, for example, if $\epsilon = 0.01$ then μ_+/μ_- can range from 0.1 to 10.0, but can not be smaller than 0.01 nor exceed 100.0. As a result, different transmission conditions can be obtained, respectively [22–24]. They are summarised in Table 1. In Table 2 the formulae to calculate the parameters a_j ($j = 1, 2, 3$) are given. The formulae in Table 2 have been found using an additional assumption: i.e. material parameters of the interphase do not change in direction perpendicular to the glue line (line where $y = 0$ holds). However, the parameters a_j can exhibit any functional dependency with respect to the variable x changing along the glue line. One can find the general relations in [23].

Let us mention here an extremely important fact with respect to the evaluation of the transmission conditions: the corresponding asymptotic analysis in the case of the plane strain is only valid when the material of the interphase is not weakly compressible (i.e. the value of Poisson's ratio ν is close to 0.5 but on a scale essentially greater than the value of the small parameter ϵ). As is clear from the Table 2, the parameter a_1 should be approaching zero when $\nu \to 0.5$, but the respective transmission condition is not longer valid.

One last remark: the transmission conditions derived by asymptotic analysis, which are presented in Table 1, are only valid at a distance from the external boundary, where an additional singular boundary layer has to be built to fulfill the external boundary conditions near the thin interphase layer. As a result, the question arises as to what the length of the zone is where the transmission conditions are not longer valid.

A commercial finite element software (MSC.Marc) is used for simulating the mechanical behaviour of the thin intermediate layer which has the dimensions $2h = H/100 = 0.01$ and $L = 10$. As a result, the value $2h$ can be taken in this case as the small parameter ϵ. The two-dimensional FE-mesh is built up of four-node, isoparametric elements with bilinear interpolation functions. In order to investigate the edge effect on both sides of the rectangle (cf. Fig. 1), a strong mesh refine-

Table 1
Possible sets of transmission conditions along the line $y = 0$ depending on the relative properties of the thin intermediate layer, 2D case

Interface	Transmission conditions			
Soft	$[u_x] - a_2\sigma_{xy} = 0$	$[u_y] - a_1\sigma_y = 0$	$[\sigma_{xy}] = 0$	$[\sigma_y] = 0$
Comparable	$[u_x] = 0$	$[u_y] = 0$	$[\sigma_{xy}] = 0$	$[\sigma_y] = 0$
Stiff	$[u_x] = 0$	$[u_y] = 0$	$[\sigma_{xy}] + \frac{\partial}{\partial x}\left(a_3 \frac{\partial u_x}{\partial x}\right) = 0$	$[\sigma_y] = 0$

Table 2
Parameters $a_j(x)$ for the plane strain and plane stress case

Case	a_1	a_2	a_3
Plane strain	$\frac{2h(1+\nu)(1-2\nu)}{E(1-\nu)}$	$\frac{4h(1+\nu)}{E}$	$\frac{2hE}{1-\nu^2}$
Plane stress	$\frac{2h(1-\nu^2)}{E}$	$\frac{4h(1+\nu)}{E}$	$2hE$

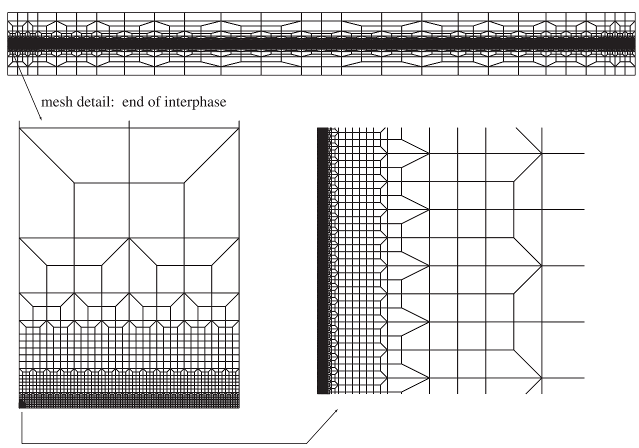

Fig. 2. Two-dimensional FE-mesh: strong mesh refinement in the investigated area.

ment in this region is performed (cf. Fig. 2). Furthermore, the mesh is generated in such a way so that it is possible to evaluate the displacements and stresses along the axes of symmetry: lines A and B (cf. Fig. 1) and along the transition zone of the materials: lines C and D. (The lines C^e and D^e belong to the bonded material and the lines C^i and D^i to the interphase.) Additionally, the density of the mesh increases near the free boundary (cf. Fig. 3) to accurately investigate the distribution of the displacement and stress fields without necessity to use any special singular element in FEM analysis. The main aim of the mesh choice is to eliminate any predefined behaviour within the numerical solution as it can exhibit different features depending upon the mechanical properties of the interphase and the bonded materials as well as the chosen interface model. We have checked the constructed FEM mesh by comparing it with known benchmarks to show that it is appropriate for the tensile and shear loading, but not for bending load cases where a phenomena known as "locking" can appear in the transition elements.

Numerical simulations have been made under the following conditions: simple uniform tensile and shear

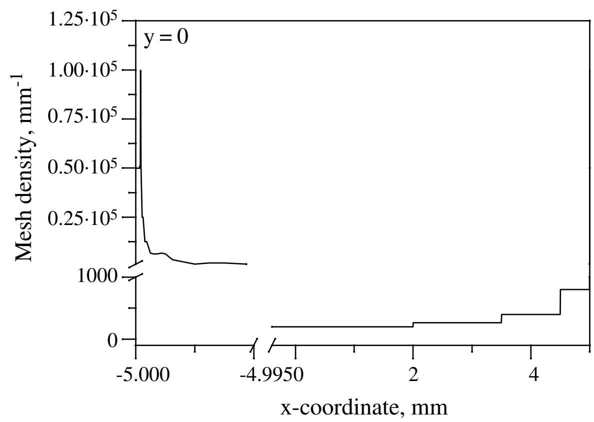

Fig. 3. Mesh density with reference to Fig. 1.

external loads (corresponding components of the given displacement $\mathbf{v}(x)$ at the top boundary of the sample are equal to $v_x(x) = 0,\ v_y(x) = 1$ and $v_x(x) = 1,\ v_y(x) = 0$, respectively) or tensile loads in the form: $v_x(x) = 0$, $v_y(x) = 0.04 \cdot x^2$. Two different samples are under consideration: symmetrical sample (both matched components are aluminum alloy AlCuMg1 (2017), with the elastic constants, Young's modulus $E_\pm = 72,700$ MPa and Poisson's ratio $\nu_\pm = 0.34$) or asymmetrical sample whose upper part consists of steel (elastic properties $E_+ = 210,000$ MPa, $\nu_+ = 0.3$), while the lower part is the aluminum alloy ($E_- = 72,700$ MPa, $\nu_- = 0.34$). Differing elastic constants are assigned to the intermediate layer and the calculations are carried out for the plane stress and plane strain states.

3. Numerical results

A lot of numerical results for the mentioned symmetrical and asymmetrical samples, different loadings and different types of the interface from Table 1 have been presented in [22,23] to estimate the range of the validity of the derived transmission conditions. In this paper we would like to concentrate our efforts mainly on the possible edge effects appearing in the problem under consideration.

In Figs. 4 and 5, distribution of displacement and stress along the lines B, C and D parallel to the glue line are depicted. As an example, the symmetrical sample consisting of two aluminum parts affixed by a weak adhesive layer with the following artificial elastic

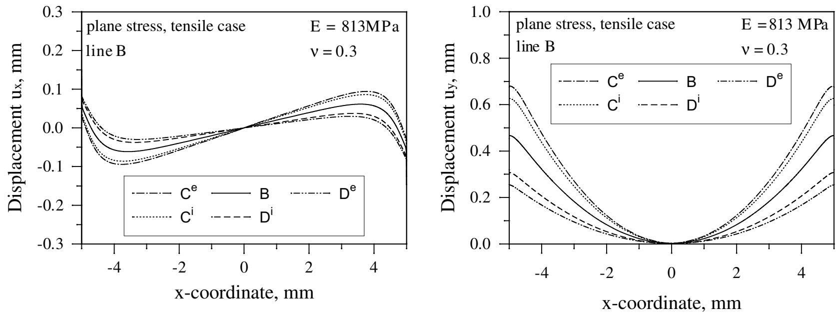

Fig. 4. Displacement distribution for asymmetric loading along lines B, C and D.

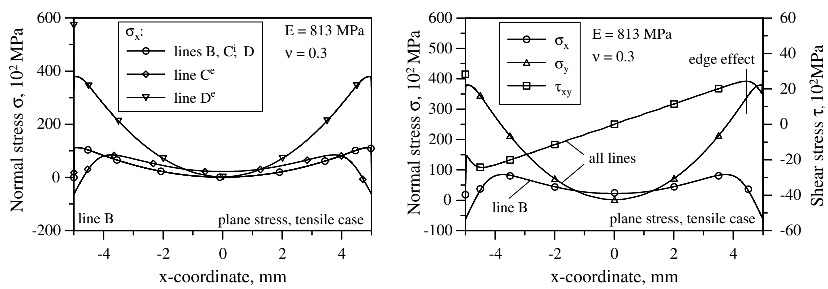

Fig. 5. Normal and shear stress distribution for asymmetric loading along horizontal lines B, C and D.

properties: $E = 813$ MPa, $\nu = 0.3$. In our classification this is the typical soft interface. Corresponding transmission conditions are presented in the first line of Table 1. For calculation, an inhomogeneous tensile load has been applied: $v_x = 0$, $v_y = x^2/25$.

From Fig. 5b one can observe that the stress components σ_y and σ_{xy} are continuous and, hence, the corresponding transmission conditions are satisfied, from the first glance, along the entire length of the sample. The last component of stress σ_x takes the same value within the interphase, but is discontinuous across the interphase boundaries, as expected due to the discontinuity of the material properties. On the other hand, displacement components u_x and u_y are dissimilar along all of the considered lines. To check the last two transmission conditions from the Table 1, for the case of the soft interface, it is necessary to calculate the jump of the displacements from different sides of the interphase. This has been done in Figs. 6a and 7a, where the respective displacement discontinuities and the corresponding stress components, normalised by the formulae from Table 1, are presented. A perfect match of the both lines is also observed.

If the simple shear or tensile loads were to be applied to the sample, then at some distances from the free edge, all displacement and stress components could be seen in Figs. 4 and 5. However, we intentionally applied more complicated loads to show that it is not so evident how to define the possible edge effects. Nevertheless, observing the curves for the stress components σ_y, σ_{xy} from Fig. 5b and the curves in Figs. 6a and 7a, one can conclude that there are points where the behaviour of the curves changes. These points are depicted by small circles determining the size of the first edge effect zone.

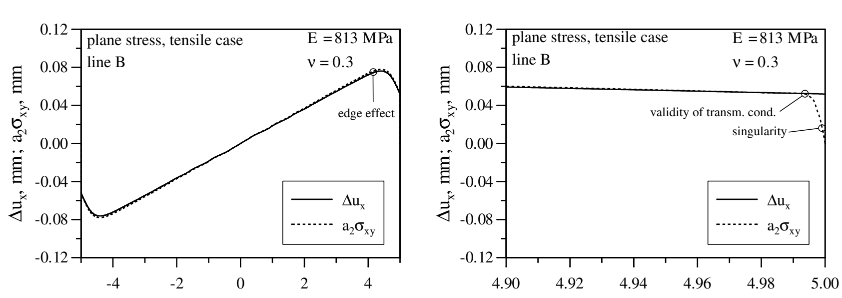

Fig. 6. Verification of the first transmission condition along the imperfect interface.

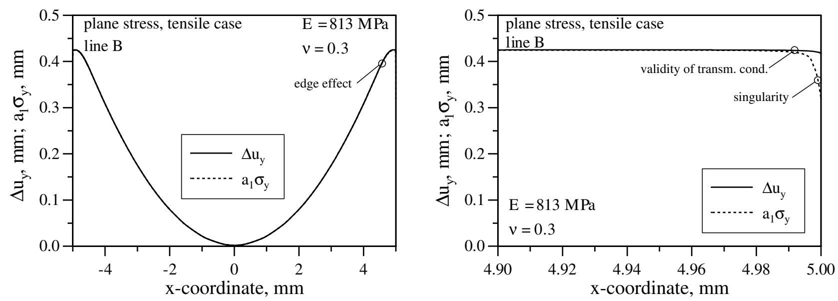

Fig. 7. Verification of the second transmission condition along the imperfect interface.

This effect is, in fact, related to Saint-Venant principle. That being: the behaviour of the solution changes due to approaching the considered points as we move along the curve towards the external boundary. Hence, the size of this zone should depend first of all upon the type of the external boundary conditions along the left and right-hand sides of the strip and the load being applied there. We are mostly interested in how the interphase properties influence the size of this zone. At first glance, one could think that this influence is not so important because of the already mentioned physical behaviour of the zone. However, this is not true.

In Fig. 8 the main tendency for the size of the edge effect zone can be observed for different material properties of the interphase layer when the same aluminum-aluminum symmetrical sample is used. As one can see from the presented results, only the case of the soft weakly compressible interface under plane strain conditions deviates in behaviour in comparison with the other cases. The reason for this is due to the fact that other transmission conditions have to be valid for such interface. Moreover, it has been shown in [23] that different external loads on top of the sample have a negligible effect in regards to the edge effect zone size. Of course, in order to discuss any edge effect zone, it is necessary to define the criteria describing the phenomenon. In this paper, an accuracy criteria of 1% is rigorously applied for the determination of any edge effects under consideration. The edge effect subjected to Saint-Venant principle (that being the simplest and clearest) is simultaneously the most difficult to be determined numerically. Only simple loads (simple shear or simple tension) give the possibility to do that without complications. Otherwise, the exact solution valid for an infinite sample with the same external loads has to be known in advance to compare with the numerical solution for the rectangle of the given length with the free edges. However, taking into account the above fact that the applied loading to the top of the sample has a slight, non-significant, influence, one can restrict the loading to simple loads. Another technique can be proposed to determine the zone with any complicated load at the top of the sample boundary. In this technique, one can apply to the right-hand side of the sample some additional loads exhibiting a zero main vector and then observe the changes in the results obtained. We used this technique in paper [23].

Furthermore, it should be underlined here that the edge effect zone is not directly connected with the region of validity of the transmission conditions for the imperfect interface. By this we mean that one can easily observe a perfect coincidence between the curves from Figs. 5b, 6a and 7a corresponding to the different parts of the imperfect transmission conditions mentioned above. Moreover, one can conclude from the diagram that the transmission solutions are satisfied along the whole glue line. However, this is not true, of course, and this only holds in the range of the figures. To make it clear, magnifications of the curves from the right-hand side of the sample are presented in Figs. 6a and 7a. In

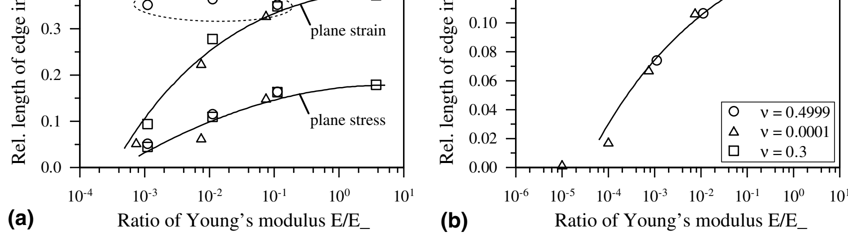

Fig. 8. Relative length of the edge effect zone.

turn, two different points can be recognised in the magnified diagrams. The first one is the point that separates the region where the imperfect transmission conditions are still valid from the region where they are not. The same 1% criteria has been applied to find this point. The other point on each diagram defines the so-called singularity dominated region near the singular point which was mentioned in the introduction. To determine this region one can approximate the solution along the interphase boundary in the proximity of its intersection with the external boundary using a simple asymptotic expansion (for example, $u_y = u_{y0} + br^{\lambda}$). In Fig. 9 such an approximation can been plotted on the logarithmic scale. Moreover, the both unknown parameters b and λ have been found numerically by the least square method. It is important to note here that we still have a lot of numerical points for such an approximation due to the constructed mesh being used (see the first section). Because the exact value of λ can be easily calculated from the respective transcendental equation given in [27], it makes it possible to estimate the size of the stress dominated zone by applying the 1% criteria in terms of the accuracy of the value of this parameter (see Fig. 9). The corresponding points visualised in Figs. 6b and 7b have been also extracted in the same way. One can see that this region is essentially smaller than the thickness of the interphase and can be estimated as $0.02 \cdot 2h$. This corresponds with the results reported in [6,12,23,27]. On the other hand, the region, where the transmission conditions are no longer valid, can be estimated as being comparable with the interphase thickness. However, the length of this region is more

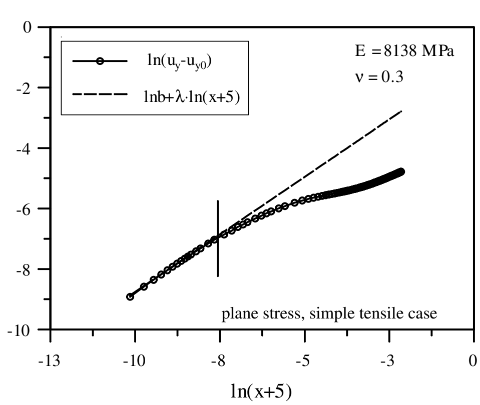

Fig. 9. Evaluation of the length of the singularity dominated zone.

variable with changing material properties of the interface than the size of the singularity dominated domain. Moreover, using the results of the paper [11,12] (where several values of the thickness have been investigated) one can conclude that the absolute size of the singularity dominated zone can not be considered as an appropriate characteristic but the only relative one (in comparison with the thickness of the interphase). The zones between the points in Figs. 6b and 7b are, in fact, intermediate regions between absolutely different behaviour of the considered elastic field. From a mathematical point of view, this is the length of the boundary layer zone which has to be build to complete the asymptotic analysis dealing with the derivation of the imperfect transmission conditions (see [24]).

Corresponding results showing the sizes of the different edge phenomena are presented in Table 3 for three different soft interfaces. All the discussed sizes have been measured parallel to the glue line. However, at least for the last edge effect, i.e. singularity dominated zone, one can also determine the singularity influence in a direction perpendicular to the interface from the singular point (as in any other direction cf. [6,17,29]). In Figs. 10a–12a the distribution of all stress components along the line parallel to the external boundary at some distance d are shown for three different cases: the symmetrical sample and simple tensile, the symmetrical sample and asymmetrical tensile load and, finally, the asymmetrical sample and simple tensile load. It has been assumed that the intermediate layer exhibits the same properties in the cases under consideration with elastic parameters $\nu = 0.3$ and $E = 813$ MPa. The value of $d = 1.953 \times 10^{-5}$ ($d = 1.953 \times 10^{-3} 2h$) has been taken in such a way that the line definitely lies within the domain where all the three above mentioned edge-effect phenomena appear. Let us note that the stress components σ_x and σ_{xy} are equal to zero along the free boundary according to the boundary conditions. However, the stress components along the line under investigation are still very small along the major part of the line ($\sigma_x(5-d,0) \approx 0.2$ MPa and $\sigma_{xy}(5-d,0) \approx -16$ MPa)). The magnitudes of the stresses in this region do not practically depend on the cases under consideration. Nevertheless, these values are not longer equal to zero as one can conclude from the first glance from Fig. 5.

On the other hand, there are two regions near the intersection points between the interphase and the

Table 3
Plane strain, tensile case, line A

E	ν	Edge effect	Validity of transmission condition	Singularity dominated domain
8138	0.3	4.1847	4.6928	4.999
813	0.3	4.4522	4.9919	4.999
81	0.3	4.7768	4.9932	4.999

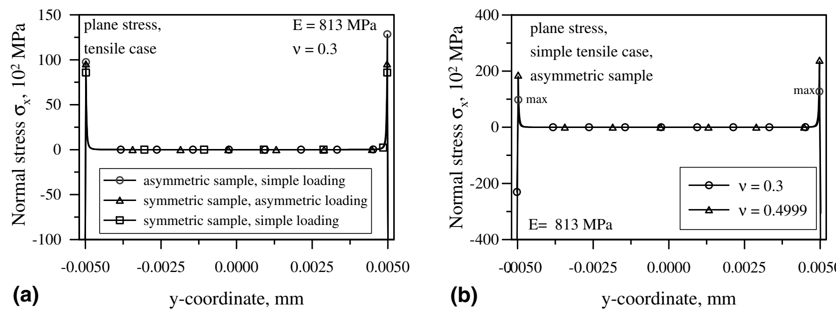

Fig. 10. Distribution of the stress σ_x along the line parallel to the free edge at distance $d = 1.953 \times 10^{-5}$.

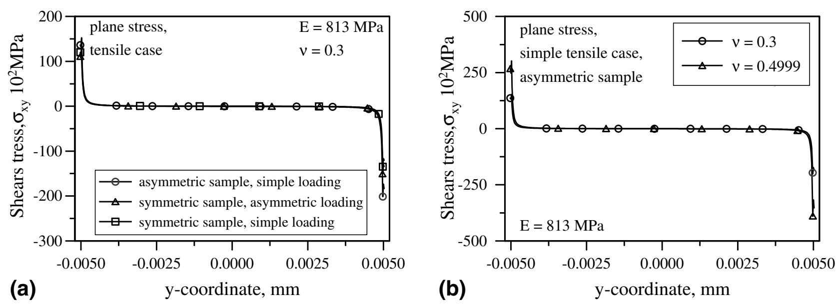

Fig. 11. Distribution of the stress σ_{xy} along the line parallel to the free edge at distance $d = 1.953 \times 10^{-5}$.

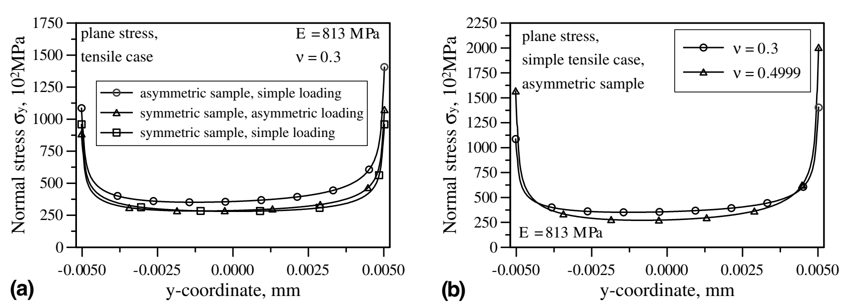

Fig. 12. Distribution of the stress σ_y along the line parallel to the free edge at distance $d = 1.953 \times 10^{-5}$.

external boundaries where the behaviour of the stresses σ_x and σ_{xy} changes drastically in Figs. 10a and 11a. Analysing the lengths of the regions, one can determine that the range of the singularity dominated domain is of the same order in the both directions (perpendicular and parallel to the interface). However, within these regions the influence of the particular cases is quite evident. Moreover, in the case of the symmetrical samples, no essential differences can be observed between the two different singular points, as it should be expected (because of the free external boundaries and practically the same distance to the loaded top and bottom boundaries of the rectangle). In fact, the values of the stress singularity exponents and the generalised stress intensity factors near the singular points should be almost equal in absolute values (but of the opposite signs for the generalised SIFs) in these cases. And in the case of the asymmetric sample (even for simple and, hence, symmetrical loading) higher peak stresses arises near the singular point with a larger difference in the elastic properties of the matched materials (in the case under consideration it is the top intersection point between the external and interphase boundary). Although, the values of the components σ_x and σ_{xy} do not change significantly along the line under consideration, the last component σ_y behaves differently. Here, all factors play an important role. Moreover, all stresses exhibit other behaviour within the interphase along the line perpendicular to its boundaries in comparison with those in the middle part of the sample, where all components change linearly (see [23]).

To also indicate the influence of the value of Poisson's ratio on the mentioned edge effects, the same results for the stresses in the case of the asymmetric sample loaded by simple tensile loading on the top are presented in Figs. 10b and 12b. One can deduce from those figures that the value of Poisson's ratio influence significantly the value of the stress singularity exponents and the generalised SIFs but not on the length of the singularity dominated zones.

It is also to be noted that the stress field appearing in the model with only the imperfect transmission conditions instead of finite thin interphase does not exhibit any singular behaviour near the free edge effect at all (cf. [11,12]). However, this is not a peculiarity of the imperfect interface itself, but a direct consequence of the geometry of the dissimilar body under consideration. Thus, in cases when the crack stops perpendicularly to the imperfect interface [18,19] or lies on it [20,21], various stress singularities can arise depending on the local mechanical behaviour of the local shape of the interphase near the crack tip and on its material properties. In this paper we always assume that the mechanical properties of the interphase do not change from point to point. As a result, for such a geometry, no stress singularity exists under any of the imperfect interface models excepts the classical perfect bonding.

Although, only the soft interface has been discussed here in details, it has been shown in [23], among others, that the stiff imperfect interface is characterised by the same lengths of the singularity dominated domains and the regions where the transmission conditions are no longer valid as has been in the case of the soft imperfect interface. This allows us to consider the results as a general rule for researchers involved in work regarding different influencing edge effects in composites with imperfect interfaces.

4. Conclusions

In the presented work, special efforts have been made to clarify all edge effects connected with imperfect bonds between two different elastic materials. Different imperfect models have been discussed with respect to the appearing edge effects. By using FEM analysis, ranges of the domains involved in the phenomena have been estimated. It has been shown that the edge effects in the case under consideration can be classified in three different type phenomena. Although each of them play an important part in influencing the behaviour of the dissimilar structure, the last two edge effects (validity of the transmission condition region and singularity dominated zone) should be of particular interest for users of finite element programs involved in edge effects. Thus, the knowledge about the validity region makes it possible to drastically decrease the number of finite elements in the constructed mesh by introducing special transmission elements instead of the thin intermediate zone between the different materials and also to prevent unsatisfactory phenomena in the numerical analysis. The information about the singularity dominated domain, in turn, makes it possible to locate the corresponding special singular element in the correct location.

Acknowledgements

G. Mishuris is grateful to Alexander von Humboldt Foundation for their support in this research.

References

[1] Achenbach JD, Zhu H. Effect of interfacial zone on mechanical behavior and failure of fibre reinforced composites. J Mech Phys Solids 1989;37:381–93.

[2] Akisanya AR, Fleck NA. Interfacial cracking from the free-edge of a long bi-material strip. Int J Solids Struct 1997;34(13):1645–65.

[3] Antipov YA, Avila-Pozos O, Kolaczkowski ST, Movchan AB. Mathematical model of delamination cracks on imperfect interfaces. Int J Solids Struct 2001;38:6665–97.

[4] Benveniste Y. On the effect of debonding on the overall behaviour of composite materials. Mech Mater 1985;3:349–58.

[5] Bogy DB. Edge bonded dissimilar orthogonal elastic wedges under normal and shear stress. J Appl Mech 1968;35:146–54.

[6] Boichuk VY. Edge effects in a composite weakly reinforced with fibers of rectangular cross section. Int Appl Mech 2001;37(5):682–8.

[7] Chaudhuri RA, Xie MS. Free-edge stress singularity in a bimaterial laminate. Compos Struct 1997;40(2):129–36.

[8] Cherepanov GP. Mechanics of brittle fracture. New York: McGraw-Hill; 1979.

[9] Dundurs J, Comninou M. Revision and perspective of the interface crack problem. Mech Compos Mater 1979;15:387–96.

[10] Erdogan F. Fracture mechanics of interfaces. In: Proceedings of the First International Conference on Damage and Failure of Interfaces DFI-I/Vienna/22–24 September 1997. Rotterdam: A.A. Balkema; 1997. p. 3–36.

[11] Haboussi M, Dumontet H, Billoet JL. Proposal of refined interface models and their application for free-edge effects. Compos Interf 2001;8(1):93–107.

[12] Haboussi M, Dumontet H, Billoet JL. On the modelling of interfacial transition behaviour in composite materials. Comput Mater Sci 2001;20:251–66.

[13] Herakovich C. Free-edge effects in laminated composites. In: Handbook of composites, vol 2, structure and design. NJ: Elsevier; 1989. p. 189–230.

[14] Kitamura T, Shibutani T, Ueho T. Crack initiation at free edge of interface between thin films in advanced LSI. Eng Fract Mech 2002;69:1289–99.

[15] Klabring A. Derivation of the model of adhesively bonded joints by the asymptotic expansion method. Int J Eng Sci 1991;29:493–512.

[16] Klabring A, Movchan AB. Asymptotic modelling of adhesive joints. Mech Mater 1998;28(1–4):137–45.

[17] Kokhanenko YV, Fesenko SV. Influence of Young's moduli of a laminated composite with a periodic system of cracks on edge effects. Int Appl Mech 2003;39(1):99–104.

[18] Mishuris G. Asymptotics of elastic solution near the crack tip terminating at a nonideal bimaterial interface (Mode I and II. Mech Compos Mater 1998;34(5):621–42 [in Russian], [in English translation—439–456].

[19] Mishuris G. Stress singularity at a crack tip for various intermediate zones in bimaterial structures (mode III). Int J Solids Struct 1999;36:999–1015.

[20] Mishuris G, Kuhn G. Asymptotic behaviour of the elastic solution near the tip of a crack situated at a nonideal interface. ZAMM 2001;81(12):811–26.
[21] Mishuris G. Interface crack and nonideal interface concept (Mode III). Int J Fract 2001;107:279–96.
[22] Mishuris G, Öchsner A, Kuhn G. FEM-analysis of nonclassical transmission conditions between elastic structures. Part 1: symmetric cases. Finite Elem Anal Des, submitted for publication.
[23] Mishuris G, Öchsner A, Kuhn G. FEM-analysis of nonclassical transmission conditions between elastic structures. Part 2: asymmetric cases. Finite Elem Anal Des, submitted for publication.
[24] Movchan AB, Movhan NV. Mathematical modelling of solids of with nonregular boundaries. London: CRC Press; 1995.
[25] Pagano NJ. Interlaminar response of composite materials. In: Composite materials series, vol. 5. NJ: Elsevier; 1989.
[26] Qian Z, Akisanya AR. An experimental investigation of failure initiation in bonded joints. Acta Mater 1998;46(14):4895–904.
[27] Qian Z, Akisanya AR. An investigation of the stress singularity near the free edge of scarf joints. Eur J Mech A/Solids 1999;18:443–63.
[28] Tahani M, Nosier A. Free edge stress analysis of general cross-ply composite laminates under extension and thermal loading. Compos Sruct 2003;60:91–103.
[29] Tsapira IM. The free edge effect in a laminated composite with the transversally isotropic filler. Int Appl Mech 2001;37(4):511–9.
[30] Yu HH, He MY, Hutchinson JW. Edge effects in thin film delamination. Acta Mater 2001;49:93–107.

Arch. Mech., **57**, 2–3, pp. 157–169, Warszawa 2005

Transmission conditions for a soft elasto-plastic interphase between two elastic materials. Plane strain state

G. MISHURIS[1)], A. ÖCHSNER[2)]

[1)] *Department of Mathematics,*
Rzeszów University of Technology, Rzeszów, Poland
e-mail: `miszuris@prz.rzeszow.pl`

[2)] *Centre for Mechanical Technology and Automation,*
Department of Mechanical Engineering,
University of Aveiro, Aveiro, Portugal

A THIN INTERPHASE between two different elastic media is under consideration. It is assumed that the intermediate layer consists of a soft elasto-plastic material whose Young's modulus is small enough in comparison with those of the bounding materials. Using an asymptotic technique, nonlinear transmission conditions for the bimaterial structure are evaluated. As a numerical example, a FEM analysis of a bimaterial structure with an interface is performed to investigate the accuracy of the derived transmission conditions.

Key words: elastic-plastic layer, imperfect interface, nonclassical transmission conditions.

1. Introduction

THIN INTERPHASES appearing in dissimilar bodies such as composite structures with adhesively bonded materials may influence significantly the whole spectrum of structural parameters: strength, dynamics, fracture, long lifetime and so on. Recently, significant efforts have been done to clarify various phenomena connected with the so-called imperfect interface approach. It consists in replacing the real thin interphase between two different materials by an infinitesimal layer of zero thickness. This layer is then modeled by special transmission conditions which incorporate information about geometrical and mechanical properties of the thin interphase. At first, such proposed conditions were based on phenomenological arguments and have been sufficiently exploited (see [3, 6, 7] among others and the respective references). Later, various imperfect transmission conditions have been evaluated by asymptotic methods in [2, 4, 8, 13] for different types of interfaces and materials. Accurate asymptotic behaviour of solutions of interface crack problems in the imperfect interface formulation have been done in [1, 14, 15] where it has been shown that the behaviour may be very complicated and essentially depends on the material and geometrical properties of the imperfect interfaces. Possible error estimates and ranges of the edge zone effects connected with utilisation of the imperfect interface models have been discussed in [16, 17] by the FEM analysis. This short overview shows that *elastic* imperfect interfaces have been intensively investigated in different directions.

However, thin elasto-plastic interfaces appear very often in real applications and the respective plastic properties may even have a greater influence than the elastic ones [11]. On the other hand, the numerical FEM simulation of the thin elasto-plastic interphase is more complicated than a pure elastic simulation. Unfortunately, results which have been obtained up to now have been absolutely insufficient and are mainly concentrated on problems of thin plastic interphases between rigid adherends [10, 12].

In the present work, imperfect transmission conditions for a soft elasto-plastic interphase are evaluated by asymptotic methods. The interface is described by the simple Hencky's deformation theory model. Only the main terms, i.e. zero-order expressions, of the asymptotic analysis are considered. Respective transmission conditions are naturally nonlinear. Higher-order expressions can be much easier to construct continuing the asymptotic procedure from the respective linear boundary problems. A numerical example based on an accurate finite element simulation shows a high efficiency of the approach, in spite of the fact that the deformation theory has its strong restrictions.

2. Basic interphase equations

In this section, only the interphase is considered. It is assumed that the material behaviour can be modeled by the elasto-plastic Hencky law [5, 12]:

$$\varepsilon = \frac{1-2\nu}{E}\sigma, \qquad \mathbf{D}_\varepsilon = \left(\phi + \frac{1}{2\mu}\right)\mathbf{D}_\sigma, \tag{2.1}$$

where ν is Poisson's ratio, μ and E are the shear and Young's moduli of the material in the elastic regime ($E = 2\mu(1+\nu)$). Here, $\mathbf{D}_\varepsilon$ and $\mathbf{D}_\sigma$ denote the deviatoric parts of the strain and stress tensors:

$$\mathbf{D}_\varepsilon = \boldsymbol{\varepsilon} - \frac{1}{3}\varepsilon\mathbf{I}, \qquad \mathbf{D}_\sigma = \boldsymbol{\sigma} - \frac{1}{3}\sigma\mathbf{I}, \tag{2.2}$$

while

$$\varepsilon = I_1(\boldsymbol{\varepsilon}) = \sum_{i=1}^{3}\varepsilon_{ii}, \qquad \sigma = I_1(\boldsymbol{\sigma}) = \sum_{i=1}^{3}\sigma_{ii} \tag{2.3}$$

are the first invariants of the tensors.

Function ϕ is assumed to be known in Eq. (2.1) and depends only on the second invariant of the strain deviator [12]:

$$\phi = \phi\left(J_2(\boldsymbol{\varepsilon})\right), \qquad \phi(0) = 0. \tag{2.4}$$

Here, as usually,

$$J_2(\boldsymbol{\varepsilon}) = I_2(\mathbf{D}_\varepsilon) = \frac{1}{2}\sum_{i,j=1}^{3} e_{ij}e_{ij} \tag{2.5}$$

and e_{ij} are components of the deviator $\mathbf{D}_\varepsilon$. It is well known that such a model describes appropriately only monotonic or near-monotonic loading and, in fact, comprises one of the nonlinear elasticity models [9, 12].

After some standard transformations, Eq. (2.1) can be rewritten in a form of nonlinear elasticity as:

$$\sigma_{ij} = 2\tilde{\mu}\varepsilon_{ij} + \tilde{\lambda}\varepsilon\delta_{ij}, \qquad i,j = 1,2,3, \tag{2.6}$$

where the generalised Lamé's coefficients have been introduced:

$$\begin{aligned} \tilde{\mu}(\phi) &= \frac{1}{2}\left(\phi + \frac{1+\nu}{E}\right)^{-1}, \\ \tilde{\lambda}(\phi) &= \frac{1}{3}\left(\phi + \frac{1+\nu}{E}\right)^{-1}\left(\frac{3\nu}{1-2\nu} + \phi\frac{E}{1-2\nu}\right). \end{aligned} \tag{2.7}$$

It should be noted here that these new coefficients coincide in the pure elastic regime ($\phi = 0$) with the elastic Lamé's parameters:

$$\tilde{\mu}(0) = \mu = \frac{E}{2(1+\nu)}, \qquad \tilde{\lambda}(0) = \lambda = \frac{\nu E}{(1+\nu)(1-2\nu)}. \tag{2.8}$$

Also the generalised Poisson's ratio can be introduced in the model:

$$\tilde{\nu}(\phi) = \frac{\tilde{\lambda}(\phi)}{2\left(\tilde{\lambda}(\phi) + \tilde{\mu}(\phi)\right)} = \frac{3\nu + \phi E}{3 + 2\phi E}. \tag{2.9}$$

It is easy to show from Eqs. (2.7) and (2.9) that for $0 < \nu < 0.5$

$$0 < \tilde{\mu}(\phi) \le \mu, \qquad \nu \le \tilde{\nu}(\phi) < \frac{1}{2}, \qquad \lambda \le \tilde{\lambda}(\phi) < \frac{1+\nu}{3\nu}\lambda, \tag{2.10}$$

where the function $\tilde{\mu}(\phi)$ monotonically decreases, while functions $\tilde{\nu}(\phi)$ and $\tilde{\lambda}(\phi)$ monotonically increase.

REMARK 1. If the initial elastic parameters of the intermediate layer are essentially smaller than those corresponding to the bonded materials, i.e.

$$\tilde{\mu}(0) \ll \mu_{\pm}, \qquad \tilde{\lambda}(0) \ll \lambda_{\pm}, \tag{2.11}$$

then one can immediately conclude from (2.10) the same properties of the generalised parameters for any $\phi \geq 0$ provided ν is not too close to zero:

$$\tilde{\mu}(\phi) \ll \mu_{\pm}, \qquad \tilde{\lambda}(\phi) \ll \lambda_{\pm}. \tag{2.12}$$

REMARK 2. It follows from (2.9) and (2.10) that $\tilde{\nu}(\phi) \to 1/2$ as $\phi \to \infty$.

REMARK 3. Function $\phi = \phi(J_2(\boldsymbol{\varepsilon}))$ can not behave arbitrarily. In fact, it should be determined from the yield criterion [12]. On the other hand, one can deduce from the monotonicity of the true stress-strain curve behaviour that the function $\tilde{\mu}(\phi(t))\sqrt{t}$ has to be non-decreasing. Moreover, in the case of hardening materials without saturation, $J_2(\boldsymbol{\sigma}) \to \infty$ as $J_2(\boldsymbol{\varepsilon}) \to \infty$, or

$$\tilde{\mu}(\phi(J_2(\boldsymbol{\varepsilon})))\sqrt{J_2(\boldsymbol{\varepsilon})} \to \infty, \qquad \text{as} \qquad J_2(\boldsymbol{\varepsilon}) \to \infty. \tag{2.13}$$

Taking into account Eq. (2.7), it is clear that condition (2.13) holds always in the case when $\phi(t)$ is a bounded function. In the oposite case, if $\phi(t) \to \infty$ as $t \to \infty$, the following estimate for the function ϕ has to be satisfied:

$$\sqrt{t}/\phi(t) \to \infty, \qquad \text{as} \qquad t \to \infty. \tag{2.14}$$

If one additionally assumes that there exists some parameter $\alpha > 0$ such that

$$\phi(t) = O(t^{\alpha}), \qquad \text{as} \qquad t \to \infty, \tag{2.15}$$

then it is easy to see that estimate (2.14) is satisfied only under the condition $0 < \alpha < 1/2$.

On the other hand, in the case of ideal plastic materials or plastic hardening laws with saturation:

$$\tilde{\mu}(\phi(J_2(\boldsymbol{\varepsilon})))\sqrt{J_2(\boldsymbol{\varepsilon})} \to \text{const}, \qquad \text{as} \qquad J_2(\boldsymbol{\varepsilon}) \to \infty. \tag{2.16}$$

This leads to:

$$\sqrt{t}/\phi(t) \to \text{const}, \qquad \text{as} \qquad t \to \infty, \tag{2.17}$$

or, under assumption (3.2), it is equivalent to $\alpha = 1/2$.

To finish the preliminary part of the paper, equations for the plane strain state are presented below. Thus, if $u_x = u_x(x,y)$, $u_y = u_y(x,y)$, $u_z = 0$ then

$$\varepsilon_z = \varepsilon_{xz} = \varepsilon_{yz} = 0, \qquad \sigma_{xz} = \sigma_{yz} = 0, \qquad \sigma_{zz} = \tilde{\lambda}(\phi)\,\varepsilon, \tag{2.18}$$

and for the remaining displacement and strain components, the following 2D relationships hold:

$$\varepsilon_x = \frac{\partial u_x}{\partial x}, \qquad \varepsilon_y = \frac{\partial u_y}{\partial y}, \qquad \varepsilon_{xy} = \frac{1}{2}\left(\frac{\partial u_y}{\partial x} + \frac{\partial u_x}{\partial y}\right) \tag{2.19}$$

and the stress components are defined by generalised Hooke's law (2.6):

$$\sigma_{ij} = 2\tilde{\mu}\varepsilon_{ij} + \tilde{\lambda}\varepsilon\delta_{ij}, \qquad i,j = 1,2, \qquad \varepsilon = \varepsilon_x + \varepsilon_y. \tag{2.20}$$

Finally, the second invariant of the strain deviator can be calculated in this case as:

$$J_2(\boldsymbol{\varepsilon}) = \varepsilon_{xy}^2 + \frac{1}{3}\left(\varepsilon_x^2 + \varepsilon_y^2 - \varepsilon_x\varepsilon_y\right). \tag{2.21}$$

3. Problem formulation and its asymptotic analysis

A bi-material domain with a thin elasto-plastic layer between two different elastic materials with Lamé's parameters $\mu_\pm, \lambda_\pm$, respectively, is considered in the following (Fig. 1). It is assumed that conditions (2.11) and, hence, (2.12) are satisfied. The intermediate layer is thin and soft so that simultaneously the conditions

$$2h = 2\epsilon h_0, \qquad \tilde{\mu} = \epsilon\tilde{\mu}_0, \qquad \tilde{\lambda} = \epsilon\tilde{\lambda}_0, \tag{3.1}$$

hold where $\epsilon \ll 1$ is a small parameter, and

$$h_0 \sim L, \qquad \tilde{\mu}_0 \sim \mu_\pm, \qquad \tilde{\lambda}_0 \sim \lambda_\pm, \tag{3.2}$$

while L is a characteristic size of the body.

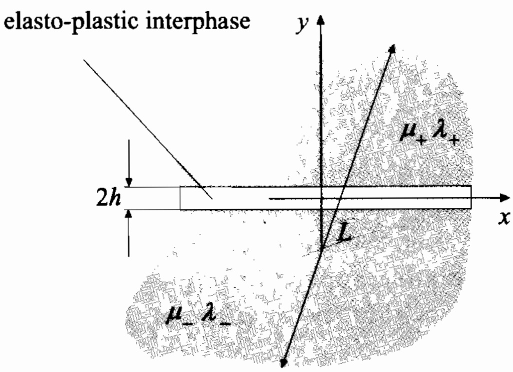

FIG. 1. Bimaterial structure under consideration.

The stresses satisfy within the interface, together with Eqs. (2.19) and (2.20), the equilibrium conditions:

$$\frac{\partial \sigma_x}{\partial x} + \frac{\partial \sigma_{xy}}{\partial y} = 0, \qquad \frac{\partial \sigma_{xy}}{\partial x} + \frac{\partial \sigma_y}{\partial y} = 0, \qquad y \in (-\epsilon h_0, \epsilon h_0)\,. \tag{3.3}$$

Along two bimaterial interfaces where $y = \pm\epsilon h_0$ holds, the perfect transmission conditions are assumed to be true:

$$u_x(x, \pm\epsilon h_0) = u_x^{\pm}(x, \pm\epsilon h_0), \qquad u_y(x. \pm\epsilon h_0) = u_y^{\pm}(x, \pm\epsilon h_0), \tag{3.4}$$

$$\sigma_{xy}(x, \pm\epsilon h_0) = \sigma_{xy}^{\pm}(x, \pm\epsilon h_0), \qquad \sigma_y(x. \pm\epsilon h_0) = \sigma_y^{\pm}(x, \pm\epsilon h_0). \tag{3.5}$$

Let us intentionally assume that the solution of the problem is known. Then, the nonlinear material parameters $\tilde{\mu}$ and $\tilde{\lambda}$ depend. generally speaking, on the geometrical position of the point under consideration:

$$\tilde{\mu} = \tilde{\mu}(x, y), \qquad \tilde{\lambda} = \tilde{\lambda}(x, y), \tag{3.6}$$

via the known strain $\varepsilon_{ij}(x, y)$ and, hence, the second invariant $J_2(\boldsymbol{\varepsilon}) = J_2(x, y)$ of the strain deviator. During the evaluation of the transmission conditions it was assumed that functions (3.6) are known. As a result, this interphase can be analysed as an inhomogeneous elastic interphase [16] and only in the last stage, an additional equation to determine the second invariant of the strain deviator will be extracted.

Here, the standard asymptotic procedure, explained in detail in [19], is applied. Namely, rescaling one of the space variables by the formula:

$$y = \epsilon\xi, \qquad \xi \in (-h_0, h_0), \tag{3.7}$$

and seeking for the solution of the problem in the form of asymptotic series:

$$\mathbf{u}(x, y) = \sum_{j=0}^{\infty} \epsilon^j \mathbf{u}_j(x, \xi), \qquad \boldsymbol{\sigma}(x, \xi) = \sum_{j=0}^{\infty} \epsilon^j \boldsymbol{\sigma}_j(x, \xi), \tag{3.8}$$

one should collect the terms of the same order with respect to the small parameter ϵ in Eqs. (2.20), (2.21) and (3.3) and in the transmission conditions (3.4)–(3.5) and then to solve step by step the corresponding boundary value problems. Thus, repeating the line of reasoning applied in [16], one can find the solution for the zero-order approximation within the interface in the following form as [16]:

$$\sigma_{xy}(x, y) = \sigma_{xy}^{\pm}(x, 0), \qquad \sigma_y(x, y) = \sigma_y^{\pm}(x, 0), \tag{3.9}$$

$$
(3.10) \qquad \begin{aligned}
u_x(x,y) &= u_x^-(x,0) + \sigma_{xy}(x,0)\int\limits_{-h}^{y} \frac{dt}{\tilde{\mu}(x,t)},\\
u_y(x,y) &= u_y^-(x,0) + \sigma_y(x,0)\int\limits_{-h}^{y} \frac{dt}{\tilde{\lambda}(x,t)+2\tilde{\mu}(x,t)},
\end{aligned}
$$

whereas the imperfect transmission conditions along the soft inhomogeneous elastic interface with known distribution of the *elastic* parameters $\tilde{\lambda}(x,y)$ and $\tilde{\mu}(x,y)$ are:

$$
(3.11) \qquad [\sigma_{xy}]_{y=0} = 0, \qquad [\sigma_y]_{y=0} = 0,
$$

$$
(3.12) \qquad [u_x]_{y=0} = \sigma_{xy}(x)\int\limits_{-h}^{h} \frac{dt}{\tilde{\mu}(x,t)}, \qquad [u_y]_{y=0} = \sigma_y(x)\int\limits_{-h}^{h} \frac{dt}{\tilde{\lambda}(x,t)+2\tilde{\mu}(x,t)}.
$$

Here, the symbol $[f]_\Gamma$ denotes as usually the jump of the function f across the surface Γ. Let us underline here that integrals in (3.12) are estimated like $O(1)$ in view of the assumptions (3.1). On the other hand, one can conclude from (3.10) and (2.19) that:

$$
(3.13) \qquad \varepsilon_y,\ \varepsilon_{xy} = O(\epsilon^{-1}), \qquad \varepsilon_x = O(1), \qquad \epsilon \to 0.
$$

Taking these estimates into account, one can rewrite Eq. (2.21) in the following manner:

$$
(3.14) \qquad J_2(\boldsymbol{\varepsilon}) = \left(\varepsilon_{xy}^2 + \frac{1}{3}\varepsilon_y^2\right)(1+O(\epsilon)), \qquad \epsilon \to 0,
$$

and utilising the generalised Hooke's law (2.20) and neglecting the terms of higher orders, one can deduce that the second invariant of the strain deviator can be calculated in the following manner:

$$
(3.15) \qquad J_2(\boldsymbol{\varepsilon}) = \frac{\sigma_{xy}^2}{4\tilde{\mu}^2} + \frac{\sigma_y^2}{3(2\tilde{\mu}+\tilde{\lambda})^2}.
$$

This equation should be considered as an additional relationship to the transmission conditions (3.11), (3.12) connecting stress and strain quantities within the thin soft elasto-plastic layer.

Note that the stress components σ_y and σ_{xy} do not depend on the variable y (compare it with (3.9)). As a result, it is natural to assume that

$$
(3.16) \qquad J_2(\boldsymbol{\varepsilon}) = J_2(x) \qquad \text{and} \qquad \phi = \phi(x).
$$

Taking this fact into account, one can simplify the transmission conditions (3.12) to obtain:

$$[u_x] = \frac{2h}{\tilde{\mu}(x)}\sigma_{xy}(x), \qquad [u_y] = \frac{2h}{\tilde{\lambda}(x) + 2\tilde{\mu}(x)}\sigma_y(x). \tag{3.17}$$

The system of five equations (3.11), (3.17) and (3.15) establish the sought for transmission conditions for the soft elasto-plastic interface. Three of the equations in the transmission conditions are nonlinear (cf. (3.17) and (3.15)). Fortunately, it is possible to reduce the number of equations. Namely, to stay only with two nonlinear transmission conditions, equations (3.17) are substituted into equation (3.15) to obtain:

$$J_2(\varepsilon) = \frac{[u_x]^2}{16h^2} + \frac{[u_y]^2}{12h^2}. \tag{3.18}$$

As a result, one can receive two nonlinear equations

$$\frac{1}{2h}\tilde{\mu}(\phi(J_2(\varepsilon))) \cdot [u_x] = \sigma_{xy}, \qquad \frac{1}{2h}(\tilde{\lambda} + 2\tilde{\mu})(\phi(J_2(\varepsilon))) \cdot [u_y] = \sigma_y, \tag{3.19}$$

which constitute together with (3.11) the complete set of the transmission conditions. Here, $J_2(\varepsilon)$ is calculated only basing on the displacement jumps $[u_x]$ and $[u_y]$ in (3.18). It should be noted that the transmission conditions (3.19) can be written in abstract form as:

$$F_x([u_x], [u_y]) = \sigma_{xy}, \qquad F_y([u_x], [u_y]) = \sigma_y, \tag{3.20}$$

where functions $F_x(t, \cdot)$ and $F_y(\cdot, t)$ monotonically increase with respect to the variable t (cf. equations (2.4), (2.7) and (3.18)). Moreover, one can conclude from (2.7) and (3.1) that the left-hand sides of equations (3.20) are of the order $O(1)$.

Equations (3.11) and (3.20) substitute the complete system of nonlinear transmission conditions for the soft elasto-plastic interface in the bimaterial structure under consideration. Another peculiarity of the conditions obtained in comparison with the imperfect elastic interface [16] is that the displacement jumps in different directions are not separated for the soft elasto-plastic interface, but both participate in each transmission condition from (3.20). However, in a particular case, when only the elastic regime appears in the elasto-plastic layer, conditions (3.20) degenerate to the imperfect elastic interface [16]:

$$\frac{\tilde{\mu}(0)}{2h} \cdot [u_x] = \sigma_{xy}, \qquad \frac{\tilde{\lambda}(0) + 2\tilde{\mu}(0)}{2h} \cdot [u_y] = \sigma_y. \tag{3.21}$$

Another possibility to separate the displacement jumps from each other, even under plastic regime, can appear for some special loading conditions (e.g. simple tensile or simple shear load), where one of the nonlinear transmission conditions (3.20) is satisfied identically whereas the other contains at the left-hand side the remaining non-zero jump (generally speaking in a nonlinear form).

REMARK 4. Transmission conditions (3.11) and (3.20) are valid, generally speaking, at some distance at the interaction of the interface with the external boundary. The range of the distance cannot be exactly predicted but can be estimated numerically, what will be done in the next section.

4. Numerical example and discussions

First of all, it is important to note that only terms of zero order have been evaluated by means of the asymptotic procedure. However, next terms can be found also in the same manner. Moreover, the boundary value problems which appear for the next terms will be linear, in contradiction to the zero-order term. However, as it has been demonstrated earlier in the case of the purely elastic interface [16], it will be shown for the elasto-plastic case that it is also sufficient to restrict the analysis to the zero-order approximation.

To show this, a numerical simulation of a bimaterial interface problem has been done. The geometry of the sample and respective loading conditions are shown in Fig. 2. The elastic materials which are glued by the interphase are assumed to be identical with Young's moduli $E_{\pm} = 72700$ MPa and Poisson's ratio $\nu_{\pm} = 0.34$. The geometrical dimensions are $L = 10$ mm, $H = 1$ mm and $2h = 0.01$ mm. As a result, the value of $\epsilon = 2h/H = 0.01$ can be considered as the small parameter. The elasto-plastic interface is represented by a linear hardening model whose parameters are described in Fig. 3. Namely, the elastic parameters: $E = 813$ MPa, $\nu = 0.3$. In the plastic region which is appearing after reaching the Huber–Mises stress of value $k_{\mathrm{t},0} = 50$ MPa, the constant hardening modulus $E_{\mathrm{p}} = 81.3$ MPa is prescribed. Let us underline that all commercial

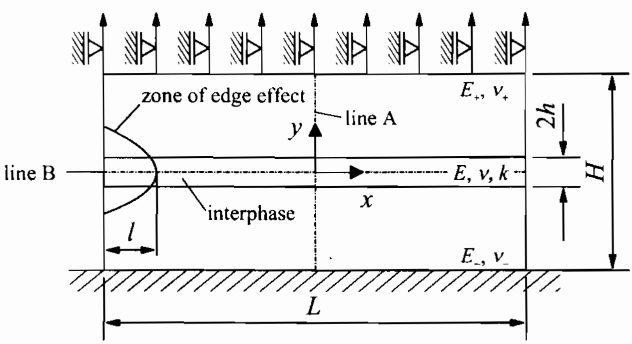

FIG. 2. Geometry and loading conditions of the bimaterial sample with a thin soft elasto-plastic interface for FEM simulation.

FEM codes are based on the more general theory of plastic flow [5, 9, 12]. As it has been mentioned above, the results with these models, i.e. deformation and plastic flow theories, coincide only under monotonic or nearly monotonic loading. Because of this, only monotonic external loading is applied (Dirichlet's boundary condition at the top of the sample).

The function ϕ from the deformation theory equations (2.1)–(2.4) was calculated by the given interphase properties of the flow theory [5, 12] and is shown in Fig 3b). Furthermore, it has been assumed that the material is obeying the Huber–Mises yield criterion.

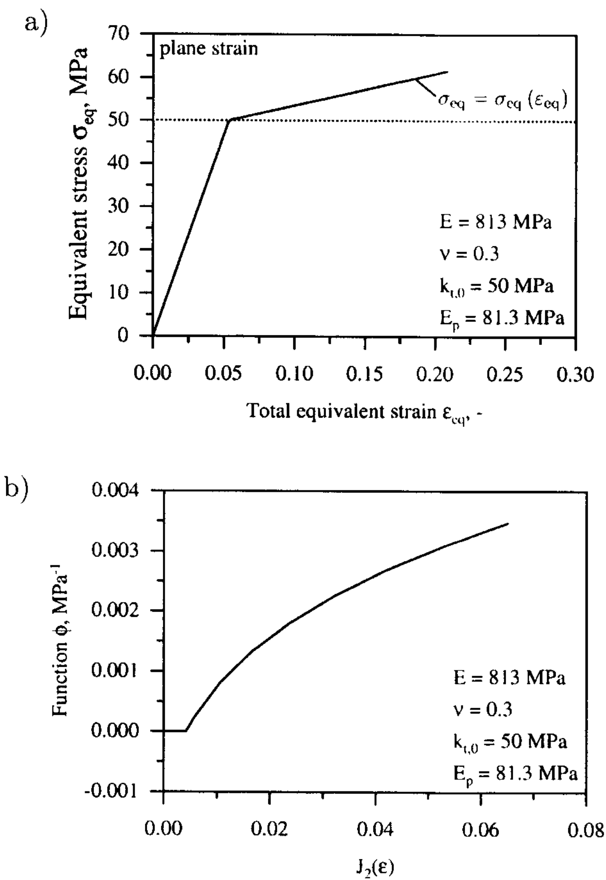

FIG. 3. Evaluation of the function ϕ from plastic flow parameters.

A simple tensile monotonic loading $(u_x(x, H/2) = 0, u_y(x, H/2) = v_y)$ is applied at the top of the bimaterial sample in the range from 0% to 0.6% of v_y/H in 100 incremental steps. Due to the symmetry of the loading and the sample geometry, two of the transmission conditions, i.e. $[\sigma_{xy}] = 0$ and $F_x([u_x], [u_y]) = \sigma_{xy}$, are satisfied identically because of $[u_x] = 0$ and $\sigma_{xy} = 0$ holds in this case. The two remaining conditions $[u_y] = 0$ and $F_y(0, [u_y]) = \sigma_y$ have to be verified. The first one is the same as in the case of the pure elastic imperfect interface [16] and is of less interest in comparison with the second one.

In Fig. 4a), a comparison of the left and right-hand side of the condition $F_y(0, [u_y]) = \sigma_y$ is presented. The traction is represented by the solid line while the values of the left-hand side function are depicted by circles in several points. The visible plastic zone appears in the middle of the interface after 30 increments. The accuracy of the evaluated transmission condition is in the same range as it has been checked for the pure elastic interface [17]. Moreover, the region where the transmission conditions are valid does not change practically, regardless whether the interphase material is in the elastic or plastic region. To illustrate this fact, a magnification of the same functions as in Fig. 4a) is presented in Fig. 4b). The 1% accuracy criterion has been chosen to indicate the validity regions. It is also important to note that the plastic zones which appear

a)

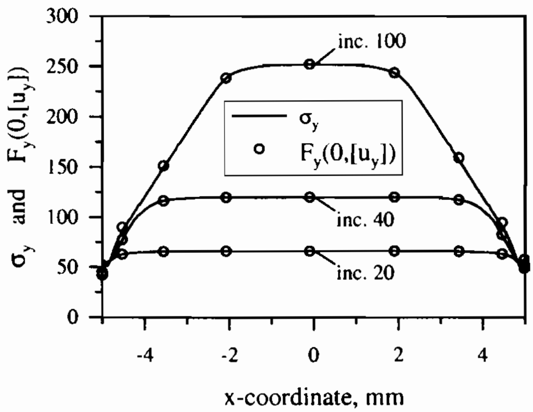

b)

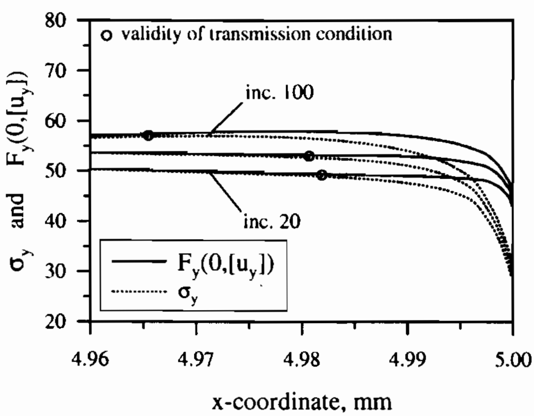

FIG. 4. Validity of the transmission conditions for thin elasto-plastic interface.

near the free edges are very small and therefore invisible in the scale of Fig. 4a). The range of the plastic zone coincides more or less with the range of singularity dominated domains for the elastic interface [17] and starts to be smaller during the plastic deformation.

Additionally to the presented analysis, investigations of possible singularity of the solution for a bimaterial body with a soft imperfect elasto-plastic interface model near the interface crack tip or near free edges should be done. Respective results concerning the pure elastic imperfect interface have been obtained in [1, 14, 15].

One of the crucial points to underline is the fact that the stress-strain state of the 2D bimaterial structure under consideration is not purely monotonic due to definition in [12]. Thus, it would be natural to expect a more significant difference between the numerically and analytically predicted interfacial conditions than it was clarified for the pure elastic interface in [16]. However, as it follows from the results presented in Fig. 4, the accuracy of the transmission conditions for the elasto-plastic interface is much better than one could expect due to the limitations of the deformation theory.

Another important fact which should be mentioned here concerns Remark 2. It may happen for very large plastic deformations that the generalised Poisson's ratio will approach its maximal value of 0.5 and, as a result, the transmission conditions evaluated here should be used with a reservation, as it follows from the results obtained in [18] for the soft, weakly compressible elastic interface. Nevertheless, if Poisson's ratio of the elasto-plastic interphase is sufficiently smaller than 0.5 in the elastic regime, then the transmission conditions evaluated in the paper can be applied in the range of usual plastic deformations. For example, the maximum value of the generalised Poisson's ratio takes in the numerical simulation the value of $\tilde{\nu} = 0.42$ after 100 increments, while $\tilde{\nu}(0) = 0.3$.

Acknowledgments

G. Mishuris is grateful to the Liverhulme Trust Foundation for support of this research. A. Öchsner is grateful to Portuguese Foundation of Science and Technology for financial support.

References

1. Y.A. ANTIPOV, O. AVILA-POZOS, S.T. KOLACZKOWSKI, A.B. MOVCHAN, *Mathematical model of delamination cracks on imperfect interfaces*, Int. J. Solids and Structures, **38**, 6665–6697, 2001.

2. O. AVILA-POZOS, A. KLARBRING, A.B. MOVCHAN, *Asymptotic model of ortotropic highly inhomogeneous layered structure*, Mech. Mater., **31**, 101–115, 1999.

3. Y. BENVENISTE, *The effective mechanical behaviour of composite materials with imperfect contact between the constituents*, Mech. Mater., **4**, 197–208, 1985.

4. Y. BENVENISTE, T. MILOH, *Imperfect soft and stiff interfaces in two-dimentional elasticity*, Mech. Mater., **33**, 309–323, 2001.

5. W.F. CHEN, *Constitutive equations for engineering materials*, Elsevier, Amsterdam-London-New York-Tokyo 1994.

6. F. ERDOGAN, *Fracture mechanics of interfaces*, Proceedings of the First International Conference on Damage and Failure of Interfaces DFI-I/Vienna/22-24 September 1997, Rotterdam-Brookfield: A.A. Balkoma 3–36, 1997.

7. Z. HASHIN, *Thermoelastic properties of fiber composites with imperfect interface*, Mech. Mater., **8**, 3333–348, 1990.

8. Z. HASHIN, *Thin interphase/imperfect interface in elasticity with application to coated fiber composites*, J. Mech. Phys. Solids, **50**, 2509–2537, 2002.

9. R. HILL, *The Mathematical Theory of Plasticity*, Clarendon Press, Oxford, 1998.

10. T. IKEDA, A. YAMASHITA, D. LEE, N. MIYAZAKI, *Failure of a ductile adhesive layer constrained by hard adherends*, Trans. ASME. J. Engng Mater. Technol., **122**, 80–85, 2000.

11. J.P. JEANDRAU, *Analysis and design data for adhesively bonded joints*, Int. J. Adhesion and Adhesives, **11**, 2, 71–79, 1991.

12. L.M. KACHANOV, *Fundamentals of the Theory of Plasticity*, MIR Publishers, Moscow 1974.

13. A. KLARBRING, A.B. MOVCHAN, *Asymptotic modelling of adhesive joints*, Mech. Mater., **28**, 137–145, 1998.

14. G. MISHURIS, *Interface crack and nonideal interface approach. Mode III*, Int. J. Fract., **107**, 3, 279–296, 2001.

15. G. MISHURIS, G. KUHN, *Asymptotic behaviour of the elastic solution near the tip of a crack situated at a nonideal interface*, ZAMM, **81**, 12, 811–826, 2001.

16. G. MISHURIS, A. ÖCHSNER, G. KUHN, *Imperfect interfaces in dissimilar elastic body: FEM-analysis*, Advanced Computational Engineering Mechanics, Z. REN, G. KUHN, L. SKERGET, M. HRIBERSEK [Eds.], Proc. of the First Workshop, Maribor Slovenia, October 9–11, 2003, University of Maribor Publishers, 2003.

17. G. MISHURIS, A. ÖCHSNER, *Edge effects connected with thin interphases in composite materials*, Composite Structures, **68**, 409–417, 2004.

18. G. MISHURIS, *Imperfect transmission conditions for a thin weakly compressible interface. 2D Problems*, Arch. Mech., **56**, 2, 103–115, 2004.

19. A.B. MOVCHAN, N.V. MOVCHAN, *Mathematical modelling of solids of with nonregular boundaries*, CRC Press, Boca Raton, 1995.

Received September 16, 2004; revised version January 17, 2005.

Available online at www.sciencedirect.com
ScienceDirect
Composite Structures 80 (2007) 361–372
COMPOSITE STRUCTURES
www.elsevier.com/locate/compstruct

2D modelling of a thin elasto-plastic interphase between two different materials: Plane strain case

Gennady Mishuris [a,*], Andreas Öchsner [b]

[a] Department of Mathematics, Rzeszów University of Technology, Rzeszów, Poland
[b] Centre for Mechanical Technology and Automation, Department of Mechanical Engineering, University of Aveiro, Aveiro, Portugal

Available online 27 June 2006

Abstract

A thin soft elasto-plastic interphase between two different media is under consideration. The intermediate layer is assumed to be of infinitesimal thickness and is modelled by non-linear transmission conditions which incorporate the elasto-plastic material behaviour of the layer. FEM analysis of a bimaterial structure with such an imperfect elasto-plastic interface shows the efficiency of the approach and illustrates some restrictions of its application.

Keywords: Elastic–plastic layer; Imperfect interface; Non-classical transmission conditions

1. Introduction

Thin interphases appearing in dissimilar bodies such as composite structures with adhesively bonded materials may significantly influence the whole spectrum of structural parameters: strength, dynamics, fracture, lifetime, and so on. Recently, significant efforts have been done to clarify various phenomena connected with the so-called elastic imperfect interface approach. It consists of replacing the real thin interphase between two different materials by an infinitesimal layer of zero thickness. This layer is then modelled by special transmission conditions which incorporate information about geometrical and mechanical properties of the thin interphase. At first, such proposed conditions were based on phenomenological approaches and have been sufficiently exploited (see [1–3] among others and the respective references). Later, various imperfect transmission conditions have been evaluated by asymptotic methods in [4–7] for different types of interfaces and materials. The accurate asymptotic behaviour of solutions of interface crack problems at the imperfect interface formulation has been investigated in [8–10] where it has been shown that the behaviour may be very complicated and essentially depending on the material and geometrical properties of the imperfect interfaces. Possible error estimates and ranges of the edge zone effects connected with utilisation of the imperfect models have been discussed in detail in [11,12] by FEM analysis. This short review shows that *elastic* imperfect interfaces have been intensively investigated in different directions.

However, thin elasto-plastic interfaces play even a more important role in real applications [13] and results which are obtained up to now are absolutely insufficient and are mainly concentrated on problems of thin plastic interphases between stiff adherends [14,15].

In the present work, imperfect transmission conditions for a soft elasto-plastic interphase are discussed. The interface is described by Hencky's deformation theory model. Only the main terms, i.e. zero-order expressions, of the asymptotic analysis are considered. Respective transmission conditions are naturally non-linear. Higher-order expressions can be later much easier constructed continuing the asymptotic procedure from the respective linear boundary problems. Numerical examples based on an accurate finite element simulations show the high efficiency

* Corresponding author. Tel.: +48 17 8651660; fax: +48 17 8543116.
E-mail address: miszuris@prz.rzeszow.pl (G. Mishuris).

0263-8223/$ - see front matter © 2006 Elsevier Ltd. All rights reserved.
doi:10.1016/j.compstruct.2006.05.017

of the approach, in spite of the fact that the deformation theory has its own strong restrictions.

2. Description of the thin elasto-plastic interface

Let us first consider only the elasto-plastic interphase and assume that its material behaviour can be modelled by Hencky's law [15,16]:

$$\varepsilon = \frac{1-2\nu}{E}\sigma, \quad \mathbf{D}_\varepsilon = \left(\phi + \frac{1}{2\mu}\right)\mathbf{D}_\sigma, \tag{1}$$

where ν is Poisson's ratio, μ and E are the shear and Young's modulae of the material in the elastic regime ($E = 2\mu(1+\nu)$). As usual, the first invariants of the strain and stress tensors are denoted by ε and σ. Furthermore, $\mathbf{D}_\varepsilon$ and $\mathbf{D}_\sigma$ are deviators of strain and stress, respectively, while $J_2(\boldsymbol{\varepsilon})$ and $J_2(\boldsymbol{\sigma})$ are their second invariants.

Function ϕ is known in Eq. (1) and it is assumed to depend only on the second invariant of the strain deviator [15]:

$$\phi = \phi(J_2(\boldsymbol{\varepsilon})), \tag{2}$$

where $\phi(t) = 0$ holds within the elastic region ($t \leqslant J_2(\boldsymbol{\varepsilon}_{\mathrm{cr}})$, $\boldsymbol{\varepsilon}_{\mathrm{cr}}$: initial yield strain tensor). It is well known that such a model appropriately describes only monotonic or nearly monotonic loading and, in fact, constitutes one of the non-linear elasticity models [15,17]. It can be rewritten in the elasticity-like form after transformations as

$$\sigma_{ij} = 2\tilde{\mu}\varepsilon_{ij} + \tilde{\lambda}\varepsilon\delta_{ij}, \quad i,j = 1,2,3, \tag{3}$$

where the generalised Lamé's coefficients are introduced by the following formulae:

$$\begin{aligned} \tilde{\mu}(\phi) &= \frac{1}{2}\left(\phi + \frac{1+\nu}{E}\right)^{-1}, \\ \tilde{\lambda}(\phi) &= \frac{1}{3}\left(\phi + \frac{1+\nu}{E}\right)^{-1}\left(\frac{3\nu}{1-2\nu} + \phi\frac{E}{1-2\nu}\right). \end{aligned} \tag{4}$$

Let us note that these coefficients simply coincide in the pure elastic regime ($\phi = 0$) with the respective elastic Lamé's parameters:

$$\tilde{\mu}(0) = \mu = \frac{E}{2(1+\nu)}, \quad \tilde{\lambda}(0) = \lambda = \frac{\nu E}{(1+\nu)(1-2\nu)}. \tag{5}$$

Using notations (4), the generalised Poisson's ratio can be defined in the following manner:

$$\tilde{\nu}(\phi) = \frac{\tilde{\lambda}(\phi)}{2(\tilde{\lambda}(\phi) + \tilde{\mu}(\phi))} = \frac{3\nu + \phi E}{3 + 2\phi E}. \tag{6}$$

In [18], new transmission conditions which describe the behaviour of a flat thin elasto-plastic interphase of constant thickness situated between two different materials have been evaluated by means of asymptotic techniques for a plane strain state. The only restriction to the model was that the adherends should be essentially stiffer than the interphase itself in all regimes (elastic or plastic ones). Assuming that the interface middle line is $y = 0$, the conditions take the following non-linear form [18]:

$$[\sigma_{xy}] = 0, \quad [\sigma_y] = 0, \tag{7}$$

$$F_x([u_x],[u_y]) = \sigma_{xy}, \quad F_y([u_x],[u_y]) = \sigma_y, \tag{8}$$

where $[f] = f(x,0+) - f(x,0-)$ is the jump of the function f along the infinitesimal interface $y = 0$. The functions on the left-hand sides of Eq. (8) are defined from the generalised Lamé's coefficients (20) given in Appendix, where the main ideas of the asymptotic analysis to evaluate the transmission conditions (7) and (8) are presented.

It is important to note that the transmission conditions (7) and (8) correspond to the main (zero-order) term of the asymptotic procedure. Next terms are also possible to construct. Moreover, they have to be found from solutions of the consequent *linear* boundary value problems for the corresponding degree of approximation. However, whereas it is also easy to prove the estimate of such an approach which is terminating the procedure at any step in the case of linear elasticity, the elasto-plastic interphase is a much more complicated problem due to the material non-linearity. In such cases, FEM analysis of modelling problems is the most effective way to check applicability of the transmission conditions and to discover its restrictions. This approach is utilised in the following.

3. Numerical examples

3.1. Metallic joints

The geometry of the sample and loading conditions are shown in Fig. 1. The real elasto-plastic behaviour of the aluminium alloy AlCuMg1 [19] is assigned to the metallic adherends which are adhesively bonded by the interface and it is assumed that both are identical with Young's modulae $E_\pm = 72{,}700$ MPa and Poisson's ratio $\nu_\pm = 0.34$. The geometrical dimensions are $L = 10$ mm, $H = 1$ mm and $2h = 0.01$ mm. As a result, the value of $\epsilon = 2h/H = 0.01$ can be considered as the small parameter.

Two different elasto-plastic interphases are considered: a linear hardening material model and an elastic-perfectly plastic material. Corresponding material parameters are described in Fig. 2(a). Namely, elastic parameters of the interphases are the same: $E = 813$ MPa, $\nu = 0.3$. In the

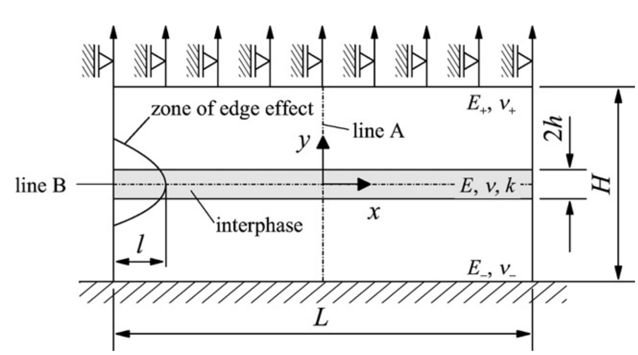

Fig. 1. Schematic representation of the problem, evaluation paths and boundary conditions of the investigated structure.

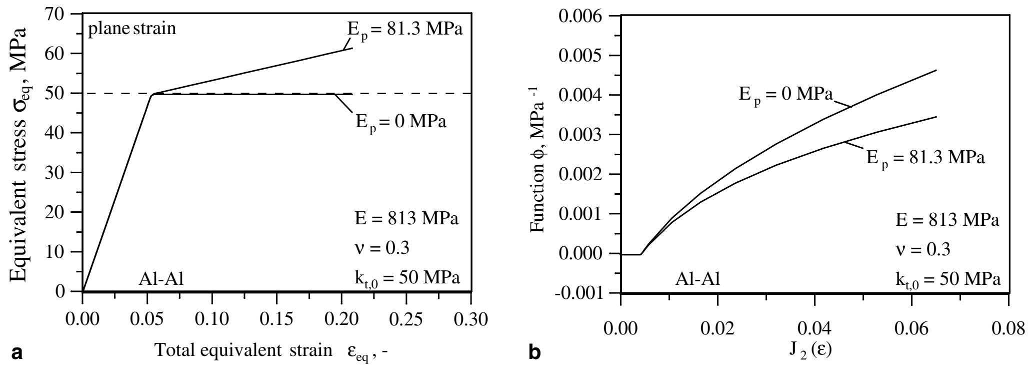

Fig. 2. (a) Material parameters of the interphase for metallic joints due to plastic flow theory and (b) function ϕ of Hencky's law.

plastic region which is appearing after reaching the Huber–Mises stress of value $k_{t,0} = 50$ MPa, the constant hardening modulus $E_p = 81.3$ MPa is prescribed for the hardening material and $k_t = k_{t,0}$ for the ideal plasticity case. Let us underline that all commercial FEM codes are based on the more general theory of plastic flow [15–17]. As it has been mentioned above, the results with these models (plastic flow and deformation theories) coincide only under monotonic or nearly monotonic loading. Because of this, only monotonic external loading is applied in the modelling approach (Dirichlet boundary condition at the top of the sample).

The respective functions ϕ involved in the deformation theory Eqs. (1) and (2) have been calculated by the given interphase properties of the flow theory [15,16] and its graphs are shown in Fig. 2(b). Furthermore, it was assumed in both cases that the elasto-plastic material is obeying the Huber–Mises yield criterion.

The commercial finite element code MSC.Marc is used for the simulation of the mechanical behaviour of the modelling thin intermediate elasto-plastic layer between two elastic adherends. The two-dimensional FE-mesh is built up of four-node, isoparametric elements with bilinear interpolation functions. In order to cover all possible edge effects [12] (cf. Fig. 1, left and right hand side of the interphase), a strong mesh refinement is performed in these regions, Fig. 3. The density of the elements along the interphase is shown in Fig. 4. Furthermore, the mesh is generated in such a way that it is possible to evaluate the displacements and stresses along the axes of geometrical symmetry, and along all the interfaces between the interphase elasto-plastic material and the adherends as well as along the lines parallel and perpendicular to the interfaces and lying within the interphase layer.

3.1.1. Elasto-plastic interphase with hardening law

3.1.1.1. Simple tensile loading. A simple monotonic tensile loading ($u_x(x, H/2) = 0, u_y(x, H/2) = v_y$) is applied to the top of the bimaterial sample in the range from 0% to 0.6% of v_y/H in 100 incremental steps.

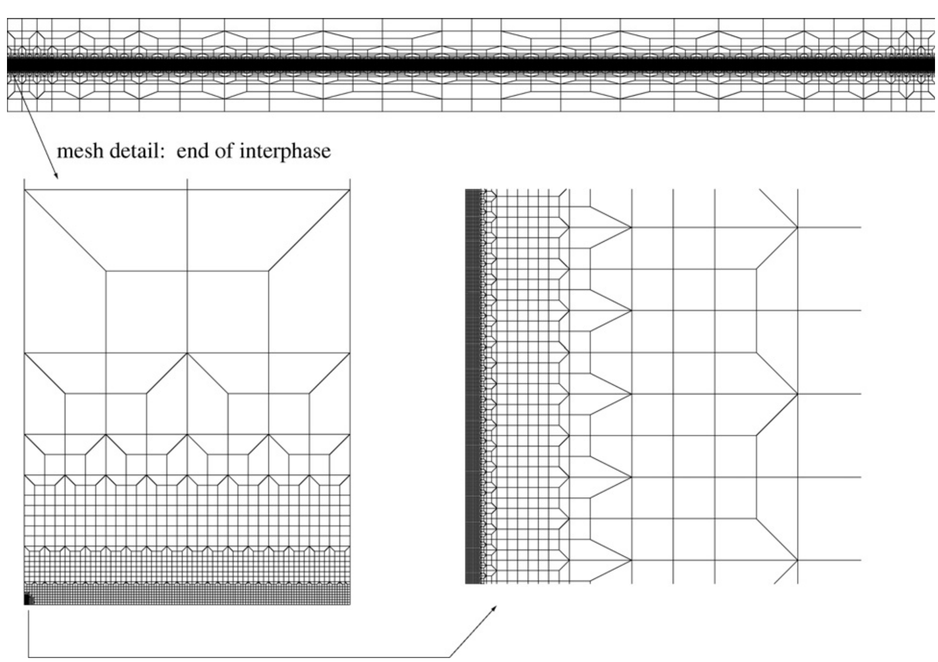

Fig. 3. Two-dimensional FE-mesh: strong mesh refinement in the investigated area.

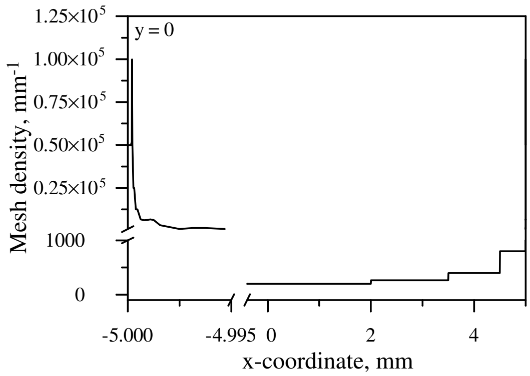

Fig. 4. Mesh density with reference to Fig. 1.

First of all, distributions of all displacements and stress components in direction perpendicular to the interface through the whole sample in its middle part (along the line A cf. Fig. 1) are shown in Figs. 5 and 6. Results presented in Figs. 5(a) and 6(a) correspond to the elastic regime while Figs. 5(b) and 6(b) are valid for the plastic deformation. As one can see, stresses within the interface are constant whereas the displacements are linear functions which completely coincides with the theoretical predictions. As a result, equivalent Huber–Mises stress and the equivalent plastic strain do not change within the interphase in direction perpendicular to its boundaries (for a fixed x). Its variation along the middle line of the elasto-plastic interphase is presented for several increments in Fig. 7.

Due to the symmetry of the loading and the sample geometry, two of the transmission conditions, i.e. $[\sigma_{xy}] = 0$ and $F_x([u_x],[u_y]) = \sigma_{xy}$, are satisfied identically because of $[u_x] = 0$ and $\sigma_{xy} = 0$ holds in this case. The remaining two conditions $[u_y] = 0$ and $F_y(0,[u_y]) = \sigma_y$ have to be verified. The first one is the same as in the case of the pure elastic imperfect interface [11], has the same order of accuracy as discovered in [11] and, because of this, it is of less interest in comparison with the second one.

In Fig. 8(a), comparisons of the left and right hand sides of the condition $F_y(0,[u_y]) = \sigma_y$ are presented. The traction is drawn by the solid line while the values of the left-hand side function in $(8)_2$ is depicted by circles in several points. The visible plastic zone appears in the middle of the interface at the 30th increment with a deformation ratio of $v_y/H = 0.18\%$. The accuracy of the evaluated transmission condition $(8)_2$ is in the same range as it has been checked for the pure elastic interface [11]. Moreover, the region where the transmission conditions are valid does not change practically regardless the interphase material is in the elastic or plastic region, Fig. 8(b). To highlight this fact, a magnification of the same functions as in Fig. 8(a) is presented in Fig. 8(b). A 1% accuracy criterion has been

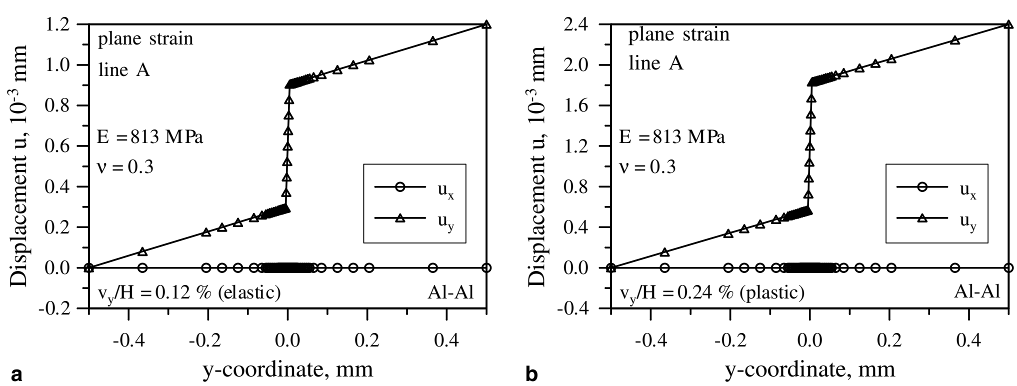

Fig. 5. Displacement distribution along line A (cf. Fig. 1) for an elastic and plastic stage inside the hardening interphase (simple tensile loading; aluminium adherends).

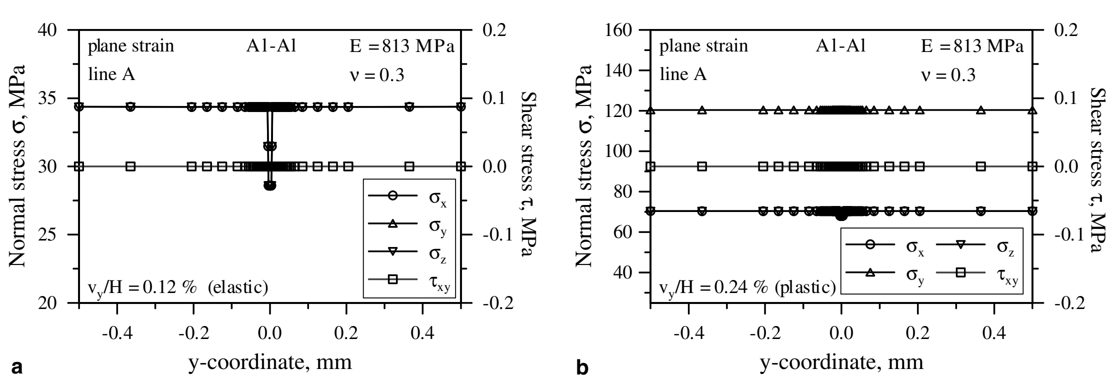

Fig. 6. Stress distribution along line A (cf. Fig. 1) for an elastic and plastic stage inside the hardening interphase (simple tensile loading; aluminium adherends).

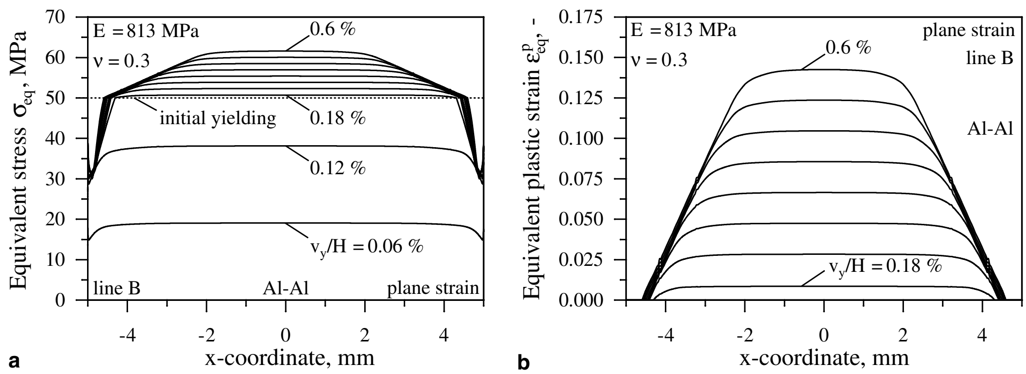

Fig. 7. Distribution of equivalent stress and strain along line B (cf. Fig. 1) for different levels of deformation (hardening interphase case; simple tensile loading; aluminium adherends).

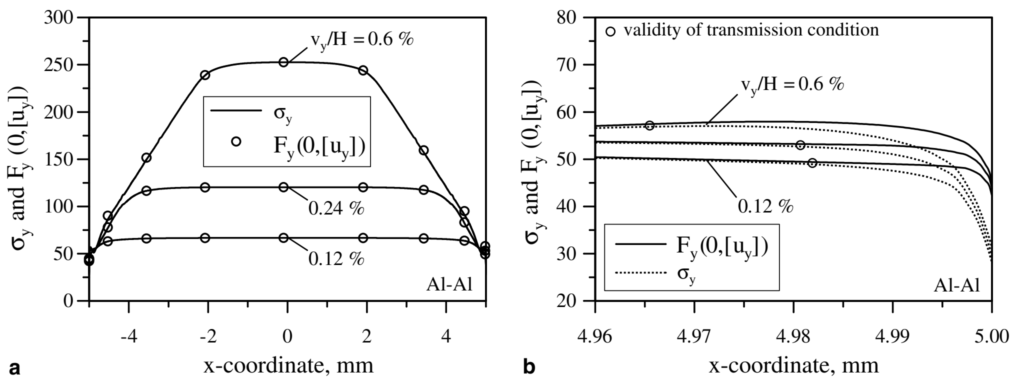

Fig. 8. Determination of the validity of the transmission condition for an elasto-plastic interphase (hardening interphase case; simple tensile loading; aluminium adherends).

chosen to indicate the validity regions for the transmission conditions. The regions are of 2–3 thickness of the interphase. It is also important to note that the plastic zones appearing near the free edges are very small and are invisible in the scale of Fig. 8(a). The zone where the transmission conditions are not longer valid coincides more or less with the range of the singularity dominated domains for the elastic interface [12] and becomes to be smaller with accumulated plastic deformation.

3.1.1.2. Combined loading. Now we apply to the top of the specimen a combined loading in such a way that in y-direction the same displacement is prescribed whereas in the perpendicular direction there is also a non-zero monotonic loading: $(u_x(x,H/2) = v_x, u_y(x,H/2) = v_y)$ in the same ranges from 0% to 0.6% for v_y/H and v_x/H, respectively, in 100 incremental steps.

In this case, the same particularities can be observed with respect to distributions of the displacements and stresses inside the thin interphase and outside the interphase within the surrounding materials. In Fig. 9, the results concerning Huber–Mises stress and equivalent plastic strain are presented in the same way as it has been done in Fig. 7. A slightly different behaviour can be observed which shows now the influence of the additional secondary loading in x-direction.

A more interesting question is about the validity of the transmission conditions. Now both of them are not trivial. Moreover, a second non-zero jump $[u_x]$ is presented in the functions F_x, F_y appearing in the transmission conditions (17). It is interesting to note that the validity region is at least not smaller than in the case of the simple tensile loading. To manifest this, we present Fig. 10 where the same values are depicted as in Fig. 8.

The same accuracy for the evaluated transmission conditions arises for the second transmission condition dealing with the jump $[u_x]$. We skip this picture only because it cannot be compared with the case of the simple tensile loading.

One of the crucial points to underline is the fact that the stress-strain state of the 2D bimaterial structure under consideration is not pure monotonic due to the definition in [15]. Thus, it would be natural to expect a more essential difference between the numerical model based on the plastic flow theory and the analytically predicted interfacial conditions based on the deformation theory in comparison with the accuracy observed for the pure elastic interface. However, as it follows from the results presented in Figs. 8 and 10, the accuracy of the transmission conditions is

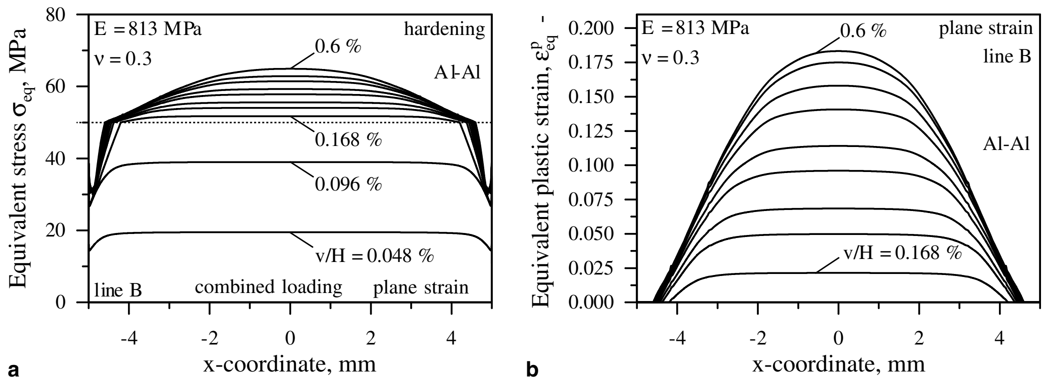

Fig. 9. Distribution of equivalent stress and strain along line B (cf. Fig. 1) for different levels of deformation (hardening interphase case; combined loading; aluminium adherends).

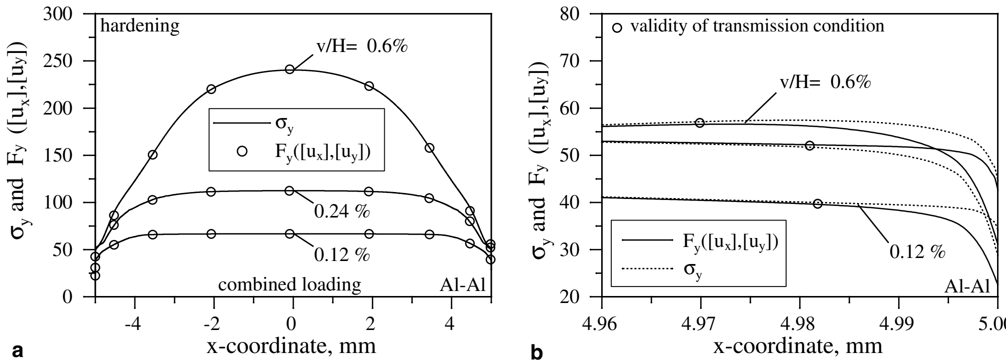

Fig. 10. Determination of the validity of the transmission condition for an elasto-plastic interphase (hardening interphase case; combined loading; aluminium adherends).

much better than one can even expect due to the limitation of the deformation theory. However, this is only true for a hardening interphase law. It will be shown in the following that the results are slightly worse in the case of perfect plasticity. It should be noted here that the adherends remained in the pure elastic regime at any stage of the applied deformation.

3.1.2. Elasto-plastic interphase with perfect plasticity

3.1.2.1. Simple tensile loading. In this case, also the same monotonic tensile loading $(u_x(x,H/2) = 0, u_y(x,H/2) = v_y)$ has been applied to the top of the bimaterial sample in range from 0% to 0.4% of v_y/H in 200 incremental steps. Because of the perfect plasticity law in the plastic region, one should increase the accuracy of the calculations.

The results concerning the behaviour of the solution within the interphase in direction perpendicular to the glue line $(y = 0)$ are similar to those shown in Figs. 5 and 6 at point $x = 0$ and hold without any conceptual change (constant stresses and linear displacements at each increment). Distributions of the equivalent Huber–Mises stress and the equivalent plastic strain along the middle line of the elasto-plastic interphase $(y = 0)$ are presented for several increments in Fig. 11. One can clearly observe the ideal plasticity plateau starting from a total deformation of $v_y/H = 0.14\%$.

The verification of the transmission condition $(8)_2$ in this case is presented in Fig. 12. Still very good agreement with the theoretical results can be observed over the whole range of the interface.

3.1.2.2. Combined loading. Let us now consider a combined loading. In this case it will be a monotonically increasing external loading $(u_x(x,H/2) = v_x, u_y(x,H/2) = v_y)$ applied to the top of the bimaterial sample in the same range from 0% to 0.4% for v_y/H and v_x/H, respectively, in 200 incremental steps.

We also restrict ourselves to show the same results as for the simple tensile loading case. Respective equivalent Huber–Mises stress and equivalent plastic strain curves are presented in Fig. 13, whereas the verification of the validity of the transmission conditions can be done based in Fig. 14.

A very important difference in comparison with the hardening law can be observed in the case of the ideal plasticity law. Namely, the region where the transmission conditions are valid is smaller than that in the case of the hardening plastic law (compare Figs. 8(b) and 10(b)) and this region essentially depends on the level of plastic deformation (compare Figs. 12(b) and 14(b)). To clarify the difference, some estimates of the zone ends have been presented in Table 1 for the hardening and the ideal plasticity law for different levels of the deformation. However, in

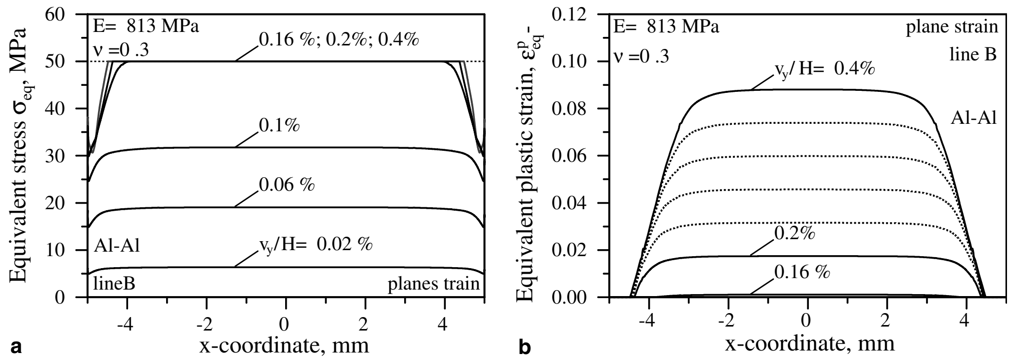

Fig. 11. Distribution of equivalent stress and strain along line B (cf. Fig. 1) for different levels of deformation (ideal plasticity interphase; simple tensile loading; aluminium adherends).

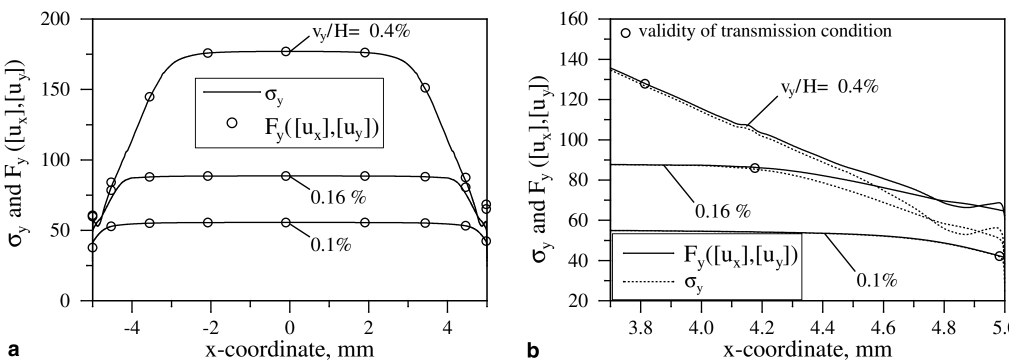

Fig. 12. Determination of the validity of the transmission condition for an elasto-plastic interphase (ideal plasticity interphase; simple tensile loading; aluminium adherends).

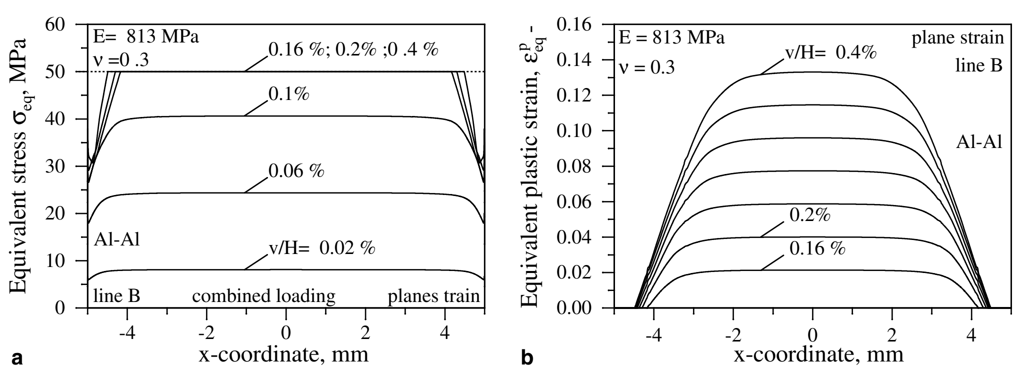

Fig. 13. Distribution of equivalent stress and strain along line B (cf. Fig. 1) for different levels of deformation (ideal plasticity interphase; combined loading; aluminium adherends).

both cases application of combined loading provided slightly better results for the applicability of the transmission conditions. This is an important result. First of all because a combined external loading is more frequent in technical applications. On the other hand, it shows that the worse accuracy appears in simple loading cases which researchers usually apply for testing.

3.2. Fibre reinforced plastics

All previous simulations and evaluations were performed for adhesively bonded metallic joints made of aluminium adherends. In the following sections, typical material parameter sets taken from the context of fibre-reinforced plastics (FRP) were assigned to the same finite element model as described in Section 3.1. For simplicity, the fibres were assumed to reveal an isotropic, homogeneous and linear-elastic behaviour and possible effects resulting from curvatures were neglected in order to compare the results with findings obtained in the previous section. For both types of fibres, i.e. glass and carbon, the interphase consists of the same elasto-plastic epoxy matrix with elastic constants $E = 3000$ MPa and $\nu = 0.4$ [20]. The plastic parameters of the interphase, i.e. initial yield stress $k_{t,0} = 45$ MPa and

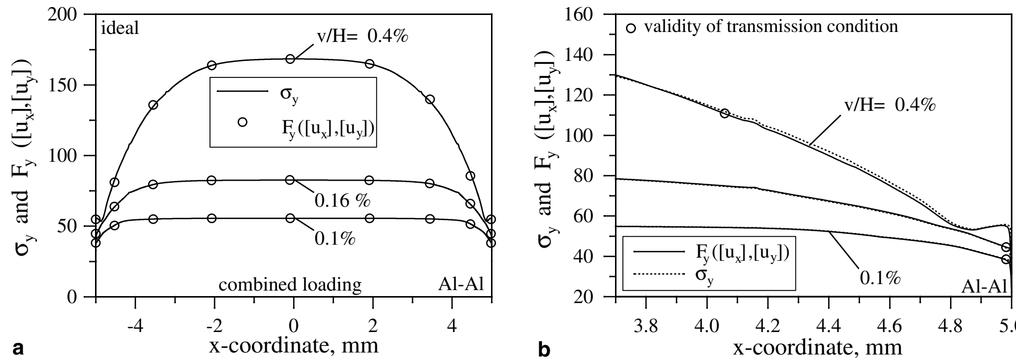

Fig. 14. Determination of the validity of the transmission condition for an elasto-plastic interphase (ideal plasticity interphase; combined loading; aluminium adherends).

Table 1
Validity of the transmission condition in terms of $\delta/(2h)$ for metallic joints

	Deformation	0.12%	0.22%	0.6%
Hardening				
	Simple tensile	1.81	1.93	3.45
	Combined loading	1.82	1.90	3.01
Ideal		0.1%	0.16%	0.4%
	Simple tensile	1.78	82.35	118.6
	Combined loading	1.82	1.80	94.2

linear hardening modulus $E_p = 2200$ MPa were taken from Ref. [21], cf. graphical representation given in Fig. 15a).

The respective function ϕ involved in the deformation theory Eqs. (1) and (2) has been calculated by the given interphase properties of the flow theory [15,16] and its graph is shown in Fig. 15(b). Furthermore, it was assumed that the elasto-plastic matrix is obeying the Huber–Mises yield criterion.

3.2.1. Glass fibres and epoxy matrix

In the following section, a typical material set for glass fibres, i.e. $E_\pm = 66{,}500$ MPa and $\nu_\pm = 0.23$ [22], is considered. The same external monotonic tensile loading as in the case of metallic joints ($v_y/H = 0.006$) is applied in 100 incremental steps. Fig. 16 shows the distribution of equivalent Huber–Mises stress and strain along the middle line ($y = 0$) of the elasto-plastic interphase for different levels of deformation. Comparing this figure with the results obtained in the previous section (cf. Fig. 7), one can observe that the behaviour is quite different. Namely, a practical constant behaviour for both quantities is obtained over a wide range of the interphase for the fibre–matrix structure. In addition to that, small maxima occur now close to the free surface while the material set for the metallic structure reveals its maximum in the middle where $x = y = 0$ holds.

Comparing the results for the equivalent plastic strains (i.e. Figs. 16(b) and 7(b)), one can see that the level for the plastic strain is much lower in the case of the fibre–matrix material set which is a direct result of the chosen material parameters. Despite the lower initial yield stress, first plastic deformation occurs a few increments later in the case of the fibre–matrix material because the equivalent yield stress is much more homogeneously distributed over the length of the interphase.

The validity of the transmission condition is shown in Fig. 17. As can be seen, a perfect fulfilment is again obtained over the range presented in Fig. 17(a). Looking at the magnification shown in Fig. 17(b), one can observe that the range of the validity decreases from $x \approx 4.9$ (cf. Fig. 8(b)) to $x \approx 4.5$ compared to the metallic configuration. This is an important information in order to decide

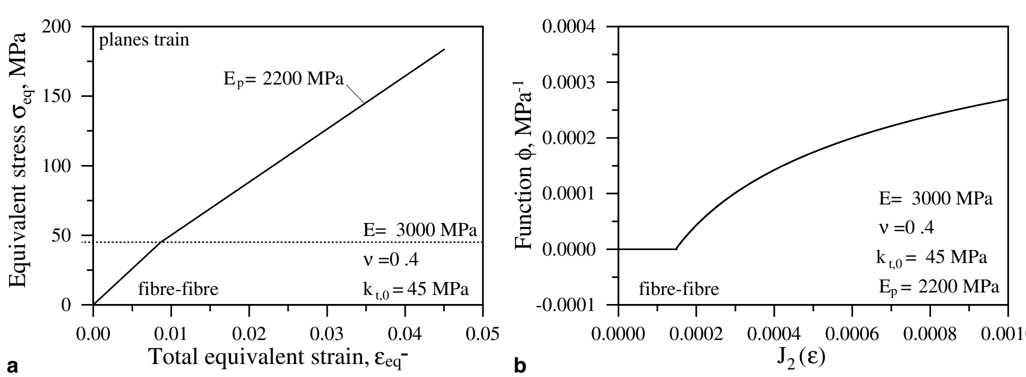

Fig. 15. (a) Material parameters of the interphase for fibre reinforced plastics due to plastic flow theory and (b) function ϕ of Hencky's law.

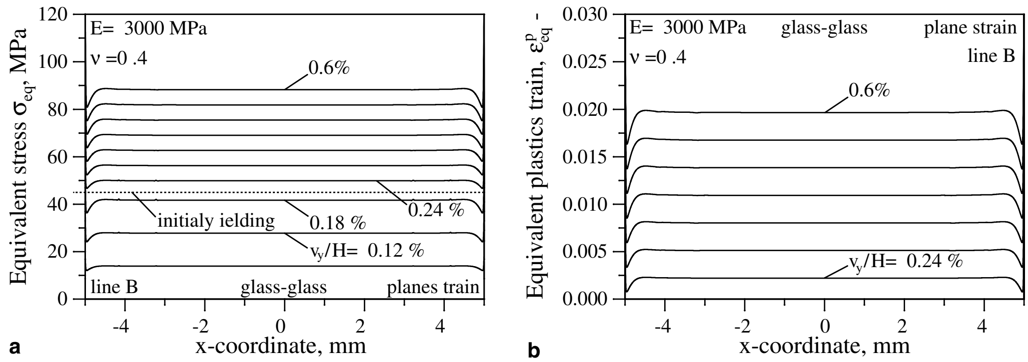

Fig. 16. Distribution of equivalent stress and strain along line B (cf. Fig. 1) for different levels of deformation (hardening interphase case; simple tensile loading; glass adherends).

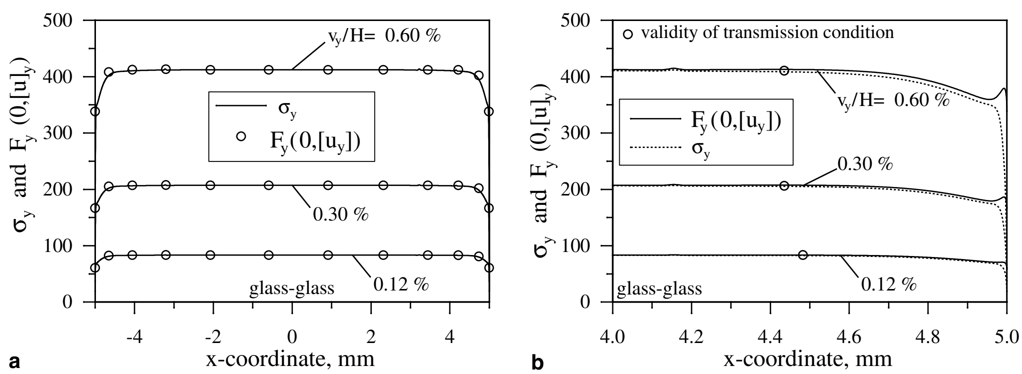

Fig. 17. Determination of the validity of the transmission condition for an elasto-plastic interphase (hardening interphase case; simple tensile loading; glass adherends).

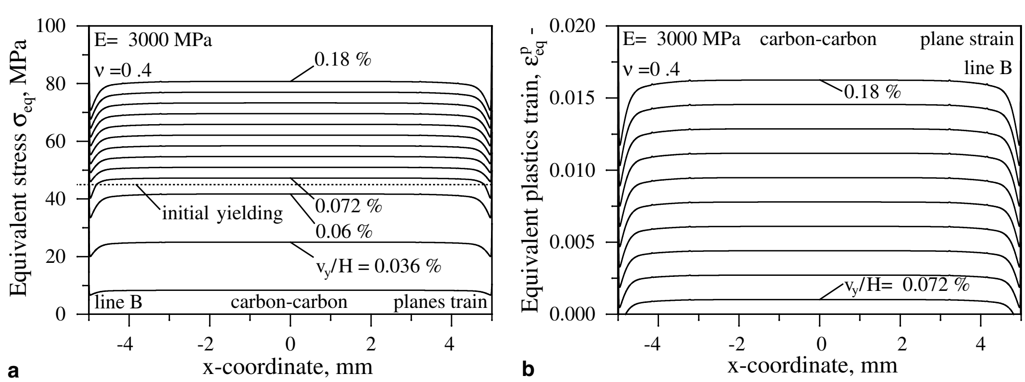

Fig. 18. Distribution of equivalent stress and strain along line B (cf. Fig. 1) for different levels of deformation (hardening interphase case; simple tensile loading; carbon adherends).

where interphase or special singularity elements should be introduced in an improved numerical approach. Nevertheless, a range of $x \approx 4.5$ for the validity is from a practical point of view still quite good.

3.2.2. Carbon fibres and epoxy matrix

A typical set for carbon fibres ($E_{\pm} = 227{,}000$ MPa and $\nu_{\pm} = 0.3$ [20]) is assigned for the adherends in the following section. In order to obtain comparable values for the equivalent plastic strain, the maximum evaluated external displacement is limited to $v_y/H = 0.0018$. As in the previous example of a fibre reinforced plastic, a homogeneously distribution of the equivalent stress and strain is obtained, cf. Fig. 18.

Looking at Fig. 19 which illustrates the validity of the transmission condition, one can see that a validity region ($x \approx 4.95$) is significantly larger than in the case of the glass–fibre material set and now comparable to the values

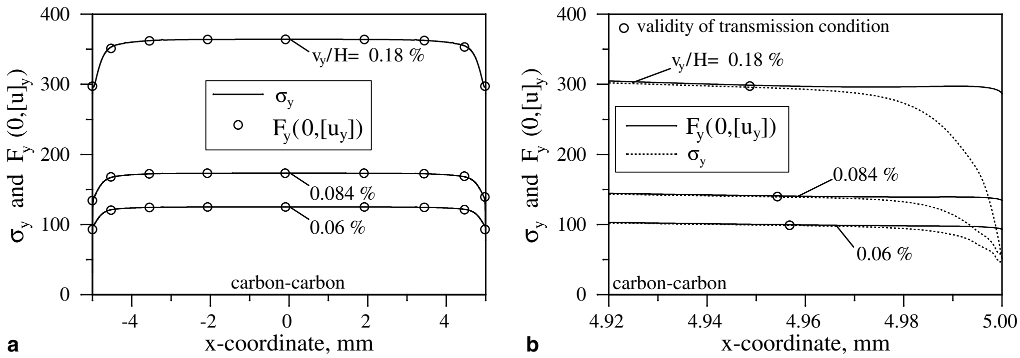

Fig. 19. Determination of the validity of the transmission condition for an elasto-plastic interphase (hardening interphase case; simple tensile loading; carbon adherends).

Table 2
Validity of the transmission condition in terms of $\delta/(2h)$ for fibre reinforced plastics (hardening)

Material	Deformation	0.12%	0.30%	0.6%
Glass–glass	Simple tensile	51.74	56.42	56.55
	Deformation	0.06%	0.084%	0.18%
Carbon–carbon	Simple tensile	4.32	4.57	5.13

obtained for the metallic joint. It should be noted here that the same range compared to the metallic joints could be obtained even though the material properties for the interphase and the level of the external loading are quite different.

The normalised values for the validity of the transmission conditions for fibre–matrix material sets are summarised in Table 2. As can be seen, the much stiffer carbon fibre reveals results comparable to the metallic joint set and significantly better than the glass fibre. Reminding that the interphase material was the same for both fibre–matrix cases, one can see that the stiffness ratio between interphase and joint materials directly influences the validity of the transmission conditions.

4. Discussions and conclusion

The very good accuracy of the presented approach will enable the introduction of novel finite elements for thin interphases. Later, we concentrate on the weak side of the method and its respective restrictions.

It follows from Eqs. (6) and (11) that $v \leqslant \tilde{v}(\phi) \leqslant 1/2$ and $\tilde{v}(\phi) \to 1/2$ for $\phi \to \infty$. Hence, it may happen for large plastic deformations that the generalised Poisson's ratio will approaches its maximal value of 0.5 and, as a result, the transmission conditions evaluated here should be used with a reservation as it follows from the results obtained in [23] for the weakly compressible soft elastic interface. Nevertheless, if Poisson's ratio of the elasto-plastic interphase is sufficiently smaller than 0.5 in the elastic regime, then in the range of usual plastic deformations, the transmission conditions which were evaluated in the paper can be applied.

For example, the maximum value of the generalised Poisson's coefficient (6) in the numerical simulation for the 100th increment with a deformation ratio of $v_y/H = 0.6\%$ (hardening case) takes the value $\tilde{v} = 0.47$, while $\tilde{v}(0) = 0.3$. Additionally, values of the generalised Poisson's ratio are presented in Fig. 20 for four different adhesive materials. Three of them (hardening law and ideal plasticity law for the interphase in metallic joints and fibre reinforced plastics) were used earlier in this paper and the last one is from Ref. [24] where properties of real adhesive have been discussed. One can conclude from Fig. 20 that the ideal plasticity case is the most dangerous in the discussed sense. Also it provides the worst results with respect to the validity of the transmission conditions (16) and (17), cf. Tables 1 and 2.

The transmission conditions (16) and (17) which were evaluated in the paper are non-linear and the jumps of the displacements in different directions with respect to the bimaterial interface cannot, generally speaking, be separated from each other. This only occurs in the elastic regime. Another possibility where the jumps are separated, even under plastic regime, appears in the case of some special loadings (simple tension or simple shear), where one of the non-linear transmission conditions (17) is satisfied identically whereas the other contains on the left-hand side the

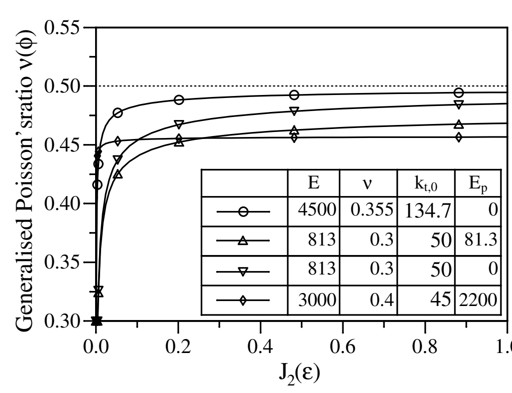

Fig. 20. Generalised Poisson's ratio (cf. Eq. (6)) for different adhesive materials.

only remaining non-zero jump (generally speaking in the non-linear form).

Additionally, to the presented analysis, investigations of the possible singularity of the solution for a bimaterial body with the soft imperfect elasto-plastic interface model near the interface crack tip or near free edge should be done. Respective results concerning pure elastic imperfect interface have been obtained in [8–10].

Acknowledgements

This work was established during a short visit of G. Mishuris at the University of Aveiro supported by the Centre for Mechanical Technology and Automation and has been completed as a part of his research activity as Marie Curie Fellow at University of Liverpool in ToK scheme with the grant MTKD-CT-2004-509809. A. Öchsner is grateful to Portuguese Foundation of Science and Technology for financial support.

Appendix

Here, only the main ideas in a comprehensive form how to evaluate transmission conditions (16) and (17) are presented. For more details and proof, a prospective reader is requested to the paper [18].

Let us consider a bi-material domain with a thin elasto-plastic layer between two different elastic materials (Fig. 1) which can be described by Hencky's law (1) in such a way that the conditions

$$2h = 2\epsilon h_0, \quad \tilde{\mu} = \epsilon\tilde{\mu}_0, \quad \tilde{\lambda} = \epsilon\tilde{\lambda}_0, \tag{9}$$

are simultaneously satisfied with some small parameter $\epsilon \ll 1$, and

$$h_0 \sim L, \quad \tilde{\mu}_0 \sim \mu_\pm, \quad \tilde{\lambda}_0 \sim \lambda_\pm, \tag{10}$$

while L is a characteristic size of the body and $\mu_\pm$, $\lambda_\pm$ are the respective generalised Lamé's coefficients of the adherends which are much higher under the same level of deformation than the corresponding values of the elasto-plastic interface. Let us note that it is sufficient to use instead of $\tilde{\mu}$ and $\tilde{\lambda}$ in estimate (9) its value in the elastic region because

$$0 < \tilde{\mu}(\phi) \leqslant \mu, \quad \lambda \leqslant \tilde{\lambda}(\phi) < \frac{1+v}{3v}\lambda \tag{11}$$

and Poisson's ratio of the interphase is rather different from zero. Moreover, one can show [18] that the function $\tilde{\mu}(\phi)$ monotonically decreases, while functions $\tilde{v}(\phi)$ and $\tilde{\lambda}(\phi)$ monotonically increase.

Within the interface together with Eq. (1), the equilibrium equations should be satisfied:

$$\frac{\partial\sigma_x}{\partial x} + \frac{\partial\sigma_{xy}}{\partial y} = 0, \quad \frac{\partial\sigma_{xy}}{\partial x} + \frac{\partial\sigma_y}{\partial y} = 0, \quad y \in (-\epsilon h_0, \epsilon h_0). \tag{12}$$

Along the two bimaterial interfaces between the layer and the adherends ($y = \pm\epsilon h_0$), the perfect transmission conditions are assumed to be along the interphase boundaries true:

$$u_x(x, \pm\epsilon h_0) = u_x^\pm(x, \pm\epsilon h_0), \quad u_y(x, \pm\epsilon h_0) = u_y^\pm(x, \pm\epsilon h_0), \tag{13}$$

$$\sigma_{xy}(x, \pm\epsilon h_0) = \sigma_{xy}^\pm(x, \pm\epsilon h_0), \quad \sigma_y(x, \pm\epsilon h_0) = \sigma_y^\pm(x, \pm\epsilon h_0). \tag{14}$$

Following for [25], we search for a possible solution in a form of asymptotic series:

$$\mathbf{u}(x,y) = \sum_{j=0}^{\infty} \epsilon^j \mathbf{u}_j(x,\xi), \quad \boldsymbol{\sigma}(x,\xi) = \sum_{j=0}^{\infty} \epsilon^j \boldsymbol{\sigma}_j(x,\xi). \tag{15}$$

To construct the asymptotic procedure [25], it is necessary to collect in all equations and in the transmission conditions the terms of the same order with respect to the small parameter ε and then to solve step by step the corresponding boundary value problems. Thus, repeating the line of the reasoning as in [11] one can find the solution for the zero-order approximation within the interface in the following form [18]:

$$[\sigma_{xy}]_{y=0} = 0, \quad [\sigma_y]_{y=0} = 0, \tag{16}$$

$$F_x([u_x],[u_y]) = \sigma_{xy}, \quad F_y([u_x],[u_y]) = \sigma_y, \tag{17}$$

$$F_x = \frac{1}{2h}\tilde{\mu}(\phi(J_2(\boldsymbol{\varepsilon}))) \cdot [u_x],$$
$$F_y = \frac{1}{2h}(\tilde{\lambda} + 2\tilde{\mu})(\phi(J_2(\boldsymbol{\varepsilon}))) \cdot [u_y]. \tag{18}$$

It was proven in [18] that all values within the interphase do not depend on the variable y in the main terms, such that $J_2(\boldsymbol{\varepsilon}) = J_2(x)$, $\phi(J_2(\boldsymbol{\varepsilon})) = \phi(x)$, and

$$J_2(\boldsymbol{\varepsilon}) = \frac{[u_x]^2}{16h^2} + \frac{[u_y]^2}{12h^2}. \tag{19}$$

Note here that functions $F_x(t,\cdot)$ and $F_y(\cdot,t)$ in (17) monotonically increase with respect to the variable t.

Eqs. (16) and (17) substitute the complete system of non-linear transmission conditions for the soft elasto-plastic interface in a bimaterial structure.

References

[1] Benveniste Y. The effective mechanical behaviour of composite materials with imperfect contact between the constituents. Mech Mater 1985;4:197–208.
[2] Erdogan F. Fracture mechanics of interfaces. In: Proceedings of the first international conference on damage and failure of interfaces DFI-I/Vienna/22–24 September 1997, Rotterdam-Brookfield. p. 3–36.
[3] Hashin Z. Thermoeleastic properties of fiber composites with imperfect interface. Mech Mater 1990;8:3333–48.
[4] Avila-Pozos O, Klabring A, Movchan AB. Asymptotic model of orthotropic highly inhomogeneous layered structure. Mech Mater 1999;31:101–15.
[5] Benveniste Y, Miloh T. Imperfect soft and stiff interfaces in two-dimensional elasticity. Mech Mater 2001;33:309–23.
[6] Hashin Z. Thin interphase/imperfect interface in elasticity with application to coated fiber composites. J Mech Phys Solids 2002;50:2509–37.

[7] Klabring A, Movchan AB. Asymptotic modelling of adhesive joints. Mech Mater 1998;28:137–45.
[8] Antipov YA, Avila-Pozos O, Kolaczkowski ST, Movchan AB. Mathematical model of delamination cracks on imperfect interfaces. Int J Solids Struct 2001;38:6665–97.
[9] Mishuris G. Interface crack and nonideal interface approach. Mode III. Int J Fract 2001;107(3):279–96.
[10] Mishuris G, Kuhn G. Asymptotic behaviour of the elastic solution near the tip of a crack situated at a nonideal interface. ZAMM 2001;81(12):811–26.
[11] Mishuris G, Öchsner A, Kuhn G. Imperfect interfaces in dissimilar elastic body: FEM-analysis. In: Ren Z, Kuhn G, Skerget L, Hribersek M, editors. Advanced Computational Engineering Mechanics. Proc. of the First Workshop, Maribor Slovenia, October 9–11, 2003. Maribor: University of Maribor Publishers; 2003. p. 101–10.
[12] Mishuris G, Öchsner A. Edge effects connected with thin interphases in composite materials. Compos Struct 2005;68:409–17.
[13] Rosselli F, Carbutt P. Structural bonding applications for the transportation industry. Sampe J 2001;37(6):7–13.
[14] Ikeda T, Yamashita A, Lee D, Miyazaki N. Failure of a ductile adhesive layer constrained by hard adherends. Trans ASME J Engng Mater Technol 2000;122:80–5.
[15] Kachanov LM. Fundamentals of the theory of plasticity. Moscow: MIR Publishers; 1974.
[16] Chen WF. Constitutive equations for engineering materials. Amsterdam: Elsevier; 1994.
[17] Hill R. The mathematical theory of plasticity. Oxford: Clarendon Press; 1998.
[18] Mishuris G, Öchsner A. Transmission conditions for a soft elasto-plastic interphase between two elastic materials. Plane strain state. Arch Mech 2005;57(2–3):157–69.
[19] Öchsner A, Winter W, Kuhn G. Damage and fracture of perforated aluminum alloys. Adv Eng Mater 2000;2(7):423–6.
[20] Blassiau S, Thionnet A, Bunsell AR. Micromechanisms of load transfer in a unidirectional carbon fibre-reinforced epoxy composite due to fibre failures. Part 1: Micromechanisms and 3D analysis of load transfer: the elastic case. Compos Struct 2006;74(3):303–18.
[21] Blassiau S, Thionnet A, Bunsell AR. Micromechanisms of load transfer in a unidirectional carbon fibre-reinforced epoxy composite due to fibre failures. Part 2: Influence of viscoelastic and plastic matrices on the mechanisms of load transfer. Compos Struct 2006;73(3):319–31.
[22] Palacz M, Krawczuk M, Ostachowicz W. The spectral finite element model for analysis of flexural-shear coupled wave propagation. Part 1: Laminated multilayer composite beam. Compos Struct 2005;68:37–44.
[23] Mishuris G. Imperfect transmission conditions for a thin weakly compressible interface. 2D Problems. Arch Mech 2004;56(2):103–15.
[24] Jeandrau JP. Analysis and design data for adhesively bonded joints. Int J Adhes Adhes 1991;11(2):71–9.
[25] Movchan AB, Movhan NV. Mathematical modelling of solids of with nonregular boundaries. Boca Raton: CRC Press; 1995.

Materials Science Forum Vol. 553 (2007) pp. 87-92
online at http://www.scientific.net
© (2007) Trans Tech Publications, Switzerland

Evaluation of Transmission Conditions for a Thin Heat-Resistant Inhomogeneous Interphase in Dissimilar Material

Gennady Mishuris[1,a], Wiktoria Miszuris[1,b], Andreas Öchsner[2,3,c]

[1]Department of Mathematics, Rzeszow University of Technology, Rzeszow, Poland
[2]Centre for Mechanical Technology and Automation, University of Aveiro, Aveiro, Portugal
[3]Department of Mechanical Engineering, University of Aveiro, Aveiro, Portugal

[a]miszuris@prz.rzeszow.pl, [b]victory@prz.rzeszow.pl, [c]aoechsner@mec.ua.pt

Keywords: heat transfer, thin layers, nonclassical transmission conditions

Abstract. Imperfect transmission conditions modelling a thin intermediate layer between two bonded materials in a dissimilar strip are derived in this paper. The interphase material is assumed to be heat-resistant and situated in a thin rectangular domain between the main materials. Different types of the interphase are investigated: homogeneous and inhomogeneous; linear and nonlinear ones.

Introduction

Thin interphases are commonly used in modern technology [1]. An inhomogeneous structure obtained in such a way may exhibit a wider variety of thermal and mechanical properties. On the other hand, numerical modelling of composites with thin interphases is still a difficult numerical task as it requires high inhomogeneity of the constructed mesh which can lead to a loss of accuracy and even numerical instability. That explains the high interest to model the interphases as a zero thickness object described by specific so-called transmission conditions along the infinitesimal interface. In the case of constant heat conductivity, the problem has been completely solved in [2], where the general approach was developed independent of the range of the heat conductivity of the thin (in comparison with the matched adherents) interphase. However, such interphases often manifest clear nonlinear or homogeneous properties connected with the production and exploitation processes [1]. In this paper, we derived the transmission conditions in the case of inhomogeneous or nonlinear heat conductivity. We concentrated our interest to a a heat-resistant interphase which is the most important case from an application point of view. We will apply the same approach as it has been done in [3, 4, 5] in the case of structural elastic and elasto-plastic interphases that allows us to overcome problems connected with possible nonlinearities. We can refer here also to other methods to deal with the thin interphases [6, 7] as well as to construct effective homogenesation properties of composite materials [8, 9, 10].

Problem formulation

Let us consider a bimaterial structure matched together with a thin intermediate layer of the constant thickness $2h$ (Fig. 1). The heat transfer equations are satisfied in the surrounding materials:

$$\nabla k_\pm \nabla T_\pm + Q_\pm = \rho_\pm c_\pm \frac{\partial T_\pm}{\partial t}, \quad (x,y) \in \Omega_\pm, \tag{1}$$

where $T_\pm$ and $Q_\pm$ are temperature and the thermal sources within the respective materials occupied domains $\Omega_\pm$ while $k_\pm$, $c_\pm$ and $\rho_\pm$ are their thermal conductivities, heat capacities and densities, respectively. We are not going to solve the problem but to derive the transmission conditions modelling the heat-resistant layer. As a result, we do not need to accurately describe here properties of the surrounding materials.

Within the thin interphase, a similar equation is given by

$$\nabla k \nabla T + Q = \rho c \frac{\partial T}{\partial t}, \quad (x,y) \in \Omega, \tag{2}$$

where T and Q are temperature and the thermal sources within the interphase and

$$k = k(x,y,t,T), \quad c = c(x,y,t,T), \quad \rho = \rho(x,y,t,T),$$

which can depend on the space and time variables as well as the unknown temperature. As usual, the heat flux inside the interphase is defined by Fourier's law:

$$\mathbf{q} = -k\nabla T.$$

Transmission conditions along the material interfaces $\Gamma_\pm = \{(x,y), x \in (-a,a), y = \pm h\}$ between the domains Ω and $\Omega_\pm$, respectively, (see Fig.1) should be written in form:

$$[\mathbf{n}\cdot\mathbf{q}]|_{\Gamma_+} = 0, \quad [T]|_{\Gamma_+} = 0, \tag{3}$$

$$[\mathbf{n}\cdot\mathbf{q}]|_{\Gamma_-} = 0, \quad [T]|_{\Gamma_-} = 0. \tag{4}$$

Here, as usual, $[f]|_\Gamma = f(x,\alpha+) - f(x,\alpha-)$ is the jump of the function f across the interface $\Gamma = \{(x,y), x \in (-a,a), y = \alpha\}$.

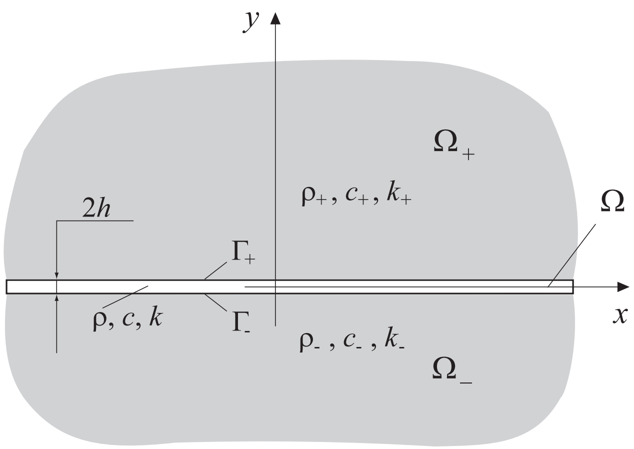

Fig. 1: Bimaterial structure with a thin interphase

Assumption 1. We consider throughout this paper that the domain

$$\Omega = \{(x,y) : y \in (-h,h), \quad x \in (-a,a)\}$$

representing the intermediate interphase is thin enough in comparison with characteristic sizes of both surrounding adherends $\Omega_\pm$ (see Fig. 1), thus $h = \epsilon\tilde{h}$ ($\epsilon << 1$).

Assumption 2. The next crucial point for this analysis is that the interphase itself is heat-resistant so that the thermal conductivity of the intermediate layer is much smaller than those of the bonded materials. In other words the ratios $k/k_\pm$ are of the same order of ϵ as it occurred for the interphase thickness:

$$k = \epsilon\tilde{k}. \tag{5}$$

Assumption 3. Finally, we want to allow that the thermal conductivity of the interface k, sources Q and the multiplicator ρc are smooth but maybe fast changing functions with respect to the interphase thickness:

$$\tilde{k} = \tilde{k}(x, y/\epsilon, t, T,), \quad Q = Q(x, y/\epsilon, t), \quad \rho_c \equiv \rho(x, y/\epsilon, t, T) \cdot c(x, y/\epsilon, t, T), \tag{6}$$

After appropriate rescalling of the space variables as shown in Fig. 2, we use the standard asymptotic approach applied in case of thin domains following for procedure from [11]:

$$y = \epsilon\xi, \quad (x, y) \in \Omega.$$

Then, equation (2) can be finally rewritten in an equivalent form as:

$$\frac{1}{\epsilon^2}\frac{\partial}{\partial\xi}\tilde{k}\frac{\partial}{\partial\xi}\tilde{T} + \frac{\partial}{\partial x}\tilde{k}\frac{\partial}{\partial x}\tilde{T} + \frac{1}{\epsilon}\tilde{Q} = \frac{1}{\epsilon}\tilde{\rho}_c\frac{\partial\tilde{T}}{\partial t}, \quad \xi \in (-\tilde{h}, \tilde{h}), \quad x \in (-a, a), \tag{7}$$

where

$$\tilde{T}(x, \xi, t) \equiv T(x, y, t),$$

and it follows from assumption (6) that:

$$\tilde{k} = \tilde{k}(x, \xi, t, \tilde{T}), \quad \tilde{Q} = Q(x, \xi, t), \quad \tilde{\rho}_c = \rho_c(x, \xi, t, \tilde{T}).$$

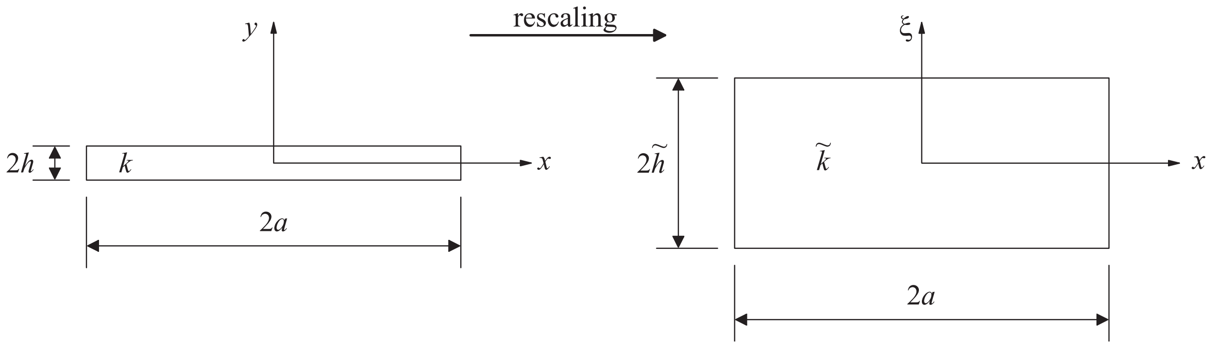

Fig. 2: Thin interphase domain before and after rescalling.

We will seek for the solution within the interphase layer in the form of an asymptotic expansion:

$$\tilde{T}(x, \xi, t, \epsilon) = \tilde{T}_0(x, \xi, t) + \epsilon\tilde{T}_1(x, \xi, t) + \epsilon^2\tilde{T}_1(x, \xi, t) + ... \tag{8}$$

and the heat flux is calculated from the asymptotic expansion:

$$\tilde{\mathbf{q}}(x, \xi, t, \epsilon) = -\tilde{k}(x, \xi, t, \tilde{T})\,[\epsilon\frac{\partial}{\partial x}, \frac{\partial}{\partial\xi}]\tilde{T} = -\tilde{k}(x, \xi, t, \tilde{T}_0)[0, 1]\frac{\partial}{\partial\xi}\tilde{T}_0 + O(\epsilon), \quad \epsilon \to 0. \tag{9}$$

Then from Eq. (7) we receive a consequence of the boundary value problems within the interphase:

$$\frac{\partial}{\partial\xi}\tilde{k}(x, \xi, t, \tilde{T}_0)\frac{\partial}{\partial\xi}\tilde{T}_0 = 0, \quad \xi \in (-\tilde{h}, \tilde{h}), \tag{10}$$

$$\frac{\partial}{\partial \xi}\tilde{k}(x,\xi,t,\tilde{T}_0)\frac{\partial}{\partial \xi}\tilde{T}_j = \mathcal{R}_j(x,\xi,t,\tilde{T}_0,...,\tilde{T}_{j-1}), \quad j=1,2,..., \quad \xi \in (-\tilde{h},\tilde{h}). \tag{11}$$

It is important to note an important difference between Eqs. (10) and (11). Namely, the first one is nonlinear while Eqs. (11) which correspond to the next terms of the asymptotic expansion are linear with respect to functions $\tilde{T}_j$. Note here that the derivative with time appears only in the right hand side of Eqs. (11).
Transmission conditions (3) and (4) can be rewritten in new notations in the forms:

$$T_+(x,\epsilon\tilde{h},t) = \tilde{T}_0(x,\tilde{h},\tau) + \epsilon\tilde{T}_1(x,\tilde{h},t) + \epsilon^2\tilde{T}_2(x,\tilde{h},t) + ..., \tag{12}$$

$$T_-(x,-\epsilon\tilde{h},t) = \tilde{T}_0(x,-\tilde{h},t) + \epsilon\tilde{T}_1(x,-\tilde{h},t) + \epsilon^2\tilde{T}_2(x,-\tilde{h},t) + ..., \tag{13}$$

$$q_y^+(x,\epsilon\tilde{h},t) = -\tilde{k}(x,\tilde{h},t,\tilde{T}(x,h,t))\left(\frac{\partial}{\partial\xi}\tilde{T}_0(x,\tilde{h},t) + \epsilon\frac{\partial}{\partial\xi}\tilde{T}_1(x,\tilde{h},t) + ...\right), \tag{14}$$

$$q_y^-(x,-\epsilon\tilde{h},t) = -\tilde{k}(x,-\tilde{h},t,\tilde{T}(x,-h,t))\left(\frac{\partial}{\partial\xi}\tilde{T}_0(x,-\tilde{h},t) + \epsilon\frac{\partial}{\partial\xi}\tilde{T}_1(x,-\tilde{h},t) + ...\right). \tag{15}$$

Expanding the left-hand sides of (12)-(15) and right-hand sides of (14)-(15) in Taylor series, we can receive the consequence of the transmission conditions. We restrict ourself in this paper only to find the main asymptotic term, i.e. $\tilde{T}_0$, of the expansion (8). As a result, we can stay in Eqs. (12)-(15) only with the terms:

$$T_+(x,0,t) = \tilde{T}_0(x,\tilde{h},t), \quad T_-(x,0,t) = \tilde{T}_0(x,-\tilde{h},t), \quad x \in (-a,a), \tag{16}$$

$$\tilde{k}(x,\tilde{h},t,\tilde{T}_0(x,\tilde{h},t))\frac{\partial}{\partial\xi}\tilde{T}_0(x,\tilde{h},t) = -q_y^+(x,0,t), \quad x \in (-a,a), \tag{17}$$

$$\tilde{k}(x,-\tilde{h},t,\tilde{T}_0(x,-\tilde{h},t))\frac{\partial}{\partial\xi}\tilde{T}_0(x,-\tilde{h},t) = -q_y^-(x,0,t), \quad x \in (-a,a). \tag{18}$$

Integrating equation (10), we obtain:

$$\tilde{k}(x,\xi,t,\tilde{T}_0)\frac{\partial}{\partial\xi}\tilde{T}_0(x,\xi,t) = C(x,t), \quad \xi \in (-\tilde{h},\tilde{h}). \tag{19}$$

Comparing (17) and (18) with (19), we immediately receive the first transmission condition:

$$q_y^+(x,0,t) = q_y^-(x,0,t), \quad x \in (-a,a), \tag{20}$$

and can additionally conclude that:

$$C(x,t) = -q_y^\pm(x,0,t), \quad x \in (-a,a). \tag{21}$$

Now, it remains to consider the ordinary differential equation (19) with respect to the variable ξ, while x and t are the only parameters. Unfortunately, it is not possible to solve Eq. (19) in a closed form for an arbitrary function $\tilde{k}$. However, we are able to do this for some specific classes of this function.

Special case 1. Let $\tilde{k}(x,\xi,t,\tilde{T}_0) = \tilde{k}_1(x,\xi,t)$, so that the heat conductivity does not depend on the temperature distribution. Then, Eq. (19) can be integrated to receive:

$$\tilde{T}_0(x,\xi,t) = C(x,t)\int_{-h}^{\xi}\frac{dz}{\tilde{k}_1(x,z,t)} + D_1(x,t), \quad \xi \in (-\tilde{h},\tilde{h}). \tag{22}$$

Constant D_1 and the second transmission conditions can be found from the two conditions given in Eqs. (16):

$$D_1(x,t) = T_-(x,0,t),$$

and

$$T_+(x,0,t) - T_-(x,0,t) = -\Lambda_1(x,t)q_y^{\pm}(x,0,t), \tag{23}$$

where

$$\Lambda_1(x,t) = \int\limits_{-\tilde{h}}^{\tilde{h}} \frac{dz}{\tilde{k}_1(x,z,t)} = \int\limits_{-h}^{h} \frac{dy}{k_1(x,y,t)}. \tag{24}$$

Special case 2. Let $\tilde{k}(x,\xi,t,\tilde{T}_0) = \tilde{k}_2(x,t,\tilde{T}_0)$, so that in this case the heat conductivity depends on time and temperature distribution but does not directly depend on the position of the point in the direction perpendicular to the interface. Then, again Eq. (19) can be integrated in other manner:

$$\int\limits_{T_-(x,0,t)}^{T_0(x,\xi,t)} \tilde{k}_2(x,t,z)dz = C(x,t)\xi + D_2(x,t), \quad \xi \in (-\tilde{h},\tilde{h}). \tag{25}$$

Constant D_2 and the second transmission condition can be found from the two conditions in (16):

$$D_2(x,t) = q_y^{\pm}(x,0,t)\tilde{h},$$

and

$$\Lambda_2(x,t,T_+(x,0,t)) - \Lambda_2(x,t,T_-(x,0,t)) = -q_y^{\pm}(x,0,t), \tag{26}$$

where

$$\Lambda_2(x,t,z) = \frac{1}{2\tilde{h}}\int \tilde{k}_2(x,t,z)dz = \frac{1}{2h}\int\ k_2(x,t,z)dz. \tag{27}$$

In the case when $\tilde{k}(x,\xi,t,\tilde{T}_0) = \tilde{k}_*(x,t)$ both of the conditions (23) and (26) coincide to each other and:

$$\Lambda_1(x,t) = \frac{2h}{k_*(x,t)}, \quad \Lambda_2(x,t,z) = \frac{1}{2h}k_*(x,t)z.$$

Genaral case. Let us assume that we have solved somehow the ordinary differential equation (19) and $\Phi(T_0,x,q) = E$ is the integral of the equation. Then the respective transmission conditions for the heat-resistant interface takes in this case the following general form:

$$\Phi(T_+(x),x,q(x)) - \Phi(T_-(x),x,q(x)) = 0, \quad q(x) = q_+(x) = q_-(x). \tag{28}$$

Concluding remarks

We can summarise the derivation procedure for two special cases in the table 1, where functions Λ_1 and Λ_2 are defined in (24) and (27), respectively.

As it follows from this analysis, the imperfect transmission transmission conditions can be successfully derived in the case of thin heat-resistant interphases for a wider class of their thermal properties. Moreover, having in hand any specific formulae for the heat conductivity one can try to derive respective nonlinear transmission conditions with taking into account relations (28).

On the other hand, it is highly important to know what is the range of the material parameters where the condition can be applied, and when it is necessary to take into account some specific effect (for example high time gradient). This investigation will be done in the next paper presented in this issue by very accurate FEM simulations. The further question is how to implement the transmission conditions in a standard commercial code in order to decrease (and in a drastic way) the number of elements involved in the simulations without any loss of the calculation accuracy.

$k = k(x, y, t)$	$[\mathbf{n} \cdot \mathbf{q}]_{y=0} = 0$	$\Lambda_1^{-1}(x, t)[T]\|_{y=0} = -\mathbf{n} \cdot \mathbf{q}\|_{y=0}$
$k = k(x, t, T)$	$[\mathbf{n} \cdot \mathbf{q}]_{y=0} = 0$	$[\Lambda_2(x, t, T)]\|_{T=T_\pm(x,0,t)} = -\mathbf{n} \cdot \mathbf{q}\|_{y=0}$

Table 1: Transmission conditions for thin heat-resistant interface. Functions Λ_1 and Λ_2 are defined in (24) and (27), respectively.

Acknowledgments

G. Mishuris has been supported by a Marie Curie Transfer of Knowledge Fellowship of the European Community's Sixth Framework Programme under contract number MTKD-CT-2004-509809. The paper has been completed during his short-time stay at the University of Aveiro. A. Öchsner is grateful to Portuguese Foundation of Science and Technology for support of this research.

References

[1] F. Rosselli, P.Carbutt: Sampe. J. Vol. 37 (2001), p. 7

[2] Y. Hashin: J. Appl. Phys. Vol. 89 (2001), p. 2262

[3] G. Mishuris and A. Öchsner: Compos. Struct. Vol. 68 (2005), p. 409

[4] G. Mishuris, A. Öchsner and G. Kuhn: CMC - Comput Mater Continua Vol. 2 (2005), p. 227

[5] G. Mishuris, A. Öchsner: Arch. Mech. Vol. 57 (2005), p. 157

[6] Y. Benveniste, T. Miloh: Mech. Mater. Vol. 33 (2001), p. 309

[7] Z. Hashin: J. Mech. Phys. Solids Vol. 50 (2002), p. 2509

[8] A.H. Nayfeh: J. Appl. Mech. Vol. 42 (1975), p. 399.

[9] Y. Benveniste: Mech. Mater. Vol. 4 (1985), p. 197

[10] Z. Hashin: Mech. Mater. Vol. 8 (1990), p. 3333

[11] A.B. Movchan, N.V. Movhan: *Mathematical Modelling of Solids of with Nonregular Boundaries* (CRC Press, Boca Raton 1995)

Materials Science Forum Vol. 553 (2007) pp. 93-99
online at http://www.scientific.net

Finite Element Verification of Transmission Conditions for 2D Heat Conduction Problems

Gennady Mishuris[1,a], Wiktoria Miszuris[1,b], Andreas Öchsner[2,3,c]

[1]Department of Mathematics, Rzeszow University of Technology, Rzeszow, Poland
[2]Centre for Mechanical Technology and Automation, University of Aveiro, Aveiro, Portugal
[3]Department of Mechanical Engineering, University of Aveiro, Aveiro, Portugal

[a]miszuris@prz.rzeszow.pl, [b]victory@prz.rzeszow.pl, [c]aoechsner@mec.ua.pt

Keywords: heat transfer, thin layers, finite element method, nonclassical transmission conditions, numerical modelling

Abstract. Imperfect transmission conditions modelling a thin 2D intermediate layer between two bonded materials in a dissimilar strip have been derived and analytically analysed in another paper of this issue. In this paper, the validity of these transmission conditions for heat conduction problems has been investigated due to the finite element method (FEM) for various cases: namely, steady-state under uniform boundary conditions with constant or functional-dependent, i.e. temperature or spatial coordinate, conductivities of the interphase, non-uniform boundary conditions and finally for transient analysis. It is shown that the accuracy of the transmission conditions is excellent over the whole range of the interphase and that typical edge effects known from structural problems are not observable under the chosen problem parameters.

Introduction

Thin films, e.g. adhesive layers, are nowadays an important part of technological processes and components [1]. As an example, adhesive layers allow for joining materials with essentially different properties at very high quality. The application of such hybrid structures in safety-relevant applications requires a highly accurate and efficient prediction of their physical behaviour, which necessitates the development of robust simulation models and techniques based on, and verified by, appropriate experimental procedures.

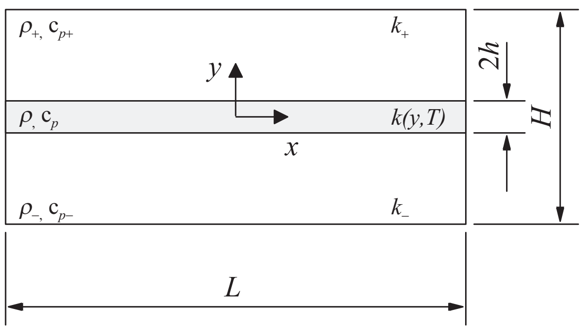

Fig. 1: Schematic representation of the problem.

In the scope of this paper, imperfect transmission conditions applied to a thin heat-resistant layer in a hybrid model structure (cf. Fig. 1) are going to be numerically investigated in order to verify the applicability and accuracy of the analytical relations for conduction problems.

Finite Element Modelling

The commercial finite element code MSC.Marc is used for the simulation of the thermal behaviour of the modelling thin intermediate layer between two adherends. Both adherends reveal constant material properties for all simulations. It should be noted here that the theoretical derivation of the transmission conditions has been performed under the precondition that the conductivity of the thin interphase is much smaller (i.e. a heat-resistant layer) than the conductivities of the adherends. In the simulations, the intermediate layer has the thickness $2h = H/100 = 0.01$ while the length of all components is equal to $L = 10$. The two-dimensional FE-mesh is built up of four-node, isoparametric elements with bilinear interpolation functions. In order to cover possible edge effects [2], a strong mesh refinement is performed near the free surface of the interphase. Further details of the finite element mesh can be found in [3]. In addition, the mesh is generated in such a way that it is possible to evaluate the temperatures and fluxes along the axes of geometrical symmetry, and along both interfaces (i.e. the line or surface where the thin layer and the adherends are in contact) as well as along lines perpendicular to the interfaces.

Results

All numerical simulations have been performed for the same aluminium adherends which reveal a constant conductivity of $k_{\pm} = 237\ \frac{\mathrm{W}}{\mathrm{m \cdot K}}$ at 300 K. Furthermore, it has been assumed that the temperature dependence of all adherend material parameters can be neglected.

Uniform boundary conditions, steady-state. The following examples refer to a steady-state solution where constant Dirichlet boundary conditions have been prescribed at the top ($y = +H/2$) and bottom ($y = -H/2$) surface (cf. Fig. 2). The thin interphase has been assumed to be made of an epoxy resin which exhibits different formulations of its thermal conductivity: namely, a constant conductivity (Eq. (1)), an interphase which linearly depends on the temperature (Eq. (2)) and finally a conductivity quadratically depending on the vertical coordinate (Eq. (3)):

$$k = 0.2\ \frac{\mathrm{W}}{\mathrm{m \cdot K}}\,, \tag{1}$$

$$k(T) = \frac{1}{70}\,(-115 + 0.43 \cdot T)\ \ \frac{\mathrm{W}}{\mathrm{m \cdot K}} = c_1 + c_2 \cdot T\,, \tag{2}$$

$$k(y) = 0.2 + 800 \cdot y^2\ \ \frac{\mathrm{W}}{\mathrm{m \cdot K}} = c_3 + c_4 \cdot y^2\,. \tag{3}$$

These three different formulations of the interphase thermal conductivity yield to quite different expressions for the transmission conditions which relate the temperature jump $[T] = T(x, y = +h) - T(x, y = -h)$ to the heat flux $q = q_y$ in the middle of the layer:

$$k = \text{const.} \ \ : \ \ [T] = -\frac{q \cdot 2h}{k}\,, \tag{4}$$

$$k = k(T) \ \ : \ \ [T] \cdot \left(c_1 + \frac{c_2}{2} \cdot (T^+ + T^-) \right) = F(T^+) - F(T^-) = -q \cdot 2h\,, \tag{5}$$

$$k = k(y) \ \ : \ \ [T] = -\frac{2}{\sqrt{c_3 c_4}} \arctan \left(\frac{h}{2} \cdot \sqrt{\frac{c_3}{c_4}} \right) \cdot q = -\frac{1}{a'} \cdot q \cdot 2h\,. \tag{6}$$

Details of the derivation are given in another paper of the authors in this issue or in the case of constant material parameters in [4, 5].

It should be noted here that due to the absence of any heat sources or sinks, thermal equilibrium demands that the heat flux q_y is constant over the thickness. Figure 2 illustrates the shape of the temperature profile perpendicular to the interphase for $x = 0$. The temperature is linearly changing in the adherends since the thermal conductivity has been assumed to be constant in space and temperature. Furthermore, the curves for different formulations of the conductivity practically coincide inside the adherends in the presented scale of the figure. Looking at the magnification of the temperature distribution (cf. Fig. 2, right) inside the interphase, different behaviour of the temperature can be observed: constant conductivity yields to a linear temperature profile while y- and T-dependency results in non-linear temperature distributions.

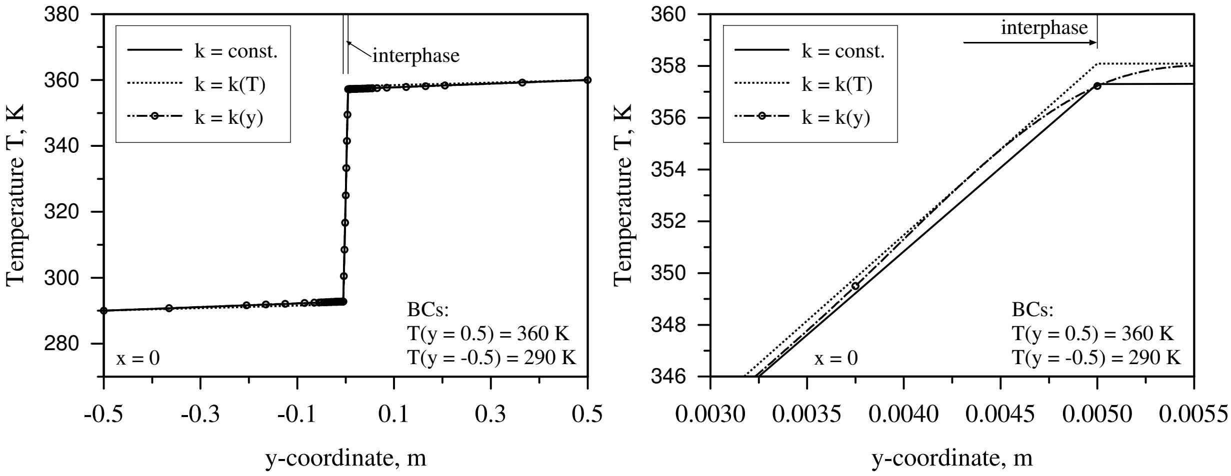

Fig. 2: Temperature distribution perpendicular to the interphase (along the line $x = 0$) for different formulations of the interphase conductivity k.

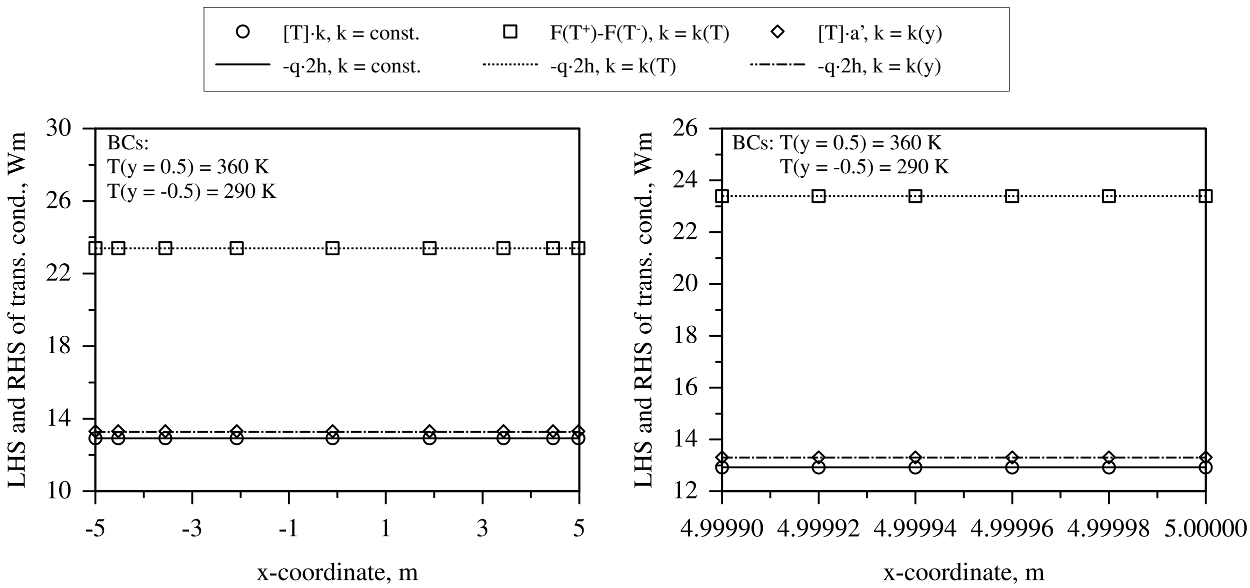

Fig. 3: Verification of the transmission condition validity along the interphase for different formulations of the interphase conductivity k.

Figure 3 presents the verification of the transmission conditions (cf. Eqs. (1)-(3)) along the whole interphase by independently extracting the right and left hand side of the equations from

FEM evaluation. As can be seen in different magnifications, the coincidence is perfect up to the free boundary of the specimens. It must be noted here that in the case of a structural-mechanical problem, different edge effects [2, 3] are occurring near the free boundary due to the contraction of the material. This cannot be observed for these heat conduction problems under the chosen properties and parameters.

Non-uniform boundary conditions, steady-state. The following steady-state example refers to the case where quadratically changing Dirichlet boundary conditions have been assigned at the top ($T(x, y = 0.5) = 360 + 3 \cdot x^2$) and the bottom ($T(x, y = 0.5) = 290 + 3 \cdot x^2$) of the specimen. The interphase reveals the temperature-dependency given in Eq. (2).

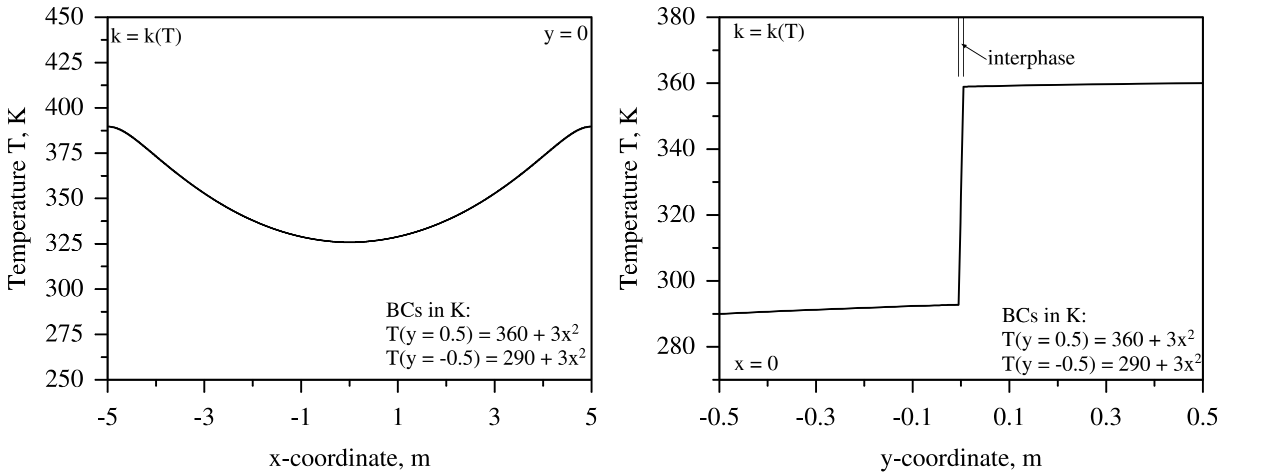

Fig. 4: Temperature distribution along (middle line, $y = 0$) and perpendicular (along the line $x = 0$) to the interphase for non-uniform boundary conditions ('parabolic' case).

The altering temperature distribution at the boundaries is reflected in the shape of the temperature profile along the interphase (cf. Fig. 4, left) while the characteristic perpendicular to the interphase (cf. Fig. 4, right) is the same as in the previous example.

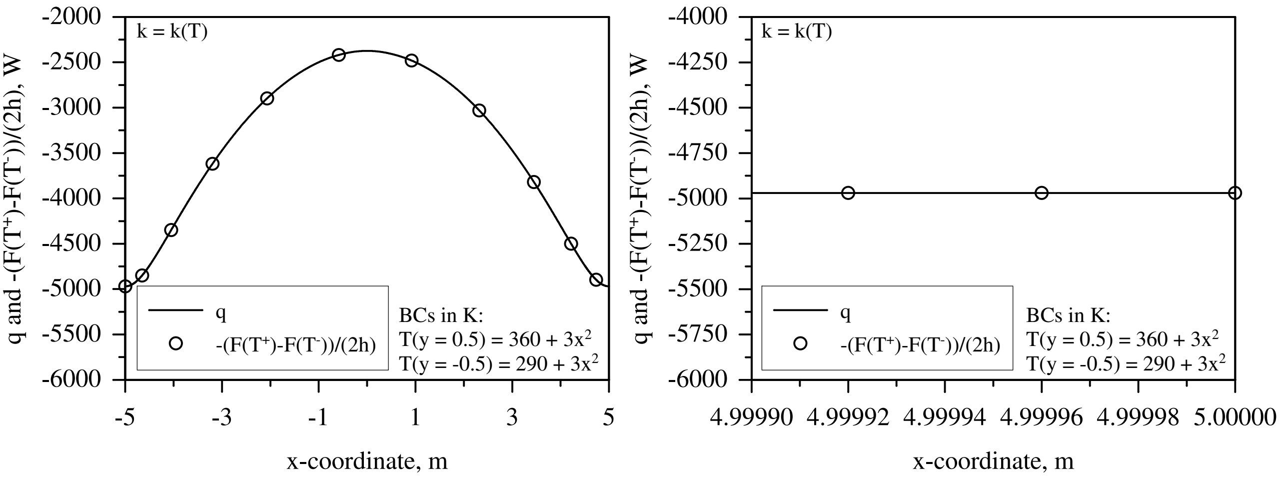

Fig. 5: Verification of the transmission condition validity along the interphase for non-uniform boundary conditions ('parabolic' case).

Looking at the graphical comparison of the left and right hand sides of the corresponding transmission condition (cf. Fig. 7), one can see that both terms yield to a curvilinear distribution. Nevertheless, the same excellent coincidence (rel. error 10^{-4} %) is obtained up to the end, i.e. the free surface, of the specimen.
In the final example of this section (so-called 'edge' case), an additional horizontal temperature gradient is superimposed to the vertical gradient by applying Dirichlet conditions to the upper right and lower left specimen corners:

$$T(x = -5.0, -0.5 \leq y \leq -0.205) = T(-5.0 \leq x \leq -4.68, y = -0.5) = 290\ \mathrm{K}\,, \tag{7}$$

$$T(x = 5.0, 0.205 \leq y \leq 0.5) = T(4.68 \leq x \leq 5.0, y = 0.5) = 360\ \mathrm{K}\,. \tag{8}$$

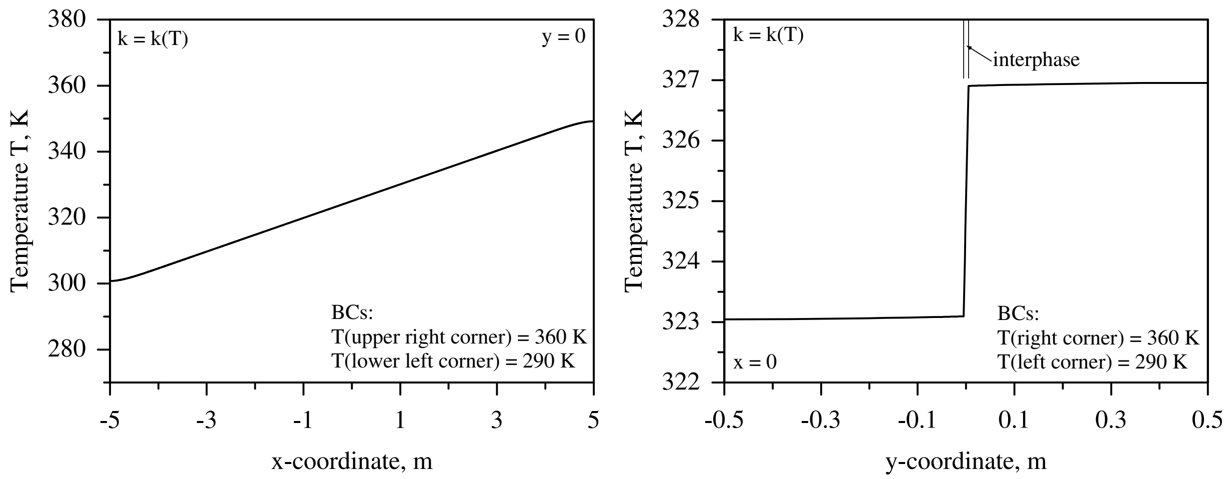

Fig. 6: Temperature distribution along (middle line, $y = 0$) and perpendicular (along the line $x = 0$) to the interphase for non-uniform boundary conditions ('edge' case).

Looking at the temperature distribution along the interphase (cf. Fig. 6, left), an approximately linear increasing distribution can be observed while the shape perpendicular to the interphase reveals the same characteristics as in the previous examples.

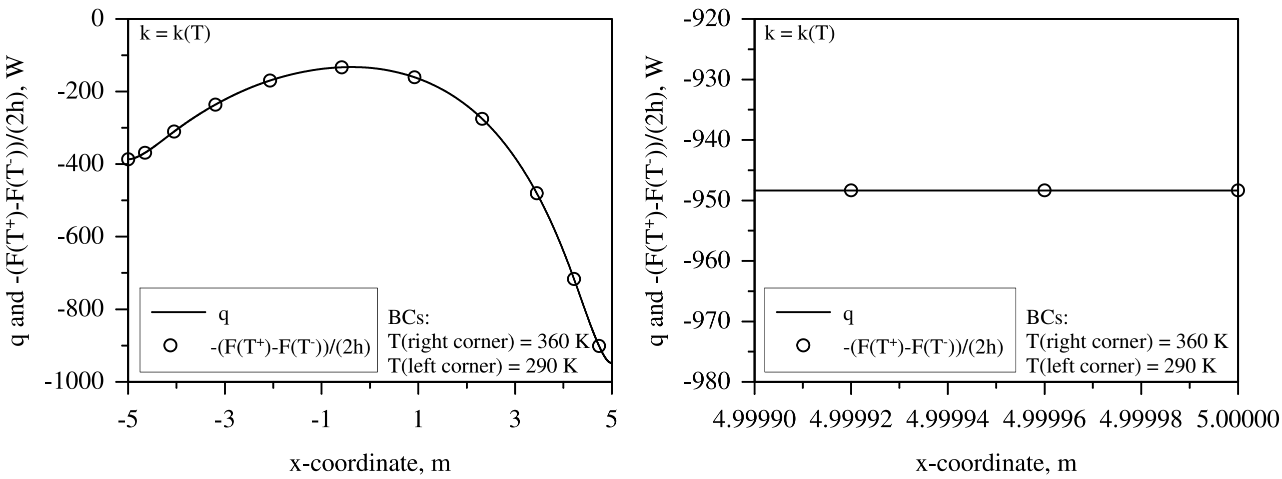

Fig. 7: Verification of the transmission condition validity along the interphase for non-uniform boundary conditions ('edge' case).

Figure 7 indicates that the superimposed horizontal heat flux does not change the validity of the transmission conditions in the vertical direction and the same good coincidence as in the previous examples is obtained.

Transient analysis. The following section addresses a transient analysis where the definition of the interphase conductivity and the boundary conditions ('edge' case) are taken as in the previous example. The boundary temperatures were linearly changed from the uniform initial temperature of 325 K, which was assigned to all nodes of the model, to the values of the previous example: 360 K at the upper right corner and 290 K at the lower left corner. For this transient analysis, the mass density ϱ and specific heat at constant pressure c_p need to be defined for all components:

$$\varrho_{\mathrm{Al}} = 2698.8\ \frac{\mathrm{kg}}{\mathrm{m}^3} \ \text{ and } \ c_{p,\mathrm{Al}} = 898.2\ \frac{\mathrm{J}}{\mathrm{kg{\cdot}K}}\ , \tag{9}$$

$$\varrho_{\mathrm{Ep}} = 1200\ \frac{\mathrm{kg}}{\mathrm{m}^3} \ \text{ and } \ c_{p,\mathrm{Ep}} = 790\ \frac{\mathrm{J}}{\mathrm{kg{\cdot}K}}\ . \tag{10}$$

For simplicity, the temperature dependency of the density and the specific heat has been neglected in Eqs. (9)-(10).

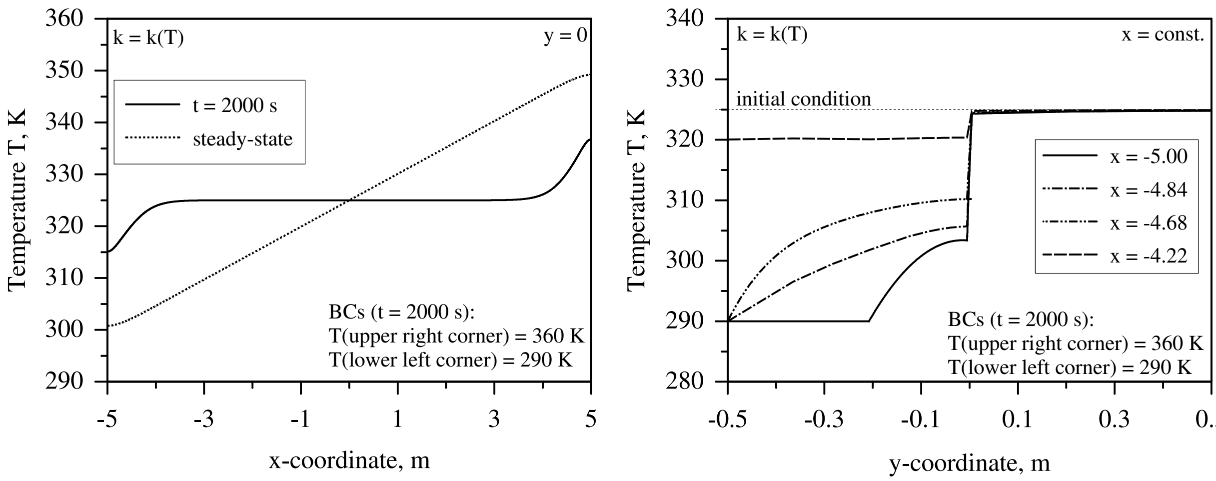

Fig. 8: Temperature distribution along (middle line, $y = 0$) and perpendicular (along the line $x = 0$) to the interphase for a transient analysis.

The temperature distribution along the interphase is shown in Fig. 8 (left) for a certain point of time in the transient regime and for the steady-state condition. As can be seen, a significant temperature change is included in the transient simulation. The high non-uniformity of the temperature perpendicular to the interphase (especially in the region close to the free surface) is shown in Fig. 8 (right).

Looking at the verification of the transmission condition shown in Fig. 9, one can see that the condition is fulfilled in general along the whole range of the interphase (left figure) while a slight deviation can be observed very near the free surface (rel. error 0.5 %), i.e. the region where higher gradients prevail during time steps of the transient regime.

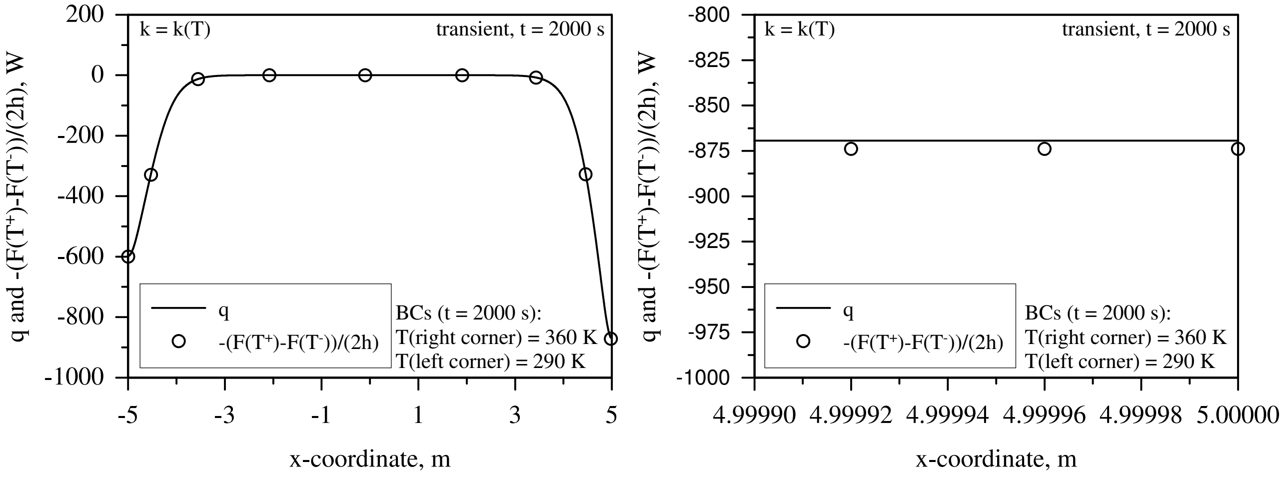

Fig. 9: Verification of the transmission condition validity along the interphase for a transient analysis.

Discussion and Outlook

Finite element analysis could proof the applicability of transmission conditions for heat-resistant inhomogeneous interphases. Extremely good accuracy could be observed over the whole range of the interphase for different formulations of the interphase conductivity and different boundary conditions. Only in the case of transient problems with high gradients per time step [6], an extension of the applied conditions seems to be appropriate. The implementation of the investigated transmission conditions into a commercial finite element code as special interphase elements is reserved for our future research work.

Acknowledgments

G. Mishuris has been supported by a Marie Curie Transfer of Knowledge Fellowship of the European Community's Sixth Framework Programme under contract number MTKD-CT-2004-509809. The paper has been completed during his short-time stay at the University of Aveiro. A. Öchsner is grateful to Portuguese Foundation of Science and Technology for support of this research.

References

[1] F. Rosselli and P. Carbutt: Sampe J. Vol. 37 (2001), p. 7

[2] G. Mishuris and A. Öchsner: Compos. Struct. Vol. 68 (2005), p. 409

[3] G. Mishuris, A. Öchsner and G. Kuhn: CMC - Comput. Mater. Continua Vol. 2 (2005), p. 227

[4] Z. Hashin: Mech. Mater. Vol. 8 (1990), p. 333

[5] Z. Hashin: J. Mech. Phys. Solids Vol. 50 (2002), p. 2509

[6] C.D. Marshall, I.M. Fishman, R.C. Diorfman, C.B. Eom and M.D. Fayer: Phys. Rev. B Vol. 45, p. 10009

///VSP/// Journal of Adhesion Science and Technology 22 (2008) 1365–1378

Journal of ADHESION SCIENCE and TECHNOLOGY
www.brill.nl/jast

A New Finite Element Formulation for Thin Non-Homogeneous Heat-Conducting Adhesive Layers

Andreas Öchsner [a,b,*] **and Gennady Mishuris** [c]

[a] Department of Applied Mechanics, Faculty of Mechanical Engineering, Technical University of Malaysia — UTM, 81310 UTM Skudai, Johor, Malaysia

[b] University Centre for Mass and Thermal Transport in Engineering Materials, School of Engineering, The University of Newcastle, Callaghan, New South Wales 2308, Australia

[c] Department of Mathematics, Rzeszow University of Technology, W. Pola 2, 35-959 Rzeszow, Poland

Abstract

A thin heat-conducting adhesive layer is considered in a two-dimensional approach. The material of the adhesive layer exhibits an arbitrary non-homogeneous thermal conductivity which is a function of the spatial coordinate perpendicular to the interface. Based on the weighted residual method, a new finite element formulation for a four-node, rectangular element is derived which is able to easily incorporate high conductivity gradients in the new thermal conductivity matrix. The approach is not based on any assumptions of the temperature distribution (e.g. linear or cubic) but considers that the heat flux must be constant in the case that no heat sources or sinks are present. A numerical example of a simple bonded joint illustrates the implementation into the commercial finite element code MSC.Marc due to special user subroutines. The numerical results are compared to a classical approach based on standard elements and the differences are discussed.

Keywords

Heat transfer, non-linear behaviour, thin layer, interface, finite element method, thermal conductivity matrix

1. Introduction

Thin adhesives are nowadays an important part of technological processes and components [1]. They allow joining of materials with considerably different properties with very high quality compared to other joining technologies. The application of such bonded structures in safety-relevant applications, e.g. structural parts for the aerospace and automotive industries, requires a highly accurate prediction of

* To whom correspondence should be addressed. Tel.: +6 017 7786228; Fax: +6 07 55 66159; e-mail: andreas.oechsner@gmail.com

 DOI:10.1163/156856108X309558

their mechanical behaviour, which necessitates the development of robust simulation models and techniques based on, and verified by, appropriate experimental procedures.

The theoretical treatment of thin interphases can be classified into three different major approaches where considerable work has been related to their mechanical properties. The first of these, and the most popular, assumes that the bi-material interface is of zero thickness, which allows the so-called "perfect contact condition" to be satisfied along the whole length of the interface [2, 3]. The perfect contact conditions occur in the case of heat conduction problems where the temperatures and fluxes remain continuous across the whole interface. However, such an approach makes it impossible to take into account any internal properties of the real interphase between the bonded materials. On the other hand, properties of adhesive materials may differ fundamentally from those of the bonded materials. For this reason, a second approach has been implemented in the theoretical modelling of bonded dissimilar materials. It consists in the assumption that there is an additional thin layer of finite thickness with its own mechanical properties (see review in [4]). However, in modern technology very thin adhesive layers (thin films) are used [5]. This fact makes it difficult to perform numerical calculations using FEM, since the need to build a complicated mesh of fundamentally different-sized elements can lead to a loss in accuracy, unstable calculations and even loss of convergence [6]. In such a case, the third approach may be very successful: the so-called imperfect interface approach. This consists in using some special non-classical transmission conditions which take into account the intrinsic properties of the thin interphase, but the conditions are still applicable along the imaginary zero-thickness interface (bondline). Such transmission conditions can be obtained from some phenomenological assumptions or from an accurate asymptotic analysis taking into account various features of the intermediate layer. Imperfect transmission conditions applied to a thin heat-resistant layer in a hybrid model structure were analytically derived in [7] and their applicability and accuracy were verified in [8].

At the early stage of numerical finite element simulation of adhesive layers, conventional finite elements were used [9, 10] to investigate the stresses within an adhesive layer. Later on, so-called interface elements [11] were developed which were applied to various fields of civil engineering such as soil-reinforcement interaction [12], rock joints [13] and discrete cracking in concrete mechanics [14]. Furthermore, interface elements are suited to model delamination and failure in composite structures [15] when combined with damage models.

The objective of this study was to develop a new finite element formulation for thin heat-conducting interphases which includes material non-homogeneities. In the scope of this paper, a spatial dependency perpendicular to the bondline is considered.

2. Basics of Heat Transfer

Heat conduction analysis is based on Fourier's law (conduction rate equation)

$$\mathbf{q} = -\mathbf{k}\nabla T, \tag{1}$$

where $\mathbf{q} = \{q_x \quad q_y\}^{\mathrm{T}}$ is the heat flux vector and $\nabla T = \left\{\frac{\partial T}{\partial x} \quad \frac{\partial T}{\partial y}\right\}^{\mathrm{T}}$ is the temperature gradient vector which is generated by the Nabla operator ∇. The continuum conductivity matrix $\mathbf{k}$ reduces for isotropic materials to $\mathbf{k} = k \cdot \mathbf{I}$, where k is the isotropic heat conductivity (scalar) and $\mathbf{I} = \lceil 11 \rfloor$ is the identity matrix.

To solve a heat conduction problem means to determine the temperature field $T = T(x, y, t)$ in its spatial and temporal dependencies. Then the heat flux field can be determined according to Fourier's law, equation (1). The unknown temperature field is obtained by solving the so-called heat diffusion equation. This partial differential equation can be obtained by applying the first law of thermodynamics to a differential control volume which gives after some transformations the continuity equation of thermodynamics. Combining the continuity equation with Fourier's law and introducing a third law describing the relationship between temperature and energy gives the heat diffusion equation in its general form as [16, 17]

$$\varrho c \frac{\partial T}{\partial t} = \nabla^{\mathrm{T}}(\mathbf{k}\nabla T) + \dot{\eta}, \tag{2}$$

where ϱ is the mass density, c the specific heat, t the time and $\dot{\eta}$ the energy rate per unit volume, i.e. a heat source or sink with the unit of thermal energy per time and volume.

3. Derivation of the New Finite Element Formulation

Let us consider in the following the special case of the two-dimensional, steady-state ($\partial T/\partial t = 0$) heat diffusion equation where no sources or sinks are present ($\dot{\eta} = 0$) and the material reveals isotropic properties ($\mathbf{k} \to k$). The basic idea of the weighted residual method [18] consists in multiplying a partial differential equation with a weighting function w and to require that the entire integral vanishes over the whole domain. For the exact solution, this expression is independent of the weighting function and is always fulfilled. Replacing the exact solution by an approximate solution produces a 'residual' function R such that $R = \nabla^{\mathrm{T}}(k\nabla T) \neq 0$. This error will be distributed according to the scalar weighting function and the integral over the entire domain Ω will be forced to be zero in a certain average sense, i.e.,

$$\int_{\Omega} w\big(\nabla^{\mathrm{T}}(k\nabla T)\big)\,\mathrm{d}\Omega = \int_{\Omega} wR\,\mathrm{d}\Omega = 0. \tag{3}$$

The application of the Green–Gauss theorem [19], i.e.

$$\int_{\Omega} w\nabla^{\mathrm{T}}(k\nabla T)\,\mathrm{d}\Omega = \int_{\Gamma} w(k\nabla T)^{\mathrm{T}}\mathbf{n}\,\mathrm{d}\Gamma - \int_{\Omega} (\nabla^{\mathrm{T}} w)(k\nabla T)\,\mathrm{d}\Omega = 0, \tag{4}$$

or

$$\int_{\Omega} (\nabla^{\mathrm{T}} w)(k\nabla T)\,\mathrm{d}\Omega = \int_{\Gamma} w(k\nabla T)^{\mathrm{T}}\mathbf{n}\,\mathrm{d}\Gamma, \tag{5}$$

gives the formulation which forms the basis for the derivation of the principal finite element equation. The basic idea of the finite element method is to approximate the unknown temperature T not in the entire domain Ω as given in equation (5) but in a sub-domain Ω_{e}, i.e. a so-called finite element. Let us consider in the following the two-dimensional sub-domain $\Omega_{\mathrm{e}} = \Omega_{\mathrm{e}}(-a \leqslant x \leqslant a, -h \leqslant y \leqslant h)$ as shown in Fig. 1.

For such a case, the left-hand side of equation (5) can be written as

$$\int_{-h}^{h}\int_{-a}^{a} (\nabla^{\mathrm{T}} wk)\nabla T\,\mathrm{d}x\,\mathrm{d}y \cdot t = \int_{-h}^{h}\int_{-a}^{a} k \begin{bmatrix} \frac{\partial w}{\partial x} & \frac{\partial w}{\partial y} \end{bmatrix} \begin{bmatrix} \frac{\partial T}{\partial x} \\ \frac{\partial T}{\partial y} \end{bmatrix} \mathrm{d}x\,\mathrm{d}y \cdot t, \tag{6}$$

where t is the constant thickness of the element. The constant thickness assumption in equation (6) is a common approach for two-dimensional elements. Rescaling the problem, i.e.

$$y = \varepsilon \cdot \chi, \qquad h = \varepsilon \cdot \tilde{h}, \tag{7}$$

$$\mathrm{d}y = \varepsilon \cdot \mathrm{d}\chi, \qquad k = \varepsilon \cdot \tilde{k}, \tag{8}$$

which stretches the vertical dimension in the same range as the horizontal dimension (cf. Fig. 2) gives (the second equation of (8) implies that a heat resistant interface, i.e. that the thermal conductivity of the intermediate layer is much smaller

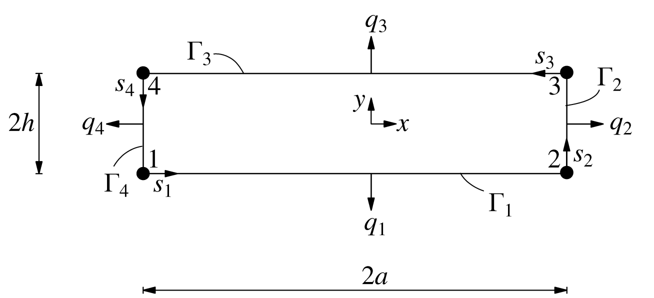

Figure 1. Two-dimensional rectangular sub-domain $(-a \leqslant x \leqslant a, -h \leqslant y \leqslant h)$ with boundaries Γ_i and boundary heat fluxes q_i.

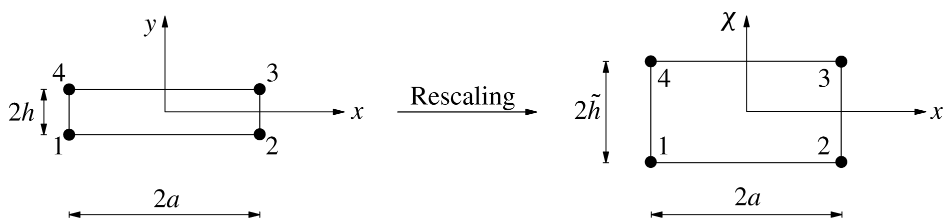

Figure 2. Thin interphase domain before and after rescaling of the vertical dimension.

than those of the bonded materials, is considered)

$$\begin{aligned}&\int_{-\tilde{h}}^{\tilde{h}}\int_{-a}^{a}\varepsilon\tilde{k}\begin{bmatrix}\frac{\partial w}{\partial x} & \frac{1}{\varepsilon}\frac{\partial w}{\partial \chi}\end{bmatrix}\begin{bmatrix}\frac{\partial T}{\partial x}\\ \frac{1}{\varepsilon}\frac{\partial T}{\partial \chi}\end{bmatrix}\mathrm{d}x\,\varepsilon\,\mathrm{d}\chi\cdot t\\ &\quad=\underbrace{\int_{-\tilde{h}}^{\tilde{h}}\int_{-a}^{a}\varepsilon\tilde{k}\frac{\partial w}{\partial x}\frac{\partial T}{\partial x}\,\mathrm{d}x\,\varepsilon\,\mathrm{d}\chi\cdot t}_{O(\varepsilon^2)}+\int_{-\tilde{h}}^{\tilde{h}}\int_{-a}^{a}\varepsilon\tilde{k}\frac{1}{\varepsilon}\frac{\partial w}{\partial \chi}\frac{1}{\varepsilon}\frac{\partial T}{\partial \chi}\,\mathrm{d}x\,\varepsilon\,\mathrm{d}\chi\cdot t.\end{aligned} \tag{9}$$

Neglecting the terms of higher orders in equation (9), the left-hand side of equation (5) can be approximated as

$$\int_{-\tilde{h}}^{\tilde{h}}\int_{-a}^{a}\varepsilon\tilde{k}\begin{bmatrix}\frac{\partial w}{\partial x} & \frac{1}{\varepsilon}\frac{\partial w}{\partial \chi}\end{bmatrix}\begin{bmatrix}\frac{\partial T}{\partial x}\\ \frac{1}{\varepsilon}\frac{\partial T}{\partial \chi}\end{bmatrix}\mathrm{d}x\,\varepsilon\,\mathrm{d}\chi\cdot t\approx\int_{-\tilde{h}}^{\tilde{h}}\int_{-a}^{a}\tilde{k}\frac{\partial w}{\partial \chi}\frac{\partial T}{\partial \chi}\,\mathrm{d}x\,\mathrm{d}\chi\cdot t. \tag{10}$$

The temperature distribution within an element is obtained by multiplying the nodal temperature vector $\mathbf{T}_\mathrm{e}$ with the vector of the so-called shape functions $\mathbf{N}_\mathrm{e}$, which are prescribed in terms of independent variables (such as the spatial coordinates). The weighting function w is approximated within an element in a similar manner as the temperature, i.e. $w=\delta\mathbf{T}_\mathrm{e}^\mathrm{T}\mathbf{N}_\mathrm{e}$, where $\delta\mathbf{T}_\mathrm{e}$ is a vector of arbitrary temperatures. Since the nodal temperatures are not a function of the spatial coordinates, the derivatives in equation (10) can be expressed as derivatives of the shape functions and the approximation of equation (5) is obtained as

$$\int_{-\tilde{h}}^{\tilde{h}}\int_{-a}^{a}\tilde{k}\frac{\partial \mathbf{N}_\mathrm{e}}{\partial \chi}\left(\frac{\partial \mathbf{N}_\mathrm{e}}{\partial \chi}\right)^\mathrm{T}\mathrm{d}x\,\mathrm{d}\chi\cdot t. \tag{11}$$

Equation (11) forms the basis for the derivation of the 4×4 elemental heat conductivity matrix $\mathbf{K}_\mathrm{e}$ of the special element.

Let us assume in the following that the conductivity of the interphase element is only a function of the y-coordinate and is evaluated at the centre of the element in the x-direction. In addition, let us assume that no sources are present in the interphase. It follows immediately from Fourier's law that the heat flux in y-direction, or after rescaling in χ-direction, can be expressed as:

$$\frac{\partial T}{\partial \chi}=\frac{c(x)}{\tilde{k}(\chi)}, \tag{12}$$

where c is an arbitrary function, independent of χ. Rearrangement and integration of equation (12) gives:

$$T(x,\chi)_1=c_1(x)+c_2(x)\int_{-\tilde{h}}^{\chi}\frac{\mathrm{d}\zeta}{\tilde{k}(\chi)}=c_1(x)+c_2(x)\big(\psi(\chi)-\psi(-\tilde{h})\big), \tag{13}$$

where the following identity is satisfied: $\partial\psi(\chi)/\partial\chi=1/\tilde{k}(\chi)$. The integration can be performed in the same manner from the opposite side, i.e. from $\tilde{h}$ until χ. Combination of both solutions is also a solution and the consideration that the c_i are arbitrary functions gives:

$$T(x,\chi) = c_4(x)\big(\psi(\chi) - \psi(\tilde{h})\big) + c_2(x)\big(\psi(\chi) - \psi(-\tilde{h})\big). \tag{14}$$

Assuming that linear elements are applied to the surrounding adherends, a linear x-dependency of the functions c_2 and c_4 is assumed in the following:

$$T(x,\chi) = (\alpha x + \beta)\big(\psi(\chi) - \psi(\tilde{h})\big) + (\gamma x + \delta)\big(\psi(\chi) - \psi(-\tilde{h})\big). \tag{15}$$

The unknown constants $\alpha, \ldots, \delta$ can be determined by evaluating the nodal temperatures $T_1, \ldots, T_4$ (cf. Fig. 2, right):

$$T_i = -\Delta\psi\big((-1)^{i+1}\alpha a + \beta\big) \quad \text{for } i = 1, 2, \tag{16}$$

$$T_i = -\Delta\psi\big((-1)^{i+1}\gamma a + \delta\big) \quad \text{for } i = 3, 4, \tag{17}$$

where $\Delta\psi = \psi(\tilde{h}) - \psi(-\tilde{h})$. From equations (16) and (17), the four unknowns $\alpha, \ldots, \delta$ can be determined and equation (15) can be finally written as:

$$\begin{aligned} T(x,\chi) = {} & \frac{1}{2\Delta\psi}\big(\psi(\chi) - \psi(\tilde{h})\big)\left(\frac{x}{a} - 1\right)T_1 \\ & + \frac{-1}{2\Delta\psi}\big(\psi(\chi) - \psi(\tilde{h})\big)\left(\frac{x}{a} + 1\right)T_2 \\ & + \frac{1}{2\Delta\psi}\big(\psi(\chi) - \psi(-\tilde{h})\big)\left(\frac{x}{a} + 1\right)T_3 \\ & + \frac{-1}{2\Delta\psi}\big(\psi(\chi) - \psi(-\tilde{h})\big)\left(\frac{x}{a} - 1\right)T_4, \end{aligned} \tag{18}$$

from which the nodal shape functions in the (x,χ)-coordinate system can be identified as the multipliers of the nodal temperatures $T_1, \ldots, T_4$. The derivatives of these shape functions can easily be obtained by considering $\partial\psi(\chi)/\partial\chi = 1/\tilde{k}(\chi)$ and $\partial\psi(-\tilde{h})/\partial\chi = 0$ as:

$$\frac{\partial N_i}{\partial \chi} = \frac{(-1)^{i+1}}{2\Delta\psi}\begin{Bmatrix} \left(\frac{x}{a} - 1\right) \\ \left(\frac{x}{a} + 1\right) \end{Bmatrix}\frac{1}{\tilde{k}(\chi)}, \quad \text{if } \begin{matrix} i = 1, 4, \\ i = 2, 3. \end{matrix} \tag{19}$$

Introducing the derivatives of the shape functions into equation (11) enables the calculation of the elemental conductivity matrix. In the following, the components of the elemental conductivity matrix will be determined:

- k_{11}:

$$\begin{aligned} k_{11} &= \int_{\chi=-\tilde{h}}^{\tilde{h}} \int_{\xi=-1}^{1} \tilde{k}\frac{1}{4\Delta\psi^2}(\xi - 1)^2 \frac{1}{\tilde{k}^2} \underbrace{a\,\mathrm{d}\xi}_{\mathrm{d}x}\,\mathrm{d}\chi\, t \\ &= \int_{-1}^{1} \frac{(\xi-1)^2}{4\Delta\psi^2} a\,\mathrm{d}\xi\, t \underbrace{\int_{-\tilde{h}}^{\tilde{h}} \frac{\mathrm{d}\chi}{\tilde{k}(\zeta)}}_{\Delta\psi} = \frac{at}{4\Delta\psi}\int_{-1}^{1}(\xi - 1)^2\,\mathrm{d}\xi \\ &= \frac{at}{4\Delta\psi}\cdot\frac{8}{3} = \frac{2}{3}\cdot\frac{a\cdot t}{\Delta\psi}. \end{aligned} \tag{20}$$

- k_{12}:

$$k_{12} = -\frac{at}{4\Delta\psi}\int_{-1}^{1}(\xi^2 - 1)\,\mathrm{d}\xi = -\frac{at}{4\Delta\psi}\cdot\frac{-4}{3} = \frac{1}{3}\cdot\frac{a\cdot t}{\Delta\psi}. \tag{21}$$

In a similar way, the other 14 components can be obtained and the 4×4 elemental conductivity matrix can be composed as

$$\mathbf{K}_\mathrm{e} = \frac{at}{3\Delta\psi}\begin{bmatrix} 2 & 1 & -1 & -2 \\ 1 & 2 & -2 & -1 \\ -1 & -2 & 2 & 1 \\ -2 & -1 & 1 & 2 \end{bmatrix}, \tag{22}$$

where

$$\Delta\psi = \int_{-\tilde{h}}^{\tilde{h}}\frac{1}{\tilde{k}(\chi)}\,\mathrm{d}\chi = \int_{-h}^{h}\frac{1}{(1/\varepsilon)k(y)}\frac{1}{\varepsilon}\,\mathrm{d}y = \int_{-h}^{h}\frac{1}{k(y)}\,\mathrm{d}y. \tag{23}$$

It should be noted here that this element formulation has been derived under the assumptions that all internal angles of the element are equal to 90° and that the thin interphase is parallel to the x-axis. A transformation to more general cases is easy to obtain.

In the special case $\tilde{k} = \text{const}$, the evaluation of $\Delta\psi$ gives

$$\Delta\psi = \int_{-h}^{h}\frac{1}{k(y)}\,\mathrm{d}y = \frac{1}{k}\int_{-h}^{h}\mathrm{d}y = \frac{2h}{k}, \tag{24}$$

and the constant stiffness matrix of a thin element with $k = \text{const}$ is immediately obtained as:

$$\mathbf{K}_\mathrm{e} = \frac{atk}{6h}\begin{bmatrix} 2 & 1 & -1 & -2 \\ 1 & 2 & -2 & -1 \\ -1 & -2 & 2 & 1 \\ -2 & -1 & 1 & 2 \end{bmatrix}. \tag{25}$$

For the evaluation of the right-hand side of equation (5), the boundary integral can be split in the following four contributions:

$$\int_{-h}^{h} wk\frac{\partial T}{\partial x}\bigg|_{x=-a}\begin{bmatrix}-1\\0\end{bmatrix}\mathrm{d}y + \int_{-a}^{a} wk\frac{\partial T}{\partial y}\bigg|_{y=h}\begin{bmatrix}0\\1\end{bmatrix}\mathrm{d}x \tag{26}$$

$$+\int_{-h}^{h} wk\frac{\partial T}{\partial x}\bigg|_{x=a}\begin{bmatrix}1\\0\end{bmatrix}\mathrm{d}y + \int_{-a}^{a} wk\frac{\partial T}{\partial y}\bigg|_{y=-h}\begin{bmatrix}0\\-1\end{bmatrix}\mathrm{d}x. \tag{27}$$

Using the same rescaling relationships as in equations (7) and (8) gives

$$\int_{-\tilde{h}}^{\tilde{h}} w\tilde{k}\varepsilon^2\left(\frac{\partial T}{\partial x}\bigg|_{x=a}\begin{bmatrix}1\\0\end{bmatrix} + \frac{\partial T}{\partial x}\bigg|_{x=-a}\begin{bmatrix}-1\\0\end{bmatrix}\right)\mathrm{d}y \tag{28}$$

$$+\int_{-a}^{a} w\tilde{k}\left(\frac{\partial T}{\partial \chi}\bigg|_{x=\tilde{h}}\begin{bmatrix}0\\1\end{bmatrix} + \frac{\partial T}{\partial \chi}\bigg|_{x=-\tilde{h}}\begin{bmatrix}0\\-1\end{bmatrix}\right)\mathrm{d}\chi, \tag{29}$$

where the integral in equation (28) is of order $O(\varepsilon^2)$ in comparison with the integral in equation (29). Thus, we can approximate the boundary integral as

$$\int_{\Gamma_e} w(k\nabla T)^{\mathrm{T}}\mathbf{n}\,\mathrm{d}\Gamma_e \approx \int_{-a}^{a} w\tilde{k}\left(\frac{\partial T}{\partial \chi}\bigg|_{x=\tilde{h}}\begin{bmatrix}0\\1\end{bmatrix} + \frac{\partial T}{\partial \chi}\bigg|_{x=-\tilde{h}}\begin{bmatrix}0\\-1\end{bmatrix}\right)\mathrm{d}\chi, \quad (30)$$

where the same approximation for the weighting function, i.e. $w = \delta\mathbf{T}_e^{\mathrm{T}}\mathbf{N}_e$, can be introduced. The vector of arbitrary temperatures, i.e. $\delta\mathbf{T}_e^{\mathrm{T}}$, can be canceled with the corresponding expression on the left-hand side of equation (5) (after replacing the weighting function w with its approximation, i.e. $w = \delta\mathbf{T}_e^{\mathrm{T}}\mathbf{N}_e$) and the integral needs to be evaluated for each node along the element boundary. For node 1, the shape function N_1 is equal to one and identically zero for all other nodes. In addition, all other shape functions are identically zero for node 1 (cf. equation (18)). The nodal evaluation of the left-hand side of equation (30) at node 1 can be written as

$$\left(-\tilde{k}\frac{\partial T}{\partial \chi}\right)_{\text{node 1}}, \quad (31)$$

which is equal to the heat flux entering the element at node 1. Similar results can be obtained for all other nodes and the right-hand side of equation (5) can be finally written after rescaling as

$$\int_{\Gamma_e} \mathbf{N}_e(k\nabla T)^{\mathrm{T}}\mathbf{n}\,\mathrm{d}\Gamma_e \approx \begin{Bmatrix} \left(-k\frac{\partial T}{\partial y}\right)_{\text{node 1}} \\ \left(-k\frac{\partial T}{\partial y}\right)_{\text{node 2}} \\ \left(+k\frac{\partial T}{\partial y}\right)_{\text{node 3}} \\ \left(+k\frac{\partial T}{\partial y}\right)_{\text{node 4}} \end{Bmatrix}, \quad (32)$$

which can be assembled with classical elements into the global load vector.

4. Implementation Into a Commercial Code and Example Calculation

4.1. General Model Description

The commercial finite element code Marc® (MSC Software Corporation, Santa Ana, CA, USA) is used for the simulation of the thermal behaviour of thin intermediate layers between two adherends. One of the real strengths of this code (as in the case of the commercial code ABAQUS) is the user subroutine feature which allows the user to substitute his own subroutines for those existing in the code. This feature provides the user with a wide latitude for solving non-standard problems such as the implementation of new finite element formulations. When such a routine is linked to the main code, the user is simply replacing the one which exists in the comercial program using appropriate control setup. The new finite element formulation is implemented as a new heat conductivity matrix by means of a special user subroutine (the so-called uselem routine in Marc®) written in Fortran.

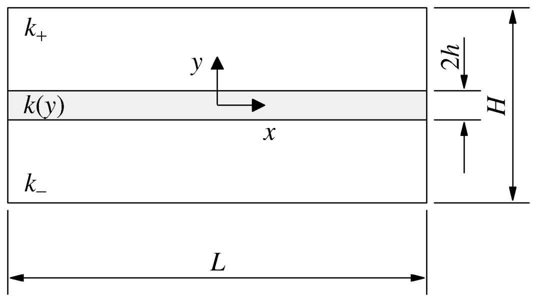

Figure 3. Schematic representation of a thin interphase acting as an adhesive layer.

Both adherends reveal constant material properties for all simulations. In the simulations, the intermediate layer has the thickness $2h = H/100 = 0.01$ while the length of all components is equal to $L = 10$, cf. Fig. 3. We do not assign any specific units since the finite element computation requires only a consistent set of units. One may assign meter, m to lengths, degree Kelvin, K for temperatures and $\frac{\mathrm{W}}{\mathrm{m \cdot K}}$ for conductivities. The two-dimensional FE-mesh is built up of four-node, isoparametric elements (so-called quad4) with bilinear interpolation functions.

Details of the different meshes and the principal idea of the new finite element formulation are shown in Fig. 4. For the classical approach shown in Fig. 4a, several elements (in the present example, eight quad4 elements are used to model the thin layer) over the thickness of the interphase are required to approximate strong material gradients in y-direction. The new finite element formulation should be able to consider such gradients based on its formulation and only a single element is required to reproduce the behaviour of the interphase, cf. Fig. 4b.

As a direct result, the number of elements assigned to the adhesive layer is significantly reduced. In our example, the adhesive elements are reduced by a factor of eight. For a good finite element mesh, the so-called aspect ratio must be considered. This ratio is the quotient between the longest and the shortest element dimensions and is by definition greater than or equal to one. If the aspect ratio is 1, the element is considered to be ideal with respect to this error estimate. Acceptable ranges for the aspect ratio are element and problem dependent, but a rule of thumb is that the ratio should be smaller than 3 for linear elements. As can be seen from Fig. 4b, the approach based on the new finite element formulation allows the application of much larger adherend elements. Thus, not only the number of adhesive elements but also the adherend elements are significantly reduced. It should be noted here that for the new approach, the number of transition elements (cf. Fig. 4a), i.e. the elements with internal angles $\ll 90°$, can be dramatically reduced or even avoided as in our example. This can be interesting for some load cases where these elements exhibit due to their distorted geometry only poor results (so-called skewness).

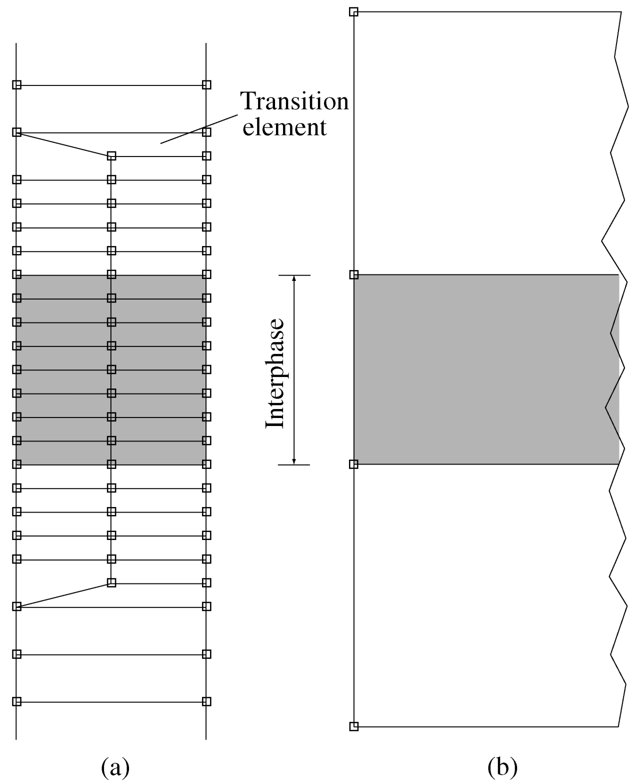

Figure 4. Mesh details: (a) classical approach with eight quad4 elements over the thickness of the interphase; (b) a single new finite element approximating the interphase.

4.2. Results

All numerical simulations have been performed for the same aluminium adherends which exhibit a constant conductivity of 237. Furthermore, it has been assumed that the temperature dependence of all adherend material parameters can be neglected and that no heat sources or sinks are located within the adherends. The different model formulations of the adhesive material are shown in Fig. 5. As can be seen, different parabolic shapes ($k(y) = c_1 + c_2 \cdot y^2$) have been assigned to the adhesive layer in order to simulate changing material properties within the interphase. It should be noted here that within the present study, only a dependency on the vertical, i.e. y, direction has been considered. A constant Dirichlet (temperature) boundary condition of 290 has been prescribed at the bottom ($y = -H/2$) surface (cf. Fig. 3). At the opposite side, a constant Neumann (flux) condition of $+600$ has been assigned to each node.

The temperature distribution over the thickness is shown in Fig. 6. As can be seen from this graphical representation, the formulation of the adhesive layer significantly influences the temperature at the upper boundary ($y = +H/2$): The higher

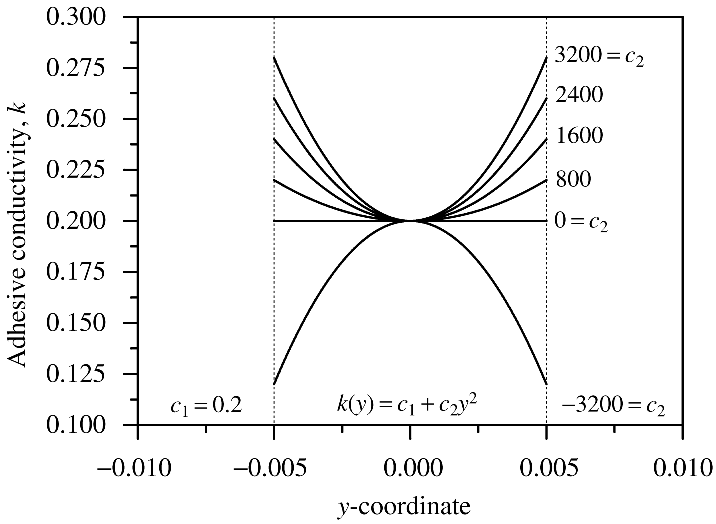

Figure 5. Different parabolic formulations of the adhesive heat conductivity k in dependence of the vertical spatial coordinate y. Parameter c_2 determines the curvature of the parabolic shape (c_1 is constant for all curves).

the coefficient c_2, the lower is the boundary value of the temperature. The same tendency can be observed for the temperature distribution within the interphase, cf. Fig. 6b.

As a direct result of the applied boundary conditions, i.e. prescribed temperature and flux, the temperature at the lower interface ($y = -0.005$) is practically constant for all adhesive conductivity formulations. Only at the upper interface ($y = +0.005$), the influence of the non-linear adhesive behaviour on the temperature is observable. Thus, a reasonable way to investigate the performance of the new finite element implementation under the chosen boundary conditions is to evaluate the temperature $T = T(y = 0.005)$. This temperature for both finite element approaches, i.e. the classical approach with many elements over the thickness and the new interphase element, is shown in Fig. 7. It can be observed that the new finite element formulation which is based on a single element over the adhesive thickness is in perfect coincidence with the classical approach based on 8 elements in the example presented.

5. Discussion and Outlook

It has been shown in the work presented that the new finite element implementation is able to reproduce the same results as the classical approach which is based on a finite element mesh with many elements over the interphase thickness. The new finite element approach is based on the constancy of the heat flux and no assumptions for any specific temperature distribution. The major advantage of the

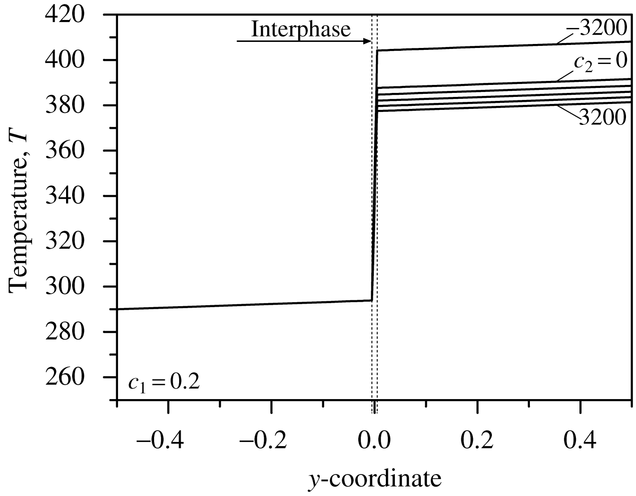

(a)

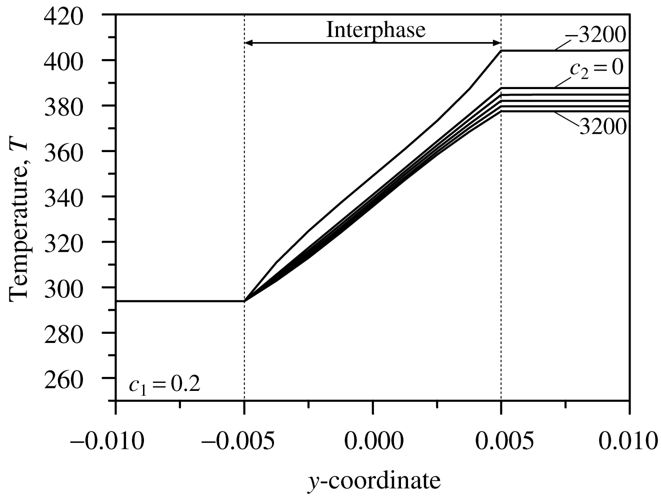

(b)

Figure 6. Temperature distribution: (a) entire thickness of the specimen; (b) within the interphase of thickness $2h = 0.01$.

new approach is that the number of elements and, thus, the number of degrees of freedom is significantly reduced. As a direct result, the computation is much faster and the generation of the finite element mesh is less time-consuming. However, it should be noted here that the temperature distribution within the interphase is no longer available in the post-processor if only a single new element over the thickness is used. This stems from the fact that the temperature values are computed at the nodes and these values can be graphically displayed in the post-processor. Introduction of the interphase elements means that there are no more nodes in the range

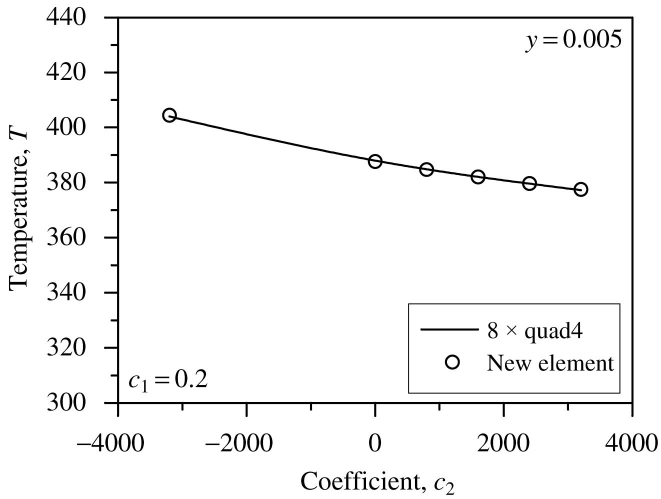

Figure 7. Comparison of the performance of the new finite element formulation by evaluating the temperature at the upper interface, i.e. $y = 0.005$.

$-h < y < h$ (cf. Fig. 1) and a detailed temperature distribution cannot be displayed. Only an evaluation of equation (18) would yield this result for the single element approach.

Further numerical testing of the new element by adjusting the horizontal ($2a$) and vertical ($2h$) dimensions revealed that the new element is not sensitive to the aspect ratio under similar boundary conditions and internal angles equal to 90°. Considerable errors can only be expected if a temperature gradient in the x-direction occurs since the approximation of equation (10) would be violated.

It should be noted here that the classical approach with linear shape functions would give for a rectangular element with dimensions $2a$ and $2h$:

$$\frac{k}{3}\cdot\frac{t}{ah}\begin{bmatrix} a^2+h^2 & \frac{1}{2}a^2-h^2 & -\frac{1}{2}a^2-\frac{1}{2}h^2 & -a^2+\frac{1}{2}h^2 \\ \frac{1}{2}a^2-h^2 & a^2+h^2 & -a^2+\frac{1}{2}h^2 & -\frac{1}{2}a^2-\frac{1}{2}h^2 \\ -\frac{1}{2}a^2-\frac{1}{2}h^2 & -a^2+\frac{1}{2}h^2 & a^2+h^2 & \frac{1}{2}a^2-h^2 \\ -a^2+\frac{1}{2}h^2 & -\frac{1}{2}a^2-\frac{1}{2}h^2 & \frac{1}{2}a^2-h^2 & a^2+h^2 \end{bmatrix}, \quad (33)$$

which converges in the special case $h \ll a$ (neglecting h inside the matrix) to equation (25). Based on this theoretical derivation, it can be concluded that a single classical element can be used for non-homogeneous interphases if the element is thin ($h \ll a$) and if the average, i.e. integral, conductivity over the thickness is computed. However, it must be highlighted that in the case of the classical element, the computation of the average conductivity must be done and assigned manually in the pre-processor of the finite element code. The advantage of the new element formulation becomes clear in the case of conductivity changes along the x-axis (i.e. a variation in the x-direction with each element) and if the geometry of the element exhibits internal angles not equal to 90°. In such cases, a manual computation of the average conductivity is no longer possible from a practical point of view.

The theoretical derivations presented within this study were based on the assumption that the adhesive layer was only dependent on the vertical (y) spatial coordinate (cf. equation (12)) and that the layer was heat resistant compared to the adherend properties (cf. equation $(8)_2$). In our future research work, more complicated and interesting cases, e.g. that the adhesive conductivity is a function of the temperature, will be investigated and implemented in the code.

Acknowledgement

G. Mishuris has been supported by a Marie Curie Transfer of Knowledge Fellowship of the European Community's Sixth Framework Programme under contract number MTKD-CT-2004-509809.

References

1. F. Rosselli and P. Carbutt, *SAMPE J.* **37**, 7 (2001).
2. A. R. Akisanya and N. A. Fleck, *Int. J. Solids Struct.* **34**, 1645 (1997).
3. J. Dundurs and M. Comninou, *Mech. Composite Mater.* **15**, 387 (1979).
4. F. Erdogan, in: *Proceedings of the First International Conference on Damage and Failure of Interfaces*, Vienna, Austria, pp. 3–36 (1997).
5. H. H. Yu and M. Y. He, *Acta Mater.* **49**, 93 (2001).
6. G. Mishuris, A. Öchsner and G. Kuhn, *CMC — Computers Materials & Continua* **2**, 227 (2005).
7. G. Mishuris, W. Miszuris and A. Öchsner, *Mater. Sci. Forum* **553**, 87 (2007).
8. G. Mishuris, W. Miszuris and A. Öchsner, *Mater. Sci. Forum* **553**, 93 (2007).
9. R. D. Adams and N. A. Peppiatt, *J. Strain Anal.* **9**, 185 (1974).
10. R. D. Adams and W. C. Wake, *Structural Adhesive Joints in Engineering*. Elsevier, London (1984).
11. J. C. J. Schellekens, Computational strategies for composite structures, *PhD Thesis*, Faculty of Civil Engineering, Delft University, Delft, The Netherlands (1993).
12. A. Gens, I. Carol and E. E. Alonso, *Comput. Geotech.* **7**, 133 (1988).
13. R. E. Goodman, R. L. Taylor and T. L. Brekke, *ASCE J. Soil Mech. Found. Div.* **94**, 637 (1968).
14. J. G. Rots, Computational modeling of concrete fracture, *PhD Thesis*, Faculty of Civil Engineering, Delft University, Delft, The Netherlands (1988).
15. M. F. S. F. de Moura, J. P. M. Goncalves, A. T. Marques and P. M. S. T. de Castro, *J. Composite Mater.* **31**, 1462 (1997).
16. F. P. Incropera, D. P. DeWitt, T. L. Bergman and A. S. Lavine, *Fundamentals of Heat and Mass Transfer*. Wiley, New York, NY (2006).
17. W. M. Rohsenow, J. P. Hartnett and Y. I. Cho, *Handbook of Heat Transfer*. McGraw-Hill, New York, NY (1998).
18. C. A. Brebbia, J. C. F. Felles and J. C. F. Wrobel, *Boundary Element Techniques: Theory and Applications*. Springer-Verlag, Berlin (1984).
19. G. R. Buchanan, *Finite Element Analysis*. McGraw-Hill, New York, NY (1995).

Defect and Diffusion Forum Vols. 273-276 (2008) pp 394-399
online at http://www.scientific.net

Online available since 2008.02.11

Evaluation of Transmission Conditions for Thin Reactive Heat-Conducting Interphases

Gennady Mishuris[1,a], Wiktoria Miszuris[1,b], Andreas Öchsner[2,c]

[1]Department of Mathematics, Rzeszow University of Technology, Rzeszow, Poland
[2]Department of Applied Mechanics, Technical University of Malaysia, Skudai, Malaysia

[a]miszuris@prz.rzeszow.pl, [b]victory@prz.rzeszow.pl, [c]aoechsner@fkm.utm.my

Keywords: heat transfer, thin layers, nonclassical transmission conditions

Abstract. Imperfect transmission conditions modelling a thin reactive intermediate layer between two bonded materials in a dissimilar strip are derived in this paper. The interphase material is assumed to be heat-resistant and situated in a thin rectangular domain between the main materials. Different types of the interphase are investigated in detail: constant and temperature dependent sources.

Introduction

Thin interphases are commonly used in modern technology [1]. An inhomogeneous structure obtained in such a way may exhibit a wider variety of thermal and mechanical properties. On the other hand, finite element modeling of composites with thin interphases is still a difficult numerical task as it requires high inhomogeneity of the constructed mesh which can lead to a loss of accuracy and even numerical instability. This explains the high interest to model the interphases as a zero thickness object described by specific so-called transmission conditions along the infinitesimal interface. In the case of constant heat conductivity, the problem has been completely solved in [2], where the general approach was developed independent of the range of the heat conductivity of the thin (in comparison with the matched adherents) interphase. Such interphases often manifest clear nonlinear or homogeneous properties connected with the manufacturing and exploitation processes [1] and the respective transmission conditions have been evaluated in [4]. In the scope of this paper, we consider other important case [5] when the nonlinearity is assigned to the source term and defines a so-called reactive interphase. Again, we concentrated our interest to a heat-resistant interphase which is the most important case from an application point of view. We will apply the same approach as it has been done in [3, 4, 6, 7]. We also refer here to other methods to deal with thin interphases [8, 9] as well as to construct effective homogenesed properties of composite materials [10, 11, 12].

Problem formulation

Let us consider a bimaterial structure matched together with a thin intermediate layer of the constant thickness $2h$ (cf. Fig. 1) and length $2a$. The heat transfer equations are satisfied in the surrounding materials:

$$\nabla k_\pm \nabla T_\pm + Q_\pm = \rho_\pm c_\pm \frac{\partial T_\pm}{\partial t}, \quad (x,y) \in \Omega_\pm, \tag{1}$$

where $T_\pm$ and $Q_\pm$ are temperatures and the thermal sources within the respective materials occupied domains $\Omega_\pm$ while $k_\pm$, $c_\pm$ and $\rho_\pm$ are their thermal conductivities, heat capacities and densities, respectively. We are not going to solve the problem but to derive the transmission conditions modelling the heat-resistant layer. As a result, we do not need to accurately describe here properties of the surrounding materials domains $\Omega_\pm$.

Within the thin interphase, a similar equation is given by

$$k\Delta T + Q = \rho c \frac{\partial T}{\partial t}, \quad (x, y) \in \Omega, \tag{2}$$

where T and Q are the temperature and the thermal sources within the interphase and $c = c(x, y, t, T), \rho = \rho(x, y, t, T)$, which can depend on the space and time variables as well as the unknown temperature. We also assume for simplicity that $k = const$. As usual, the heat flux inside the interphase is defined by Fourier's law:

$$\mathbf{q} = -k\nabla T.$$

Transmission conditions along the material interfaces $\Gamma_\pm = \{(x, y), x \in (-a, a), y = \pm h\}$ between the domains Ω and $\Omega_\pm$, respectively, (see Fig.1) should be written in the form:

$$[\mathbf{n} \cdot \mathbf{q}]|_{\Gamma_+} = 0, \quad [T]|_{\Gamma_+} = 0, \tag{3}$$

$$[\mathbf{n} \cdot \mathbf{q}]|_{\Gamma_-} = 0, \quad [T]|_{\Gamma_-} = 0. \tag{4}$$

Here, as usual, $[f]|_\Gamma = f(x, \alpha+) - f(x, \alpha-)$ is the jump of the function f across the interface $\Gamma = \{(x, y), x \in (-a, a), y = \alpha\}$.

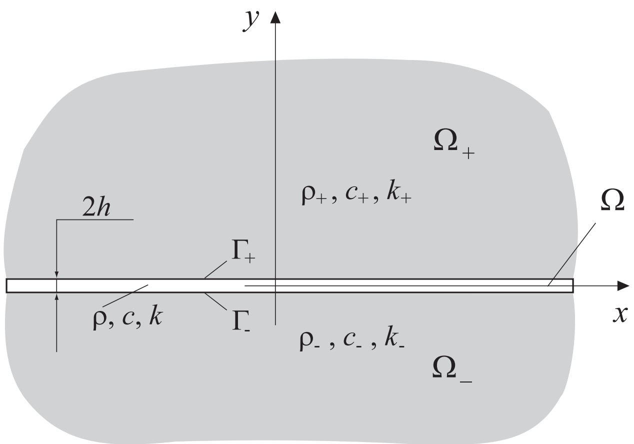

Fig. 1: Bimaterial structure with a thin reactive interphase Ω.

Assumption 1. We consider throughout this paper that the domain

$$\Omega = \{(x, y) : y \in (-h, h), \quad x \in (-a, a)\}$$

representing the intermediate interphase is thin enough in comparison with characteristic sizes of both surrounding adherends $\Omega_\pm$ (see Fig. 1), thus $h = \epsilon\tilde{h}$ ($\epsilon << 1$).

Assumption 2. The next crucial point for this analysis is that the interphase itself is heat-resistant so that the thermal conductivity of the intermediate layer is much smaller than those of the bonded materials. In other words the ratios $k/k_\pm$ are of the same order of ϵ as it has been appeared for the interphase thickness:

$$k = \epsilon\tilde{k}. \tag{5}$$

Assumption 3. Finally, we want to allow that the thermal conductivity of the interface k, sources Q and the multiplicator ρc are smooth but may be fast changing functions with respect to the interphase thickness:

$$Q = \frac{1}{\epsilon}\,\tilde{Q}(T), \quad \rho_c \equiv \rho(x, y/\epsilon, t, T)\cdot c(x, y/\epsilon, t, T), \quad \rho_c/\tilde{k} \sim 1. \tag{6}$$

After appropriate rescalling of the space variables as shown in Fig. 2, we use the standard asymptotic approach applied in case of thin domains following for procedure given in [13]:

$$y = \epsilon\xi, \quad (x, y) \in \Omega.$$

Then, Eq. (2) can be finally rewritten in an equivalent form as:

$$\frac{1}{\epsilon^2}\tilde{k}\frac{\partial^2}{\partial\xi^2}\tilde{T} + \tilde{k}\frac{\partial^2}{\partial x^2}\tilde{T} + \frac{1}{\epsilon^2}\,\tilde{Q} = \frac{1}{\epsilon}\tilde{\rho}_c\frac{\partial\tilde{T}}{\partial t}, \quad \xi \in (-\tilde{h}, \tilde{h}), \quad x \in (-a, a), \tag{7}$$

where

$$\tilde{T}(x, \xi, t) \equiv T(x, y, t), \quad \tilde{\rho}_c \equiv \rho_c(x, \xi, t, \tilde{T}).$$

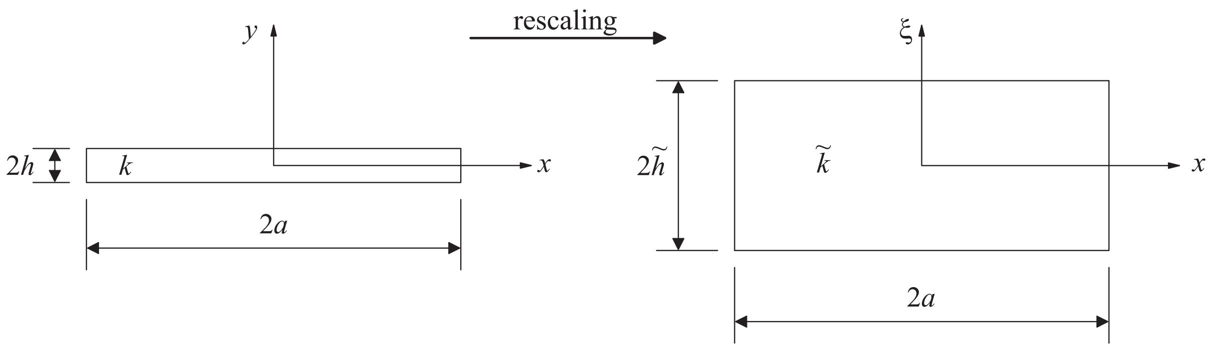

Fig. 2: Thin interphase domain before and after rescalling.

We will seek for the solution within the interphase layer in the form of an asymptotic expansion:

$$\tilde{T}(x, \xi, t, \epsilon) = \tilde{T}_0(x, \xi, t) + \epsilon\tilde{T}_1(x, \xi, t) + \epsilon^2\tilde{T}_1(x, \xi, t) + ... \tag{8}$$

and the heat flux is calculated from the asymptotic expansion:

$$\tilde{\mathbf{q}}(x, \xi, t, \epsilon) = -\tilde{k}\,[\epsilon\frac{\partial}{\partial x}, \frac{\partial}{\partial\xi}]\tilde{T} = -\tilde{k}[0, 1]\frac{\partial}{\partial\xi}\tilde{T}_0 + O(\epsilon), \quad \epsilon \to 0. \tag{9}$$

Then from Eq. (7) we receive a consequence of the boundary value problems within the interphase:

$$\tilde{k}\frac{\partial^2}{\partial\xi^2}\tilde{T}_0 + \tilde{Q}(\tilde{T}_0) = 0, \quad \xi \in (-\tilde{h}, \tilde{h}), \tag{10}$$

$$\tilde{k}\frac{\partial^2}{\partial\xi^2}\tilde{T}_j + \tilde{Q}'(\tilde{T}_0)T_j = \mathcal{R}_j(x,\xi,t,\tilde{T}_0,...,\tilde{T}_{j-1}), \quad j=1,2,..., \quad \xi \in (-\tilde{h},\tilde{h}). \tag{11}$$

It is important to note an important difference between Eqs. (10) and (11). Namely, the first one is nonlinear while Eqs. (11) which correspond to the next terms of the asymptotic expansion are linear with respect to functions $\tilde{T}_j$. Note here that the derivative with time appears only in the right hand side of Eqs. (11).
Transmission conditions (3) and (4) can be rewritten in new notations in the forms:

$$T_+(x,\epsilon\tilde{h},t) = \tilde{T}_0(x,\tilde{h},\tau) + \epsilon\tilde{T}_1(x,\tilde{h},t) + \epsilon^2\tilde{T}_2(x,\tilde{h},t) + ..., \tag{12}$$

$$T_-(x,-\epsilon\tilde{h},t) = \tilde{T}_0(x,-\tilde{h},t) + \epsilon\tilde{T}_1(x,-\tilde{h},t) + \epsilon^2\tilde{T}_2(x,-\tilde{h},t) + ..., \tag{13}$$

$$q_+(x,\epsilon\tilde{h},t) = -\tilde{k}\left(\frac{\partial}{\partial\xi}\tilde{T}_0(x,\tilde{h},t) + \epsilon\frac{\partial}{\partial\xi}\tilde{T}_1(x,\tilde{h},t) + ...\right), \tag{14}$$

$$q_-(x,-\epsilon\tilde{h},t) = -\tilde{k}\left(\frac{\partial}{\partial\xi}\tilde{T}_0(x,-\tilde{h},t) + \epsilon\frac{\partial}{\partial\xi}\tilde{T}_1(x,-\tilde{h},t) + ...\right), \tag{15}$$

where $q_\pm = [0,1]\mathbf{q}_\pm$ are the second components of the vector of flux in the respective domains.

Expanding the left-hand sides of (12)-(15) and right-hand sides of (14)-(15) in Taylor series, we can receive the consequence of the transmission conditions. We restrict ourself in this paper only to find the main asymptotic term, i.e. $\tilde{T}_0$, of the expansion (8). As a result, we can stay in Eqs. (12)-(15) only with the terms:

$$T_+(x,0,t) = \tilde{T}_0(x,\tilde{h},t), \quad T_-(x,0,t) = \tilde{T}_0(x,-\tilde{h},t), \quad x \in (-a,a), \tag{16}$$

$$\tilde{k}\frac{\partial}{\partial\xi}\tilde{T}_0(x,\tilde{h},t) = -q_+(x,0,t), \quad \tilde{k}\frac{\partial}{\partial\xi}\tilde{T}_0(x,-\tilde{h},t) = -q_-(x,0,t), \quad x \in (-a,a). \tag{17}$$

Integrating Eq. (10), we obtain:

$$\left(\tilde{k}\frac{\partial}{\partial\xi}\tilde{T}_0(x,\xi,t)\right)^2 = C(x,t) - \Phi(\tilde{T}_0(x,\xi,t)), \quad \xi \in (-\tilde{h},\tilde{h}), \tag{18}$$

where we have introduced the notation:

$$\Phi(\tilde{T}) = 2\tilde{k}\int_{T_-}^{\tilde{T}}\tilde{Q}(z)dz. \tag{19}$$

Comparing (17) with (18), we immediately receive $C(x,t) = q_-^2(x,0,t)$ and additionally we have the first transmission condition:

$$q_+^2(x,0,t) - q_-^2(x,0,t) + \Phi(T_+(x,0,t)) = 0, \quad x \in (-a,a). \tag{20}$$

Assumption. In the following, we assume that the temperature is a monotonic function within the interphase with respect to the ξ-direction. In other words

$$\tilde{T}_0'(x,\xi,t) \neq 0, \quad x \in (-a,a), \quad \text{as a result:} \quad q_+(x,0,t)\cdot q_-(x,0,t) > 0. \tag{21}$$

Then we can conclude that

$$q_-^2(x,0,t) > \Phi(T_0(x,\xi,t)), \quad x \in (-a,a). \tag{22}$$

Then Eq. (18) can be rewritten in an equivalent form:

$$\tilde{k}\frac{\partial}{\partial\xi}\tilde{T}_0(x,\xi,t) = -q_-(x,0,t)\sqrt{1-\Phi(\tilde{T}_0(x,\xi,t))/q_-^2}, \quad \xi \in (-\tilde{h},\tilde{h}). \tag{23}$$

It is important to note that if $\Phi(T_+) = 0$, i.e. that the sources in average sense are compensated within the interphace, then $q_+(x,0,t) = q_-(x,0,t)$, as it follows from (20).

Now, it remains to consider the ordinary differential equation (23) with respect to the variable ξ, while x and t are the only parameters. Let us introduce an auxiliary function:

$$\Psi(q_-,\tilde{T}) = \int\limits_{T_-}^{\tilde{T}} \frac{dz}{\sqrt{1-\Phi(z)/q_-^2}}. \tag{24}$$

Then the solution to (23) can be written in the general form:

$$\tilde{k}\Psi(q_-(x,0,t),\tilde{T}_0(x,\xi,t)) = -(\xi+\tilde{h})q_-(x,0,t), \quad \xi \in (-\tilde{h},\tilde{h}). \tag{25}$$

The second transmission condition can be immediately extracted from Eq. (25):

$$\tilde{k}\Psi(q_-(x,0,t),T_+(x,0,t)) = -2\tilde{h}q_-(x,0,t). \tag{26}$$

Unfortunately, it is not possible to write the transmission conditions (20) and (26) in terms of simple functions. Below, we present some specific examples where the conditions can be written in closed forms.

Special case 1. Let the source being essential but independent on the temperature distribution $Q = \epsilon^{-1}Q_0$. Then, function $\Phi(\tilde{T})$ from (19) is calculated as $\Phi(\tilde{T}) = 2\tilde{k}Q_0(\tilde{T}-T_-)$ and the first transmission condition can be rewritten in the form:

$$q_+^2(x,0,t) - q_-^2(x,0,t) = -2\tilde{k}\,Q_0\big(T_+(x,0,t) - T_-(x,0,t)\big), \quad x \in (-a,a), \tag{27}$$

whereas the second transmission condition takes after some algebra the following form:

$$q_+(x,0,t) - q_-(x,0,t) = 2\tilde{h}Q_0, \quad x \in (-a,a). \tag{28}$$

Taking into account Eq. (28), the first transmission condition can be also additionally simplified to obtain:

$$T_+(x,0,t) - T_-(x,0,t) = -\frac{\tilde{h}}{\tilde{k}}\left(q_+(x,0,t) + q_-(x,0,t)\right), \quad x \in (-a,a). \tag{29}$$

Special case 2. Let $Q = \epsilon^{-1}Q_0 T$, then $\Phi(\tilde{T}) = \tilde{k}Q_0(\tilde{T}^2 - T_-^2)$. Note here that a power law, e.g. $Q = cT^m$, is very common for low temperatures [5] for small temperature increments. The first transmission condition (20) can be now written in the form:

$$q_+^2(x,0,t) - q_-^2(x,0,t) = -\tilde{k}Q_0\left(T_+^2(x,0,t) - T_-^2(x,0,t)\right), \quad x \in (-a,a). \tag{30}$$

After some algebra, the second transmission condition (26) in the case $Q_0 > 0$ can be rewritten in the following form:

$$\arcsin\frac{T_+\sqrt{\tilde{k}Q_0}}{\sqrt{q_+^2+\tilde{k}Q_0T_+^2}} - \arcsin\frac{T_-\sqrt{\tilde{k}Q_0}}{\sqrt{q_-^2+\tilde{k}Q_0T_-^2}} = -2\tilde{h}\sqrt{\frac{Q_0}{\tilde{k}}}\,\mathrm{sign}\big(q_-(x,0,t)\big), \quad x \in (-a,a). \tag{31}$$

In case when $Q_0 < 0$ condition (26) is written in other form:

$$\ln \frac{|q_+| + T_+\sqrt{-Q_0\tilde{k}}}{|q_-| + T_-\sqrt{-Q_0\tilde{k}}} = -2\tilde{h}\sqrt{\frac{-Q_0}{\tilde{k}}}\,\mathrm{sign}\big(q_-(x,0,t)\big), \quad x \in (-a,a). \tag{32}$$

Note that in both cases the standard heat-resisting interface [4] will be obtained if one assumes $Q_0 \to 0$ from the derived transmission conditions:

$$q_+ = q_-, \quad T_+ - T_- = -\frac{2\tilde{h}}{\tilde{k}} q_\pm, \quad x \in (-a,a). \tag{33}$$

Concluding remarks

Let us underline again that the second transmission condition (26) (and consecutively, the conditions (28), (32), (31) and (32)) have been justified only under additional assumption that the temperature is monotonic in ξ-direction inside the interphase. Thus if one use the transmission conditions for numerical simulation one needs to check at the end of computations the validity of the assumption (21). If this is not fulfilled, additional analysis is necessary.

However, even if the assumption is true, it is highly important to know the range of the material parameters where the condition can be applied, and when it is necessary to take some specific effects (for example high time gradient) into account. This investigation will be done in the next paper presented in this issue by very accurate FEM simulations.

Acknowledgments

G. Mishuris has been supported by a Marie Curie Transfer of Knowledge Fellowship of the European Community's Sixth Framework Programme under contract number MTKD-CT-2004-509809.

References

[1] F. Rosselli, P.Carbutt: Sampe J. Vol. 37 (2001), p. 7

[2] Y. Hashin: J. Appl. Phys. Vol. 89 (2001), p. 2262

[3] G. Mishuris, A. Öchsner: Compos. Struct. Vol. 68 (2005), p. 409

[4] G. Mishuris, W. Miszuris, A. Öchsner: Mater. Sci. Forum Vol. 553 (2007), p. 87

[5] C.L. Tsai, H. Weinstock, W.C. Overton, Jr: Cryogenics Vol. 18 (1978), p. 562

[6] G. Mishuris, A. Öchsner, G. Kuhn: CMC - Comput. Mater. Continua Vol. 2 (2005), p. 227

[7] G. Mishuris, A. Öchsner: Arch. Mech. Vol. 57 (2005), p. 157

[8] Y. Benveniste, T. Miloh: Mech. Mater. Vol. 33 (2001), p. 309

[9] Z. Hashin: J Mech Phys. Solids Vol. 50 (2002), p. 2509

[10] A.H. Nayfeh: J. Appl. Mech. Vol. 42 (1975), p. 399.

[11] Y. Benveniste: Mech. Mater. Vol. 4 (1985), p. 197

[12] Z. Hashin: Mech. Mater. Vol. 8 (1990), p. 3333

[13] A.B. Movchan, N.V. Movhan: *Mathematical Modelling of Solids of with Nonregular Boundaries* (CRC Press, Boca Raton 1995)

Defect and Diffusion Forum Vols. 273-276 (2008) pp 400-405
online at http://www.scientific.net

Online available since 2008.02.11

Finite Element Verification of Transmission Conditions for Thin Reactive Heat-Conducting Interphases

Andreas Öchsner[1,a], Wiktoria Miszuris[2,b]

[1]Department of Applied Mechanics, Technical University of Malaysia, Skudai, Malaysia
[2]Department of Mathematics, Rzeszow University of Technology, Rzeszow, Poland

[a]aoechsner@fkm.utm.my, [b]victory@prz.rzeszow.pl

Keywords: heat transfer, thin layers, nonclassical transmission conditions, finite element method

Abstract. Imperfect transmission conditions modelling a thin reactive 2D intermediate layer between two bonded materials in a dissimilar strip have been derived and analytically analysed in another paper of this issue. In this paper, the validity of these transmission conditions for heat conduction problems has been investigated due to the finite element method (FEM) for two formulations of a reactive layer: namely, based on a constant and a temperature-dependent source or sink formulation. It is shown that the accuracy of the transmission conditions is excellent for the investigated examples.

Introduction

Thin films, e.g. adhesive layers, are nowadays an important part of technological processes and components [1]. As an example, adhesive layers allow for joining materials with essentially different properties at very high quality. The application of such hybrid structures in safety-relevant applications requires a highly accurate and efficient prediction of their physical behaviour, which necessitates the development of robust simulation models and techniques based on, and verified by, appropriate experimental procedures.

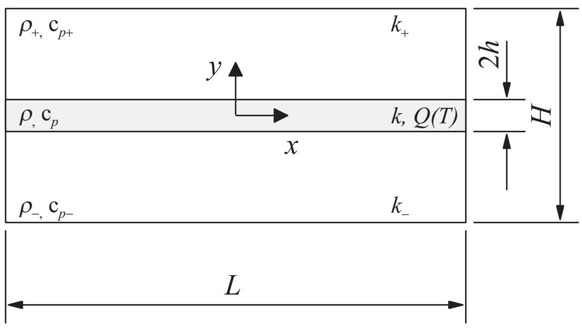

Fig. 1: Schematic representation of the problem.

Transmission conditions for 2D heat conduction problems without reaction were investigated in [2, 3]. In the scope of this paper, imperfect transmission conditions applied to a reactive thin heat-resistant layer in a hybrid model structure (cf. Fig. 1) are going to be numerically investigated in order to verify the applicability and accuracy of the analytical relations for reactive conduction problems.

Finite Element Modelling

The commercial finite element code MSC.Marc is used for the simulation of the thermal behaviour of the modelling thin intermediate layer between two adherends. Both adherends reveal constant material properties for all simulations. It should be noted here that the theoretical derivation of the transmission conditions has been performed under the precondition that the conductivity of the thin interphase is much smaller (i.e. a heat-resistant layer) than the conductivities of the adherends. A reaction in the interphase is modelled as a thermal heat source or sink. The source or sink formulation is implemented by means of a special user subroutine (flux) written in FORTRAN. The application of this subroutine requires a transient solution in order to incorporate the source expression. However, only the steady-state solution (for the given parameters, this solution is obtained in all investigated cases for $2 \cdot 10^5$ s) will be discussed in the following. In the simulations, the intermediate layer has the thickness $2h = H/100 = 0.01$ while the length of all components is equal to $L = 10$. The two-dimensional FE-mesh is built up of four-node, isoparametric elements with bilinear interpolation functions. In order to cover possible edge effects [4], a strong mesh refinement is performed near the free surface of the interphase. Further details of the finite element mesh can be found in [5]. In addition, the mesh is generated in such a way that it is possible to evaluate the temperatures and fluxes along the axes of geometrical symmetry, and along both interfaces (i.e. the line or surface where the thin layer and the adherends are in contact) as well as along lines perpendicular to the interfaces.

Results

All numerical simulations have been performed for the same aluminium adherends which reveal a constant conductivity of $k_{\pm} = 237 \, \frac{\mathrm{W}}{\mathrm{m \cdot K}}$ at 300 K, a mass density of $\varrho_{\pm} = 2698.8 \, \frac{\mathrm{kg}}{\mathrm{m}^3}$ and a specific heat of $c_{\pm} = 898.2 \, \frac{\mathrm{J}}{\mathrm{kg \cdot K}}$. Furthermore, it has been assumed that the temperature dependence of all adherend material parameters can be neglected and that no heat sources or sinks are located within the adherends.

Constant source The following examples refer to a steady-state solution where constant Dirichlet boundary conditions have been prescribed at the top ($y = +H/2$) and bottom ($y = -H/2$) surface (cf. Fig. 1). It could been shown in [3] that for such uniform boundary conditions, no edge effects at the free surface can be observed and that the verification of the transmission conditions can be done based along any arbitrary line $x = \text{const}$. The thin interphase has been assumed to be made of an epoxy resin ($k = 0.2 \, \frac{\mathrm{W}}{\mathrm{m \cdot K}}$, $\varrho = 1200 \, \frac{\mathrm{kg}}{\mathrm{m}^3}$, $c = 790 \, \frac{\mathrm{J}}{\mathrm{kg \cdot K}}$) which exhibits different values of its constant source and sink formulation:

$$Q = \pm c \,. \tag{1}$$

In the case of such a constant source formulation, it could be shown in another paper of this issue that the first (1^{st}TC) and second transmission condition (2^{nd}TC) can be obtained as

$$q_+^2(x,+h) - q_-^2(x,-h) = -2kQ(T_+(x,+h) - T_+(x,-h)) \,, \tag{2}$$

and

$$q_+(x,+h) - q_-(x,-h) = 2hQ \,, \tag{3}$$

where the values of the temperature and the heat flux in y-direction at the interface, i.e. $y = \pm h$, are evaluated. Figure 2 illustrates the shape of the temperature profile perpendicular to the interphase for $x = 0$. In the case that no source or think is acting, i.e. $Q = 0$, a linearly changing temperature distribution is obtained. A heat source ($Q > 0$) results in an increase of the temperature in the interphase and a deviation from the linear distribution while a heat think ($Q < 0$) inverts this effect.

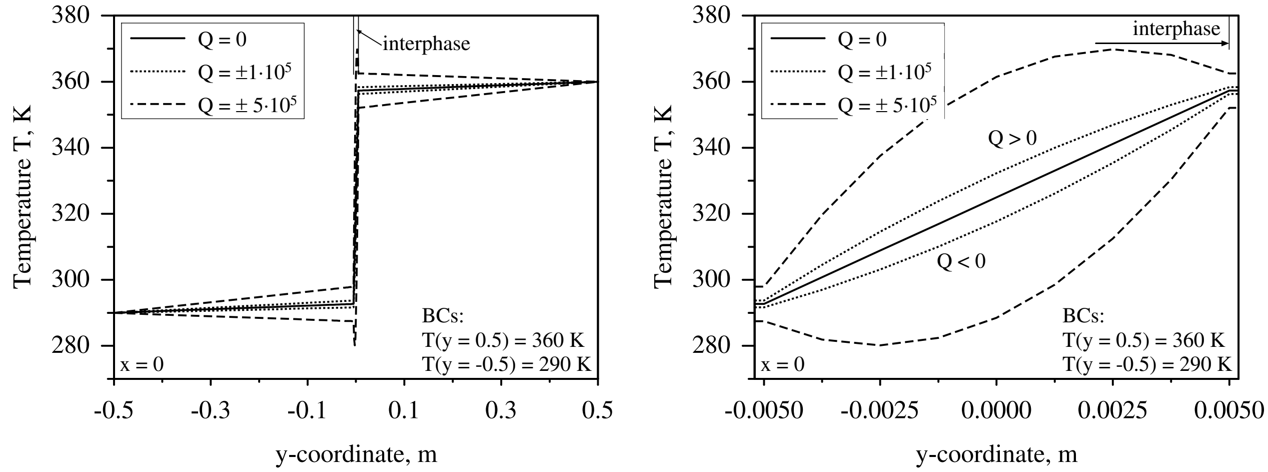

Fig. 2: Temperature distribution perpendicular to the interphase (along the line $x = 0$) for different formulations of the source.

In the case that no heat sources or sinks are present, thermal equilibrium demands that the heat flux q_y is constant over the thickness, cf. Fig. 3 solid line. A heat source or think, i.e. energy addition to or substraction from the system, results in a non-uniform distribution (some kind of z-shape) of the vertical heat flux.

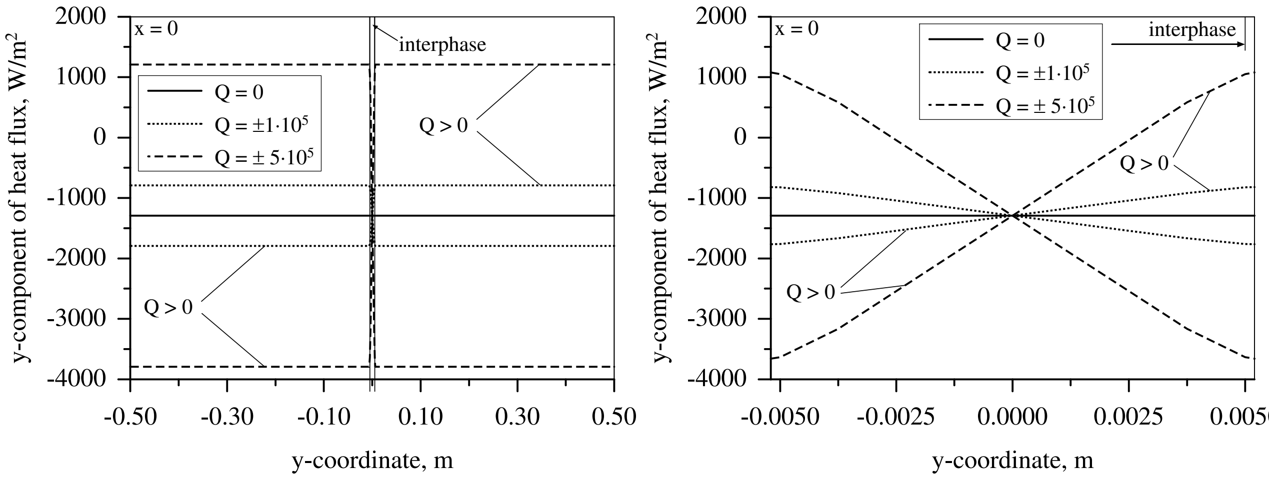

Fig. 3: Distribution of the heat flux perpendicular to the interphase (along the line $x = 0$) for different formulations of the source.

It should be noted here that the jump of the heat flux q_y can be checked based on a simply energy balance (which is equivalent to the 2[nd] TC), i.e. the fluxes (heat transfer rate per unit area perpendicular to the direction of the transfer) at the interface ($y = \pm h$) in relation to the source (energy rate per unit volume) by computing $|q_+ - q_+| = |Q| \cdot 2h$. In the scope of a finite element analysis where the heat flux is evaluated at the integration points, it is better to take the values of the heat flux at $y = \pm H/2$ since the values at $y = \pm h$ are extrapolated from the integration points and averaged with the surrounding values.

Table 1 presents the verification of the transmission conditions (cf. Eqs. (2)-(3)) along the line $x = 0$ by independently extracting the right and left hand side of the equations from FEM evaluation. The absolute value of the error has been obtained by calculating the difference of the LHS and RHS and relating this difference to the RHS of the respective transmission condition. As can be seen for different formulations of the source, the coincidence is practically perfect. It should be noted here that the transmission conditions work very good in the case $Q = \pm 5 \cdot 10^{-5}$ where a non-monotonic temperature distribution is obtained (cf. Fig. 2). This was one of the conditions for the derivations of the respective transmission conditions.

Q	LHS 1^{st}TC	RHS 1^{st}TC	error	LHS 2^{nd}TC	RHS 2^{nd}TC	error
0	0	0	0	0	0	0
$+1 \cdot 10^5$	$-2.584126337 \cdot 10^6$	$-2.5841200 \cdot 10^6$	$\sim 10^{-6}$	1000.004	1000.000	$\sim 10^{-6}$
$-1 \cdot 10^5$	$2.584126337 \cdot 10^6$	$2.5841200 \cdot 10^6$	$\sim 10^{-6}$	-1000.004	-1000.000	$\sim 10^{-6}$
$+5 \cdot 10^5$	$-1.292060000 \cdot 10^7$	$-1.2920600 \cdot 10^7$	~ 0	5000.000	5000.000	~ 0
$-5 \cdot 10^5$	$1.292060000 \cdot 10^7$	$1.2920600 \cdot 10^7$	~ 0	-5000.000	-5000.000	~ 0

Table 1: Verification of the transmission condition validity along the line $x = 0$ for different values of the constant source or sink, cf. Eqs. (2) and (3).

Linear temperature dependence of the source The following examples refer to a steady-state solution where boundary conditions and materials properties are chosen as in the previous example. The thin interphase exhibits now different formulations of temperature-dependent sources and sinks in the form:

$$Q = \pm c \cdot T \,. \tag{4}$$

In the case of a linear temperature dependency, the the first (1^{st}TC) can be obtained as

$$q_+^2(x, +h) - q_-^2(x, -h) = -kQ(T_+^2(x, +h) - T_+^2(x, -h)) \,. \tag{5}$$

The second transmission condition (2^{nd}TC) can be written for the case of a source ($Q > 0$) as

$$\arcsin \frac{T_+\sqrt{kQ}}{\sqrt{q_+^2 + kQT_+^2}} - \arcsin \frac{T_-\sqrt{kQ}}{\sqrt{q_-^2 + kQT_-^2}} = -2h\sqrt{\frac{Q}{k}} \cdot \mathrm{sign}(q_-) \,, \tag{6}$$

and in the case of a sink ($Q < 0$) as

$$\ln \frac{|q_+| + T_+\sqrt{-Qk}}{|q_-| + T_-\sqrt{-Qk}} = -2h\sqrt{\frac{-Q}{k}} \cdot \mathrm{sign}(q_-). \tag{7}$$

The basic characteristic of the temperature (cf. Fig. 4) and flux distribution (cf. Fig. 5) perpendicular to the interphase is the same as in the previous example: A heat source ($Q > 0$) results in an increase of the temperature in the interphase and a deviation from the linear distribution ($Q = 0$) while a heat think ($Q < 0$) inverts this effect while the distribution of the flux takes again a z-shape. Table 2 presents the verification of the transmission conditions (cf. Eqs. (5)-(7)) along the line $x = 0$ by independently extracting the right and left hand side of the equations from FEM evaluation. The error is for the presented cases of the same

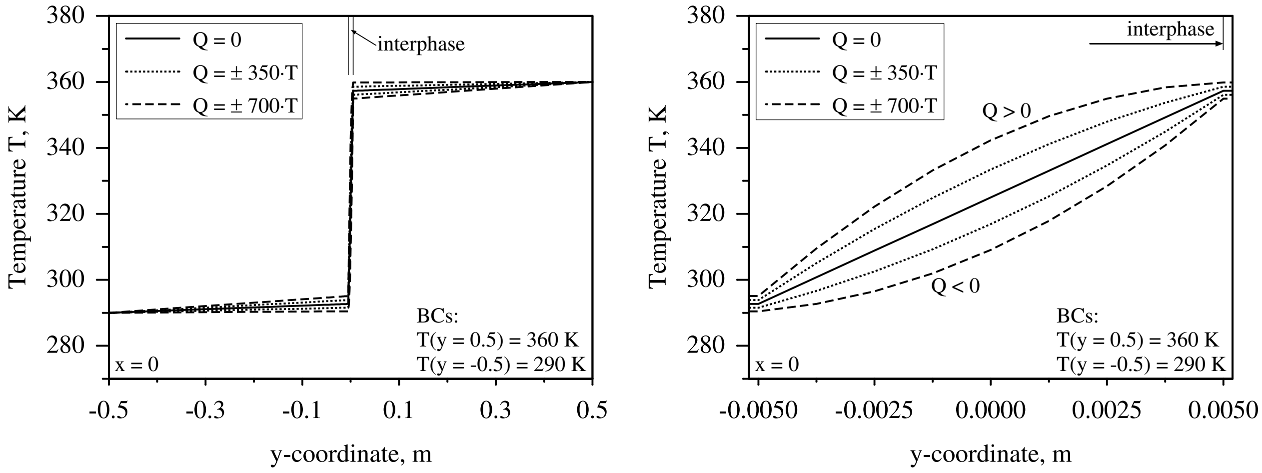

Fig. 4: Temperature distribution perpendicular to the interphase (along the line $x = 0$) for different formulations of the source.

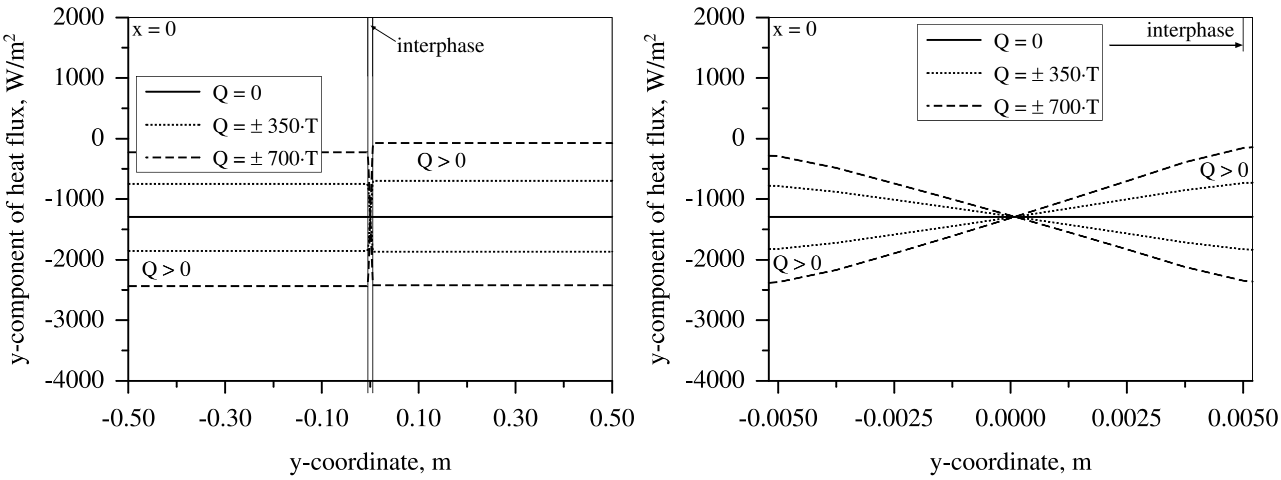

Fig. 5: Distribution of the heat flux perpendicular to the interphase (along the line $x = 0$) for different formulations of the source.

magnitude. Increasing the magnitude of the source expression (e.g. to $\pm 1000 \cdot T$) results in a non-monotonic temperature distribution inside the interphase (cf. Fig. 6) and the second transmission condition (6) and (7) fails. Such a case requires further theoretical treatment and is not covered within the given set of transmission conditions. It should be noted here that if the numerical simulation provides the same flux sign from different sides of the interface, then the conditions are justified. This means that there is a simple criteria for the user to decide if any further adjustment is necessary to be implemented in the computation.

Discussion and Outlook

Finite element analysis could proof the applicability of transmission conditions for reactive heat-resistant interphases. Extremely good accuracy could be observed over the whole range of the interphase for different formulations of the interphase reactivity if the temperature distribution is monotonic in the interphase. The investigation of non-monotonic temperature distributions

Q	1^{st}TC			2^{nd}TC		
	LHS in 10^6	RHS in 10^6	error	LHS	RHS	error
$+350 \cdot T$	-2.953040092	-2.953714114	$\sim 10^{-4}$	0.4182537246	0.4183300133	$\sim 10^{-4}$
$-350 \cdot T$	2.926256300	2.925572089	$\sim 10^{-4}$	0.4183936650	0.4183300133	$\sim 10^{-4}$
$+700 \cdot T$	-5.934144040	-5.936940450	$\sim 10^{-4}$	0.5913703654	0.5916079783	$\sim 10^{-4}$
$-700 \cdot T$	5.826983886	5.824374720	$\sim 10^{-4}$	0.5918125961	0.5916079783	$\sim 10^{-4}$
$+10^3 \cdot T$	-8.512875735	-8.518489254	$\sim 10^{-4}$	0.5223167368	0.7071067812	$\sim 10^{-1}$
$-10^3 \cdot T$	8.293877599	8.288563544	$\sim 10^{-4}$	0.3000266983	-0.7071067812	$\sim 10^{0}$

Table 2: Verification of the transmission condition validity along the line $x = 0$ for different values of the temperature-dependent source or sink, cf. Eqs. (5)-(7).

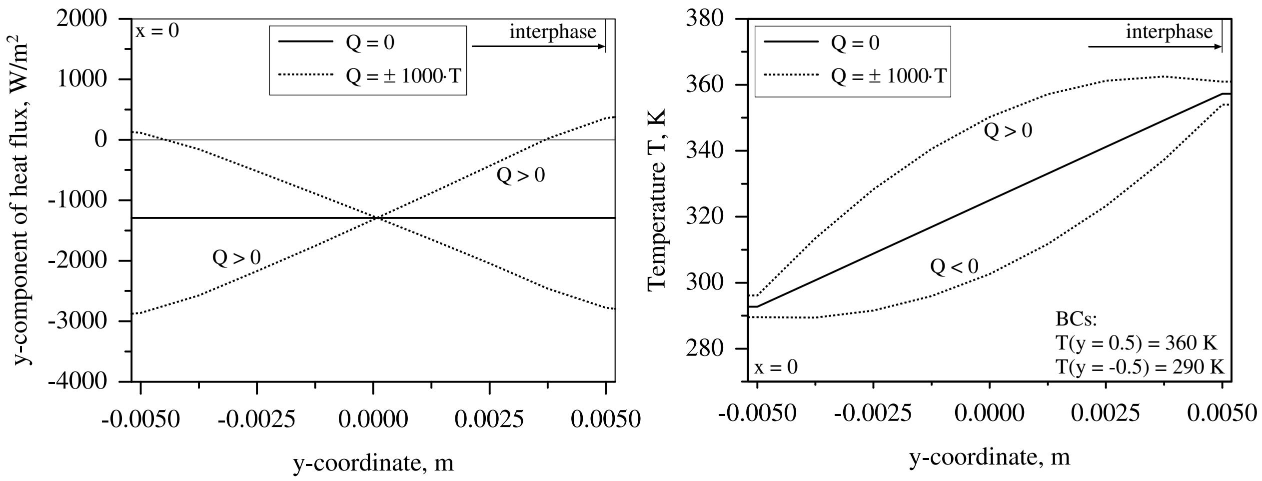

Fig. 6: Heat flux and temperature distribution perpendicular to the interphase (along the line $x = 0$) for a strong source.

and the implementation of the investigated transmission conditions into a commercial finite element code as special interphase elements is reserved for our future research work.

Acknowledgments

Helpful discussions with Prof. G. Mishuris are gratefully achnowledged.

References

[1] F. Rosselli and P. Carbutt: Sampe J. Vol. 37 (2001), p. 7

[2] G. Mishuris, W. Miszuris and A. Öchsner: Mater. Sci. Forum Vol. 553 (2007), p. 87

[3] G. Mishuris, W. Miszuris and A. Öchsner: Mater. Sci. Forum Vol. 553 (2007), p. 93

[4] G. Mishuris and A. Öchsner: Compos. Struct. Vol. 68 (2005), p. 409

[5] G. Mishuris, A. Öchsner and G. Kuhn: CMC - Comput. Mater. Continua Vol. 2 (2005), p. 227

Defect and Diffusion Forum Vols. 283-286 (2009) pp 521-526
online at http://www.scientific.net

Online available since 2009/Mar/02

Transmission Conditions for Thin Reactive Heat-Conducting Interphases: General Case

Gennady Mishuris[1,2,a], Wiktoria Miszuris[3,b], Andreas Öchsner[4,5,c]

[1]Institute of Mathematics and Physics, Aberystwyth University, UK
[2]Wales Institute of Mathematical and Computational Sciences, UK
[3]Department of Mathematics, Rzeszow University of Technology, Rzeszow, Poland
[4]Department of Applied Mechanics, Technical University of Malaysia - UTM, Skudai, Malaysia
[5]University Centre for Mass and Thermal Transport in Engineering Materials,
The University of Newcastle, Callaghan, Australia

[a]ggm@aber.ac.uk, [b]victory@prz.rzeszow.pl, [c]andreas.oechsner@gmail.com

Keywords: heat transfer, thin layers, nonclassical transmission conditions

Abstract. Imperfect transmission conditions modelling a thin reactive intermediate layer between two bonded materials in a dissimilar strip are derived in this paper in most general case extending results obtained previously in [1]. The interphase material is assumed to be heat-resistant and situated in a thin rectangular domain between the main materials.

Introduction

Thin interphases are commonly used in modern technology [2]. An inhomogeneous structure obtained in such a way may exhibit a wider variety of thermal and mechanical properties. On the other hand, finite element modeling of composites with thin interphases is still a difficult numerical task as it requires high inhomogeneity of the constructed mesh which can lead to a loss of accuracy and even numerical instability. This explains the high interest to model the interphases as a zero thickness object described by specific so-called transmission conditions along the infinitesimal interface. In the case of constant heat conductivity, the problem has been completely solved in [3], where the general approach was developed independent of the range of the heat conductivity of the thin (in comparison with the matched adherends) interphase. Such interphases, however, often manifest pronounced non-linear or non-homogeneous properties connected with the manufacturing and exploitation processes [2] and the respective transmission conditions have been evaluated in [4]. In the scope of this paper, we consider another important case [5] when the non-linearity is assigned to the source term and defines a so-called reactive interphase. Again, we concentrate our interest to a heat-resistant interphase which is the most important case from an practical point of view. We will apply the same approach as it has been done in [6, 7, 8, 4]. We also refer here to other methods to deal with thin interphases [9, 10] as well as to construct effective homogenised properties of composite materials [11, 12, 13].

Problem formulation

As in [1, 14], a bimaterial structure consisting of two different materials bonded together with a thin intermediate heat resistant interphase of thickness $2h$ (cf. Fig. 1) is considered in the following. Inside the layer, the thermal sources $\tilde{Q}(\tilde{T})$ are presented and $\tilde{k}$ is the thermal conductivity of the interphase. It was shown that to solve the problem for the temperature, $\tilde{T}$, distribution in the structure, the heat resistant interphase can be replaced by non-linear transmission conditions obtained from the classical perfect transmission conditions defined on both sides of the thin interphase:

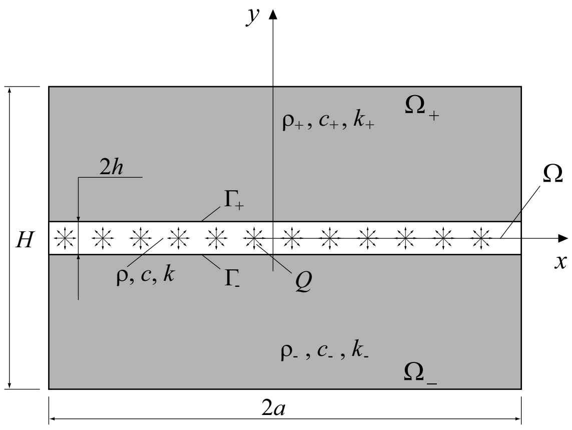

Fig. 1: Bimaterial structure with a thin reactive interphase Ω.

$$T_+(x,0,t) = \tilde{T}_0(x,\tilde{h},t), \quad T_-(x,0,t) = \tilde{T}_0(x,-\tilde{h},t), \quad x \in (-a,a), \tag{1}$$

$$\tilde{k}\frac{\partial}{\partial \xi}\tilde{T}_0(x,\tilde{h},t) = -q_+(x,0,t), \quad \tilde{k}\frac{\partial}{\partial \xi}\tilde{T}_0(x,-\tilde{h},t) = -q_-(x,0,t), \quad x \in (-a,a), \tag{2}$$

where $T_\pm$ and $q_\pm$ are temperature and heat flux along the top and the bottom of the thin interphase, respectively, whereas $\tilde{T}_0$ is the leading asymptotic term of the temperature distribution within the thin heat resistant interphase after rescaling of the problem (see for details [1]), which satisfies the equation:

$$\left(\tilde{k}\frac{\partial}{\partial \xi}\tilde{T}_0(x,\xi,t)\right)^2 = q_-^2(x,0,t) - \Phi(\tilde{T}_0(x,\xi,t)), \quad \xi \in (-\tilde{h},\tilde{h}), \tag{3}$$

where we have introduced the notation:

$$\Phi(\tilde{T}) = 2\tilde{k}\int_{T_-}^{\tilde{T}} \tilde{Q}(z)dz. \tag{4}$$

One of the transmission conditions can be written as:

$$q_+^2(x,0,t) - q_-^2(x,0,t) + \Phi(T_+(x,0,t)) = 0, \quad x \in (-a,a). \tag{5}$$

Moreover, it follows immediately that

$$q_-^2(x,0,t) \geq \Phi(\tilde{T}_0(x,\xi,t)), \quad x \in (-a,a), \tag{6}$$

for any internal point ξ inside the interphase.

For values of ξ situated close enough to $-\tilde{h}$, Eq. (3) can be rewritten in the form:

$$\frac{\tilde{k}\frac{\partial}{\partial \xi}\tilde{T}_0(x,\xi,t)}{\sqrt{1-\Phi(\tilde{T}_0(x,\xi,t))/q_-^2(x,0,t)}} = -q_-(x,0,t)\,, \tag{7}$$

where we have taken into account the fact that $\Phi(\tilde{T}_{-})=0$. To construct the second transmission condition, it was assumed in [1] that the temperature within the interphase is distributed monotonically. Although such assumption is quit realistic, it has been shown in [14] that specific cases may appear when it is not valid (for example, if significant heat sources act within the interphase).

In this paper, we are going to consider a more general case without any assumption on the behaviour of the possible solution within the interphase. We only leave the condition that the sources within the interphase have the same sign (all non-negative, $\tilde{Q}(\tilde{T})\geq 0$ or all non-positive $\tilde{Q}(\tilde{T})\leq 0$). As a result, the only conclusion can be made that the function $\Phi(\tilde{T}_0)$ is monotonic (non-decreasing or non-increasing, respectively).

REMARK 1. If one is interested in the case when the sources take different signs within the interphase, the respective situation is much more complicated as the temperature field may be extremely non-uniform in direction perpendicular to the interphase. If any additional information is available (for example that the field is independent on the other variable, i.e. in direction along the interphase), one can consider the initial thin interface as a set of N thinner interphases in every of them the previous condition of the source sign will be valid and the result reported below could be further generalised.

ASSUMPTION. Let now $q_{+}\cdot q_{-}<0$, than there exists a point $\xi=\xi_*$ inside the interphase such that $q(\xi_*)=0$ (or $\tilde{T}_0'(\xi_*)=\frac{\partial\tilde{T}_0}{\partial\xi}|_{\xi=\xi_*}=0$) and it follows from Eq. (3) that in this point

$$q_{-}^2=\Phi(\tilde{T}_*),\quad \tilde{T}_*=\tilde{T}_0(\xi_*)=\Phi^{-1}(q_{-}^2)\,. \tag{8}$$

Note that the inverse function Φ^{-1} exists because of the monotony of the function Φ. Let us consider in the following a function Ψ with

$$\Psi(q_{-},\tilde{T})=\int\limits_{T_{-}}^{\tilde{T}}\frac{dz}{\sqrt{1-\Phi(z)/q_{-}^2}}. \tag{9}$$

Then, Eq. (7) can be integrated in the intervals $(-\tilde{h},\xi_*)$ and $(\xi_*,\tilde{h})$ under consideration of the sign of flux $q(\xi)$ within the corresponding intervals to give:

$$\tilde{k}\Psi(q_{-},\tilde{T})=-q_{-}\cdot(\xi+\tilde{h})\,,\quad \tilde{k}\Psi(q_{-},\tilde{T}_{+})-\tilde{k}\Psi(q_{-},\tilde{T})=-q_{-}\cdot(\xi-\tilde{h}). \tag{10}$$

These two relations can be written in the intermediate point $\xi=\xi_*$ in equivalent forms by adding and subtracting each other as:

$$\tilde{k}\Psi(q_{-},\tilde{T}_{+})=-2q_{-}\cdot\xi_*,\quad \tilde{k}\Psi(q_{-},\tilde{T}_{+})-2\tilde{k}\Psi(q_{-},\tilde{T}_*)=2q_{-}\cdot\tilde{h}. \tag{11}$$

Equation $(11)_2$ provides the remaining transmission condition if we take into account Eq. $(8)_2$

$$\tilde{k}\Psi(q_{-},\tilde{T}_{+})-2\tilde{k}\Psi(q_{-},\Phi^{-1}(q_{-}^2))=2q_{-}\cdot\tilde{h}. \tag{12}$$

REMARK 2. It is easy to check that in the special case of $\xi_*=\tilde{h}$ (or $\tilde{T}_*=T_{+}$) the obtained transmission condition coincides with that evaluated in [1].

REMARK 3. When the problem has been solved due to the transmission conditions (5) and (12), the position of the extremal value of the temperature within the thin heat resistant interphase layer can be easily found from Eq. $(11)_1$.

Remark 4. If the position of the extremal value of the temperature is situated outside the interphase then the chosen transmission condition (12) maybe not valid for the considered case and one should exchange it by the transmission conditions (26) defined in the previous paper [1]. The verification condition to be checked is:

$$\frac{\tilde{k}}{2\tilde{h}}\left|\Psi(q_-,\tilde{T}_+)\right| \le |q_-|. \tag{13}$$

As in the previous papers [1, 14], transmission (5), (12) cannot be written in the general case in terms of simple functions. Below, we present some specific examples where the conditions can be written in relatively simple expressions.

Special case 1. Let the source be essential but independent of the temperature distribution, i.e. $Q = \epsilon^{-1}Q_0$. Then, function $\Phi(\tilde{T})$ from Eq. (4) can be calculated as $\Phi(\tilde{T}) = 2\tilde{k}Q_0(\tilde{T} - T_-)$ and the first transmission condition (5) can be rewritten in the form:

$$q_+^2(x,0,t) - q_-^2(x,0,t) = -2\tilde{k}\,Q_0 \cdot \big(T_+(x,0,t) - T_-(x,0,t)\big), \quad x \in (-a,a). \tag{14}$$

The auxiliary function (9) allowing to recover from (10) the distribution of the temperature $\tilde{T}$ within the interphase can be easily computed to give:

$$\Psi(q_-,\tilde{T}) = \frac{{q_-}^2}{\tilde{k}Q_0}\left(1 - \sqrt{1 - \frac{2\tilde{k}Q_0}{{q_-}^2}(\tilde{T} - \tilde{T}_-)}\right).$$

Then, after some algebra, the second condition (12) takes the following form:

$$\mathrm{sgn}\,(q_-(x,0,t)) \cdot |q_+(x,0,t)| + q_-(x,0,t) = -2\tilde{h}Q_0, \quad x \in (-a,a). \tag{15}$$

However, it holds due to our initial assumption that $\mathrm{sgn}\,(q_-(x,0,t)) = -\mathrm{sgn}\,(q_+(x,0,t))$. This means that condition (15) can be equivalently rewritten in the form:

$$q_+(x,0,t) - q_-(x,0,t) = 2\tilde{h}Q_0, \quad x \in (-a,a), \tag{16}$$

which completely coincides with the condition obtained in [1] under other assumptions for the same source distribution. This in turn allows us to simplify the first transmission condition to the form

$$T_+(x,0,t) - T_-(x,0,t) = -\frac{\tilde{h}}{\tilde{k}} \cdot \left(q_+(x,0,t) + q_-(x,0,t)\right), \quad x \in (-a,a). \tag{17}$$

Remark 5. As we have shown in our previous paper [14] for a high level constant source, the temperature $\tilde{T}(\xi)$ is not necessarily a monotonic function within the interface (the flux $q(\xi)$ can change its sign), whereas the transmission condition previously evaluated under monotonicity assumption were valid. Our recent analysis has clarified this phenomenon.

Special case 2. Let $Q = \epsilon^{-1}Q_0T$, then $\Phi(\tilde{T}) = \tilde{k}Q_0 \cdot (\tilde{T}^2 - T_-^2)$. Note here that a power law, e.g. $Q = c \cdot T^m$, is very common for low temperatures [5] of for small temperature increments. The first transmission condition (5) can be written now in the form:

$$q_+^2(x,0,t) - q_-^2(x,0,t) = -\tilde{k}Q_0\,\left(T_+^2(x,0,t) - T_-^2(x,0,t)\right), \quad x \in (-a,a). \tag{18}$$

Now, the auxiliary function (9) takes different forms depending on whether we consider a source ($Q_0 > 0$) or a sink ($Q_0 < 0$). Namely:

$$Q_0 > 0: \quad \Psi(q_-, \tilde{T}) = \frac{|q_-|}{\sqrt{\tilde{k}Q_0}} \left(\arcsin \frac{\tilde{T}\sqrt{\tilde{k}Q_0}}{\sqrt{{q_-}^2 + \tilde{k}Q_0\tilde{T}_-^2}} - \arcsin \frac{\tilde{T}_-\sqrt{\tilde{k}Q_0}}{\sqrt{{q_-}^2 + \tilde{k}Q_0\tilde{T}_-^2}} \right).$$

After some algebra, the second transmission condition (12) in the case $Q_0 > 0$ can be rewritten in the following form:

$$\arcsin \frac{\tilde{T}_+\sqrt{\tilde{k}Q_0}}{\sqrt{{q_-}^2 + \tilde{k}Q_0\tilde{T}_-^2}} + \arcsin \frac{\tilde{T}_-\sqrt{\tilde{k}Q_0}}{\sqrt{{q_-}^2 + \tilde{k}Q_0\tilde{T}_-^2}} = \pi + 2\tilde{h}\sqrt{\frac{Q_0}{\tilde{k}}} \cdot \operatorname{sgn}(q_-), \quad x \in (-a, a), \tag{19}$$

where the following verification condition holds:

$$\left| \arcsin \frac{\tilde{T}_+\sqrt{\tilde{k}Q_0}}{\sqrt{{q_-}^2 + \tilde{k}Q_0\tilde{T}_-^2}} - \arcsin \frac{\tilde{T}_-\sqrt{\tilde{k}Q_0}}{\sqrt{{q_-}^2 + \tilde{k}Q_0\tilde{T}_-^2}} \right| \leq 2\tilde{h}\sqrt{\frac{Q_0}{\tilde{k}}}. \tag{20}$$

In the case when $Q_0 < 0$, one can compute the auxiliary function (9) as

$$Q_0 < 0: \quad \Psi(q_-, \tilde{T}) = \frac{|q_-|}{\sqrt{-\tilde{k}Q_0}} \log \left| \frac{\tilde{T}\sqrt{-\tilde{k}Q_0} + \sqrt{(\tilde{T}_-^2 - \tilde{T}^2)\tilde{k}Q_0 + q_-^2}}{\tilde{T}_-\sqrt{-\tilde{k}Q_0} + |q_-|} \right|.$$

Then, transmission condition (12) can be written under consideration of Eq. (18) in another form as:

$$\ln \frac{\left(|q_+| + T_+\sqrt{-Q_0\tilde{k}}\right)\left(|q_-| + T_-\sqrt{-Q_0\tilde{k}}\right)}{|\tilde{k}Q_0\tilde{T}_-^2 + q_-^2|} = 2\tilde{h}\sqrt{\frac{-Q_0}{\tilde{k}}} \operatorname{sgn}(q_-), \tag{21}$$

where the following additional condition

$$\tilde{k}Q_0\tilde{T}_-^2 + q_-^2 \neq 0,$$

will be satisfied automatically during the computations. Finally the verification condition takes place:

$$\left| \ln \frac{|q_+| + T_+\sqrt{-Q_0\tilde{k}}}{|q_-| + T_-\sqrt{-Q_0\tilde{k}}} \right| \leq 2\tilde{h}\sqrt{\frac{-Q_0}{\tilde{k}}}. \tag{22}$$

Unfortunately, the situation is even more complicated than it may look from the first glance from our analysis. Namely, all the transmission conditions and respective verification conditions have to be checked at every point x along the imperfect interface. Effectively this means that several intervals can exist where the type of the transmission conditions may change. The respective borders should be found adaptively from an iterative procedure in such a way that all the verification conditions provide in the edge points equalities instead of inequalities.

On the other hand, it is highly important to know the range of the material parameters where the conditions can be applied, and when it is necessary to take some specific effects (for

example high time gradient) into account.
In the following, the example presented in [14] will be re-evaluated by means of the new conditions. Table 1 compares the new approach with the values from [14] where a significant drop (factor $10^3 \dots 10^4$) in the accuracy has been reported for strong temperature-dependent sources. As can be seen, the new evaluation of the second transmission condition based on Eqs. (19) and (21) brings the accuracy back in the same range as for for moderate sources (error 10^{-4}).

Q	2^{nd}TC			
	LHS	RHS	error	method
$+10^3 \cdot T$	0.5223167368	0.7071067812	$\sim 10^{-1}$	Ref. [14]
$-10^3 \cdot T$	0.3000266983	-0.7071067812	$\sim 10^{0}$	Ref. [14]
$+10^3 \cdot T$	2.436062015	2.434485873	$\sim 10^{-4}$	Eq. (19)
$-10^3 \cdot T$	0.7074743000	0.7071067812	$\sim 10^{-4}$	Eq. (21)

Table 1: Comparison of transmission condition evaluation along the line $x = 0$ for a strong temperature-dependent source or sink.

Acknowledgments

W. Miszuris has been supported by a Marie Curie Transfer of Knowledge Fellowship of the European Community's Sixth Framework Programme under contract number MTKD-CT-2004-509809.

References

[1] G. Mishuris, W. Miszuris, A. Öchsner: Defect Diffus. Forum Vols. 273-276 (2008), p. 394

[2] F. Rosselli, P.Carbutt: Sampe J. Vol. 37 (2001), p. 7

[3] Y. Hashin: J. Appl. Phys. Vol. 89 (2001), p. 2262

[4] G. Mishuris, W. Miszuris, A. Öchsner: Mater. Sci. Forum Vol. 553 (2007), p. 87

[5] C.L. Tsai, H. Weinstock, W.C. Overton, Jr: Cryogenics Vol. 18 (1978), p. 562

[6] G. Mishuris, A. Öchsner: Compos. Struct. Vol. 68 (2005), p. 409

[7] G. Mishuris, A. Öchsner, G. Kuhn: CMC - Comput. Mater. Continua Vol. 2 (2005), p. 227

[8] G. Mishuris, A. Öchsner: Arch. Mech. Vol. 57 (2005), p. 157

[9] Y. Benveniste, T. Miloh: Mech. Mater. Vol. 33 (2001), p. 309

[10] Z. Hashin: J Mech Phys. Solids Vol. 50 (2002), p. 2509

[11] A.H. Nayfeh: J. Appl. Mech. Vol. 42 (1975), p. 399.

[12] Y. Benveniste: Mech. Mater. Vol. 4 (1985), p. 197

[13] Z. Hashin: Mech. Mater. Vol. 8 (1990), p. 3333

[14] A. Öchsner, W. Miszuris: Defect Diffus. Forum Vols. 273-276 (2008), p. 400

[15] A.B. Movchan, N.V. Movhan: *Mathematical Modelling of Solids of with Nonregular Boundaries* (CRC Press, Boca Raton 1995)

2.4 Characterisation of Cellular and Porous Materials

PERGAMON

Mechanics Research Communications 30 (2003) 573–579

MECHANICS
RESEARCH COMMUNICATIONS

www.elsevier.com/locate/mechrescom

On the uniaxial compression behavior of regular shaped cellular metals

Andreas Öchsner *, Klaus Lamprecht [1]

Institute of Applied Mechanics, University of Erlangen-Nuremberg, D-991058 Erlangen, Germany

Received 9 July 2002

Abstract

The numerical simulation of random cellular metals is still connected to many unsolved problems due to their stochastic structure. Therefore, a periodic model of a cellular metal is developed for fundamental studies of the mechanical behavior and is numerically investigated under uniaxial compression. The influence of differing hardening behaviors and differing boundary conditions on the characteristics of the material is investigated. Recommendations for the numerical simulation are derived. In contrast to common models, experimental samples of the same geometry are easy to manufacture and the results of the experiments show good agreement with the finite element calculations. Based on the proposed concept of a unit cell with periodic boundary conditions, it is possible to derive constitutive equations of cellular materials under complex loading conditions.

Keywords: Cellular metal; Nonlinear behavior; Plasticity; Finite element analysis; Compression test

1. Introduction

Cellular metals, e.g. metallic foams, exhibit unique properties and are currently being considered for use in lightweight structures such as cores of sandwich panels or as passive safety components of automobiles (Ashby et al., 2000). Many methods for fabrication of these materials have been developed and can be classified into four groups: foams made from melts, from powders, by sputtering and by deposition (Banhart, 2001). Some methods have been known since the fifties, and each production method results in a characteristic cellular structure. A typical open-cell aluminum structure made by the melt route is shown in Fig. 1(a). However, there are technological problems related to the control of structure and properties of the material, which remain to be solved. The vast majority of existing techniques do not allow precise control of shape, size and distribution of the pores. That brings about a wide scatter in mechanical and other characteristics of the materials and components.

* Corresponding author. Tel.: +49-9131-8528516; fax: +49-9131-8528503.
E-mail address: oechsner@ltm.uni-erlangen.de (A. Öchsner).
[1] Since June 2002 with: Chair of Manufacturing Technology, University of Erlangen-Nuremberg, D-91058 Erlangen, Germany.

doi:10.1016/S0093-6413(03)00058-2

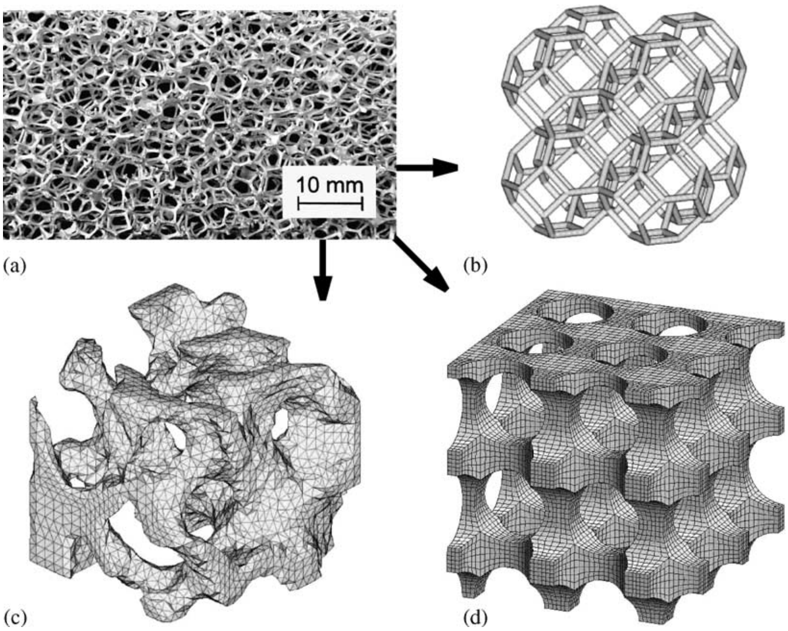

Fig. 1. Random cellular material and different modeling approaches. (a) Open-cell Al foam (Duocel®), (b) polyhedron cells (beam elements) (Ströhla et al., 2000), (c) CT scan (Ströhla et al., 2000) and (d) perforated cube.

The mechanical properties of cellular metals, in particular their resistance to plastic deformation, the evolution and progress of damage and fracture within the material, are determined by the microstructure and the cell wall material respectively. The most important structural parameters which characterize a cellular metal are the morphology of the cell (geometry, open or closed cell), the topology, the mean cell size and the relative density, ρ/ρ_S (the macroscopic density, ρ, divided by that of the solid material of the cell wall, ρ_S).

A schematic uniaxial compression stress–strain curve (cf. Fig. 2 starts with linear elasticity at low stresses, followed by a transition zone which extends over a long collapse plateau, truncated by a regime of densification in which the stress rises exponentially. Many investigations focus on the large strain defor-

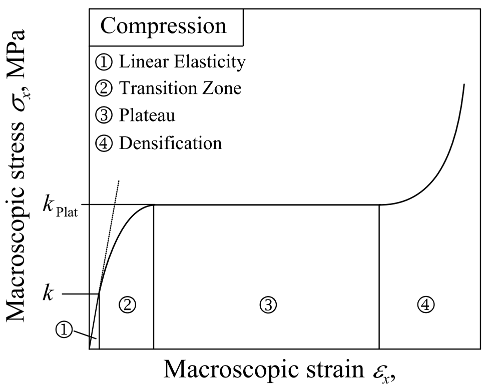

Fig. 2. Schematic uniaxial compression stress–strain curve for a metal foam.

mations. The initial yield stress k is then equated with the plateau stress k_{Plat}, so that the transition zone, which can be clearly marked in the case of certain cellular metals, remains unconsidered. In this paper, we will investigate the elastic zone up to the first part of the plateau under uniaxial compression loading. There are two strategies used to simulate the mechanical behavior of random (cf. Fig. 1(a)) cellular solids. Almost all theoretical structure–property relations are based on periodic unit cells (e.g. Gibson and Ashby, 1997; Daxner et al., 2000). Geometrically identical specimens of these periodic unit cells, for experimental verifications, are difficult to realize and the prediction of the mechanical properties of random cellular solids requires the introduction of fitting parameters (e.g. damage variable). Recently produced so-called lattice block materials are of regular periodic structure, but the manufacturing route is quite elaborate (Deshpande, 2001). The other possibility is an exact scan of the geometry using computertomography (CT scan, cf. Fig. 1(c)). This requires the availability of this high-tech equipment and if high resolution in the FE mesh is needed, then only a small part of the object (not representative) can be scanned due to the resulting large amount of elements (this is limited by the hardware of the computer, i.e. RAM, disk). Therefore, the simple model of a perforated cube (cf. Fig. 1(d)) was developed for fundamental studies which is easy to manufacture at low price (CNC drilling) and offers the possibility of an experimental validation of numerical simulations. With a hole diameter of 3 mm (smaller diameters can result in a failure of the drill bit) and a hole spacing of 4 mm, a relative density of $\rho/\rho_S = 0.2712$ could be realized.

2. Modeling considerations of the perforated cube structure

The commercial finite element code MSC.Marc was used for the simulation of the macroscopic properties of the chosen cell structure, Fig. 1(d). First, the influence of the mesh density on the results was investigated.

For the purpose of achieving a proper mesh quality, one eighth of the unit cell was subdivided into four bodies. Each of these bodies consists of six faces which in turn are made up of four edges and four vertices. The parameters N_1 and N_2 indicate the number of elements along the edges of these sub-bodies and must not be confused with geometric dimensions (see Fig. 3, center). For a preliminary series of compression test simulations, the mesh parameters N_1 and N_2 have been varied according to Table 1 in order to determine a suitable mesh density. The table also shows the resulting amount of nodes and elements of the differing finite element meshes. Dependent upon different mesh densities, Fig. 4(a) illustrates the resulting stress–strain curves that have been evaluated from the uniaxial compression tests on a macroscopic level. Especially within the domain of elastic material behavior, an essential influence of the mesh density on the

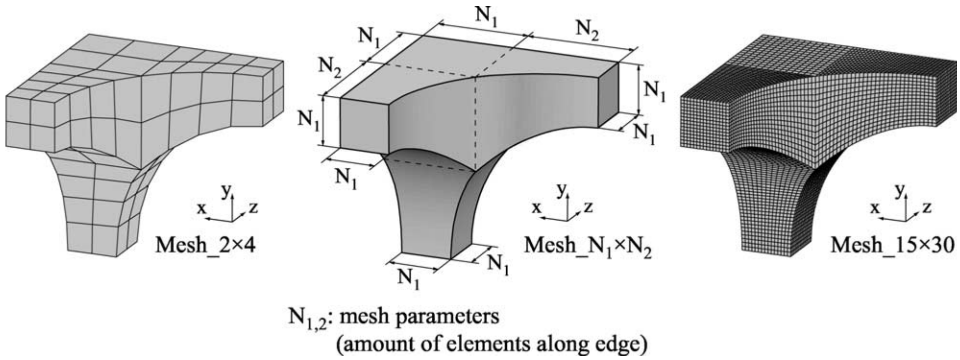

Fig. 3. One eighth of the perforated cube and mesh parameters.

Table 1
Mesh parameters and computing resources

Notation	Nodes	Elements	Result file [MB]	Computing time [10^3 s]
2×4	135	56	1.09	0.482
3×6	352	189	3.21	0.645
5×10	1296	875	13.95	2.753
7×14	3200	2401	37.60	7.002
10×20	8591	7000	108.49	44.828
15×30	27 139	23 625	363.63	317.378

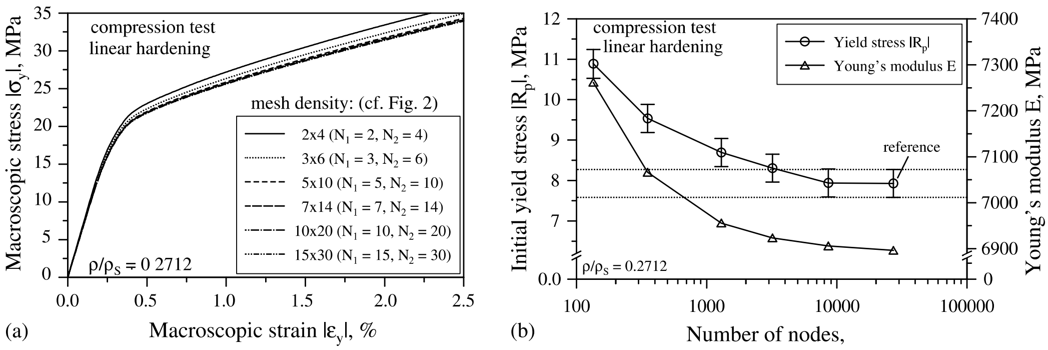

Fig. 4. FE results for different mesh densities.

results of the calculations cannot be observed on basis of the representation in Fig. 4(a). If one considers the model with the finest discretization (Mesh_15×30) as reference, significant deviations in the stress–strain curve can only be recognized after the elastic limit is exceeded. But even for models with extremely coarse meshes (Mesh_2×4) the maximum deviation of the macroscopic stress σ_y is only about 6%. Minor deviations from the reference result can be achieved by increasing the density of the finite element mesh. In addition to the σ_y–ε_y-curves the initial yield stress R_p and Young's modulus E were evaluated on a macroscopic level. Fig. 4(b) shows a graphical representation of both values as a function of the mesh density (number of nodes within the finite element mesh). It is quite obvious that both R_p and E show a strong drop (semi-logarithmic representation!) at first, but then reach an almost constant value as the mesh density increases. In order to avoid excessive computing time the finite element mesh 10×20 was chosen for all further investigations. This allows a reduction in computing time of almost 85% compared to the reference simulation (cf. Table 1), without a significant influence on the results of the calculations.

The mechanical behavior of a cellular metal and its mathematical characterization can be described based upon the principles of continuum mechanics, if a 'representative volume element' (RVE) is considered, Fig. 1(d). In the case of cellular materials, this RVE needs to comprise of at least 5–10 unit cells, in order to avoid edge influence and to obtain macroscopic values of the structure. The precise number depends, however, on the corresponding cell structure and should be examined separately. Since the intention of this paper is to model only isotropic solids, no further account was taken of the anisotropy caused by the particular pore distribution and only strain states having principle strain distributions parallel to the x-, y- and z-axes (cf. Fig. 3) should be considered. A fine mesh with solid elements (linear shape functions) of such a structure consisting of 5–10 unit cells would lead, however, to a large amount of unknowns and a huge amount of computing time. Therefore, only a typical repeating portion (unit cell) was simulated. Due to the symmetry of the unit cell, only one eighth needs to be considered. The mechanically correct constraints are in this case of great importance, Fig. 5. One possibility would be to consider one surface of the unit cell as a

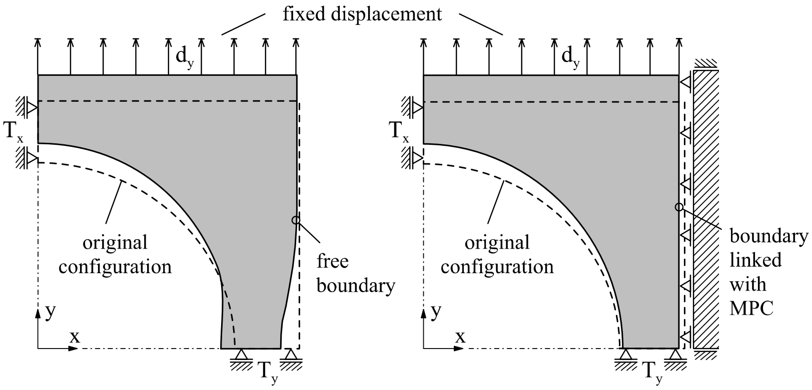

Fig. 5. Unit cell with differing boundary conditions.

free boundary. However, to simulate the mechanical behavior of a *cell structure*, only a periodic boundary provides the correct constraint. With the aid of so-called multiple point constraints (MPC), the used FE-system offers the possibility to realize such a boundary condition where all nodes on a certain surface have the same x-displacement: $u_{x_i} = \cdots = u_{x_j}$. The effect of differing boundary conditions on the deformation is shown in Fig. 5.

3. Results of FE simulations

The results of the simulated compression tests for a unit cell, a unit cell with MPC and a cell structure (Fig. 1(d)) are compared in Fig. 6(a). The stress–strain diagram of the cell structure coincides quite well with the MPC unit cell. The curve for the unit cell is clearly below the other two and shows right from the beginning clear deviations in the elastic range. The progress of Poisson's ratio of the structure and the unit cell with MPC shows a clearer difference than the progress of the stress–strain diagram does. Thus one can conclude, that a cell structure consisting of $5 \times 5 \times 5$ cells still cannot be regarded as a representative volume since the edge influence is still too big. It is noticeable here, that greater cell structures are not computable due to actual hardware limitations of the computers. The progress of Poisson's ratio of the unit

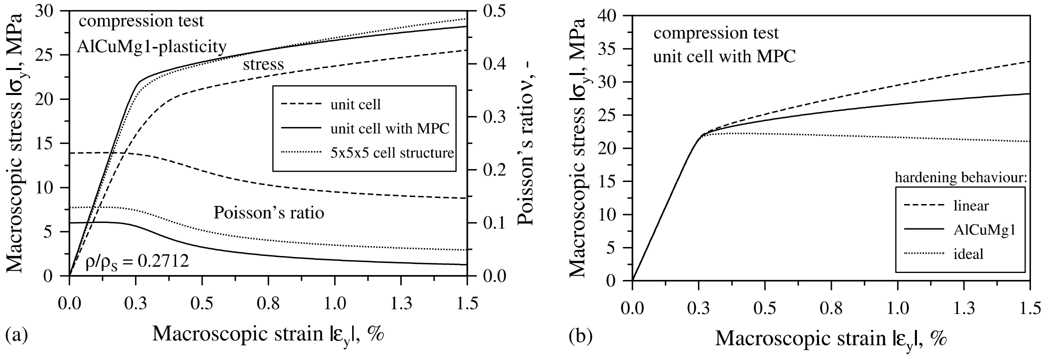

Fig. 6. Macroscopic stress–strain diagrams.

cell is considerably higher than the two other simulations. Thus it can be stated, that the simulation of a cell structure by means of a simple unit cell can lead to considerable errors.

For the investigation of the influence of the cell wall material on the macroscopic stress–strain behavior, the following simulations were carried out with a periodic boundary condition. Besides the realistic hardening behavior of an aluminum alloy (AlCuMg1), the two border cases – ideal plasticity ($k = 301.0611$ MPa = const.) and linear hardening ($k = 1/20 \cdot E_S \cdot \varepsilon_{\mathrm{eff}}^{\mathrm{p}}$) – were considered. A clear dependence in the plastic region can be seen, Fig. 6(b).

4. Comparison of FE results with experiments

To compare the numerical simulations with experimental data, specimens were machined from cubes made of aluminum alloy AlCuMg1. From three sides, 49 holes with a diameter of 3 mm were drilled in a square pattern in a cube with the outer dimensions of 28 mm × 28 mm × 28 mm. Fig. 7 shows a specimen before and after the compression test.

The compression tests were performed elongation controlled (elongation speed 1 mm/min) in a universal electro magnetic testing machine (SCHENCK) with a capacity of 100 kN. The strains were recorded by means of a mechanical strain-gauge extensiometer (SANDNER) attached between the two pressure feet. A typical compression stress–strain diagram is shown in Fig. 8. It can be seen that the overall behavior of the

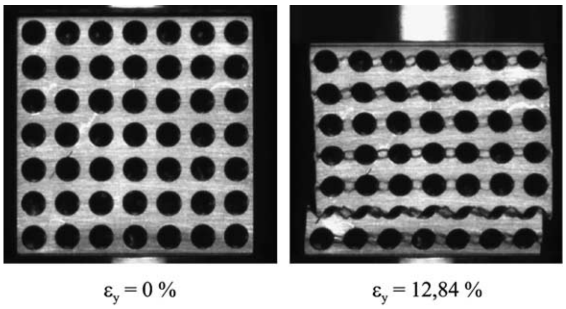

Fig. 7. Experimental specimen before and after compression test.

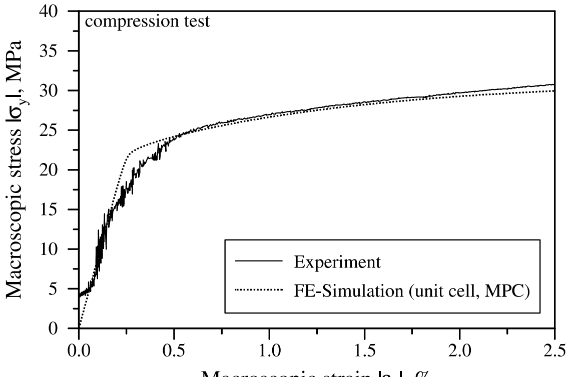

Fig. 8. Comparison of experimental data with FE simulation.

specimen is in agreement with the finite element simulation. The scatter at the beginning of the diagram comes from the load cell which is not sensitive enough in this range. The transition from the elastic to the plastic zone is in the case of the experiment a little bit smoother. The simulation of the cell structure and unit cell have already shown this effect which results partly from the edge influence.

5. Conclusions

In the current work, a simple model of a cellular metal was proposed for fundamental studies of the mechanical behavior. Within the scope of the numerical simulation of the macroscopic behavior of cellular metals based on unit cells, the use of periodic boundary conditions provides a dramatic reduction of CPU time and a correct representation of the mechanical behavior. Furthermore, a reasonably good agreement with experimental results can be shown. Under certain circumstances it may be necessary that a cell structure built up from several cells should be modeled (e.g. anisotropic damage). Then, the resulting calculation of a unit cell with periodic boundary conditions provides an elegant way to show whether the number of the cells in the structure can be regarded as a representative structure. The numerical and experimental investigation of the plastic behavior under multi-axial loading conditions to obtain appropriate constitutive equations is reserved for future research work.

References

Ashby, M.F., Evans, A., Fleck, N.A., Gibson, L.J., Hutchinson, J.W., Wadley, H.N.G., 2000. Metal Foams: A Design Guide. Butterworth-Heinemann, Boston.

Banhart, J., 2001. Prog. Mater. Sci. 46, 559.

Daxner, T., Böhm, H.J., Rammerstorfer, F.G., Denzer, R., Maire, M., 2000. Mat.-wiss.u. Werkstofftech. 31, 447.

Deshpande, V.S., Fleck, N.A., Ashby, M.F., 2001. J. Mech. Phys. Solids 49, 1747.

Gibson, L.J., Ashby, M.F., 1997. Cellular Solids. Cambridge University Press, Cambridge.

Ströhla, S., Winter, W., Kuhn, G., 2000. Mat.-wiss.u. Werkstofftech. 31, 444.

Mechanics of Composite Materials, Vol. 41, No. 3, 2005

STRUCTURAL MODELING OF THE MECHANICAL BEHAVIOR OF PERIODIC CELLULAR SOLIDS: OPEN-CELL STRUCTURES

T. Fiedler,*,* A. Öchsner,*,******
J. Gracio,*,** and G. Kuhn****

Keywords: *cellular metal, effective properties, nonlinear behavior, plasticity, yield surface, finite element analysis, relative density*

The numerical simulation of random cellular metals, e.g., metal foams, is still connected with many unsolved problems due to their stochastic structure. Therefore, a periodic model of cellular metals is developed and its mechanical behavior is investigated numerically under uniaxial and multiaxial stress states. The main advantage of the model is that a wide range of relative densities can be covered and that test specimens of the same geometry are possible to manufacture without oversimplifying their shape. The influence of different hardening behavior and different boundary conditions on the characteristics of the material is investigated. Furthermore, the effect of internal pore pressure on its uniaxial behavior and on the shape of yield surface are determined.

Introduction

Nature frequently uses cellular materials for creating load-carrying and weight-optimal structures. Natural materials such as wood, cork, bones, and honeycombs, thanks to their cellular design, fulfil structural as well as functional demands. For a long time, the development of artificial cellular materials has been aimed at utilizing the outstanding properties of biological materials in technical applications. As an example, the geometry of honeycombs (hexagonal structures) was identically converted into aluminum structures, which have been used since the '60s as cores of lightweight sandwich elements in aviation and space industry [1]. Nowadays, especially foams made of polymeric materials are widely used in all fields of technology. For example, Styrofoam® and hard polyurethane foams are widely used as packaging materials. Other typical application areas are the fields of heat and sound absorption. During the last years, techniques for foaming metals and metal alloys and for manufacturing novel metallic cellular structures have been developed [2]. These cellular materials, owing to their specific properties, have a high potential for future oriented applications [3]. The combination of specific mechanical and physical properties distinguishes them from the traditional dense metals, and applications with multifunctional requirements are of special interest in the context of such cellular metals. Their high stiffness, in conjunction with the very low specific weight, and their high gas per-

*Center for Mechanical Technology and Automation, University of Aveiro, Aveiro, Portugal. **Institute of Applied Mechanics, Erlangen-Nuremberg University, Erlangen, Germany. ***Department of Mechanical Engineering, University of Aveiro, Aveiro, Portugal. Russian translation published in Mekhanika Kompozitnykh Materialov, Vol. 41, No. 3, pp. 405-422, May-June, 2005. Original article submitted April 12, 2005.

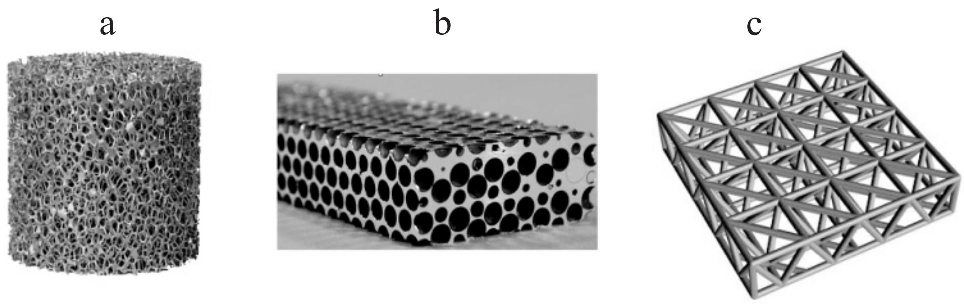

Fig. 1. Different types of cellular metals: a) open-cell metal foam (Duocel®); b) hollow alumina spheres embedded in a magnesium matrix [2]; c) lattice block material [5].

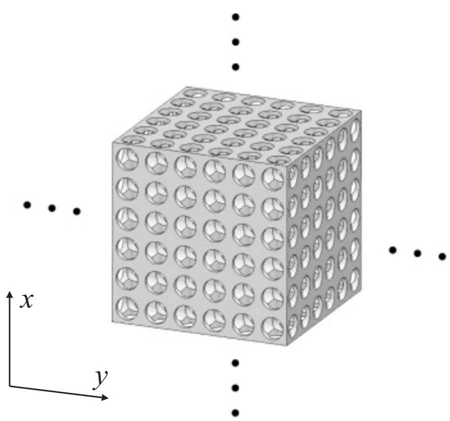

Fig. 2. Representative volume element (RVE) of a simple perforated cell structure.

meability, combined with the high thermal conductivity, can be mentioned as examples. Possible applications are expected in the area of weight-optimal safety components in automotive industry and in lightweight composite structures [4].

Cellular materials comprise a wide range of different arrangements and forms of cell structures (Fig. 1). Metallic foams (Fig. 1a) are being investigated intensively, and they can be produced with a closed- or open-cell structure. Their main characteristic is the very low density. The most common foams are made of aluminum alloys. Quite a regular arrangement of cells are obtained in structures with hollow spheres, which are often called syntactic foams (Fig. 1b). A perfect regular structure results from interconnecting networks of straight beams, which are known as lattice block materials (Fig. 1c).

What all these different cellular materials have in common is that their mechanical properties, in particular the resistance to plastic deformation and the evolution and progress of damage and fracture in the materials, are determined by their microstructure and the cell wall material. The most important structural parameters characterizing these cellular metals are the cell morphology (geometry, open or closed cells), their topology, the mean cell size, and the relative density $\rho_{rel} = \rho/\rho_s$ (the macroscopic density ρ divided by that of the solid material of cell walls ρ_s). Usually, material properties of cellular materials are given in the literature as functions of the relative density.

In this paper, an attempt is made to investigate the elastoplastic properties of cellular materials by using a regular model structure that covers a wide range of the relative density. Uniaxial and multiaxial stress states are considered in order to derive the corresponding material characteristics.

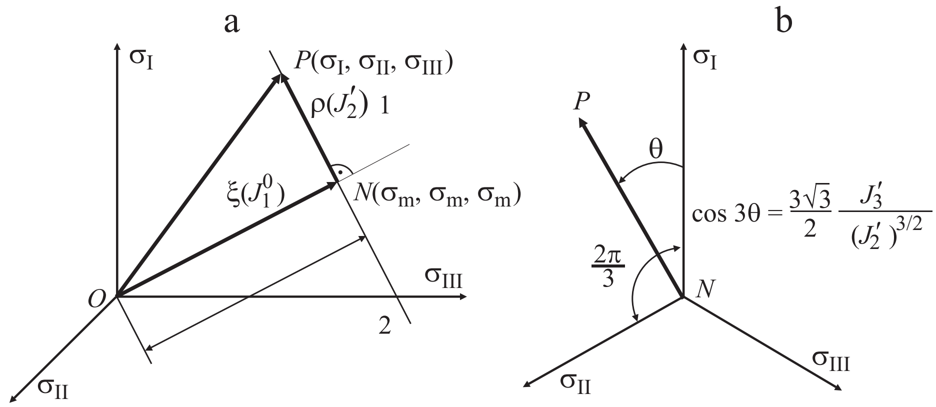

Fig. 3. Geometrical interpretation of stress invariants: a — in the space of principal stress; b — in an octahedral plane. 1 — hydrostatic axis; 2 — octahedral plane.

Constitutive Modeling of Cellular Materials

The mechanical behavior of cellular metals can be described by applying the principles of continuum mechanics to a "representative volume element" (RVE) (Fig. 2). In the case of a cellular material, the RVE must comprise at least 5 to 10 unit cells (UC), in order to reflect its macroscopic properties. Their precise number depends on the corresponding cell structure and should be examined separately. The aim of this paper is to model only isotropic solids, therefore, the anisotropy caused by a particular pore distribution is disregarded, and only strain states with principle strains parallel to the x- and y-axes are considered (Fig. 2). This modeling technique, which is based on homogenous cell structures, has already been used for describing the plastic behavior of porous metals [6, 7] and for modeling damage effects [8-10]. First investigations were done for uniaxial loads by the present authors in [11].

Elastic behavior. Under the classical assumptions of small strains and a linear relationship between the second-order stress tensor σ_{ij} and the strain tensor ε_{ij}, the elastic stress–strain relation is given by the generalized Hooke's law

$$\varepsilon_{ij} = \frac{1+\nu}{E}\left(\sigma_{ij} - \frac{\nu}{1+\nu}\delta_{ij}\sigma_{kk}\right), \tag{1}$$

where E is Young's modulus and ν is the Poisson ratio. In uniaxial tension or compression, the only nonzero stress component σ_{xx} causes an axial strain ε_{xx} and transverse strains $\varepsilon_{yy} = \varepsilon_{zz}$.

Thus, one can determine the elastic constants, i.e., Young's modulus and the Poisson ratio from Eq. (1) as

$$E = \frac{\sigma_{xx}}{\varepsilon_{xx}}, \quad \nu = -\frac{\varepsilon_{yy}}{\varepsilon_{xx}} = -\frac{\varepsilon_{zz}}{\varepsilon_{xx}}. \tag{2}$$

Plastic behavior. Three essential elements of a plastic analysis are the yield criterion, the flow rule, and the hardening rule, [12]. The yield criterion relates the stress state to the onset of yielding. The flow rule relates the stress state to the corresponding increments of plastic strains $d\varepsilon_{ij}^{p}$, when a plastic flow occurs. The hardening rule describes how the yield criterion is modified upon deformation beyond the initial yield point. In what follows, we will concentrate on the mathematical and graphical representation of the yield criterion, which is one of the main topics in this paper. The yield criterion for an isotropic material can generally be expressed as

$$F = F(\sigma_{ij}, \kappa, \alpha_{ij}), \tag{3}$$

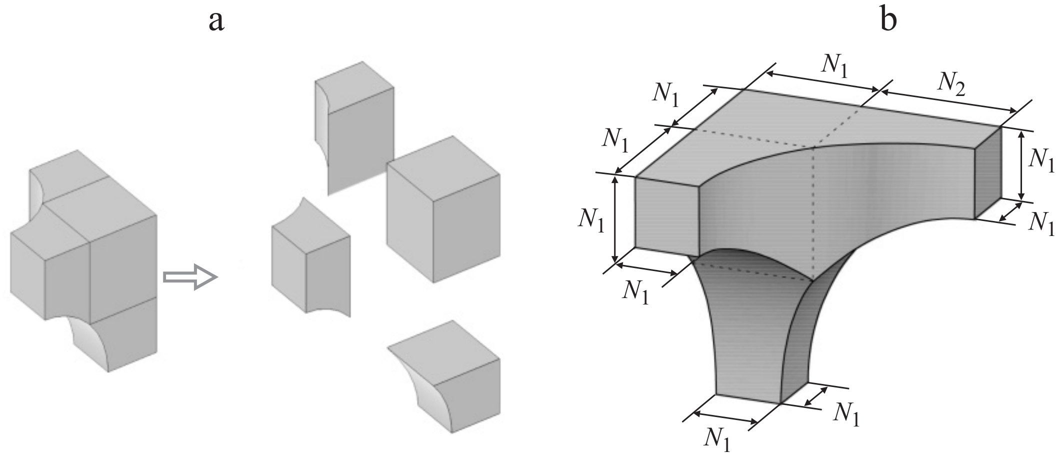

Fig. 4. Meshing of the geometry: a — subdivision of a unit cell (one eighth) for a regular meshing; b — mesh parameters N_1 and N_2.

where κ is the parameter of isotropic hardening and α_{ij} are the parameters of kinematic hardening. The stress tensor σ_{ij} can be split in its spherical σ_{ij}^0 and deviatoric σ'_{ij} parts. In terms of the three stress invariants J_1^0, J'_2, and J'_3, where J_1^0 is the first invariant of the stress tensor and J'_2 and J'_3 are the second and third invariants of the deviatoric tensor [13], Eq. (3) can be written in the form

$$F = F(J_1^0, J'_2, J'_3\ \kappa, \alpha_{ij}), \tag{4}$$

and the initial yield criterion in the form

$$F = F(J_1^0, J'_2, J'_3). \tag{5}$$

In the 6D stress space, the yield condition $F = 0$ defines a closed hypersurface, called the yield surface. In the 3D space of principle stresses σ_{I}, σ_{II}, and σ_{III}, this surface is two-dimensional. In this space, all planes perpendicular to the hydrostatic axis are called octahedral planes. The octahedral plane passing through the origin is called the deviatoric plane, or π-plane [13].

The geometrical interpretation of the stress invariants introduced is given in Fig. 3 [14].

Finite-Element Simulation

General remarks. For simulating the macroscopic properties of a perforated cell structure, the commercial FE code MSC.Marc was used. Due to the symmetry of all geometry and of the loads applied, only one eight of the unit cell was considered.

First, the geometry of structural elements has to be meshed before calculations. For optimal results, the shape of the elements should show a minimum distortion [15]. To fulfill this requirement, the Mapped-Meshing algorithm provided by the commercial code, which automatically generates a homogenous mesh for simple geometries, was used. Then, after meshing with quadratic elements, the subbodies obtained are reunited, and the coincident nodes are merged. The simple geometries are created by dividing the one eighth of the unit cell into four subbodies (Fig. 4a). In order to merge the meshes of the subbodies, the number of elements of two facing surfaces must be identical. Consequently, the mesh created can be characterized by two mesh parameters, N_1 and N_2, as indicated in Fig. 4b.

After the discretization, material properties and boundary conditions must be specified. Within this project, the material properties of an AlCuMg1 aluminum alloy (E_s = 72,700 N/mm^2, ν_s = 0.34, and the initial tensile yield stress k_s = 300

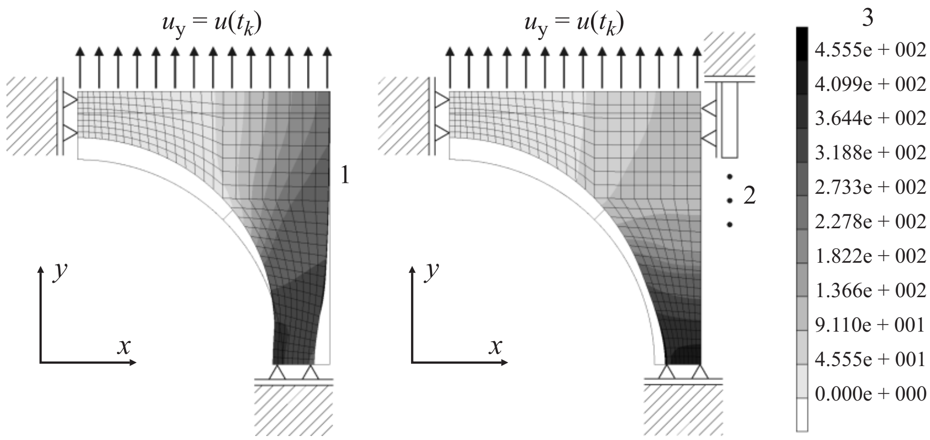

Fig. 5. Unit cell with different boundary conditions and their influence on the shape and the stress distribution: 1 — free surface; 2 — MPC; 3 — equivalent von Mises stress.

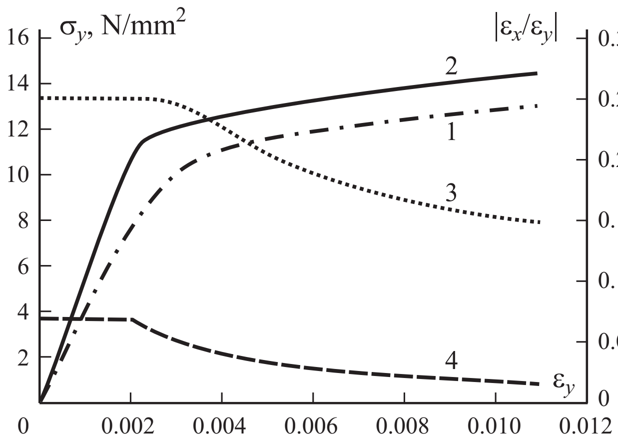

Fig. 6. Influence of boundary conditions on the stress–strain curve and Poisson ratio. 1 — without MPCs, 2 — with MPCs, 3 — $\varepsilon_x/\varepsilon_y$ (without MPCs), 4 — $\varepsilon_x/\varepsilon_y$ (with MPcS). $\rho_{rel} = 0.2$.

N/mm^2; the subcsrip s denotes the solid base material), which were obtained at the Institute of Applied Mechanics (Erlangen-Nuremberg University), were used. The boundary conditions can be separated into those related to the applied macroscopic load and the restrictions caused by the influence of neighboring geometry of the periodic structure. In what follows, only boundary conditions of the second group are described. First, the boundary conditions must be symmetric in order to model the behavior of the whole geometry of the cell structure, although only one eighth of it has been meshed. Then, the free boundaries of the unit cell must be considered. Here, two different approaches were investigated: a free surface and multipoint constraints (MPCs) imposing a periodic boundary. These MPCs ensure that all nodes on a certain surface have the same displacement perpendicular to this surface. Figures 5 shows the effect of the boundary conditions on deformations of the structure and the stress distribution inside the model geometry. On the left figure, the deformation of the model with a free surface is displayed. A strong contraction of the neck along the y-axis is visible. In contrast to this behavior, the special definition of MPCs leads to a lower uniform deformation and a different distribution of the equivalent von Mises stress inside the structure.

The influence of MPCs becomes more evident when the results of an FE analysis are visualized.

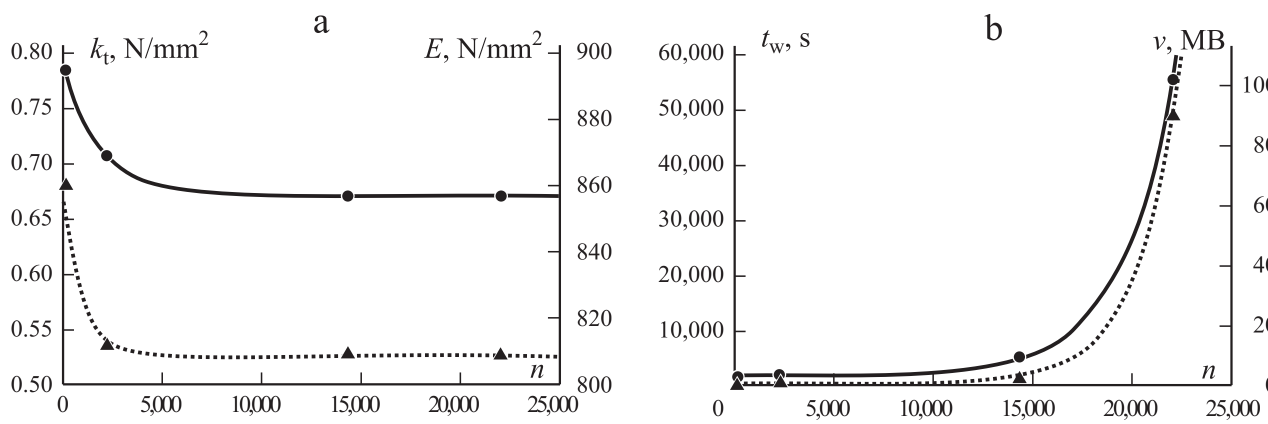

Fig. 7. Influence of mesh density: a — convergence of Young's modulus E (▲) and the initial yield stress k_t (●) with increasing mesh density; b — the wall time t_w (▲) and file size v (●) vs. the number of nodes n. $\rho_{rel} = 0.1$.

Figure 6 illustrates the stress–strain curves and Poisson ratios ν obtained with and without the application of MPCs. It is seen that the MPCs considerably affect the stress–strain curve and significantly lower the Poisson ratio. Since the MPCs allow for the influence of neighboring unit cells of the periodic structure and only RVEs are considered, the MPCs are utilized in all further investigations.

Investigation of mesh density. According to [15], the results obtained by the FEM converge to exact solutions with increasing mesh density. Consequently, a sufficiently fine and homogenous mesh should be generated. However, the computer hardware (i.e., the disk space or RAM) available restricts the fineness of discretization. Figure 7a shows Young's modulus and the macroscopic initial yield stress in relation to the number of nodes, which indicates the mesh density. Both the characteristic quantities considered converge to a constant value for high mesh densities. By taking the results given by the finest mesh as a reference, a 6.35% deviation for Young's modulus and 16.89% for the initial yield stress can be observed for the lowest mesh density. For the second highest mesh density, these deviations decrease to 0.08% (Young's modulus) and 0.01% (the initial yield stress). Figure 7b illustrates the size v of the result file and the wall time t_w in relation to the number of nodes. Both the quantities show an exponential increase with rising mesh density. As a compromise between the accuracy of the FE-analysis and wall time, the second highest mesh density was chosen. Similar investigations were performed for all other relative densities. The final results for the mesh density, represented by the number of nodes and elements, are summarized in Tab. 1. Figure 8 illustrates all the relative densities of the perforated cell structure considered.

Results

Uniaxial tensile tests. To determine Young's modulus E, the Poisson ratio ν, the macroscopic initial yield stress k_t, and the 0.2%-yield strength $R_{p0.2}$ of the material, uniaxial tensile tests were simulated. A Fortran subroutine was implemented to calculate the macroscopic stresses and strains. The results obtained are illustrated in Fig. 9. The figure contains stress–strain curves for each relative density. In the linearly elastic region, all the curves show a characteristic linear increase. The slope of a curve defines Young's modulus for the respective relative density. With rising relative densities, the stress level and Young's modulus both increase (also see Fig. 10).

For the tensile tests, two different types of hardening behavior were used: the real behavior of the AlCuMg1 alloy (polynomial approximation of the flow curve with respect to the equivalent plastic strain as $k_s(\varepsilon^p_{eff}) = 300 + 2455.4\varepsilon^p_{eff} -$

TABLE 1. Selected Mesh Density in Relation to the Relative Density

Relative density ρ_{rel}	Number of nodes	Number of elements
0.1	14,329	2808
0.2	19,197	3968
0.3	19,660	4131
0.4	20,207	4300
0.5	17,435	3700
0.6	28,532	6253
0.7	28,485	6272
0.8	35,515	7936
0.9	32,249	7168

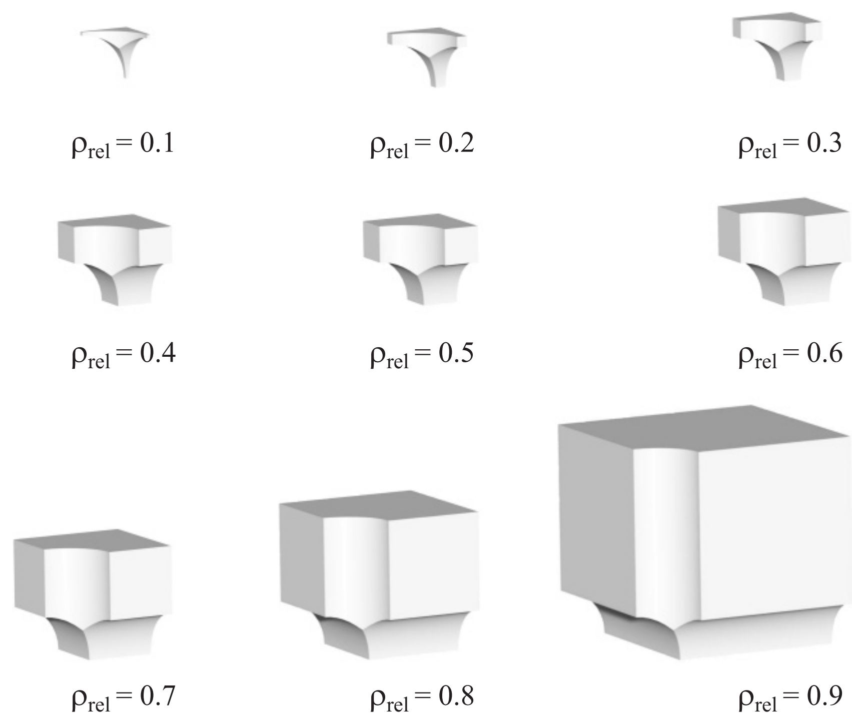

Fig. 8. 3D view of structures with different relative densities.

$13{,}304.0(\varepsilon^{p}_{eff})^2 + 49{,}557.2(\varepsilon^{p}_{eff})^3 - 1.2(\varepsilon^{p}_{eff})^4 + 1.5\cdot 10^5(\varepsilon^{p}_{eff})^5 - 88{,}689.9(\varepsilon^{p}_{eff})^6$, if $\varepsilon^{p}_{eff} \le 0.52$; otherwise 611.8 N/mm^2 = const) and perfect plasticity (k_s = 300 N/mm^2). Both the cases are shown in Fig. 9. The dash-dot lines correspond to the perfectly plastic behavior, and the continuous lines shows the stress–strain curves in the case of polynomial hardening. For the perfectly plastic behavior, the stress–strain curves are taking a slightly lower course in the plastic region, because the hardening of the base material is neglected.

From the uniaxial stress–strain curves, the basic material parameters can be determined. First, Young's modulus is calculated according to Eq. (2). Figure 10 shows a disproportional increase in Young's modulus with relative density. At the relative density ρ_{rel} = 0.058, the connectivity of the material is lost, and Young's modulus reaches the zero value. In the cases

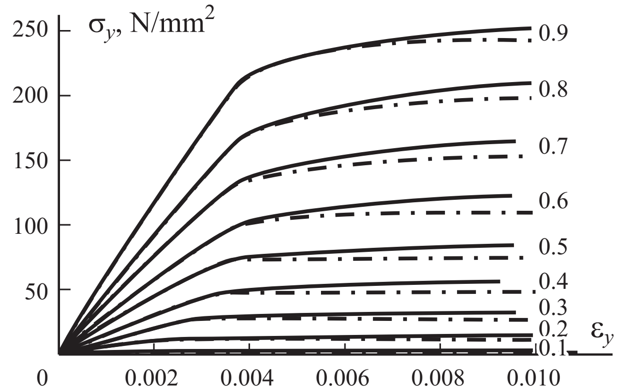

Fig. 9. Macroscopic stress–strain diagrams for different relative densities. Explanations in the text.

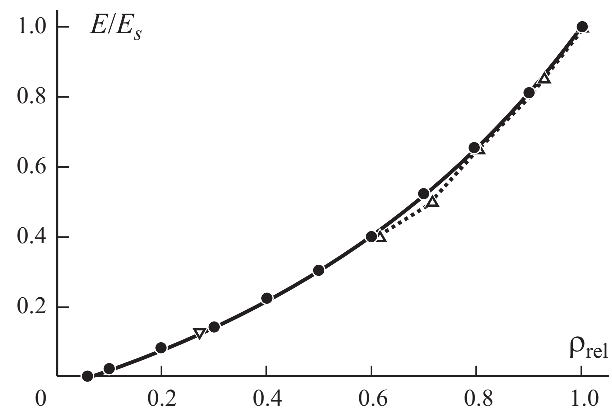

Fig. 10. Relative Young's moduli vs. the relative density: (●) — FE analysis; (△) — 2D experiment [16]; (▽) — 3D experiment [16].

of high relative densities, Young's modulus converges to the stiffness of the solid material. The figure also contains experimental results from 2D and 3D investigations. It is seen that the experimental values agree excellently with FE results.

In Fig. 11, the Poisson ratio as a function of relative density is shown. For relative densities exceeding 0.4, the graph shows a linear relationship, whereas for lower densities a slight nonlinearity is visible. Like Young's modulus, the Poisson ratio reaches the zero value close to the relative density $\rho_{\mathrm{rel}} = 0.058$ and converges to its value for the solid material with growing relative density.

Finally, the yield stresses were determined. To this end, the first increment for which the equivalent stress reached the yield stress of the base material was recorded, and the macroscopic stress in the y-direction was equated to the initial macroscopic yield stress. The normalized initial yield stress $k_{\mathrm{t}}/k_{\mathrm{ts}}$ depends linearly on the relative density. In contrast, the normalized 0.2%-yield strength $R_{\mathrm{p0.2}}/k_{\mathrm{ts}}$, as well as Young's modulus, increases disproportionately with the relative density.

Pure shear test. With the intent to directly determine the shear modulus, pure shear tests were also simulated. Our main concern was to verify the validity of the continuum mechanics approach. This analysis requires the generation of a pure shear stress state. In Fig. 13, different possible boundary conditions for a periodic cellular material are illustrated. Figure 13a shows the generation of a pure shear state by applying the shear stresses τ_{xy} to a material. However, to define appropriate

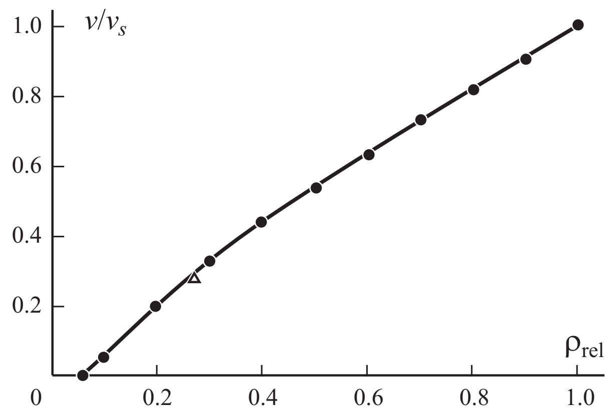

Fig. 11. Relative Poisson ratio vs. the relative density: (●) — FE analysis; (△) — experiment [17].

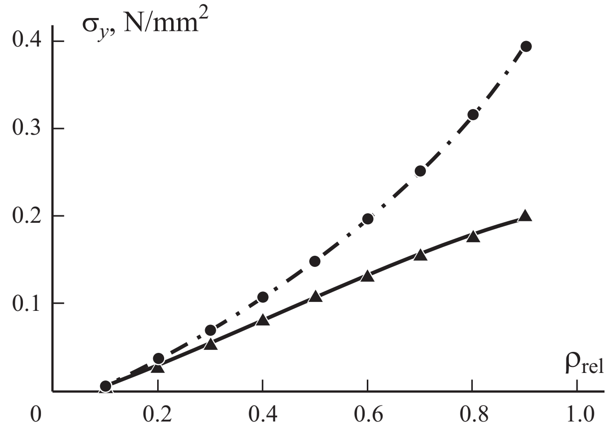

Fig. 12. Relative yield stress vs. the relative density: $R_{p0,2}/k_{ts}$ (●); k_t/k_{ts} (▲).

boundary conditions in the case of a periodic cellular material, it is advisable to transform the shear stresses into the principal stresses. Since our intent is to simulate isotropic solids, all the normal stresses must be applied in the same material axes. Therefore, only possibility 2 (Fig. 13b) can be chosen in order to be in agreement with the uniaxial tests.

The shear modulus G can be determined in two different ways. The first possibility is to calculate G from the ratio between the shear stress τ_{xy} and the shear strain γ_{xy}, with $|\tau_{xy}|=|\sigma_x|$ and $|\gamma_{xy}|=|\varepsilon_x|+|\varepsilon_y|$:

$$G=|\tau_{xy}|/|\gamma_{xy}|. \tag{6}$$

As an alternative, G can be calculated from Young's modulus and the Poisson ratio according to the relation

$$G=\frac{E}{2(1+\nu)}. \tag{7}$$

Table 2 shows the values of the shear modulus determined by using both the methods. As is seen, the maximum difference does not exceed 0.12% and decreases with growing relative density. Thus, we can assert that the continuum mechanics approach provides realistic results within the linearly elastic region for an equivalent isotropic solid.

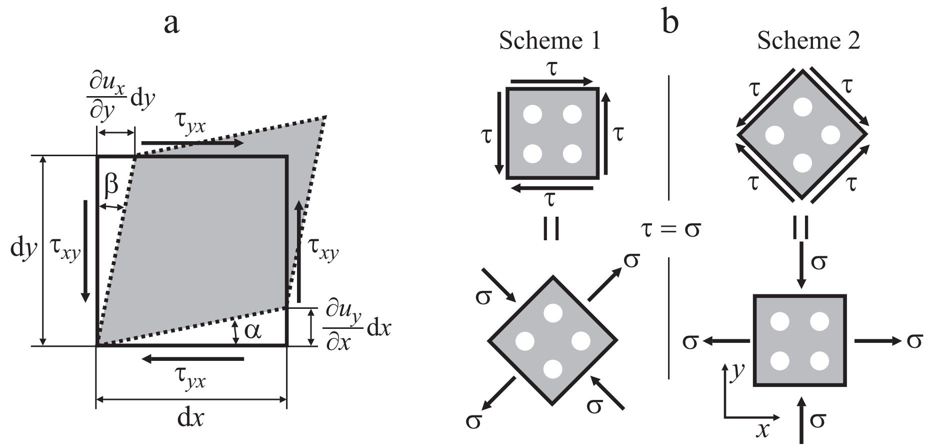

Fig. 13. Different loading conditions for the realization of pure shear stress states. Explanations in the text.

TABLE 2. Comparison of Poisson Ratios

ρ_{rel}	G, N/mm^2, (6)	G, N/mm^2, (7)	Deviation, %
0.1	606.07	605.30	0.12
0.2	2562.32	2559.67	0.10
0.3	4672.07	4668.00	0.09
0.4	6923.86	6917.96	0.09
0.5	9364.75	9358.07	0.07
0.6	12,047.55	12,050.60	0.03
0.7	15,034.03	15,034.03	0.06
0.8	18,431.41	18,420.88	0.06
0.9	22,371.66	22,359.89	0.05

Influence of internal pore pressure. Possible applications of cellular metals can be found in heat exchangers, baffles, flame barriers, and other items influenced by an internal pore pressure p_i. The effect of this pressure was investigated for different relative densities.

Figure 14 shows stress–strain curves for a perforated cell structure with $\rho_{rel} = 0.5$. As a reference, the case without an internal pore pressure is shown. Also, the stress–strain curve obtained under the influence of an internal pore pressure (the initial value is 35 N/mm^2, which is modified during deformation according to the ideal gas law) is presented. Compared to the reference curve, the initial macroscopic tensile yield stress is shifted to lower values, whereas the compressive yield stress reaches higher negative values. The deviation of the macroscopic initial yield stress from the corresponding value of the reference curve ($p_i = 0$ N/mm^2) is 25.5 N/mm^2 both in tension and compression. The third graph in the figure shows that the deviation is still existent after the initial tensile strain (for $\sigma_y = 0$) is removed by simply shifting the stress–strain curve to the origin of coordinates.

A symmetric deviation can also be observed in Fig. 15. Here, the initial yield stresses are shown for different internal pore pressures varying from 0 to 50 N/mm^2. The deviation of the yield stresses is linear and grows with internal pore pressure.

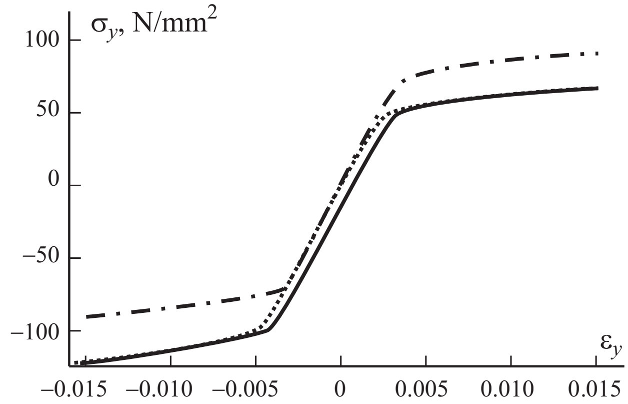

Fig. 14. Influence of internal pore pressure p_i on the macroscopic stress—strain diagram: (——) — 35 N/mm^2; (-·-·-) — 0 N/mm^2; (·····) — shift.

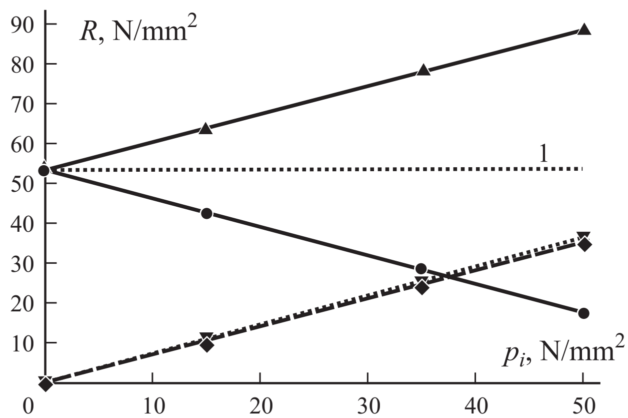

Fig. 15. Influence of internal pore pressure on the initial uniaxial yield stress: (●) — uniaxial tensile yield stress; (▲) — uniaxial compressive yield stress; (▼) — deviation of the tensile yield stress; (◆) — deviation of the compressive yield stress. 1 — uniaxial yield stress without an internal pressure. $\rho_{\text{rel}} = 0.8$.

For all the other relative densities investigated, the same linear character is observed. Furthermore, the deviation of the initial yield stress seems to be independent of the relative density.

Multiaxial tests. To investigate the shape of yield surface, multiaxial stress states are simulated, and the shape in the corresponding octahedral plane is drawn according to the following transformation, which projects the principle stresses first onto the octahedral plane (angle of transformation ϑ, $\cos\vartheta = 1/\sqrt{3}$) and then into the Cartesian coordinate system (x, y) shown in Fig. 16a:

$$y = \frac{2}{\sqrt{6}}[\sigma_{\text{I}} - 0.5(\sigma_{\text{II}} + \sigma_{\text{III}})], \tag{8}$$

$$x = \frac{1}{\sqrt{2}}(\sigma_{\text{III}} - \sigma_{\text{II}}). \tag{9}$$

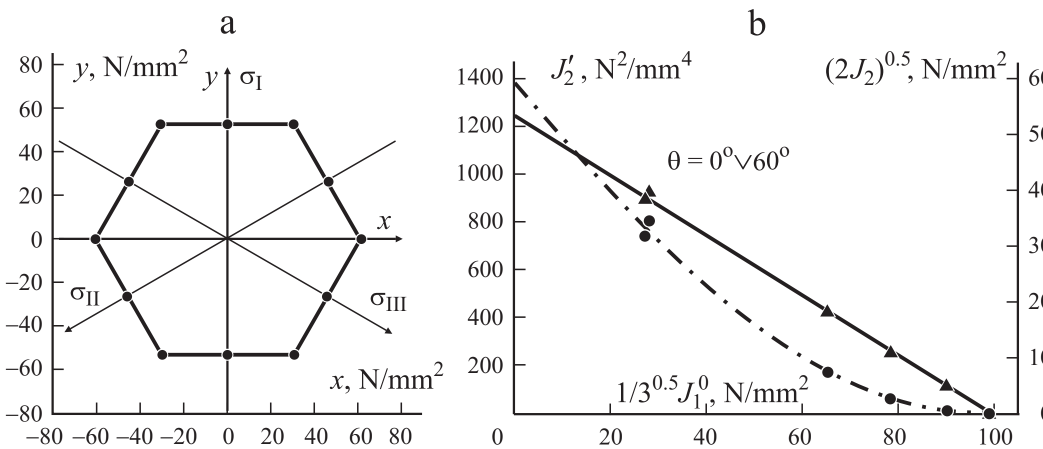

Fig. 16. Shape of the yield surface in the deviatoric plane $\rho_{rel} = 0.7$ (a) and along the hydrostatic axis (b): J'_2 (●); $(2J_2)^{0.5}$ (▲).

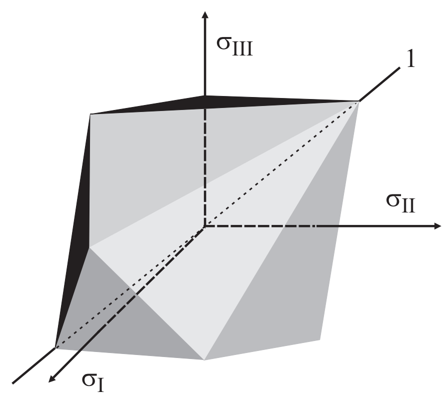

Fig. 17. Yield surface in the space of principal stresses. 1 — hydrostatic axis.

Here, it is important whether the plastic behavior is pressure sensitive, i.e., depends on J_1^0 or not. If there is no such a dependence, i.e., the yield surface does not change along the hydrostatic axis, all stress states can be considered in a single octahedral plane. Otherwise only stress states with the same hydrostatic stress can be represented in the same octahedral plane with J_1^0 = const. As a results, e.g., uniaxial tensile ($J_1^0 = \sigma_I$) and pure shear ($J_1^0 = 0$) tests cannot be represented in the same octahedral plane. In order to construct the yield surface for the pressure-sensitive material examined, different multiaxial stress states with $J_1^0 = 0$, e.g., $\sigma_I = -\sigma_{II}$ $(\sigma_{III} = 0)$ or $\sigma_I = -2\sigma_{II} = -2\sigma_{III}$ $(\sigma_I > 0 \vee \sigma_I < 0)$, were realized, and the corresponding yield stresses were plotted in the deviatoric plane, Fig. 16. The regular hexagon obtained corresponds to the outer bound of convex yield conditions in the octahedral plane [14]. The filled circles in Fig. 16 are results from the finite-element simulation. It should be noted here that this shape changes only in size (self-similarly) along the hydrostatic axes.

To clarify the influence of the hydrostatic stress on the yield surface, its sections through the hydrostatic axis for $\theta = 0° \vee 60°$ (Fig. 3) are shown in Fig. 16b. In this figure, the second invariant J_2' is plotted on the left vertical axis, and a concave curve is obtained. However, to investigate the convexity of a yield surface (as required by Drucker's stability postulate), the so-called Haigh–Westergaard coordinates J_1^0 and $\sqrt{2J_2'}$ are appropriate. In this coordinate system (Fig. 16b), a straight line is obtained, and the convexity is confirmed. Figure 17 illustrates the yield surface in the space of principal stresses, and a double-sided pyramid generated by twelve planes is seen.

Conclusion

A periodic model of a cellular metal has been developed for fundamental studies of the mechanical behavior of cellular materials over a wide range of relative densities. The numerical simulation of its uniaxial mechanical behavior agreed well with experimental results for 2D and 3D cellular structures. The effect of different hardening behavior was much smaller than the effect of different relative densities. The investigations of the mechanical behavior in the case of internal pore pressure revealed that, even under quasi-static conditions, the uniaxial stress–strain behavior was significantly influenced, and different results in tension and compression were obtained. Under the condition that all normal stresses are applied in the same material axes, a convex yield surface depending on all three stress invariants were obtained. These results will be used to simulate the mechanical behavior of sandwich structures with periodic cellular core materials in our further research work.

Acknowledgements. T. Fiedler is grateful to the European Union, which supported this work within the framework of the ERASMUS/SOKRATES program. A. Öchsner is grateful to Portuguese Foundation of Science and Technology for the financial support.

REFERENCES

1. H. Hertel, Leichtbau, Berlin, Springer Verlag (1960).
2. C. Körner and R. F. Singer, "Processing of metal foams — challenges and opportunities," Adv. Eng. Mater., **2**, No. 4, 159-165 (2000).
3. M. F. Ashby and T. J. Lu, "Metal foams: a survey," Sci. China, Ser. B, **46**, 521-532 (2003).
4. M. F. Ashby, A. Evans, N. A. Fleck, L. J. Gibson, J. W. Hutchinson, and H. N. G. Wadley, Metal Foams: A Design Guide, Butterworth-Heinemann, Boston (2000).
5. T. Furio and M. Zoccala, The Future of Ship Doors — Lattice Block Materials (2001) (published online).
6. M. S. Gadala, M. L. Mullins, and M. A. Dokainish, "A Modified plasticity theory for porous solids," Int. J. Num. Meth. Eng. **15**, 649-660 (1980).
7. R. J. Green, "A plasticity theory for porous solids," Int. J. Mechn. Sci. **14**, 215-224 (1972).
8. A. L. Gurson, Plastic Flow and Fracture Behavior of Ductile Materials Incorporating Void Nucleation, Growth, and Interaction, PhD Thesis, Brown University (1975).
9. D.-Z. Sun, "Micromechanical modelling of ductile damage in metals," Tagungsband der 28, Tagung des DVM-Arbeitskreises Bruchvorgänge, 287-304, Bremen (1996).
10. V. Tvergaard, "On localization in ductile materials containing spherical voids," Int. J. Fract. **18,** 237-252 (1982).
11. A. Öchsner and K. Lamprecht, "On the uniaxial compression behavior of regular shaped cellular metals," Mech. Research Comm., No. 30, 573-579 (2003).
12. H. Armen, "Assumptions, models, and computational methods for plasticity," Comput. Struct. **10**, 161-174 (1979).
13. G. Backhaus, Deformationsgesetze, Akademie-Verlag, Berlin (1983).
14. W.-F. Chen and D. J. Hahn, Plasticity for Structural Engineers, Springer, New York (1988).

15. B. Klein, FEM Grundlagen und Anwendungen der Finite-Element-Methode, Friedr. Vieweg & Sohn Verlag/GWV Fachverlage GmbH, Wiesbaden (2003).
16. A. Öchnser, Experimentelle und numerische Untersuchung des elasto-plastischen Verhaltens zellularer Modellwerkstoffe, PhD Thesis, University Erlangen-Nuremberg (2003).
17. T. Fiedler, Experimentelle Untersuchung zellularer Werkstoffe unter biaxialen Spannungszuständen, Student Project, University Erlangen-Nuremberg (2002).

Archive of Applied Mechanics 73 (2003) 261 – 269 © Springer-Verlag 2003
DOI 10.1007/s00419-003-0287-4

On an elastic-plastic transition zone in cellular metals

A. Öchsner, W. Winter, G. Kuhn

Summary A theory of plasticity is proposed for cellular metals to describe their elastic-plastic transition zone at small strain. Under certain conditions, only a plane strain test is necessary to determine the yield surface. The method to derive the elastic–plastic behaviour [14, 15] was originally proposed for classical metals. A simple cubic model of a cellular metal is used to demonstrate the method by the finite element method. Recommendations for the numerical simulation are given. The influence of the relative density and the hardening behaviour of the cell wall material is investigated.

Keywords Cellular metal, Nonlinear behaviour, Plasticity, Yield surface, Relative density

1 Introduction

Cellular metals, e.g. metallic foams, exhibit unique properties and are currently under consideration for use in lightweight structures of automobiles, aircrafts, etc. as well as passive safety components, [3]. There have been developed many methods for their fabrication and one can classify them into four groups: foams made from melts, from powders, by sputtering and by deposition, [5]. Some fabrication methods have been known since the fifties, and each of them results in a characteristic cellular structure. There are technological problems related to the control of the material structure, since the vast majority of existing technologies do not allow for precise control of the shape, size and distribution of the cellular pores. That brings about a wide scatter in mechanical and other characteristics of these materials and components.

Recently developed fabrication methods for hollow spherical structures result in quite homogeneous pore structures, Fig. 1. First experimental investigations show that the material properties of comparable samples seem to be entirely reproducible, [1]. The mechanical properties of cellular metals, in particular their resistance to plastic deformation, the evolution and progress of damage and fracture within the material, are determined by the microstructure and the cell wall material, respectively. The most important structural parameters which characterize a cellular metal are the morphology of its cell (geometry, open or closed cell), the topology, the mean cell size and the relative density, ρ/ρ_S (the macroscopic density, ρ, divided by that of the solid material of the cell wall, ρ_S).

A schematic uniaxial compression stress-strain curve for a cellular metal is shown in Fig. 2. It shows linear elasticity at low stresses, followed by a transition zone which is followed by a long collapse plateau, truncated by a regime of densification, in which the stress rises exponentially. Many investigations focus on the large deformations taking place in zones 3 and 4. The initial yield stress k is then equated with the plateau stress k_{Plat}, so that the transition zone, which can be clearly distinguished in certain cellular metals, remains unconsidered. Relationships for the elastic and plastic (plateau) behaviour of low-density foams are given in [9].

In this paper, we will investigate the elastic-plastic transition zone 2 under multi-axial loading conditions and apply to cellular metals an interesting method to characterize the

Received 27 June 2002; accepted for publication 20 March 2003

A. Öchsner (✉), W. Winter, G. Kuhn
Institute of Applied Mechanics,
University of Erlangen-Nuremberg,
Egerlandstrasse 5, 91058 Erlangen, Germany
e-mail: oechsner@ltm.uni-erlangen.de

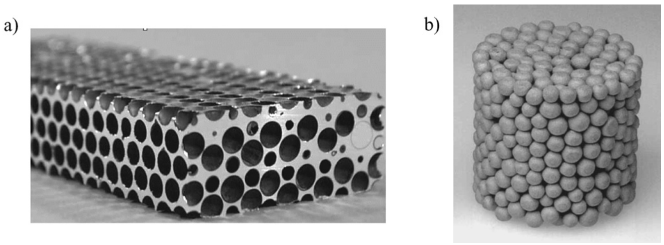

Fig. 1. **a** Syntactic foam: hollow alumina spheres embedded in a magnesium matrix and **b** Hollow sphere foam $Fe_{0.88}Cr_{0.12}$, [13]

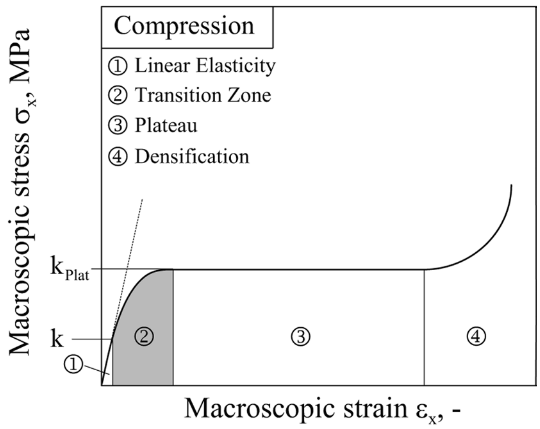

Fig. 2. Schematic uniaxial compression stress-strain curve for a metal foam

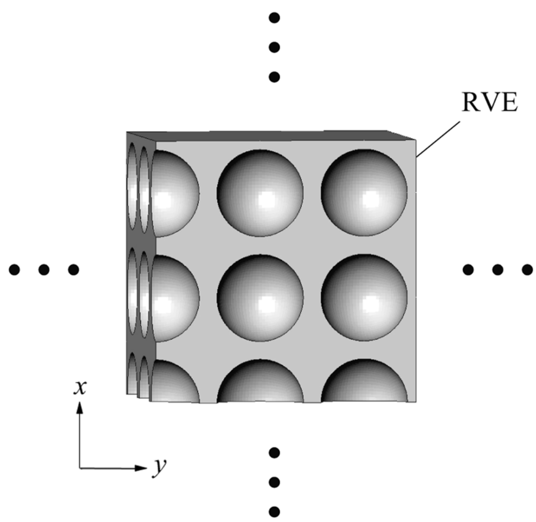

Fig. 3. Representative volume element of the simple cubic cell structure

elastic-plastic behaviour that was originally proposed for full dense metals, [14, 15]. Beside a uniaxial test for the determination of the elastic constants, only a plane strain experiment is necessary to describe the elastic-plastic behaviour. A simple cubic cell structure is used, Fig. 3, that exhibits properties similar to those of the samples shown in Fig. 2 to demonstrate principally the procedure, and to verify the theory by finite element (FE) simulations. Transfer to other cell structures should be possible too.

2
Constitutive modeling of cellular metals

The mechanical behaviour of a cellular metal and its mathematical characterisation can be described based upon the principles of continuum mechanics, if a representative volume element (RVE) is considered, Fig. 3. In the case of cellular materials, this RVE needs to comprise of at least five to ten unit cells (UC), in order to represent macroscopic values. The precise number depends, however, on the corresponding cell structure and should be examined separately.

Since the intention of this paper is to model only isotropic solids, no further account is taken of the anisotropy caused by the particular pore distribution, and only strain states having principle strain distributions parallel to the x- and y-axes are considered (cf. Sec. 3). This modelling technique, based on homogenous cell structures, has already been applied for the description of the plastic behaviour of porous metals, [8, 10], and for the modeling of damage effects, [11, 16, 17]. However, the elastic-plastic transition zone (cf. Fig. 2) was not investigated in those works.

2.1 Elastic behaviour

Under the classical assumptions of small strains and linear relationships between the second-order stress tensor σ_{ij} and the strain tensor ε_{ij}, the elastic stress-strain relation is given by the general Hooke's law

$$\varepsilon_{ij} = \frac{1+\nu}{E}\left(\sigma_{ij} - \frac{\nu}{1+\nu}\,\delta_{ij}\sigma_{kk}\right) = C^{-1}_{ijkl}\sigma_{ij} \ , \tag{1}$$

where E is the Young's modulus, C_{ijkl} the fourth-order stiffness moduli tensor and ν the Poisson's ratio. In a uniaxial tension or compression test, the only non-zero stress component σ_{xx} causes axial strain ε_{xx} and transverse strains $\varepsilon_{yy} = \varepsilon_{zz}$. Thus, one can determine the elastic constants, i.e. the Young's modulus and the Poisson's ratio from Eq. (1).

2.2 Plastic behaviour

The three essential ingredients of plastic analysis are: the *yield criterion*, the *flow rule*, and the *hardening rule*, [2]. The yield criterion relates the state of stress to the onset of yielding. The flow rule relates the state of stress σ_{ij} to the corresponding increments of plastic strain $d\varepsilon^p_{ij}$, when an increment of plastic flow occurs. The hardening rule describes how the yield criterion is modified by straining beyond initial yield.

The yield criterion for an isotropic material can generally be expressed as

$$F = F(\sigma_{ij}, \kappa, \eta_{ij}) = 0 \ , \tag{2}$$

where κ is the isotropic hardening parameter and η_{ij} the kinematic hardening parameters respectively. The state of stress σ_{ij} can be split in its spherical σ^o_{ij} and deviatoric part $\sigma'_{ij} = s_{ij}$ and then expressed in terms of the combinations of the three stress invariants J^o_1, J'_2 and J'_3, where J^o_1 is the first invariant of the spherical stress tensor and J'_2 and J'_3 are the second and third invariants of the deviatoric tensor, [4]. Thus, one can replace Eq. (2) by

$$F = F(J^o_1, J'_2, J'_3, \kappa, \eta_{ij}) = 0 \ . \tag{3}$$

The elastic relation (1) prevail when $F < 0$. When the stresses are such that $F = 0$, yielding begins or is already in progress. The case of $F > 0$ is not physically possible. The flow rule is stated in terms of a function Q, which is described in units of stress, and is called a *plastic potential*. With $d\lambda$ a scalar called *plastic multiplier*, the plastic strain increments are given by

$$d\varepsilon^p_{ij} = d\lambda \frac{\partial Q}{\partial \sigma_{ij}} \ . \tag{4}$$

The flow rule is said to be *associated* if $Q = F$, otherwise it is *nonassociated*. Hardening can be modelled as isotropic (i.e. initial yield surface expands uniformly without distortion and translation as plastic flow occurs) or as kinematic (i.e. initial yield surface translates as a rigid body in stress space, maintaining its size, shape and orientation), either separately or in combination.

2.3 Elastic-plastic behaviour under plane strain condition

Under the assumption of small strains, the total strain increment $d\varepsilon_{ij}$ is assumed to be the sum of the elastic strain increment $d\varepsilon^e_{ij}$ and the plastic strain increment $d\varepsilon^p_{ij}$

$$d\varepsilon_{ij} = d\varepsilon^e_{ij} + d\varepsilon^p_{ij} \ , \tag{5}$$

where the elastic strain increment can be obtained from Hooke's law (1) and the plastic strain increment from the flow rule (4). The elastic-plastic transition zone of metals can be described according to [15] by the following yield criterion:

$$F = \underbrace{\alpha\left(J_1^o\right)^2 + J_2'}_{f} - (k^s)^2 = 0 \quad , \tag{6}$$

where the parameter α and the shear yield stress k^s control the transition in the elastic-plastic range. When α is zero, Eq. (6) reduces to the well-known von Mises criterion, e. g. [12]. Application of the chain rule gives the derivative of the scalar function F, with respect to the
264 stress tensor σ_{ij} as

$$\frac{\partial F(J_1^o, J_2')}{\partial \sigma_{ij}} = \frac{\partial F}{\partial J_1^o} \cdot \frac{\partial J_1^o}{\partial \sigma_{ij}} + \frac{\partial F}{\partial J_2'} \cdot \frac{\partial J_2'}{\partial \sigma_{ij}} = 2\alpha J_1^o \delta_{ij} + s_{ij} \quad . \tag{7}$$

If Hooke's law (1) is applied for the elastic component and the associated flow rule (4) for the plastic component, the complete stress-strain relationship for a material obeying the yield criterion (6) is expressed as

$$d\varepsilon_{ij} = d\lambda \cdot \left(2\alpha J_1^o \delta_{ij} + s_{ij}\right) + \frac{1+\nu}{E}\left(d\sigma_{ij} - \frac{\nu}{1+\nu}\,\delta_{ij} d\sigma_{kk}\right) \quad . \tag{8}$$

Here the scalar parameter α must be determined experimentally. Following [14, 15], a plane strain state is examined for that purpose. In a plane strain state of a planar cube (no wall friction, principal directions are I, II, III), we may have e.g.

$$\sigma_I > 0 \quad \wedge \quad \varepsilon_I \neq 0 \quad , \tag{9}$$

$$\sigma_{II} \neq 0 \quad \wedge \quad \varepsilon_{II} = 0 \quad , \tag{10}$$

$$\sigma_{III} = 0 \quad \wedge \quad \varepsilon_{III} \neq 0 \quad , \tag{11}$$

where σ_I, σ_{II} and ε_I are the measured values. Using Eqs. (9)–(11) with the associated flow rule (4) and (8), the increments of the plastic strains are given by:

$$d\varepsilon_I^p = d\lambda\left[2\alpha(\sigma_I + \sigma_{II}) + \frac{1}{3} \cdot (2\sigma_I - \sigma_{II})\right] \quad , \tag{12}$$

$$d\varepsilon_{II}^p = d\lambda\left[2\alpha(\sigma_I + \sigma_{II}) + \frac{1}{3} \cdot (2\sigma_{II} - \sigma_I)\right] \quad . \tag{13}$$

Dividing Eq. (13) by (12) and rearranging, the function α is obtained as

$$\alpha = \frac{1}{6} \cdot \frac{\sigma_{\mathrm{I}}\left(1 + 2 \cdot \frac{d\varepsilon_{II}^p}{d\varepsilon_I^p}\right) - \sigma_{II}\left(\frac{2 + d\varepsilon_{II}^p}{d\varepsilon_I^p}\right)}{(\sigma_I + \sigma_{II})\left(1 - \frac{d\varepsilon_{II}^p}{d\varepsilon_I^p}\right)} \quad . \tag{14}$$

For small plastic strains (respectively at the beginning of the yielding), the quotient is $d\varepsilon_{\mathrm{II}}^p / d\varepsilon_{\mathrm{I}}^p \ll 1$ (respectively $= 0$) and the quantity α can be approximated by

$$\alpha \approx \frac{1}{6} \cdot \frac{\sigma_I - 2\sigma_{II}}{\sigma_I + \sigma_{II}} \quad . \tag{15}$$

The increment of plastic strain can be determined from Eq. (5)

$$d\varepsilon_I^p = d\varepsilon_I - d\varepsilon_I^e \quad , \tag{16}$$

$$d\varepsilon_{II}^p = \underbrace{d\varepsilon_{II}}_{=0} - d\varepsilon_{II}^e = -d\varepsilon_{II}^e \quad , \tag{17}$$

while the elastic strain increment can be obtained from Hooke's law (1).

In the hardening theory of plasticity, the hardening parameter in the yield criterion must be related to the experimental uniaxial stress-strain curve. To this end, one needs to define a stress variable, called *effective stress*, which is a function of the stresses and some strain variable, called *effective strain*, which is a function of the plastic strains, so that they can be plotted and used to correlate the test results obtained by different loading conditions, [7]. Since the effective stress should reduce to the stress σ_I in a uniaxial test, it follows that the function $f(\sigma_{ij})$ must be some constant c multiplied by the effective stress σ_{eff} to some power n

$$f(\sigma_{ij}) = c \cdot \sigma_{eff}^n \quad . \tag{18}$$

For the uniaxial test, $\sigma_{eff} = \sigma_I$ and $\sigma_{II} = \sigma_{III} = 0$, coefficient comparison gives $c = \alpha + \frac{1}{3}$ and $n = 2$, and the effective stress can be expressed as

$$\sigma_{eff} = k = \sqrt{\frac{\alpha(J_1^o)^2 + J_2'}{\alpha + \frac{1}{3}}} \overset{\text{pl.strain}}{\Rightarrow} \sqrt{\frac{3\alpha(\sigma_I + \sigma_{II})^2 + \sigma_I^2 + \sigma_{II}^2 - \sigma_I\sigma_{II}}{3\alpha + 1}} \quad . \tag{19}$$

The effective plastic strain increment $d\varepsilon_{eff}^p$ can be defined in terms of the plastic work per unit volume in the form

$$dw^p = \sigma_{eff} \mathrm{d}\varepsilon_{eff}^p = \sigma_{ij} d\varepsilon_{ij}^p \overset{\text{pl.strain}}{\Rightarrow} \sigma_I d\varepsilon_I^p + \sigma_{II} d\varepsilon_{II}^p + \underbrace{\sigma_{III}}_{=0} d\varepsilon_{III}^p \quad . \tag{20}$$

It follows from Eq. (20) using Eqs. (1) and (19), that in the case of a plane strain test the effective plastic strain increment is given by the following equation

$$d\varepsilon_{eff}^p = \frac{1}{\sigma_{eff}} \cdot \left[\sigma_I d\varepsilon_I^p - \frac{1}{E}\, \sigma_{II}(d\sigma_{II} - v d\sigma_I) \right] \quad . \tag{21}$$

3
Finite element simulation

The commercial FE code MSC.Marc was used for the simulation of the macroscopic properties of the chosen cell structure, Fig. 3. A fine mesh with solid elements (quadratic shape functions) of such a cell structure consisting of five to ten unit cells would lead, however, to a large amount of unknowns and a huge computing time. Therefore, only a typical repeating portion (unit cell) was simulated. Due to the symmetry of the unit cell, only one eighth needs to be considered. The mechanically correct constraints are of great importance in this case, Fig. 4. Some researchers use one surface of the unit cell as a free boundary. However, to simulate the

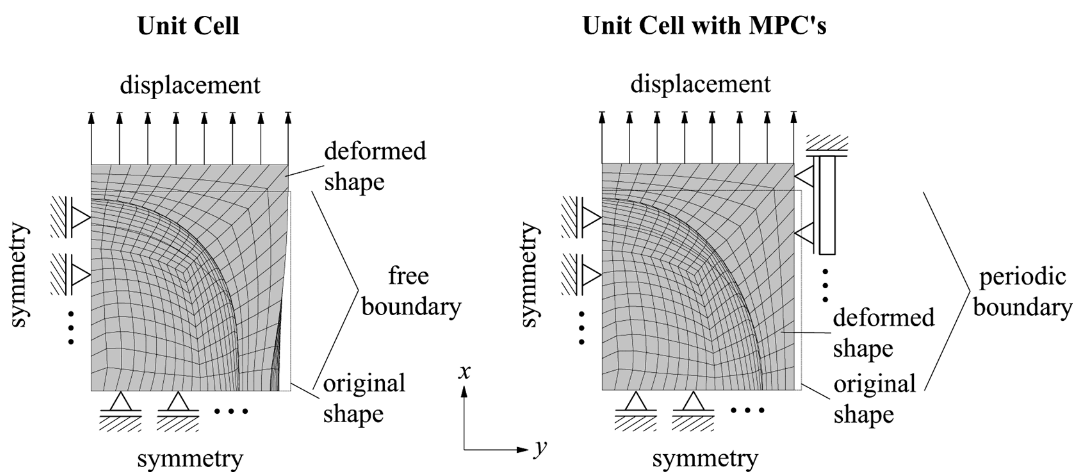

Fig. 4. Finite element model of a unit cell with boundary conditions and applied loads for uniaxial tension

mechanical behaviour of a *cell structure*, only a periodic boundary provides the correct constraint. With the aid of multiple point constraints (MPC), the used FE-system offers the possibility to realize such a boundary condition where all nodes on a certain surface have the same x-displacement.

The effect of different boundary conditions on the deformation can be seen in Fig. 4. The possible errors due to inadequate boundary conditions on the Young's modulus E, the Poisson's ratio ν and initial tensile yield stress k^{init} can be taken from Table 1. All the following simulations were carried out with this periodic boundary. Six different relative densities were realised (cf. Table 2) and the influence of the different hardening behaviours of the base material on the results were investigated . Besides the realistic hardening behaviour of an
266 aluminium alloy (AlCuMg1), the two limiting cases: ideal plasticity ($k = 301.06$ MPa $=$ const.), and linear hardening ($k = 1/20 \cdot E_S \cdot \varepsilon^p_{eff}$) were considered. The base material was assumed to be isotropic and to obey the von Mises yield criterion with the associated flow rule. A number of computer runs were carried out to ensure the convergence of the selected mesh. The final mesh data is summarized in Table 2.

Under certain circumstances it may be necessary that a cell structure built up from several cells should be modelled (e.g. anisotropic damage). Then, the resulting calculation of a unit cell with periodic boundary conditions provides an elegant way to show whether the number of the cells in the structure can be regarded as a representative structure.

4 Results

4.1 Uniaxial tension tests

From the point of view of continuum mechanics, a state under pure shear stress (result: shear modulus G) and a state under pure hydrostatic stress (result: bulk modulus K) should aim to determine the elastic constants, since the constants are independent from each other in this case. However, the experimental determination of the elastic constants is mostly based on a simple realisable tension or compression test, from which Young's modulus and Poisson's ratio can be obtained. Therefore, a uniaxial tension test is considered in the following. A typical stress-strain diagram for such a uniaxial tension test is shown in Fig. 5. The initial elastic region appears as a straight line, where the Young's modulus can be calculated from Eq. (1). Application of Eq. (1) also gives the Poisson's ratio as a negative ratio of the lateral to the axial strain. The initial (macroscopic) yield stress is recorded when the equivalent stress of an integration point reaches the yield stress of the base material.

The results for the normalized Young's modulus and Poisson's ratio as a function of the relative densities are summarized in Fig. 6. A clear decrease of the elastic stiffness and contraction number with decreasing relative density can be seen. These values form the basis for the evaluation of the plastic material behaviour. In this graph, the limit of the relative density (contact of two pores) of the chosen cell model, $(\rho/\rho_S)_{limit} = 0.48$, is marked. Since the chosen

Table 1. Comparision of uniaxial tensile test results for different boundary conditions

Unit cell	Unit cell with MPC's	Deviation
$E = 39969$ MPa	$E = 42784$ MPa	6.58%
$\nu = 0.3229$	$\nu = 0.2784$	15.98%
$k^{init} = 81.4$ MPa	$k^{init} = 114.7$ MPa	28.97%

Table 2. Selected mesh density

Relative density	Number of nodes	Number of elements
0.95	11297	2400
0.90	8713	1800
0.80	4835	960
0.70	7421	1500
0.60	11769	2352
0.50	13464	2700

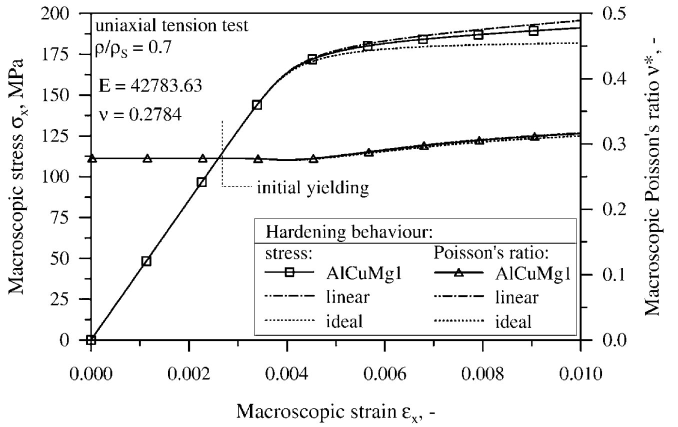

Fig. 5. Uniaxial tensile stress-strain curves and Poisson's ratios for a unit cell with a relative density of $\rho/\rho_S = 0.7$

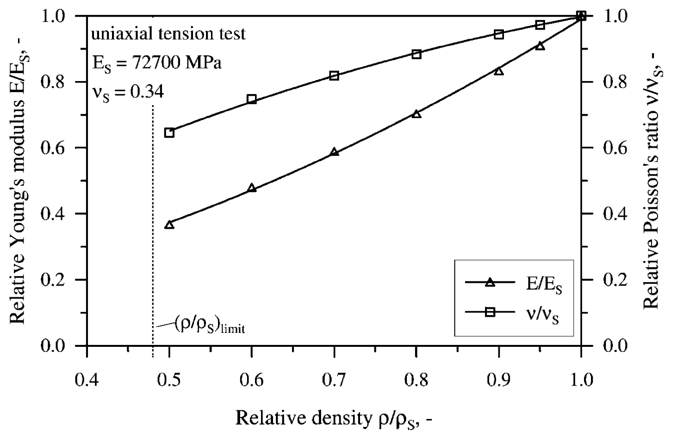

Fig. 6. Relative Young's modulus and relative Poisson's ratio plotted against relative density

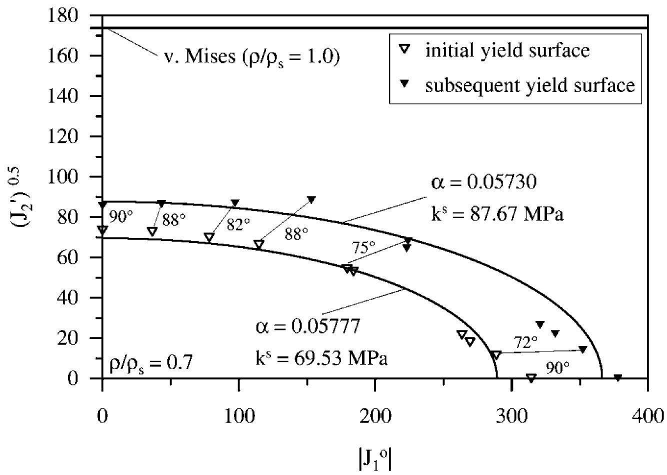

Fig. 7. The initial and subsequent yield surface for a relative density of $\rho/\rho_S = 0.7$

cell structure should be an idealised model of a cellular metal where in the theoretical case $E/E_S \to 0$ for $\varrho/\varrho_S \to 0$ holds, the investigated relative densities of the cell structure should not be so close to $(\rho/\rho_S)_{limit}$, since $E/E_S \to 0$ for $\varrho/\varrho_S \to (\rho/\rho_S)_{limit}$ is valid. This drop in stiffness is not discussed in this paper. It should be noted here, that Young's modulus and Poisson's ratio can be converted into shear and bulk moduli by the classical relationships for isotropic materials, e. g. [6].

4.2
Multiaxial tests

For the determination of the yield criterion, one needs to realize different multi-axial stress or strain states. Figure 7 shows the numerical results obtained for the yield stress and the slope of the yield criterion at points of first yielding and a subsequent yield surface obtained by connecting points with the same value of plastic work w^p. Altogether ten states of strain were analysed. It can be seen that the points can be fitted by a yield criterion according to Eq. (4), which is an elliptical curve in the $\left(\sqrt{J_2'}, J_1^o\right)$ - plane (semi axes: $k^s/\sqrt{\alpha}$ and k^s). This elliptical shape is also common in the context of soil mechanics or sintered metals. To check the normality criterion (associated flow rule), the angle between the incremental plastic strain vector and the tangent to the yield surface has been calculated and is shown in Fig. 7. An acceptable agreement has been obtained for most of the stress states. It should be noted that the values were more accurate for smaller plastic strain increments.

268

4.3 Plane strain tests

The results of the measured stresses of a plane strain test are shown in Fig. 8. In the elastic region $\varepsilon_{II}^e = 0$ is valid and from Eq. (1) we get $\nu = \sigma_{II}/\sigma_I = 0.2784$, a new relationship for the calculation of Poisson's ratio. This value was obtained from the uniaxial tension test, see Table 1. This ratio changes in the elastic-plastic transition zone and converges towards the straight line $\sigma_{II} = 0.4185\sigma_I$ (case of rigid-plastic yielding of a von Mises material; cf. Eq. (17) with (13)). It is interesting that in the case of ideal plasticity the convergence is not so marked since the stress increase is prevented due to the constant yield stress. In conventional plasticity, it is assumed that the volume remains constant for the material undergoing plastic deformation ($d\varepsilon_{kk}^p = 0$). In the deformation of cellular metals, however, the volume does not remain constant in the plastic region.

The progression of the parameter $\alpha = \alpha(\varepsilon_{eff}^p)$ according to Eq. (14) is shown in Fig. 9. For the first few increments after initial yielding, the approximation according to Eq. (15) was used. The parameter decreases constantly from the initial value $\alpha = 0.05777$ but does not reach zero,

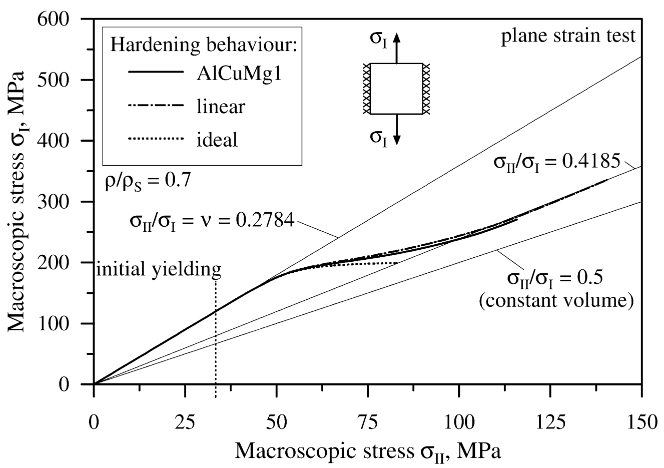

Fig. 8. The progress of stress in a plane strain test for a relative density of $\rho/\rho_S = 0.7$

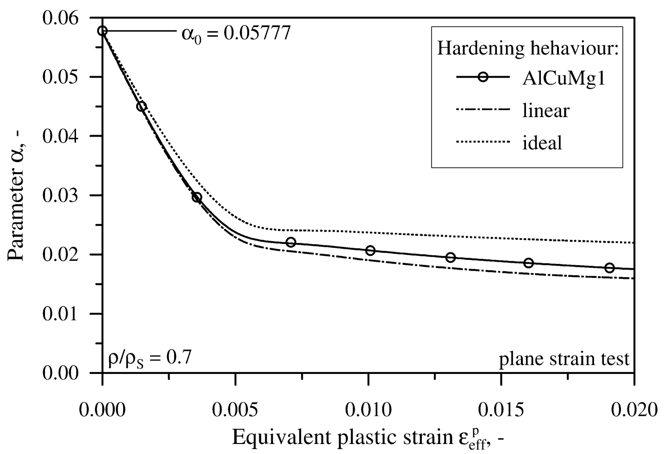

Fig. 9. The dependence of the parameter α on the equivalent plastic strain for a relative density of $\rho/\rho_S = 0.7$

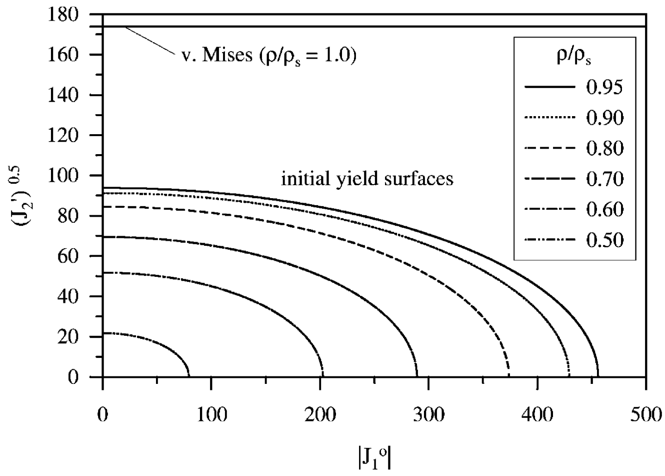

Fig. 10. Initial yield surface as a function of the relative density

as in the case of classical metals. The progression of k or k^s is not shown here, since the results can also be obtained from the uniaxial test, Fig. 5.

Under the given assumptions, it is now possible to determine the yield surface by a plane strain test. Figure 10 summarizes the shape of the initial yield surface for differing relative densities.

5
Conclusion

A method that was originally proposed for the elastic-plastic transition zone of metals [14, 15], has been successfully applied to a simple model of a cellular metal. Under the assumption of the validity of a yield criterion according to (6) and the associated flow rule, a simple plane strain test offers the possibility to determine the yield surface for different relative densities. The application of the method to other cell structures (e.g. for open cell structures with low density) and experimental realisations are reserved for future research.

References

1. **Anderson, O.; Waag, U.; Schneider, L.; Stephani, G.; Kieback, G.:** Novel metallic sphere structures: processing and properties. In: Banhart, J. et al. (Eds.) Metal Foams and Porous Metal Structures, pp. 183–188. Bremen: Verlag MIT Publishing 1999
2. **Armen, H.:** Assumtions, models, and computational methods for plasticity. Comput Struct 10 (1979) 161–174
3. **Ashby, M.F.; Evans, A.; Fleck, N.A.; Gibson, L.J.; Hutchinson, J.W.; Wadley, H.N.G.:** Metal foams: A design guide. Boston: Butterworth-Heinemann 2000
4. **Backhaus, G.:** Deformationsgesetze. Berlin: Akademie-Verlag 1983
5. **Banhart, J.; Baumeister, J.:** Production methods for metallic foams. In: Shwartz, D. et al. (Eds.) porous and cellular materials for structural applications: MRS Symposium Proceedings 521, pp. 121–132. Warrendale: Materials Research Society 1998
6. **Chen, W.F.; Hahn, D.J.:** Plasticity for structural engineers. New York: Springer-Verlag 1988
7. **Chen, W.F.; Zhang, H.:** Structural plasticity: theory, problems, and CAE software. New York: Springer-Verlag 1991
8. **Gadala, M.S.; Mullins, M.L.; Dokainish, M.A.:** A modified plasticity theory for porous metals. Int. J. Numer Methods Eng. 15 (1980) 649–660
9. **Gibson, L.J.; Ashby, M.F.:** Cellular solids. Cambridge: Cambridge University Press 1997
10. **Green, R.J.:** A plasticity theory for porous solids. Int. J. Mech. Sci. 14 (1972) 215–224
11. **Gurson, A.L.:** Plastic flow and fracture behavior of ductile materials incorporating void nucleation, growth, and interaction. Providence, RI: Brown University: PhD Thesis 1975
12. **Hill, R.:** The mathematical theory of plasticity. Oxford: Oxford University Press 1998
13. **Körner, C.; Singer, R.F.:** Processing of metal foams – challenges and opportunities. Adv Eng Mater 2 (2000) 159–165
14. **Mahrenholtz, O.; Ismar, H.:** Ein Modell des elastisch-plastischen Übergangsverhaltens metallischer Werkstoffe. Abhandlungen der Braunschweigischen Wissenschaftlichen Gesellschaft 30 (1979) 138–144
15. **Mahrenholtz, O.; Ismar, H.:** Zum elastisch-plastischen Übergangsverhalten metallischer Werkstoffe. Ing-Arch 50 (1981) 217–224
16. **Sun, D.-Z.:** Mikromechanische Modellierung duktiler Schädigung in Metallen. In: Tagungsband der 28. Tagung des DVM-Arbeitskreises Bruchvorgänge, pp. 287–304 Bremen: DVM 1996
17. **Tvergaard, V.:** On localization in ductile materials containing spherical voids. Int. J. Fracture 18 (1982) 4, 237–252